DESIGN AND IMPLEMENTATION OF HUMAN CROWD DENSITY ESTIMATION SYSTEM WITH ENERGY HARVESTING IN WIRELESS SENSOR NETWORK PLATFORM

by

SOLAHUDDIN YUSUF BIN FADHLULLAH

Thesis submitted in fulfillment of
the requirements for the degree of
Doctor of Philosophy

May 2017

ACKNOWLEDGMENTS

TABLE OF CONTENTS

CHAPTER FIVE: RESULTS AND DISCUSSIONS

LIST OF PUBLICATIONS

Page

LIST OF FIGURES

Page

The dashed outline of R1 indicates disconnection resulting in the loss connections of the EN from C.

represents the average of 10 RSSI measurements. The horizontal lines show the prediction threshold of each technique that separate between low, medium and high density. The vertical lines indicate the density region of the proposed H-CDE. The high density threshold of all the models is the same as H-CD$_{EHD}$.

LIST OF ABBREVIATIONS

ANOVA   Analysis of Variance

APS   Application Support Sub-layer

API   Application Programming Interface

ASCII   American Standard Code for Information Interchange

AT   Transparent

BLE   Bluetooth Low Energy

BMS   Battery Management System

CSI   Channel State Information

CSMA-CA   Carrier Sense Multiple Access - Collision Avoidance

DMM   Digital Multimeter

DOE   Design of Experiments

DSSS   Direct Sequence Spread Spectrum

DS   Dynamic Human Crowd and Static Receiver

EH   Energy Harvesting

EM   Electromagnetic

EN   End Node

ETSI   European Telecommunications Standards Institute

FHSS   Frequency Hoping Spread Spectrum

GPS   Global Positioning System

GSM   Global System for Mobile Communications

GUI   Graphical User Interface

H-CDE   Human Crowd Density Estimation

HD   High Density

IDE   Integrated Development Environment

IEEE   Institute of Electrical and Electronics Engineers

IC   Integrated Circuit

ICNIRP	International Commission on Non-Ionizing Radiation Protection
ID	Identification
IoT	Internet of Things
ISM	Industrial, Scientific and Medical
ITU	International Telecommunication Union
I-V	Current versus Voltage
LD	Low Density
Li-ion	Lithium ion
LAN	Local Area Network
LOS	Line-of-Sight
LQI	Link Quality Indicator
MAC	Medium Access Control
MANET	Mobile Ad Hoc Network
MD	Medium Density
MPPT	Maximum Power Point Tracking
MSK	Minimum-shift Keying
MTU	Maximum Transmission Unit
NLOS	Non-Line-of-Sight
ODFM	Orthogonal Frequency Division Multiplexing
PAN	Personal Area Network
PC	Personal Computer
PC-ABS	Polycarbonate - Acrylonitrile Butadiene Styrene
PHY	Physical
PMU	Power Management Unit
PSDU	Physical Service Data Unit
PV	Photovoltaic
QFN	Quad-Flat No-Leads

RF	Radio Frequency
RFID	Radio Frequency Identification
RP-SMA	Reverse Polarity-SubMiniature version A
RSSI	Received Signal Strength Indicator
RTOS	Real-Time Operating System
RX	Receiver
S	Static Human Crowd and Receiver
SCPL	Sequential Counting, Parallel Localizing
SD	Secure Digital
SPI	Serial Peripheral Interface
S1	Series 1
S2	Series 2
T-R	Transmitter and Receiver
TX	Transmitter
UART	Universal Asynchronous Receiver/Transmitter
USA / US	United States of America
USB	Universal Serial Bus
WBAN	Wireless Body Area Network
Wi-Fi	Wireless Fidelity
WISP	Wireless Identification and Sensor Platform
WPAN	Wireless Personal Area Network
WSN	Wireless Sensor Network

REKA BENTUK DAN IMPLEMENTASI SISTEM PENGANGGARAN KEPADATAN MANUSIA DENGAN PENUAIAN TENAGA DALAM PLATFORM RANGKAIAN PENGESAN TANPA WAYAR

ABSTRAK

Kepadatan yang tinggi dalam khalayak ramai boleh menjadi berbahaya kerana wujudnya potensi untuk pergerakan sekumpulan manusia secara tiba-tiba yang menyebabkan rempuhan dalam kes kecemasan. Untuk mengurangkan kecederaan mahupun kehilangan nyawa dalam kemalangan yang berkaitan dengan isu kepadatan manusia, sistem pengawasan kepadatan manusia berdasarkan frekuensi radio telah dibangunkan sebagai satu alat keselamatan. Sistem yang didapati pada masa kini mempunyai keupayaan pengawasan yang terhad; saiz pengawasan khalayak yang rendah, jarak pengesanan yang rendah, keperluan bilangan alat komunikasi yang tinggi dan jangka hayat operasi yang terhad. Faktor-faktor ini memberi kesan secara langsung kepada unsur praktikal dan ketepatan sistem penganggaran kepadatan manusia tersebut. Untuk mengurangkan kelemahan keupayaan pengawasan, satu sistem untuk mengesan kepadatan khalayak diusulkan berdasarkan kepada teknologi ZigBee dan rangkaian pengesan tanpa wayar yang meningkatkan jarak pengesanan khalayak kepada 30 m dengan hanya satu nod diperlukan setiap 37.5 m^2. Hal ini dicapai tanpa mengurangkan bilangan khalayak (50 orang) yang boleh dikesan oleh sistem. Untuk menambahbaik ketepatan anggaran, kesan khalayak terhadap isyarat diselidik menggunakan kaedah statistik 'One-way Analysis of Variance' dan 'Design of Experiments'. Hasil dapatan mengesahkan saiz khalayak memberi kesan yang paling besar terhadap kelemahan isyarat. Untuk interaksi di antara sifat-sifat khalayak, didapati saiz khalayak bersama bilangan alat penerima dan bentuk khalayak bersama bilangan alat penerima memberi kesan signifikan terhadap kekuatan isyarat. Faktor-faktor ini kemudian dimasukkan ke dalam algoritma H-CDE yang diusulkan. Algoritma pengesanan khayalak ini dan pengelasannya menunjukkan purata sebanyak 71.2 peratus ketepatan dalam mengenalpasti tahap kepadatan khalayak yang juga

dapatan terbaik berbanding algoritma lain. Untuk mengatasi masalah kuasa yang terhad, mekanisma tuaian tenaga solar diperkenalkan ke dalam sistem H-CDE untuk memanjangkan jangka hayat operasi pengawasan. Kajian menunjukkan mekanisma tuaian tenaga ini mampu untuk memanjangkan operasi sistem pengawasan secara berterusan jika sistem ini mendapat paling kurang 5 hingga 6 jam pendedahan kepada sinaran matahari setiap 33 jam kitaran. Sumbangan kajian ini ialah pada penambahbaikan sistem berdasarkan teknologi frekuensi radio untuk mengesan kepadatan khalayak, penambahbaikan pada ketepatan penganggaran kepadatan khalayak yang didokongi oleh analisis statistik dan lanjutan operasi sistem melalui mekanisma tuaian tenaga.

DESIGN AND IMPLEMENTATION OF HUMAN CROWD DENSITY ESTIMATION SYSTEM WITH ENERGY HARVESTING IN WIRELESS SENSOR NETWORK PLATFORM

ABSTRACT

A crowd with high density can be dangerous due to the potential of a sudden surge of large moving bodies causing stampede in cases of emergencies. To mitigate casualties in crowd-related disaster, radio frequency-based crowd density estimation and monitoring system is being developed as a safety tool. Current systems have limited monitoring capabilities; low size of crowd monitored, low detection range, high number of transceivers required and finite operational lifetime. These factors directly influence the practicality and prediction accuracy of the system. To mitigate the limited sensing capability, a human crowd density estimation (H-CDE) system based on ZigBee and wireless sensor network technology is proposed that increases the crowd detection range to 30 m with only one transmission node required every 37.5 m^2. This is achieved without sacrificing the amount of crowd detectable by the system (50 people). To improve the estimation accuracy, the effect of crowd on signal propagation is investigated using One-way Analysis of Variance and Design of Experiments statistical methods. The results verified that the crowd size significantly affects the signal attenuation. In the interactions between the crowd properties, crowd size * number of receiver and crowd pattern * number of receiver were found to significantly affect signal propagation. These factors are then integrated into the proposed H-CDE algorithm. The H-CDE algorithm and its crowd classification yielded an average of 71.2 % accuracy in identifying the level of crowd density, which is the best compared to other algorithms found in the literature. To solve the finite power problem, a solar energy harvesting mechanism is introduced into the H-CDE system to extend the operation of the monitoring system. It is demonstrated that the proposed energy harvesting mechanism could operate perpetually, given that the system is exposed to good sunlight at least for 5 to 6 hours

in every 33-hour cycle. The contribution of the research is on the improved RF-based crowd density detection system, improved crowd estimation accuracy which is backed by statistical analysis and extension of its operations through the energy harvesting mechanism.

CHAPTER ONE

INTRODUCTION

1.1   Background

Human crowd density estimation (H-CDE) is used to predict the magnitude of human concentration in an area. Understanding about the crowd itself is known as crowd science, whereas the estimation effort is an engineering problem and agenda. A highly crowded area has great potential for injuries and accidents. Thus, H-CDE is important to manage human safety and reduce crowd-related disasters.

Conventional H-CDE systems are based on visuals captured from CCTV. The problem with CCTV is that it is resource extensive in terms of labour and financial cost. On the other hand, radio frequency (RF)-based crowd monitoring system could complement the existing system by offering automated and flexible operation.

Crowd density estimation using RF is less developed compared to visual-based systems due to problems related to the unpredictable wireless medium. The wireless medium is susceptible to white noise; random signals where all possible frequencies are present in the atmosphere, which may qualitatively and quantitatively affect a transmission. The behavior of wireless propagation in the shape of reflection, diffraction and scattering, in addition to absorption and multipath, has also created significant problems and challenges to overcome.

Improved techniques have been developed that shows that the RF-based crowd estimation is feasible. The works of Morrison, Bell and Chalmers (2009), Mowafi, Zmily, Abou-Tair and Abu-Saymeh (2013), Yuan, Zhao, Qiu and Xi (2013), Weppner and Lukowicz (2013), Xu et al. (2013), Weppner, Lukowicz, Blanke and Troster (2014), Xi et al. (2014), Yuan (2014), Haochao et al. (2015) and Hiroi, Shinoda and Kawaguchi (2016) on H-CDE is examined. Furthermore, as the H-CDE system requires wireless sensing, the Wireless Sensor Network (WSN) platform is normally adopted as the foundation of the

networking requirement. Thus, in addition to the existing body of knowledge within the literature, the ability to monitor the crowd density using RF in WSN platform is further explored and presented in this work.

Understanding human crowd features such as crowd size, movement, and spread provides insight into signal fluctuations caused by bodily obstructions. The effects of human crowd properties towards the signal attenuation have been studied by Nakatsuka, Iwatani and Katto (2008), Reusens et al. (2009), Arai, Kawamura and Suzuki (2010), Yuan (2014), Xi et al. (2014) and Haochao et al. (2015). Studies showed that the crowd properties, particularly crowd size, would influence the algorithm formulation and accuracy of the systems.

A problem related to H-CDE system is finite power, especially in portable devices. In full- and semi-mobile deployments or at areas where the mains power is not available, the system necessitates the use of battery as the power source. After a period of time, the battery needs to be replaced or recharged manually. A potential solution to this problem is the introduction of energy harvesting (EH) mechanism into the system. Implementing EH extends longevity of a system and in some cases, allows perpetual operation.

The literature on EH design for RF systems can be traced as early as 2004 by the work of Zhang, Sadler, Lyon and Matroniso (2004) until a fairly recent one such as the research by Ramos, Girbau, Collado and Georgiadis (2015). In essence, the reviews on the EH systems would present the architecture and design discussions necessary for the development of the EH mechanism for the H-CDE application.

To the best of knowledge, an H-CDE system with solar EH capabilities for WSN is the first of its kind. This three in one solution expands the application of each technology. With this expansion, new challenges are discovered that give rise to interesting scope of research.

Lives do matter. The aim of crowd monitoring is to heighten security as to reduce the casualties of precious human lives. Currently, not a single H-CDE system can ensure a

perfect solution to the crowd problem but a collective effort may provide a sufficient degree of crowd security. This stance is a motivation to this research. The proposed H-CDE system of this research may improves upon the works of others. The developed system is also designed based on statistical framework, and is viewed as a novel approach to the problem.

1.2   Problem Statement

The current non-participatory method of H-CDE system found in the literature has three main problems. The problems are explained in points below.

i.   The sensing capability of the H-CDE system is affected by the combination of the range of wireless coverage, the crowd size monitored and the density of receivers. For example, the system developed by Yuan, Zhao, Qiu and Xi (2013) could achieve a very high estimation accuracy of up to 90 %. However, their system has only 4 m of wireless coverage per transceiver and requires a dense deployment of transmitting nodes; one in every 9 m^2 to capture the wireless signal. Moreover, they only predicted the crowd density for up to 12 people. These made their system less feasible in real deployments due to short wireless coverage, small crowd size and dense node requirement.

ii.   The algorithm for the H-CDE systems is primarily modeled based on the effect of the crowd size body obstruction on the Received Signal Strength Indicator (RSSI) (Xu et al., 2013; Yuan, Zhao, Qiu & Xi, 2013; Xi et al., 2014 and Haochao et al., 2015). However, the findings provided by Yuan (2014), Xi et al. (2014) and Haochao et al. (2015) indicates that crowd movement and distribution also have considerable impact on the RSSI and thus affect the overall estimation accuracy. On the contrary, these crowd properties were never integrated into the formulation of

any of the available algorithms. Whereby these factors might actually improve upon the prediction accuracy.

iii.   One of the difficulties facing traditional networked and remote sensing deployment is limited power (Vullers, Schaijk, Visser, Penders & Hoof, 2010; Wan, Tan & Yuen, 2011). Often, batteries are used to power up the devices. For H-CDE application, the system developed by Yuan, Zhao, Qiu and Xi (2013) could support the longest operation at 83 hours. Still, this creates the problem of limited operational lifetime where the battery needs to be replaced or manually recharged after a period of time.

1.3   Objectives

The objectives of the research are:

i.   To improve the sensing capability of the H-CDE system by extending the wireless coverage based on receiver quantity and node density requirement.

ii.   To improve the accuracy of the H-CDE algorithm by formulating a new algorithm as to reach the targeted minimum of 70 % overall prediction accuracy.

iii.   To increase the operational lifetime of the proposed H-CDE node by implementing EH solar mechanism to allow continuous recharging of the battery when sufficient solar light is available.

The sensing capability of the H-CDE system is improved by extending the wireless coverage to 30 m per receiver and the node density requirement is lessened to one every 37.5 m^2. The size of the crowd monitored follows the work of Haochao et al. (2015) which can accommodate up to 50 people. The algorithm proposed is based on multiple crowd properties that significantly affect the signal attenuation in wireless transmission. The

parameters being investigated are crowd size, pattern, movement and crowd distance from the transmitter.

1.4 Research Contributions

This research proposed two improvements. The first is on the accuracy in estimating the crowd density level. The accuracy of the system is improved by formulating a new algorithm that considers the effect of multiple crowd properties (crowd size, pattern and the number of receiver). To identify the important crowd properties, statistical techniques using One-way ANOVA and Design of Experiments were conducted. At the same time, the overall prediction accuracy is also ensured whilst the wireless coverage is extended beyond what is offered in the literature. The requirement of the transceiver placements are also lessened while retaining the size of crowd monitored according to what is currently offered in current research.

The second contribution is on the power solution. This research proposed the use of solar EH to mitigate the finite power problem faced in current H-CDE systems. The EH mechanism proposed allows the system to replenish its own energy and thus operates continuously. The EH mechanism is also designed to support the H-CDE application in both fixed and portable deployments.

1.5 Research Scopes

There are three main assumptions made in the development of the system. The first is the use of square- or rectangular-shaped grids in defining the size of the monitored area. This is consistent with previous works in the literature that aggregate the area into smaller grids based on the range capability of the RF module. The proposed H-CDE system of this research utilizes the rectangular-shaped grid with a length and width of 30 and 5 m respectively. In total, an area of 150 m^2 is monitored using four sensing nodes. The

importance of the wireless coverage and area monitored is that both would influence the accuracy level of the H-CDE system.

The second assumption is that for non-participatory H-CDE systems, both portable and fixed devices were utilized. This is also consistent to previous works reported within the current body of literature. Here, portability is defined as the ability to move the node conveniently and flexibly during setup although the nodes were actually statistically placed in their positions during crowd sensing. Thus, this research would include the portable factor in designing the overall system.

The final boundary of this research is the specific focus on system rather than module development. This research implemented the hardware and software embedment, and interfacing between different modules readily available in the market. As such, the proposed H-CDE system zooms in on the application; algorithm improvement, system design and statistical usage for verification purposes.

1.6   Thesis Layout

Chapter Two reviews the various methodologies and problems with the current H-CDE and EH systems from the existing literature. Chapter Three gives a detailed explanation on the software and hardware design methodologies of the system. Chapter Four lists and discusses the system implementation and experimental procedures relevant to the performance gauging of the H-CDE system. The tests cover the topics of RF, EH, and H-CDE. Chapter Five validates the results of the tests conducted and also discusses the plausible explanation of the findings. The analyses help in justifying the design decisions made for the system. Chapter Six concludes the previous chapters, particularly Chapter Five, to address the objectives of the research. Recommendations for future improvements are also discussed.

CHAPTER TWO
LITERATURE REVIEW

This chapter begins with a short discussion on the wireless problems faced by H-CDE system designers. Next, this chapter examines the existing body of literature on H-CDE and the effect of human crowd properties on signal attenuation from a radio transmission perspective. Then, a brief discussion on the limited power problem and EH are given. This is followed by a thorough review of previous research that implements EH in WSN platform. Lastly, the discussions on the issues pertaining to the current design of the H-CDE and EH system are presented.

2.1   The Radio Design Problem

There are two major problems for RF-based H-CDE. First, RF systems are designed to avoid occlusions to maximize transmission range. Such transmitters are often placed in high line-of-sight (LOS) positions. However, RF-based H-CDE depends on the signal interference itself to sense the crowd, making the design approach different from traditional wireless systems.

Secondly, transmit power, frequency and bandwidth are governed by the standards set by the telecommunication bodies (ITU for USA and ETSI for Europe). Increasing the transmit power to increase the coverage is not always an option. High transmit power may be hazardous to humans, as electromagnetic (EM) waves penetrate and get absorbed by the body. Meanwhile, higher frequencies get absorbed easily by the environment and are naturally composed of high and dangerous energy towards human beings as described by the Planck-Einstein relation (Appendix A) which is best understood using Quantum Field Theory (Appendix B). Eventually, system design is often limited by trade-offs between transmit power, frequency, bandwidth, cost, availability and usability.

These factors create a challenging scenario for low to medium range WSN deployment for the purpose of crowd density estimation. The current RF-based H-CDE systems developed by the scientific community could not possibly cater for thousands of people simultaneously. However, pilot studies of H-CDE provide a proof of concept and on-going progress towards developing better and practical systems.

2.2 Human Crowd Density Estimation

RF-based H-CDE is performed by either the participatory (device-handling) or non-participatory (device-free) techniques. The former requires user to carry the sensing device (Burke et al., 2006; Campbell et al., 2008) whereas the latter is less intrusive to human activities (Patwari & Wilson, 2010).

The participatory method depends on people-counting by distributing tags (or devices) to their subjects and detection using portable or fixed readers. Counting the number of people (tags) alone does not necessarily lead to density estimation. However, it is still possible to estimate crowd density within a given area by mapping the number of tags to geo-location technologies such as Global Positioning System (GPS). Alternatively, the number of counted people divided per area square may also give an indicator of the crowdedness. The problem is that the issue of true scalability is arguable due to requiring the dedicated involvement of participants.

Non-participatory is a parameter-based estimation in which data such as the RSSI obtained between the T-R is analysed. In fact, other kinds of parameters such as the Link Quality Indicator (LQI) and Channel State Information (CSI) are still based on information of received power albeit with additional features. Grids are normally assigned to the area under study to detect the location of the subjects and by employing appropriate algorithms on the RSSI information, the crowd density is then calculated. This approach allows better scalability and easier deployment compared to the participatory technique.

The process of the H-CDE is divided into three parts. The first stage is the Training Phase where raw data is collected to train the algorithm. This is to ensure higher prediction accuracy by sensing the environment with or without the presence of crowd. Once the relevant parameters have been identified and quantified, the algorithm is fully developed and ready to be deployed in the Monitoring Phase. The Monitoring Phase will categorize the crowd density level or predicts the number of people based on the defined signal strength threshold.

Non-participatory H-CDE is mainly deployed in fixed node placement. However, mixed deployments are also adopted by Xu et al. (2013) and Haochao et al. (2015). Although they fixed the placement of transmitters, they could flexibly allocate the receivers in different places. If required, they only need to re-train the algorithm through the Training Phase for every change in the receiver's placement to ensure prediction accuracy.

Table 2.1 lists and highlights the literature on H-CDE. The common platforms used in these works are Bluetooth and Wi-Fi. Weppner et al. (2014), Morrison, Bell and Chalmers (2009), and Yuan (2014) used similar methodology for crowd sensing. These authors use the combination of Bluetooth (people counting) and GPS/Wi-Fi (geo-location) features readily available in smartphones for data collection. Together, these technologies collectively provide information on crowd density in an area.

However, Bluetooth has two huge problems. First, the public rarely has any reason to turn on Bluetooth on their smartphones. The main concern is power consumption. In addition to Wi-Fi and GPS, turning on Bluetooth drains the battery even faster. Unless a smartphone is equipped with Bluetooth Low Energy (BLE), power usage remains a major issue.

Table 2.1: Related works on the RF-based H-CDE systems

Sensing feature	Related work	Platform	Highlights
Participatory	WISP-based by Mowafi et al. (2013)	RFID	Provides framework on crowd density, identification and geographical data at mass event gathering.
	Participatory Bluetooth by Weppner et al. (2014)	Bluetooth and GPS	A system for estimating crowd density and flow at urban environment using Bluetooth on smartphones.
	Augmented Stadium by Morrison, Bell and Chalmers (2009)	Bluetooth and GPS	Provides information visualisation tool for understanding crowd activities, density, location and speed of travel based on MANETs and wireless mesh networking.
	Hand phone crowd monitoring by Yuan (2014)	Wi-Fi and Bluetooth	A proposed collaborative Wi-Fi and Bluetooth features via mobile phones for density estimation.
Non-participatory	Bluetooth collaboration by Weppner and Lukowicz (2013)	Bluetooth	Proposed 6 features that estimate crowd density based on signal strength in an area of 2352.25 m^2.
	Electronic Frog Eye (EFE) by Xi et al. (2014)	Wi-Fi	Utilizes Channel State Information to estimate crowd density, speed, distribution and distance.
	WSN-based (WB) by Yuan, Zhao, Qiu and Xi (2013)	TelosB 802.15.4	Proposed a three phase iterative process of training, monitoring and calibrating to estimate crowd density.
	Wi-Counter by Haochao et al. (2015)	Wi-Fi	Performs crowd counting from three phases; crowdsourcing, offline and online training.
	SCPL by Xu et al. (2013)	CC1000	Grid-based system that utilized high number of transmitters and receivers for crowd counting and localization.
	BLE H-CDE by Hiroi, Shinoda and Kawaguchi (2016)	Bluetooth	Used combination of tag counting and RSSI information to predict the crowd density in indoor environment.

Secondly, most smartphones are equipped with Class 2 Bluetooth (even those at version 4.x) which has an operating range of up to 10 m. The range is too short and performed even worse in dense crowd. As a result, Weppner et al. (2014) and Morrison, Bell and Chalmers (2009) reported an appalling 0.05 % and 5.10 % for detected Bluetooth users in their respective works. Other studies that depended on Bluetooth device discovery also showed very low detection rate (Table 2.2) although Versichele, Neutens, Delafontaine and Weghe (2012a) and Versichele, Neutens, Goudeseune, Bossche and Weghe (2012b) did propose a ratio method to estimate the actual number of people. Only 1.49 % of participants had activated GPS in a survey by Weppner et al. (2014). These percentages are too low to represent an actual healthy portion of the overall population density.

Table 2.2: Related studies that depended on Bluetooth device detection

Authors	Bluetooth detection (%)	Type of analysis	Event
O'Neill et al. (2006)	12.15	Urban design	-
Versichele et al. (2012a)	5.39	Human movement	Festival
Versichele et al. (2012b)	13.00	Crowd mapping	Sports

Mowafi et al. (2013) also faced the same problem as Weppner et al. (2014) and Morrison, Bell, and Chalmers (2009). The RFID-based WISP has a short, 3 meter detection range, making it susceptible to coverage blind spots. In addition, the system developed by Mowafi et al. (2013) also did not provide real-time monitoring. As a summary, the participatory technique is feasible for large deployment but requires huge commitment from the people that is often unachievable due to privacy, commercial and design issues.

Perhaps realising the inherited problem of the participatory method, Weppner and Lukowicz (2013) developed a non-participatory system based on Bluetooth. They utilized the RSSI information from Bluetooth devices and applied 6 features to estimate the crowd

density. Bluetooth devices of the public were detected using static and mobile agents carrying detection devices. Although they claim a 64.9 % of average detection accuracy, their system still suffers from the same problems as before, namely low detection range and scalability issues. The scalability issue arises due to their low (8 %) Bluetooth device detection compared to the whole population.

Similarly, Hiroi, Shinoda and Kawaguchi (2016) also faced the same problems as Weppner and Lukowicz (2013). They distributed BLE tags to each participant, and attempted to estimate the crowd density by counting the number of people around each node. Their system nominally detects the crowd within around 10 meters range around the active nodes. This confirms the limitation of their system, which are low range and scalability issues.

Xi et al. (2014) and Haochao et al. (2015) developed systems based on Wi-Fi signals for device-free crowd counting. Although they did not focus specifically on crowd density, their systems can still perform density estimation. This can be done by dividing the estimated amount of people with the area of measurement. Haochao et al. (2015) utilized Wi-Fi features in smartphones, whereas Xi et al. (2014) used some types of access points or mini computers deployed both at checkpoints and indoors. The problem with these systems is that the coverage is still too short. Both of these systems were tested below 10 m of coverage that only suits small or confined areas.

Another study utilizing crowd counting method is that of Xu et al. (2013). They developed an algorithm called sequential counting, parallel localizing (SCPL) to count and then estimate the location of individuals in grids. The downside of their work is that the number of subjects was only four, which may only fit niche applications.

The work of Yuan (2014) proposed a grid-based WSN system akin to that of Xu et al. (2013) that estimated crowd density from three iterative phases: training, monitoring, and

calibrating. Nevertheless, his system still suffers from the same problem mentioned before, with only 8 m of coverage per node, which is a very short distance.

2.2.1   Non-Participatory Method: Accuracy and Feasibility

A vital criterion in an estimation effort is the level of accuracy. At first glance, the estimation accuracy may indicate the overall efficiency of the system. However, deeper inspections reveal that the accuracy level is dependent on several related parameters. For instance, Yuan, Zhao, Qiu and Xi (2013) reported a 90 % prediction accuracy for a crowd of up to 12 people. However, a huge drawback of their system is that each of their nodes was designed to provide only 4 m of coverage radius, which is evidently very short. For a huge area, they require a large amount of nodes, essentially rendering their system impractical in real establishment.

On the other hand, Xu et al. (2013) offers the best coverage for H-CDE, with 20 m of detection range. Nevertheless, their system could only determine the density of up to 4 people, which is again, very low. This is another example that highlights the same issue as before, where the feasibility of the system is limited.

Another equally important perimeter is the transceiver node density. This parameter indicates the amount of node distributed within the area for crowd sensing. A densely distributed node would become less practical as it may intrude with the crowd's movement. This may raise scalability issues in real world deployment by being both intrusive and impractical due to the associated cost.

Table 2.3 shows the relevant parameters on the current H-CDE systems. Haochao et al. (2015) provides the best feasible H-CDE system due to their more balanced approach in design. Their only apparent drawback is their mediocre RF detection range at 12 m.

Table 2.3: Related parameters on non-participatory H-CDE system

Authors	Crowd size (people)	Average Accuracy	Detection radius per node	Node density
Xu et al. (2013)	4	84 %	20 m	1 per 7.1 m^2
Yuan, Zhao, Qiu and Xi (2013)	12	90 %	4 m	1 per 9.0 m^2
Xi et al. (2014)	30	60 %	8 m	Not disclosed
Haochao et al. (2015)	50	83 %	12 m	1 per 12.0 m^2
Hiroi, Shinoda and Kawaguchi (2016)	40	58 %	10 m	Not disclosed

Improving both the system's accuracy and feasibility are difficult due to factors such as limitations in hardware capability and design methodology. For example, increasing the crowd detection range may be detrimental to the accuracy of the system. This is acknowledged by Yuan, Zhao, Qiu and Xi (2013) where they found out that increasing the range of detection beyond 6 m would bring down the accuracy of their system to less than 70 %. This is a 20 % reduction of accuracy when the range is increased by a mere 2 m. Similarly, accuracy degradation may occur with increasing number of people within the crowd beyond its intended threshold. Hence, these highlighted major gaps that still need to be addressed by researchers as to offer a more practical solution to real crowd problems.

In summary, the performance of the H-CDE system needs to be evaluated not only based on its accuracy, but also on its practicality. There is a need of a balance between the prediction accuracy, size of people monitored, node density and the range of wireless coverage a system can provide. Hence, improvements on systems using non-participatory H-CDE method should focus on these parameters.

2.2.1 (a) Crowd Size-based Algorithm

The algorithm for the H-CDE would determine the accuracy of the system. The primary method in formulating the H-CDE algorithm is to measure the average signal loss (RSSI) inflicted by a single person or group of people. The average RSSI is then adjusted through several rectification techniques to improve its accuracy. The collected RSSI is then compared with the adjusted average RSSI to estimate the crowd density. This technique basically relies on the crowd size to determine the density level.

Figure 2.1, 2.2 and 2.3 show the algorithms proposed by Xu et al. (2013), Yuan, Zhao, Qiu and Xi (2013) and Xi et al. (2014) respectively. These authors introduced the Training Phase to obtain the initial RSSI data to train their algorithms. Once the related parameters have been determined, the density level is estimated in the Monitoring Phase.
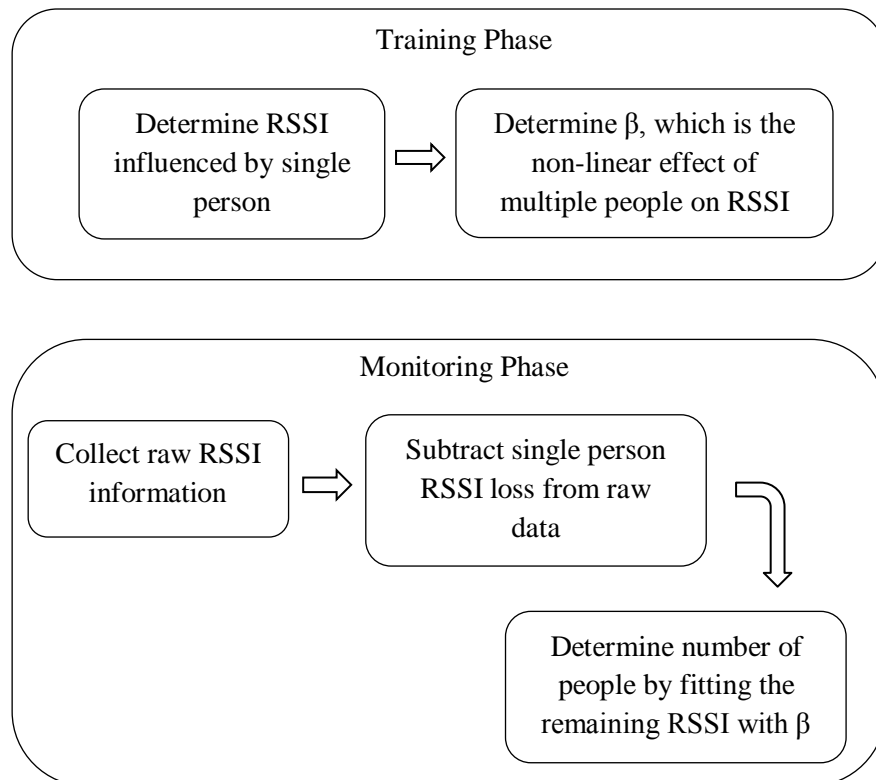
Figure 2.1: Block diagram of the SCPL algorithm by Xu et al. (2013)

The SCPL crowd density estimation for a single grid given by Xu et al. (2013) is:

$$Crowd\ size = \beta(RSSI_x) - |RSSI_1| \qquad (2.1)$$

where $RSSI_X$ is the raw RSSI measured, $RSSI_1$ is the RSSI of a single person at T-R distance d and β (0.83) is the non-linear effect of multiple people on RSSI. The resulting RSSI is then matched with a pre-defined values to determine the number of people. The SCPL uses a single person for training phase to reduce overhead. However, as SCPL was only tested on a maximum of 4 people, thus the level of crowd denseness was not defined.
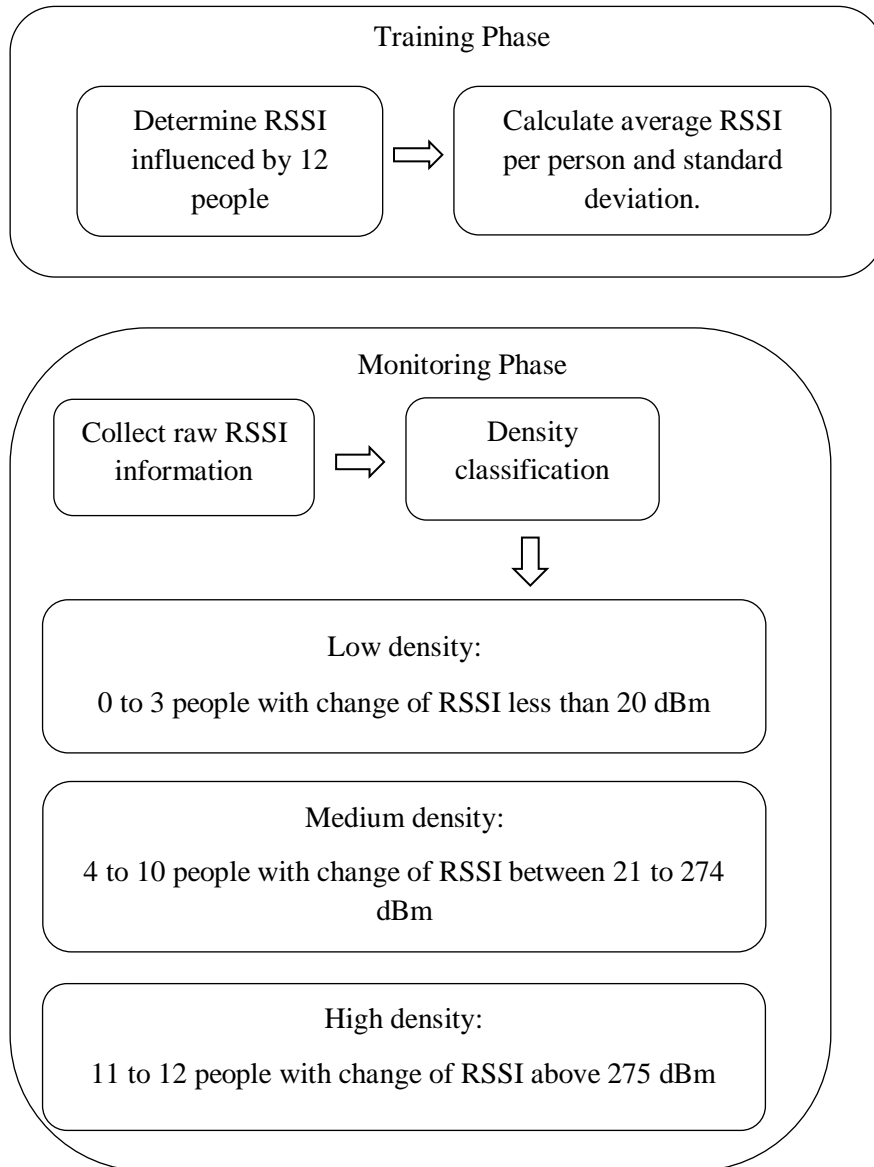
Figure 2.2: Block diagram of the WB algorithm by Yuan, Zhao, Qiu and Xi (2013)
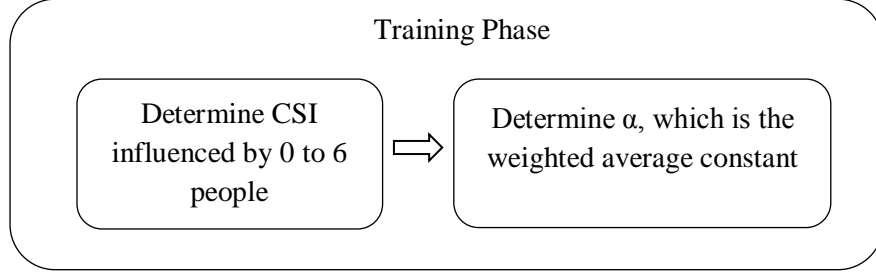
Figure 2.3: Block diagram of the EFE algorithm by Xi et al. (2014)

In contrast, Yuan, Zhao, Qiu and Xi (2013) essentially looked into the collective signal losses inflicted by a crowd of 12 people to determine the average RSSI. The density level is defined by the accumulated change of RSSI collected from all the nodes deployed as in Figure 2.2. The formulation of the WB H-CDE is given as:

$$Total\ signal\ loss = \sum_{k=1}^{n} \left(\frac{RSSI_x}{RSSI_{ave}} \right) \qquad (2.2)$$

where n is the number of nodes, $RSSI_X$ is the measured RSSI and $RSSI_{ave}$ is the average signal loss inflicted by 12 people.

In the Training Phase, Xi et al. (2014) deployed up to 6 people to measure the effect of multiple body obstruction on the CSI. Although they claimed to use CSI, however they did not utilize the phase shift effect in their algorithm. Thus, the CSI signal strength that they measured is exactly the same as the RSSI. The EFE algorithm developed by Xi et al. (2014) is given as:

$$Crowd\ size = \frac{\alpha(RSSI_x)}{(RSSI_x)} \qquad (2.3)$$

where α (0.5) is the weighted average on RSSI and $RSSI_X$ is the measured RSSI. The resulting value is then matched with a defined ratio value to determine the crowd size. Unfortunately, Xi et al. (2014) did not define any density categorization of the crowd.

In summary, the H-CDE systems presented in this sub-section depend solely on one crowd properties for their algorithm formulation, which is the crowd size. As will be discussed in Section 2.2.3, there are multiple crowd properties that may affect the signal loss and thus influence the accuracy of the crowd estimation effort.

Another important finding is that only Yuan, Zhao, Qiu and Xi (2013) defined the crowd density severity into low, mediocre and high density based on the RSSI. The work by Xu et al. (2013) and Xi et al. (2014) did not specifically propose any density classification and would therefore depend on people counting in the overall area to predict the crowd density.

2.2.1 (b) Path loss-based Algorithm

The path loss algorithm is generally used to count the number of people, instead of directly predicting the crowd density. The path loss algorithm calculates the reduction in power density of a wireless signal as it propagates through space (Haochao et al., 2015). Typically, in NLOS, the path loss is modelled after the T-R distance, path loss exponent and shadowing effect caused by physical obstruction.

From the data provided by Haochao et al. (2015), the path loss model of their system is plotted as shown in Figure 2.4, giving the exponential equation as:

$$PL = -74 + 44e^{(-0.126x)} \qquad (2.4)$$

The average signal loss incurred per person from a crowd of 30 people is 2.43 dBm. Similar to crowd size-based algorithm, the path loss-based algorithm developed depends on the RSSI from the size of the crowd. Haochao et al. (2015) also did not define the level of crowdedness whether it is high or low in their research.
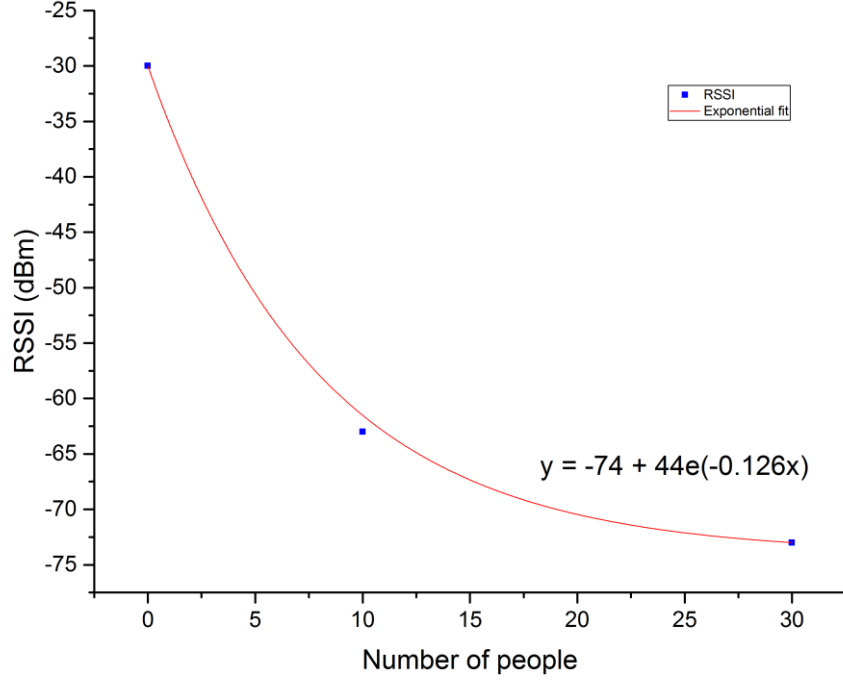
Figure 2.4: Exponential fit for the data on signal loss versus crowd size provided by Haochao et al. (2015)

On the other hand, Hiroi, Shinoda and Kawaguchi (2016) defined the density of people as shown in Figure 2.5 by counting the number of people which gathered near a single point. In essence, their actual technique in determining the crowd size is by mapping the average RSSI recorded by each node to the number of people and then summing them together. However, the level of crowd density could not be connected to the RSSI data as the information was ambiguous and not disclosed by them. Nevertheless, the authors provided the formulation of the Knife-edge diffraction path loss algorithm which is given as:

$$PL = 6.9 + 20 \log \sqrt{(v - 0.1)^2 + 1} + v - 0.1 \qquad (2.5)$$

$$v = h \sqrt{\frac{2}{\lambda} \left(\frac{1}{d_1} + \frac{1}{d_2} \right)}$$

where v is the Fresnel parameter, h is the height of the tag above direct LOS, λ is the wavelength, d_1 and d_2 is the distance from the receiver and transmitter to the node respectively. The formula still allows the prediction of signal loss in terms of T-R distance and height of the node.

19

In summary, the path loss model of Haochao et al. (2015) still primarily relies on the effect of signal loss inflicted by the size of the crowd. Both Haochao et al. (2015) and Hiroi, Shinoda and Kawaguchi (2016) did not specifically classify the density of the crowd based on the RSSI that they measured. These leave pending questions on the actual density that they can measure and the feasibility of their systems in real world application.

	The Number of Participant around a Scanner	Density (People/m²)
(a) Empty	0	0
(b) Low	1-2	0.10-0.16
(c) Moderate	3-6	0.24–0.48
(d) High	7-10	0.56–0.80
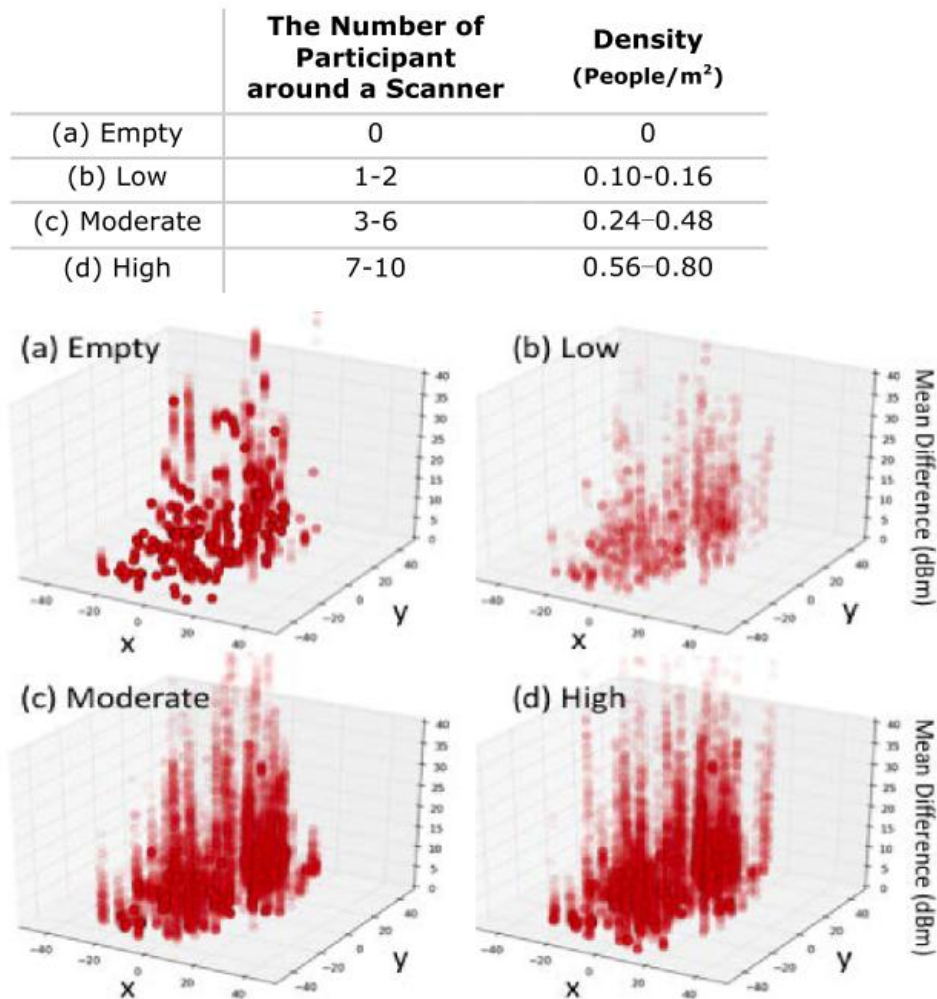
Figure 2.5: Density classification (top) and people count (bottom) provided by Hiroi, Shinoda and Kawaguchi (2016)

2.2.2 Wireless Coverage

Extending the range of the coverage area will directly improve the feasibility of the system. However, the selection of wireless technology and module is related closely to the

power requirement of the system and also the size of the crowd monitored. The power requirement and crowd size issues are discussed separately in Section 2.3 and 2.2.3 respectively. The current wireless standard used in H-CDE is listed in Table 2.4.

Table 2.4: Comparison between wireless standards for H-CDE

Standard / Product	Nominal voltage	Operating frequency	Average current consumption	LOS Range	NLOS Range
ZigBee (Xbee PRO) (Digi, 2015)	3.3 V	2.4 GHz	50.5 mA (+12 dBm)	1500 m	< 60 m
802.15.4 (for TelosB) (Memsic, 2011)	3.0 V	2.4 GHz	23 mA (+0 dBm)	100 m	< 20 m
Bluetooth (BLE, Class 1) (Texas Instruments, 2013a)	3.3 V	2.4 GHz	31.6 mA (+4 dBm)	150 m	< 30 m
Wi-Fi (Smartphone) (Ardito, 2013)	5.0 V	2.4 GHz	100 mA	100 m	< 30 m
CC1000 (Texas Instrument, 2009)	3.0 V	868 MHz	14.8 mA (+5 dBm)	100 m	< 20 m
RF24 (nRF24L01+) (Nordic, 2007)	3.3 V	2.4 GHz	11.3 mA (+0 dBm)	< 100 m	< 10 m
CyFi (Cypress, 2014)	3.3 V	2.4 GHz	34.1 mA (+4 dBm)	100 m	< 20 m

The Wi-Fi standard is deemed unsuitable due its application context of high throughput in local area network (LAN), which would require higher power. In fact, the H-CDE application only requires low data rate for crowd sensing. The BLE looks promise with 30 m of NLOS wireless range. However, in the works of Hiroi, Shinoda and Kawaguchi (2016), they only utilized BLE to around 10 m of range with a disappointing 58 % of estimation accuracy.

The best specification found so far is the ZigBee-based PRO module. The PRO version offers better coverage compared to its non-PRO counterpart. The ZigBee PRO

allows up to 60 m of NLOS albeit at a higher average current consumption. This means that the H-CDE sensing range could be potentially extended past the current-best 20 m mark set by Xu et al. (2013). Thus, the usage of the ZigBee PRO module opens up opportunity for improvement in H-CDE application.

2.2.3 Human Crowd Properties

The effects of the human crowd and its properties on signal attenuation were investigated due to two reasons. First, for 2.4 GHz, the EM signal is absorbed by the tissue of the body and the water inside it (Meli, 2013) and thus causing the signal loss. Secondly, the crowd properties such as the crowd size, movement and distribution would also affect the signal loss. This meant that the accuracy of the crowd density estimation effort would be influenced by these factors.

Related works on human crowd properties are tabulated in Table 2.5. The crowd properties could be classified into three main categories as listed as follows.

i. Body attenuation factor (crowd size)

From Section 2.2.1, it is known that the crowd size is the primary parameter in the H-CDE formulation. Still, there are certain studies that were specifically conducted to understand more about the effect of body attenuation.

Xi et al. (2014), Haochao et al. (2015) and Arai, Kawamura and Suzuki (2010) modeled the human body as a uniform signal obstructer. This made their study on crowd properties much easier as the signal loss inflicted by different body parts can be neglected.

In contrast, Reusens et al. (2009) investigated the effect of the arm, leg, back and torso which is beneficial for research in wireless body area network (WBAN). They found out that the highest signal loss is along the torso. However, to simplify signal loss prediction, they also proposed a whole body path loss model as given in equation 2.6.

$$PL = PL_0 - 10n \log_{10} (d/d_0) \qquad (2.6)$$

where PL_0 is the path loss reference at distance d_0 (10 cm), n is the path loss exponent and d is the T-R separation. The reported values of PL_0 and n are -35.2 dBm and 3.11 respectively with a standard deviation of 6.1 dBm. By representing the whole body as single uniform obstructer, the effect of signal loss can then be focused on the number of people (crowd size) and its impact on H-CDE.

Table 2.5: A list of RF-based research on human crowd properties

Related work	Crowd properties	Application	Highlights
Nakatsuka, Iwatani and Katto (2008)	Crowd movement	Crowd density estimation using Wi-Fi	Static and dynamic crowd inflict almost the same signal attenuation.
Reusens et al. (2009)	Human arm, leg, back, torso, whole body	2.45 GHz wireless body area network	Developed path loss models for different body parts. Compared the empirical model with the simulation - agreeable results.
Xi et al. (2014)	Walking speed and crowd distribution	Crowd counting using Wi-Fi	Fast and slow moving crowd inflict almost similar signal loss.
Haochao et al. (2015)	Whole body and crowd size	Crowd counting using Wi-Fi	Assumed every body part absorbs the same amount of EM energy. Investigated the crowd attenuation factor up to 30 people.
Arai, Kawamura and Suzuki (2010)	Crowd size, movement and flow	Crowd behavior using 2.4 GHz ZigBee	Created matrices of signal attenuation for the crowd properties investigated.
Yuan (2014)	Crowd distribution	Crowd density monitoring using smartphones	A crowd lumped together gives higher estimation accuracy compared to scattered groups of people.

ii.   Crowd movement

Nakatsuka, Iwatani and Katto (2008) and Arai, Kawamura and Suzuki (2010) investigated the effect of static and dynamic crowd towards signal attenuation. Nakatsuka, Iwatani and Katto (2008) found out that the RSSI between static and dynamic crowd were almost the same. Arai, Kawamura and Suzuki (2010) reported that static crowd have less signal fluctuations compared to dynamic crowd (less than 1.2 m/s walking speed). However, they failed to conclude further the significance of the difference.

Xi et al. (2014) reported that low and high walking speed have similar signal strength pattern, while a hybrid gives a higher estimation error. They also found that the crowd estimation accuracy is unrelated to the communication distance, as long as it is below 8 m. The information gathered here indicates that moving or non-moving crowd would inflict similar signal attenuation in wireless environment.

iii.   Crowd distribution

Xi et al. (2014) and Yuan (2014) both used the same distribution of people where they grouped the crowd into two groups of six people, three groups of four people and a single group of twelve people each. However, the problem with their approach is that the proximity of the crowd distribution was neither defined nor verified. Furthermore, they also failed to conclude on the actual impact of their investigations toward the prediction accuracy of their systems.

The discussions presented so far revealed that there seems to be a disconnection between the crowd properties that influence the signal loss with the algorithms developed to detect the density level of the crowd. For example, Yuan (2014), Xi et al (2014) and Haochao et al. (2015) confirmed the impact of the different crowd properties such as movement and distribution on their systems but otherwise, excluded their findings in forming their respective H-CDE algorithms. This left a gap where the crowd properties, in addition to crowd size, could actually be useful in improving the algorithm accuracy of H-CDE system.

The effect of crowd distance on the accuracy of the system was also never addressed. For example, Xi et al. (2014) varied the distances of the crowd between the T-R separation but prior justification were never given on that particular setup. In fact, they actually merged the experiment on crowd distribution and crowd distance into a single one. However, they only presented discussion on the effect of the former while ignoring the latter. Whereas the distance of the people, be it near or far from the transceiver, may affect the value of RSSI measured.

Another gap identified is the lack of knowledge in linking the impact of each of the crowd properties to one another. All of the research listed in Table 2.5 simply assumed that each crowd factor would not be influenced by another factor. In reality, this assumption is naïve as multiple factors would influence the overall signal and accuracy of the system. Thus, more research is needed to better understand the crowd and its effect on signal loss.

2.3   Power Issue in Human Crowd Density Estimation System

Finite power in the sensing devices is a problem that still plagues most WSN establishment. Limited power meant that after a certain amount of time, the device needs to be manually charged by humans. This made the overall system less feasible in real deployments.

The power solutions for non-participatory H-CDE systems are tabulated in Table 2.6. Obviously, the most suitable power source for moveable devices is batteries. The WB H-CDE system by Yuan, Zhao, Qiu and Xi (2013) provides the best operational lifetime at 83 hours. This is equivalent to nearly 4 days of operation before the battery needs to be replaced.

Table 2.6: Power solution for non-participatory H-CDE systems

Authors	Power source	Voltage	Capacity	Current consumption	Lifetime approximation
SCPL by Xu et al. (2013)	CR2032 battery	3.0 V	225 mAh	15 mA	15 hours
WB by Yuan, Zhao, Qiu and Xi (2013)	2 x AA batteries	3.0 V	2000 mAh	24 mA	83 hours
EFE by Xi et al. (2014)	Laptop battery	-	-	-	4 hours
Wi-Counter by Haochao et al. (2015)	Smartphone battery	-	2100 mAh	70 mAh	60 hours
BLE H-CDE by Hiroi, Shinoda and Kawaguchi (2016)	CR2032 battery	3.0 V	225 mAh	13 mA	17 hours

This also indicates that using batteries is unfeasible in the long run. To solve the limited power problem, the EH mechanism offers the best existing solution. Thus, the EH mechanism embedded to the H-CDE system in WSN platform should be pursued to address the limitation in the power problem.

2.3.1 Energy Harvesting

The world is mainly powered by fossil fuels; natural gas, petroleum, diesel and coal. These hydrocarbons are finite energy sources. Such sources also have negative environmental impacts. Thus, the aim of EH is to solve these two problems.

Energy harvesting provides renewable and cleaner energy source that is important for sustainability of humans on Earth. Natural elements such as sunlight and wind are captured or manipulated to generate energy. Mechanical effects from humans and machines, such as vibration and stress, can also be scavenged for energy production.

The traditional EH sources and performances in small and medium deployments are shown in Table 2.7 (Gungor & Hancke, 2009; Paradiso & Starner, 2005; Raghunathan, Kansal, Hsu, Friedman & Srivastava, 2005; Vullers, Schaijk, Visser, Penders & Hoof, 2010; Wan, Tan & Yuen, 2011). To date, harvesting energy from the sunlight remains as the most cost-effective method, partly due to the maturity of the photovoltaic (PV) technology.

Table 2.7: Energy harvesting sources and their capabilities

Energy source	Power density
Outdoor solar	10-100 mW/cm^2
Indoor solar	10-100 μW/cm^2
Piezoelectric	100-330 μW/cm^3
Vibration (machinery)	100-116 μW/cm^2 / 200-800 μW/cm^3
Vibration (human)	4 μW/cm^2
Thermoelectric (machinery)	1-10 mW/cm^2
Thermoelectric (human)	30-60 μW/cm^2
Acoustic noise (100 dB)	960 nW/cm^2
Radio Frequency	0.1-0.9 μW/cm^2
Outdoor wind turbine	3.5 mW/cm^2
Electromagnetic (machinery)	200-1000 μW/cm^2
Airflow	0.4-1 mW/cm^3

The majority of PV cells today are made of crystalline silicon. This is a cheap material but could only offer about 20 % of sunlight to electricity conversion efficiency. A pure silicon PV cell might reach 30 % efficiency albeit with higher cost. A better but expensive alternative is using gallium arsenide PV cell that has an efficiency range from 30 to 40 %.

The harvesting module is rated in power, which is essentially based on the formula of $P = I * V$. Designer must pay attention to the V_{output}, V_{oc}, I_{output} and I_{sc} which respectively represents an ideal voltage output, open-circuit voltage, ideal current output and short-circuit current output of a module. It has to be noted that a module might not be able to perform in its ideal condition, and therefore some reserves must be made to mirror the actual performance.

Presently, solar EH is the only practical solution for H-CDE systems that require constant power of around 150 mW to 500 mW for medium range wireless transmission. The EH technology embedded into WSN platform is explored in the next session.

2.3.2 Energy Harvesting in Wireless Sensor Network

The introduction of EH into WSN nodes will increase operational longevity and to an extent, perpetually replenish its power, allowing it to survive on its own from the energy scavenged from the ambient. The EH node concept is depicted in the block diagram in Figure 2.6 (Glatz et al., 2008; Niyato, Hossain, Rashid & Bhargava, 2007).
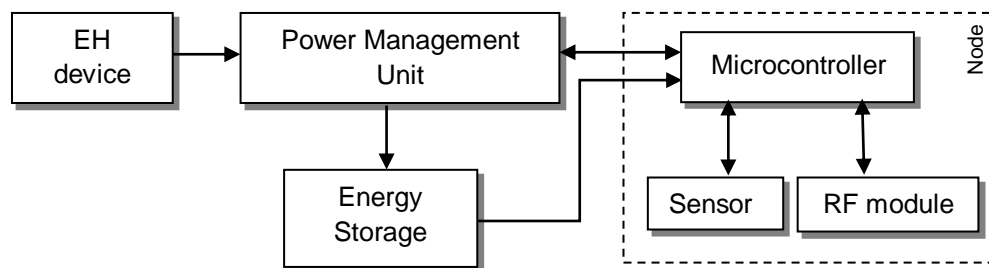
Figure 2.6: System architecture of an EH node

However, implementing EH is challenging, as issues pertaining to performance, efficiency, safety, size, and feasibility needs to be addressed appropriately. This creates a positive and on-going research environment on EH in WSN platform. Table 2.8 lists the related works on EH nodes since 10 years back.

Table 2.8: Related works on energy harvesting nodes

System	Solar cell (mW)	Storage type: supercapacitor and/or battery	Voltage range (V)	MPPT	Highlights
Prometheus	130	22 F and 200 mAh Li-Po	1.5 – 4.4	X	Perpetual operation based on low-powered Telos mote.
Everlast	450	100 F	2.5 – 2.7	√	Supercapacitor based node design.
AmbiMax	400	22 F and 200 mAh Li-Po	2.5 – 4.1	√	Add-on board for EH from multiple sources.
Heliomote	190	1800 mAh Ni-MH	2.2 – 3.0	X	EH add-on board for Mica2 mote.
ZebraNet	400	2000 mAh li-ion	3.1 – 5.0	√	GPS-assisted wilderness animal tracking.
Adaptive MPPT	Up to 400	300 mAh Ni-MH	1.5 – 3.5	√	Implements adaptive ad hoc algorithm for MPPT efficiency.
Battery-less node	N/A	3.3 F	5.0 – 10.5	X	Transmission in a single capacitor charge.
Ultracapacitor based EH	10 000	1 F and 7500 mAh	5.0 – 12.0	X	Bulky medium-powered EH node.
SolarBiscuit	150	1 F	3.6 – 5.0	X	Low-powered battery-less EH node.
HydroSolar	400	Two 2500 Ni-MH	2.1 – 3.6	√	Design modeling for micro-power EH node.
SHiMmer	360	250 F	1.8 – 3.3	X	Structural monitoring without human intervention.

√ = Implemented
X = Not implemented

Supercapacitor is a plausible alternative to the battery as a storage medium. A supercapacitor, otherwise known as ultracapacitor, is simply a high capacity capacitor. The

comparison between supercapacitor and lithium-ion (li-ion) battery is tabulated in Table 2.9. Supercapacitors are rated in Farad and therefore related to Coulombs. Thus, unlike batteries, capacitors are not addressed in Amperage unit. The capacity gauge between the capacitor and battery is further discussed in Appendix C.

Table 2.9: Performance comparison between the supercapacitor and li-ion battery at high capacity. A tick (√) indicates better performance

Parameter	Supercapacitor	Li-ion battery
Density	X	√
Voltage output	X	√
Charging rate	√	X
Discharging rate	√	X
Life cycle	√	X
Weight	X	√
Dimension	X	√

The obvious advantage of a supercapacitor is its theoretically infinite life cycle. This makes a supercapacitor suitable for low-powered and perpetual operation. Whereas li-ion battery typically has 5 years of life cycle before requiring a replacement unit. Nonetheless, in most systems li-ion battery is the preferable storage medium due to the combination of density, voltage level and size factor.

The Everlast (Simjee & Chou, 2006; Simjee & Chou, 2008) and SHiMmer (Musiani, Lin & Rosing, 2007) systems provided frameworks for continuously operating nodes based on very high density supercapacitor as the storage medium. However, the prevailing problem with this kind of supercapacitor is the low voltage output, typically below 3.0 V. To achieve higher voltage, the supercapacitors needed to be connected in series but in turn their capacitance will significantly drop. For example, in series, two supercapacitors rated at 2.3 V

and 100 F will accumulate 5.6 V but only 50 F. The capacitance is halved, as shown in the calculation below.

$$\frac{1}{\frac{1}{100\,F} + \frac{1}{100\,F}} = 50\,F$$

This problem can be mitigated by combining supercapacitors in parallel and series, but it is a weak design approach as it may increase both the size and cost of the system.

SolarBiscuit (Minami, Morito, Morikawa & Aoyama, 2005) and Battery-less node (Kim, Kang, Park, Baek & Park, 2009) were able to design capacitor-based EH nodes with higher voltage albeit at very low capacitor density. Again, this reflects the same problem related to supercapacitors; high voltage but lower density, or low voltage but higher density. This trade-off limits the supercapacitor to niche applications.

Prometheus by Xiaofan, Polastre and Culler (2005) and AmbiMax by Chulsung and Chou (2006) combined both supercapacitor and battery into their node design. The former focused on perpetual and low-powered node but unfortunately did not implement Maximum Power Point Tracking (MPPT) for added efficiency. The latter made strong emphasis on MPPT design and implementation. Both of these works are well presented in their respective design goals. Another related work is the Ultracapacitor-based EH by Naveen and Manjunath (2011). Their design is meant for higher powered nodes, but the efficiency of their design remains ambiguous.

The research that followed the traditional path of battery-based nodes are Heliomote (Raghunathan, Kansal, Hsu, Friedman & Srivastava, 2005), ZebraNet (Zhang, Sadler, Lyon & Matroniso, 2004), Adaptive MPPT (Alippi & Galperti, 2008) and HydroSolar (Taneja, Jaein & Culler, 2008). Heliomote and Adaptive MPPT were both designed as an add-on board for Mica2 nodes. Despite a careful design approach, the former did not implement MPPT. This gap is filled by the latter, but its design is unsuited to mobile applications.

HydroSolar is another system developed as an add-on board for Telos node. The designers of the HydroSolar node proposed a complete model and clear guideline for designing a low-powered solar EH system. The H-CDE system greatly benefits from the framework laid out by the HydroSolar system.

Finally, the work of ZebraNet shared excellent insight and experience on hardware design issues pertaining to a GPS-based EH node. The GPS nodes are placed at collars on zebras that run in the wilderness to track their mobility pattern. Designing a portable node is more challenging than the traditional fixed nodes due to sizing, mounting, weightage, and solar cell alignment.

Currently, the bulk of the EH-WSN research from the literature focuses on improving two aspect; power consumption and supply (Ding, Hou and Xing, 2013). These two cover a broad topic of node efficiency in terms of transmission and routing protocol, topology, sleep mode, clustering, collaboration and expending its application. In addition, with the emergence of companies offering EH-WSN solution such as National Instruments, Libelium and Linear Technologies, the research role on design framework and architecture has mainly shifted from academic institutions towards established commercial entities.

Still, to the best of knowledge, there are three recent works from the literature that are relevant to the EH-WSN framework design. The best example is the Smartmote by Nanda et al. (2014). Smartmote has almost a complete and updated package and its main features are tabulated in Table 2.10.

However, upon closer examination, there are several drawbacks of the system that could be improved.

- The transmission range is only reliable up to 120 m outdoors and 10 m indoors. This is considered low.
- The buck converter can be removed with careful EH element and PMU selection.

- The Fuel Gauge can be replaced with a much simpler over- and under-voltage protection mechanism.

- Smartmode is programmed with 128 resolutions for charging 1000 mAh Li-Po battery. The storage capacity can be improved.

- The overall power consumption is quite high; 67.57 mA in average and 132.34 mA at its peak.

- The chosen (5.6 V, 73 mA) solar cell is actually not properly matched for the Smartmote due to its maximum power consumption rating. The system would depend a lot on the buck converter to provide sufficient current. It is suspected that if the optimal sunlight irradiance is cut by half, the system would suffer transmission problems.

- It requires 9 hours of battery charging to reach 90 % capacity. This means that the node requires more than a day of bright light to fully charge its battery.

Table 2.10: Features available on the Smartmode

Features	Description
Protection	Electrostatic discharge (ESD) and electromagnetic compliance (EMC)
Dynamic Voltage Scaling (DVS)	Changeable microcontroller operational frequency based on need
MPPT	Maximize harvested energy
PMU	Buck-boost converter and low-dropout (LDO) regulator
Transmission protocol	802.15.4 and ZigBee
Security	128 AES
Fuel Gauge	Battery voltage sensing
Sensor	Varying types supported
Over the air programming	Allows software updates to be sent wirelessly to the node, without shutting it down

Next, the work of Ramos, Girbau, Lazaro, Collado and Georgiadis (2015) is referred. They proposed a solar-powered RFID with temperature sensing and calibrating capabilities. The sensing feature made their system akin to a WSN. The focus of their design is on empowering a battery-less ultra-wideband (UWB) RFID with energy harvesting mechanism to measure the temperature of the environment.

The main problem is that the design looks overly complicated. Temperature sensing using traditional WSN technology has been around for a long time with major benefits not available to their proposed system. The UWB RFID is verified experimentally to have only around 1.5 m of transmission distance. Plus, the EH mechanism deployed only uses a voltage regulator, which is generally inefficient due to internal loss. Lastly, the battery-less design is risky considering their solar cell is rated at 28 mA (short-circuit current), raising reliability issues in light deprived conditions.

Another design of interest is the works of Schmid, Gaedeke, Scheibe and Stork (2012). The authors proposed a combination of MPPT with direct coupling switching to increase EH efficiency. They argued that MPPT usage in low-powered systems (few µW and mW) is not suitable due to internal loss and to solve this problem, they suggested the direct coupling method.

The problem with their approach is that the direct coupling switching mechanism is only beneficial if the power harvested is less than 25 mW. At this power rate, most systems would cease to operate and the point of using the direct coupling is already lost. The system also operates at a low voltage of a minimum of 1.8 V which is matched with an array of 20 solar cells producing an optimal output of 6 V and 77 mA. Instead, a boost converter coupled with a solar cell with higher current but lower voltage output might be a better alternative to minimize reliance on the converter to supply sufficient current to its CC2520 RF module. Furthermore, the transmission distance based on the RF module used is low, reaching only around 100 m outdoors in LOS signal propagation.

2.3.3 Issues in Developing the Energy Harvesting Mechanism

So far, the reviews from Section 2.3 reveal three problems that must be addressed in designing the EH mechanism for an H-CDE system. First, there is a lack of dedicated design on 3.3 V system. The 3.3 V is one of the de facto voltage levels in small and portable wireless devices and putting an emphasis on this can improve overall power efficiency. Furthermore, RF transmission requires sufficient power as to reach the intended wireless range. For example, the 1.8 V module utilized by Schmid, Gaedeke, Scheibe and Stork (2012) typically could only reach less than 20 m of coverage in NLOS scenario.

Secondly, the EH element needs to be matched with the specification of the H-CDE application. Specifically, the PMU and wireless module would influence the entire design of the EH mechanism. With the expanded wireless coverage for crowd monitoring, the system may also demand higher power. Thus, a careful match between sub-systems within the system may reduce power loss from the input until the output.

Third, the capacity of the battery storage should be increased to ensure reliable operation. At the same time, the EH mechanism should be able to recharge the battery within an acceptable amount of time to make it practical for actual usage. Finally, any amendment and improvement to the design should not interfere with the RF transmission and must also be ensured to be safe for usage.

All of these problems stem from the absence of a dedicated EH mechanism for H-CDE system. Table 2.11 shows that EH and H-CDE has never been implemented together in WSN platform. The common approach taken by researchers is to focus only on a single aspect; to exclusively implement EH or H-CDE. However, a system with a comprehensive EH design may not be suitable for H-CDE application whereas a system's architecture focusing solely on H-CDE may not be able to implement EH properly.

When combined, the knowledge gaps identified warrants the need of further scientific research. An improved design on H-CDE system should be proposed to tackle the current limitations.

Table 2.11: Availability of WSN, EH and H-CDE elements in related works

Related work	WSN	EH	H-CDE
Mowafi et al. (2013)	√	X	√
Weppner et al. (2014)	√	X	√
Morrison, Bell and Chalmers (2009)	√	X	√
Yuan (2014)	√	X	√
Weppner and Lukowicz (2013)	√	X	√
Xi et al. (2014)	√	X	√
Yuan, Zhao, Qiu and Xi (2013)	√	X	√
Haochao et al. (2015)	√	X	√
Xu et al. (2013)	√	X	√
Nanda et al. (2014)	√	√	X
Ramos, Girbau, Lazaro, Collado and Georgiadis (2015)	√	√	X
Schmid, Gaedeke, Scheibe and Stork (2012)	√	√	X
Naveen and Manjunath (2011)	√	√	X

√ = Implemented
X = Not implemented

2.4 Summary

The overall accuracy of the H-CDE system is dependent on the coverage, node density and crowd size supported by the system. These parameters would affect the feasibility of the system. Findings signify that Haochao et al. (2015) has the most balanced and practical H-CDE system to date.

The accuracy of the density estimation also relies on the algorithm developed. There are two methods for non-participatory H-CDE which are crowd-sized based algorithm and path loss modelling. The basic formulation of both techniques is based on the average RSSI incurred by the bodily obstruction of the people. In essence, the crowd size is the main factor influencing the formula of the H-CDE algorithm.

The crowd size is only one of the properties of the crowd. There are also other parameters such as crowd movement and distribution that have been verified to influence the RSSI measured. However, the current body of literature does not consider these remaining parameters into the algorithm.

The wireless standard and module selected determines the range and therefore the applicability of the H-CDE system. Wi-Fi (Haochao et al., 2015; Xi et al., 2014), Bluetooth (Hiroi, Shinoda and Kawaguchi (2016) and 802.15.4 (Yuan, Zhao, Qiu and Xi, 2013) technologies has been utilized for crowd sensing which offer coverage of up to 20 m. Still, there are opportunities for improvement with the availability of improved RF modules.

In the power segment, the current H-CDE systems rely primarily on battery as the power source. The system by Haochao et al. (2015) offers the highest battery capacity at 2100 mAh although the system proposed by Yuan, Zhao, Qiu and Xi (2013) could last the longest at 83 hours of continuous operation. This power limitation also raises the question of feasibility in real environment. Thus, EH offers the best solution for this problem.

Table 2.12 tabulates the best features available from current systems reported within the literature. The table also highlights information on the limitations of current systems as well as the opportunities for enhancements.

Table 2.12: Best features on current systems. (Colour code: blue for H-CDE and red for power / EH)

Parameter	Best case / Main focus	System developer
Accuracy	Up to 90 %	WB by Yuan, Zhao, Qiu and Xi (2013)
Deployment range	20 m	SCPL by Xu et al. (2013)
Crowd size	50	Wi-Counter by Haochao et al. (2015)
Node density	1 per 12 m^2	Wi-Counter by Haochao et al. (2015)
Crowd properties	Crowd size	SCPL by Xu et al. (2013), WB by Yuan, Zhao, Qiu and Xi (2013), EFE by Xi et al. (2014), Wi-Counter by Haochao et al. (2015) and BLE H-CDE by Hiroi, Shinoda and Kawaguchi (2016)
Battery storage	2100 mAh	Haochao et al. (2015)
Operational lifetime	83 hours	WB by Yuan, Zhao, Qiu and Xi (2013)
Portability	Solar cell	ZebraNet (Zhang, Sadler, Lyon & Matroniso, 2004)

As a final note, there are still gaps in the current H-CDE and EH systems in WSN platform. More research is still required to expand the functionality and feasibility of the crowd monitoring application. In addition, the combination of H-CDE, EH and WSN in a single platform also requires its own pilot study.

METHODOLOGY

The design methodology of the proposed H-CDE system is divided into three sections as shown in Figure 3.1. The first is on the improvement of the accuracy by enhancing the system's sensing capability. Second is on the improvement of the estimation algorithm while the third is on the extension of the operational lifetime of the system. These reflect the three objectives on the research.
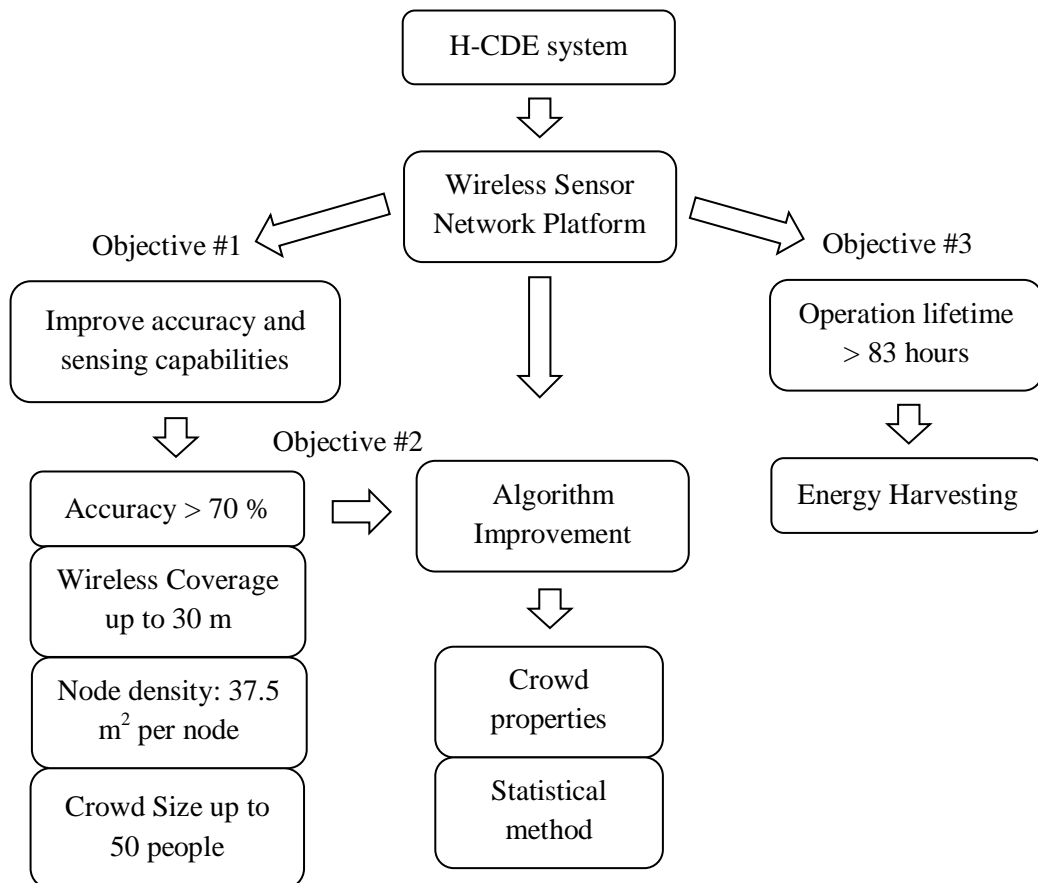
Figure 3.1: Overall research approach for the proposed H-CDE system

The accuracy and feasibility of the proposed system is heightened by focusing on improving three parameters; transceiver wireless range, node density and the size of crowd monitored. The proposed improvements of these parameters are as illustrated in the figure.

To ensure better accuracy, the algorithm is further developed by implementing statistical techniques to identify the significant crowd properties. These crowd properties would be represented as important variables within the algorithm. In the final section, the solar EH mechanism is embedded into the H-CDE system to solve the finite power problem.

3.1 Wireless Sensor Network Platform

The proposed H-CDE system adopts the centralized WSN architecture as illustrated in Figure 3.2. Essentially, the WSN is the networking backbone of the H-CDE monitoring system. The Coordinator is responsible for network establishment and sustenance, data collection and processing while the End Nodes act as the sensing devices. The End Node would report the RSSI information periodically to the Coordinator whereby any disturbance on the RSSI would indicate the presence of crowd.
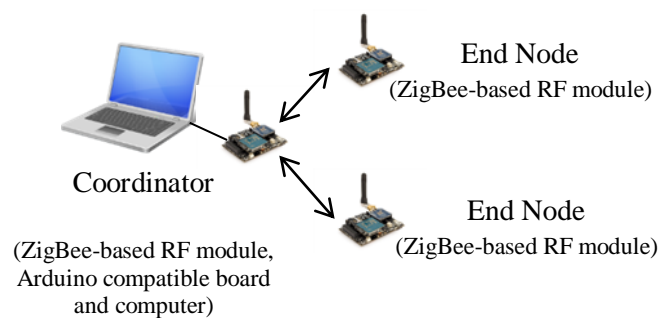
Figure 3.2: Centralized WSN deployment

The WSN data transmission is handled by the ZigBee-based transceivers. The data collected by the transceivers is processed for H-CDE by the Arduino-based Coordinator. The Coordinator would then store and display the real-time density status of the crowd through the GUI at the computer. The roles taken by the Coordinator and End Nodes are tabulated in Table 3.1.

Table 3.1: Functionality of the Coordinator and End Node of the WSN

Function	Coordinator	End Node
Network creation and recovery	√	X
Crowd sensing (RSSI-based)	X	√
H-CDE algorithm	√	X
Cloud access	√	X

√ = Applicable
X = Not applicable

The microcontroller-based Arduino is opted instead of other WSN platforms such as the MSP430 (Bol et al., 2013; Mikhaylov & Tervonen, 2010), Telos (Zhao et al., 2013; Yuan, Qiu, Xi & Zhao, 2013) and Mica (Luo & Chen, 2012; Aguirre, Gaviria & Aedo, 2009) as it allows rapid hardware prototyping, flexible customization and excellent community support.

3.2   Crowd Density Estimation

The information on the existing sensing capabilities is previously presented in Table 2.3. With the improvement proposed by this research, the table is updated as given in Table 3.2. The site under study is 30 m in length and 5 m in width for a total area of 150 m^2, which represents a single grid in the proposed WSN H-CDE deployment. The 150 m^2 area also matches the area of study by Xu et al. (2013). However, Xu and his team require 21 transceivers as opposed to only 4 proposed by this research.

The H-CDE algorithms of all the related works will be applied to this same 150 m^2 area for prediction accuracy verification and the results presented in Chapter 5. Comparisons between the experimental layouts are pictured in Figure 3.3.

Table 3.2: Comparison between the proposed H-CDE system with other related works

Authors	Crowd size (people)	Detection radius per node	Node density
Proposed H-CDE system	50	30 m	1 per 37.5 m^2
Xu et al. (2013)	4	20 m	1 per 7.1 m^2
Yuan, Zhao, Qiu and Xi (2013)	12	4 m	1 per 9.0 m^2
Xi et al. (2014)	30	8 m	Not disclosed
Haochao et al. (2015)	50	12 m	1 per 12.0 m^2
Hiroi, Shinoda and Kawaguchi (2016)	40	10 m	Not disclosed
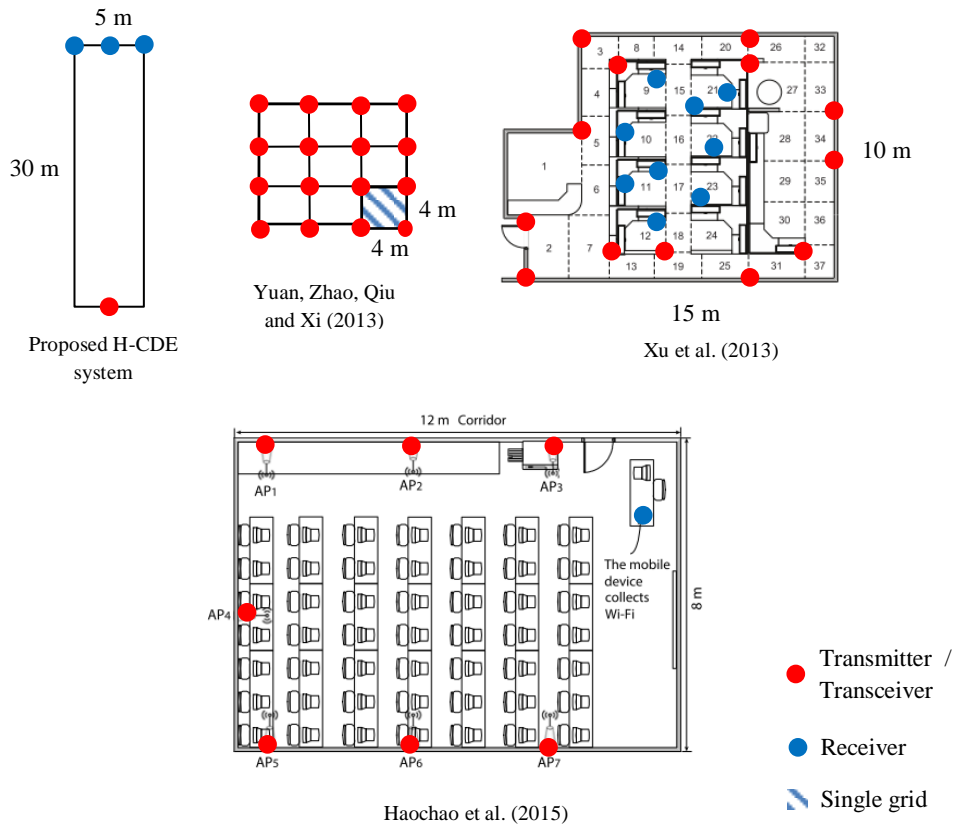
Figure 3.3: Layout comparisons. The layouts of Xi et al. (2014) and Hiroi, Shinoda and Kawaguchi (2016) were not illustrated as the information was not made available.

3.2.1 (a) Algorithm and Estimation Accuracy

Section 2.2.1 in Chapter Two reveals that the conventional method of estimating the crowd density is by taking the average signal loss (RSSI) per person from body obstruction and then subjecting it to normalization. The method is depicted in Figure 3.4. By dividing the measured RSSI with the normalized average RSSI per person, the crowd density level can be estimated from the classification defined.
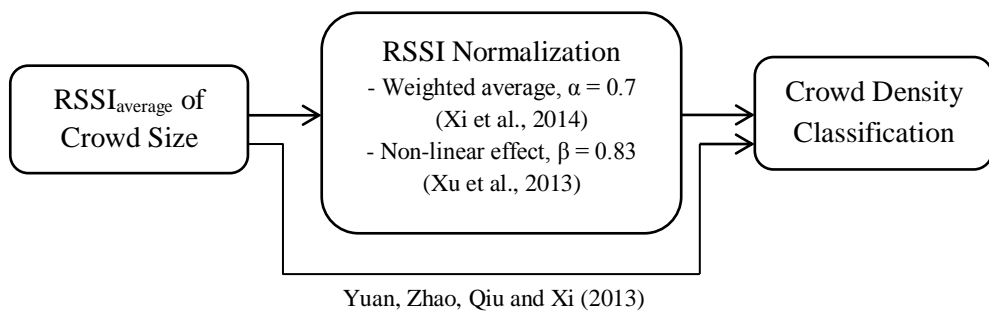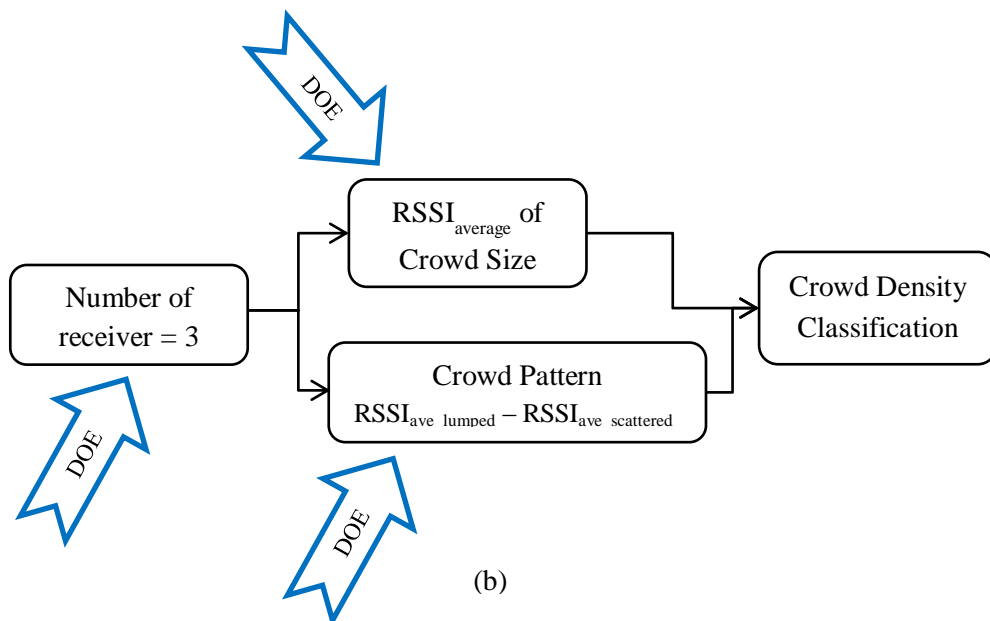
Figure 3.4: Comparison between the algorithms of (a) related works with (b) the proposed H-CDE system

The method offered by the proposed H-CDE system is different in that three additional features were introduced for improving the estimation accuracy. First, in addition to the signal loss inflicted by body obstruction of the whole crowd (crowd size), the effect of crowd pattern (distribution) was also integrated into the algorithm.

Secondly, the number of receiver is limited to 3 whereas this parameter is not justified by any previous works on H-CDE. Third, the inclusion of the crowd size, crowd pattern and number of receiver into the proposed algorithm were justified using DOE statistical analysis.

3.2.1 (b) Density Classification

Yuan, Zhao, Qiu and Xi (2013) provided the most transparent information on classifying the density severity of the crowd compared to other works in the literature. Table 3.3 shows their classification based on RSSI. The RSSI is calculated from the average signal loss measured at each node and also incurred per person per node from a total of 16 nodes. However, they do not indicate the method in aggregating the density level versus the number of people. As they trained their algorithm for up to 12 people, thus, they only monitored and classify the density level for up to 12 people. It is therefore assumed that they fitted their density level based on trial and error process to get the most accurate prediction.

As the mechanism to classify the density level is devoid from deeper discussion, the proposed H-CDE system would implement the classification based on the average signal loss incurred per person per node similar to Yuan, Zhao, Qiu and Xi (2013). For determining the threshold between different levels of crowd density, the following conditions were proposed:

Table 3.3: Density classification by Yuan, Zhao, Qiu and Xi (2013)

Density Level	Number of people	Signal loss per node (RSSI)	Signal loss per node per person (RSSI)
Low	0 to 3	< 1.25 dBm	0.42 dBm
Medium	4 to 10	1.31 until 27.13 dBm	1.71 dBm node
High	11 to 12	> 22.92 dBm	1.56 dBm

i. The trained data is based on 15 people and 3 receiver nodes whereas the total monitored crowd size is 50. This is to reduce overhead as explained further in Section 3.2.2 (b). From the 15 people, it is further divided into three groups, 5, 10 and 15 people to verify the signal loss effect on increasing number of people. This is a similar approach as Yuan, Zhao, Qiu and Xi (2013), Xi et al. (2014) and Haochao et al. (2015).

ii. For low density level, the RSSI threshold is defined from the average signal loss inflicted by the lowest group of people (5 people). To increase prediction accuracy, the threshold is enhanced by adding the signal loss effect from crowd pattern. The crowd pattern is discovered to be significant in inflicting signal attenuation from the DOE experiment conducted when coupled with three receiver nodes.

iii. For medium density level, the RSSI threshold is defined based on the maximum signal loss inflicted by 15 people; the maximum crowd size sampled in the Training Phase. In contrast, Yuan, Zhao, Qiu and Xi (2013) used only 10 out of 12 people (83.3 %) whereas the proposed H-CDE uses 15 out of 15 people (100 %) of the sampled data to represent medium density. The effect of crowd pattern is also introduced into the proposed H-CDE classification.

iv. The high density level is defined based on the RSSI that goes beyond the maximum signal loss inflicted by the medium level (16 to 50 people). The effect of crowd pattern is also introduced into the classification to improve prediction accuracy.

Hence, the proposed crowd density classification is given as follows:

Low density (LD): $LD \leq RSSI_{ave\_5} + RSSI_{crowd\_pattern}$ (3.1)

Medium density (MD): $RSSI_{ave\_5} + RSSI_{crowd\_pattern} < MD \leq RSSI_{max\_15} + RSSI_{crowd\_pattern}$ (3.2)

High density (HD): $HD > RSSI_{max\_15} + RSSI_{crowd\_pattern}$ (3.3)

where $RSSI_{ave\_5}$ is the average signal attenuation of a crowd consisting of 5 people, $RSSI_{crowd\_pattern}$ is the average signal difference between scattered and lumped crowd of the crowd pattern * number of receiver interaction and $RSSI_{max\_15}$ is the maximum signal attenuation of the 15 people crowd. The $RSSI_{max\_15}$ is chosen instead of the average as to set the upper limit of the effect of 15 people. This is due to the crowd modelled discretely (5, 10 and 15 people) using DOE instead of a continuous number (17, 18, 19).

3.2.1 (c) Path Loss Model

The signal path loss model consists of mathematical equations which attempt to estimate the signal propagation and attenuation. The benefits of the models are that they allow radio-planning and link-budget. For H-CDE, the path loss model is used to estimate the number of people.

In Section 2.2.1, two path loss models were identified from the works of Haochao et al. (2015) and Hiroi, Shinoda and Kawaguchi (2016). In short, they formulated their model based on the RSSI from the size of the crowd and the distance between the T-R respectively.

The H-CDE system proposed an empirical model similar to Reusens et al. (2009) and Haochao et al. (2015) which is based on the path loss shadowing model, which its root can be traced back in the early works of Seidel and Rappaport (1992). The model by Seidel and Rappaport (1992) is given as:

$$PL = PL_0 - 10n \log_{10}(d) - X$$ (3.4)

where PL_0 is the RSSI at 1 m T-R separation, n is the path loss exponent, d is the T-R distance and X is the shadowing effect caused by the crowd. To adapt the model to H-CDE, the path loss model is modified as:

$$PL = PL_0 - 10n \log_{10}(d) - RSSI_{crowd\_pattern} - BAF \qquad (3.5)$$

where $RSSI_{crowd\_pattern}$ and BAF represents the average signal loss incurred by the effects of crowd pattern and the body attenuation factor; the effect of crowd size of signal attenuation respectively. The value of the path loss exponent, n, $RSSI_{crowd\_pattern}$ and BAF are calculated from the data collected in the DOE section.

As before, the introduction of these two parameters are the results of the DOE method where crowd pattern and size were identified to be significant parameters in inflicting the loss of signal in crowded environment. This should increase the accuracy of the model to suit H-CDE application.

3.2.2 Statistical Methods

The correct type of statistical analysis to be conducted depends on the objective of the research on crowd properties. A one-way ANOVA is able to determine statistically significant differences among the means (average) of two or more groups (Minitab, 2012). The 'one-way' signifies that only a single parameter is of interest in the test. On the other hand, the DOE is the most suitable method to determine the complete effect and inter-correlation between numerous factors which cannot be achieved by the ANOVA.

3.2.2 (a) One-way Analysis of Variance

ANOVA is not unique to a specific discipline. It is simply a tool to assist scientists in testing the hypothesis and making the better decision or conclusion. For example, Younis et

al. (2014) uses ANOVA to verify the efficiency of the model proposed for wastewater treatment using microwave irradiation, Ya'acob, Hizam, Radzi and Kadir (2013) applied ANOVA to model the PV array temperature model and Rai et al. (2013) utilized ANOVA to identify the significant parameters in building materials using red mud.

Table 3.4 shows the type of analysis which is matched to the current knowledge on the effect of crowd properties for RF-based H-CDE. The crowd size has already been identified as a significant parameter in inflicting high signal losses. This is confirmed by the reliance of previous researchers in forming their H-CDE algorithms based on the RSSI measured from crowd size (Xi et al., 2014; Haochao et al., 2015; Xu et al., 2013; Yuan, Zhao, Qiu and Xi, 2013; Hiroi, Shinoda and Kawaguchi, 2016). Thus, only the DOE method is needed to investigate the influence of crowd size in incurring the signal loss with the presence of other crowd properties.

Table 3.4: Justification for the statistical methods conducted

Crowd properties	Significant effect on signal loss	One-way ANOVA	DOE
Size	Known	X	√
Distribution	Unknown	X	√
Distance	Unknown	X	√
Movement	Minimal understanding	√	X

On the other hand, there is insufficient knowledge on the effect of crowd distribution and distance towards signal loss and hence, their effect on the estimation accuracy. Xi et al. (2014) and Yuan (2014) conducted tests on the distribution of the crowd but came short from concluding any strong remarks on their effect towards the prediction accuracy. The effect of crowd distance from the T-R separation was also never thoroughly investigated by any of the researchers. These gaps require the use of DOE to determine their overall effects on signal attenuation.

In contrast, the effect of crowd movement was briefly discussed by Nakatsuka, Iwatani and Katto (2008). They found out that the effects of static and dynamic crowd is almost the same. To verify this claim, the One-way ANOVA method is suitable to be used to investigate this single parameter.

If the average difference of the signal attenuation between static and dynamic crowd is statistically insignificant, then the effect of a moving crowd can be removed from the DOE test. The hypotheses are given as follows:

$$H_0 : \mu_S = \mu_S \qquad\qquad (3.6a)$$

$$H_1 : \mu_S \neq \mu_{DS} \qquad\qquad (3.6b)$$

where H_0 and H_1 are the null and alternate hypothesis respectively, μ_S, is the mean for static human crowd and receiver, μ_{DS} is the mean for dynamic human crowd and static receiver.

For the analysis, Tukey's method is one of the four available comparison methods for one-way ANOVA. Tukey's method is used to control the rate of type I error (false positive) by comparing the means for each pair of factor levels using a family error rate. A family error rate is the probability of causing the false positive error. Tukey's method also adjusts the individual confidence level based on the 5 % family error rate chosen. The most important parameters produced by this analysis are *P*-value, *S* and *R*-square.

The *P*-value determines whether the null hypothesis will be accepted or rejected. If *P* is less or equal to the selected α-level, then the means are significantly different. If *P* is larger than α, then the means are not significantly different. The value of α is set according to the norm of the field of study. Typically, the α-level is set to 5 %, which corresponds to 95 % confidence level of the hypothesis.

The parameters of *S* and *R*-square measure how well the model generated by the statistical tool fits the data. *S* represents the standard deviation which is the average distance

data values deviate from the fitted values. *R*-squared is a statistical measure of how close or varied that data compared to the prediction model.

3.2.2 (b) Design of Experiments

Design of Experiments (DOE) is a statistical method that brings several benefits when applied to scientific problems. The benefits are listed below (Litvinski & Gherbi, 2013; Liu, Chen, Jing & Chen, 2010; Montgomery, 2009). At its core, DOE is a strategy of experimentation, from pre- to post experiment.

i.   A DOE corrects experimental framework. It ensures that the procedure and setup of the experiment are statistically correct before any measurement is made. For example, a DOE implements randomness and repetition that addresses the issue of biasness.

ii. The DOE validates the findings of the proposed model and the results. It can be used as a validation mechanism when the proposed solution has no equivalent comparison in the literature or from modelling simulation.

iii. It allows the verification of all interactions between parameters involved and the degree of their significance. This solves the problem of 'one-factor-at-time experiments' which is the incomplete conclusion resulted from the effect of a single parameter measured one at a time. This can be seen from the works of Yuan, Zhao, Qiu and Xi (2013) and Yuan (2014) where their research may suffer from unintentional biased results as each parameter is investigated separately from one another.

iv. DOE determines the optimized output from a system that has multiple inputs (factors).

DOE has been implemented in many scientific disciplines including in telecommunication field. For example, Chen, Chen and Li (2011) presented an optimized design of dual-antenna for passive RFID tags. Using DOE and verified using software simulation, they were able to identify the most optimal and simplified geometric parameters to design a complicated dual-antenna structure. Another example is where Angrisani, Moriello, D' Apuzzo and D' Arco (2011) utilized DOE to help them shape the power performance assessment for digital signal processing in wireless systems. With DOE, they were able to reduce the number of experiments and identify significant parameters as to retain a level of relevance in creating the assessment methodology.

There are several types of designs for DOE. The selection of design is based on the objective and sample size of the experiment. Table 3.5 shows the characteristics of each type of design.

Table 3.5: Selection guide for DOE

Type of design	Characteristics
Factorial	- For small number of factors with few levels. - Interaction is expected to be strong and important. - Every factor contributes significantly. - Either full factorial (full interaction) or fractional (partial) factorial.
Taguchi	- For intermediate number of factors, up to 50. - Few significant interactions are expected from the factors. - Only a few variables contribute significantly.
Response surface	- For finding the optimized response. - For finding factor response that satisfies the specification sought. - Vital few factors expected.

The main purpose for the DOE implementation is to identify three crowd properties (in addition with the use of different number of receivers) and their interactions that have significant effects on the signal attenuation. Thus, the full factorial DOE matches with this aim. The DOE also provides the input for the Training Phase. These inputs (crowd properties) would influence the H-CDE algorithm for crowd density classification. A list of factors and their respective levels for the DOE has been tabulated in Table 3.6.

Table 3.6: Factors and levels of the DOE test

Factors	Level 1	Level 2	Level 3
Crowd size (people)	5	10	15
Crowd pattern	Scattered	Lumped	-
Crowd location (m)	10	20	30
Number of receiver	1	2	3

The DOE test is subjected to limitations and their scopes are listed below;

(1) Modelling an individual body attenuation factor was not pursued as different body parts and body size absorb almost the same amount of energy (Xi et al., 2014; Haochao et al., 2015; Arai, Kawamura and Suzuki, 2010). This creates the assumption that the orientation of the human body (frontal, sideways and back) would in average, produce almost similar signal attenuation. The average height and mass of the people forming the crowd are 163.20 cm and 66.28 kg, and are all of an Asian ethnicity.

(2) The effect of relative heights of the T-R antennas was not investigated. The H-CDE system depends entirely on body obstructions to measure the signal loss and train the algorithm. Prior test showed that a high placed T-R would bypass the crowd and can produce a line-of-sight signal measurement. Thus, it is assumed that highest signal loss is at the torso region (Aguirre et al., 2012; Reusens et al., 2009). Secondly, it has

also been assumed that the most dominant transmitted signal would be from the direct rays reflected, refracted and diffused from the human body.

(3) In addition to the requirement of the EH feature, the experiments were conducted outdoors to minimize the RF interference and avoid the complex multipath propagation experienced indoors.

(4) The size of the crowd in DOE was limited to 15 people. This is meant to reduce the overhead in training the algorithm during the Training Phase. This number represents 30 % of the total crowd size monitored (50 people). This technique is also used by Xu et al. (2013), Xi et al. (2014) and Haochao et al. (2015) with ratios of 25, 40 and 60 % between the size of crowd during Training versus Monitoring Phase. In addition, the crowd size of 5 and 10 were also investigated to provide more RSSI data for the algorithm training to improve its accuracy.

(5) The crowd pattern is defined into two categories; lumped and scattered. The distance between a person to the next is 0.30 m and 0.65 m for lumped and scattered respectively. These values were measured based on the placements of up to four people within the 1 m^2 area. The 1 m^2 test is one of the methods in defining the crowd density (Still, 2000).

(6) Although guidelines were given to the participants of the experiments, the freedom of natural human traits such as slight free movements, approximation of proximity, and comfortable standing stance were allowed to better imitate actual human behaviours.

(7) The effect of crowd location on signal attenuation relative to the T-R distance is never thoroughly studied. For example, Yuan (2014) and Xi et al. (2014) loosely positioned their crowd as near or far from the transmitter without defining its specific distance. In this research, the effects of the crowd location were set at 10 m (nearest to the transmitter,) 20 m and 30 m (nearest to the receivers) for experimentation. This is also in accordance to the requirement of DOE for incrementing the value of the variable to test its effect.

53

(8) The number of receiver is limited to three to offer improvement in the node density required per area squared. The use of three receivers with one coordinator would mean that the deployment of the proposed H-CDE system requires in average, one node per 37.5 m^2. The nearest competitor is Xu et al. (2013) at one node per 20 m^2. The less dense, the better.

3.2.3 Wireless Range Extension

Figure 3.5 illustrates the block diagram of the selection methodology for the RF module parameters which matches with the proposed H-CDE application. The following paragraphs in this section discuss these selections.

Protocol	Series	Frequency	Mode
•ZigBee	•Series 2 •PRO	•2.4 GHz	•API
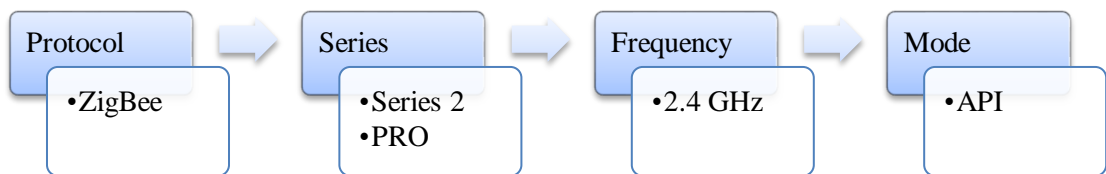
Figure 3.5: RF Module selection methodology for wireless range extension

Based on the reviews from Section 2.2.2, the most suitable RF module to increase the crowd detection range is the Xbee module, which is based on the ZigBee protocol. ZigBee is a network layer protocol on top of the IEEE 802.15.4 standard. The 802.15.4 standard defines the physical (PHY) and medium access control (MAC) layers for low-rate wireless personal area network (WPAN). Documentation of the standard is available in the IEEE Digital Library (IEEE, 2006).

Most importantly, the ZigBee protocol targets low-powered and low data rate application which is the position taken by the proposed H-CDE system. The low power requirement is due to power savings principle in WSN and H-CDE establishments. Whereas remote sensing naturally has low demand in data rate which is also a feature to save power.

Table 3.7 shows the features of Xbee products. The main difference between Series 1 (S1) and Series 2 (S2) is the ability of the latter to multi-hop and create mesh network whereas the former requires higher layer support to perform these features. The mesh networking capability makes the S2 more suitable than the S1 for WSN deployment.

Table 3.7: The features on three types of Xbee products

Features	Series 1 (802.15.4) (Digi, 2015)	DigiMesh (Digi, 2008)	Series 2 (ZigBee) (Digi, 2015)
Copyright holder	IEEE	Digi International	ZigBee Alliance
Firmware	Upgradeable freely to DigiMesh	DigiMesh	ZB or Znet 2.5
Hardware	802.15.4	DigiMesh or 802.15.4	S2, S2B and S2C
Mesh network	X	√	√
Network type	Centralized (or simple point-to-point)	Ad hoc	Centralized

√ = Implemented
X = Not implemented

The specifications of the Xbee modules are given in Table 3.8 (Digi, 2015). The Xbee PRO version differs from the non-PRO by higher transmit power output and thus wider coverage. Although the non-PRO version could provide up to 30 m coverage indoors, however, its usage is meant for a typical office setup. Thus, the PRO version is more suitable to cater for bodily obstruction of up to 50 people.

There are two choices of frequency for the ZigBee standard; 2.4 GHz and 900 MHz. The 900 MHz module utilizing 902 to 928 MHz frequency band is disallowed in Malaysia as the spectrum is reserved for GSM (SKMM, 2007). Alternatively, the 868 MHz module could be used. However, these modules have very high current consumption (around 500 mA for the Xbee PRO variant), making them unfeasible for low-power usage. Thus, the 2.4 GHz frequency is opted.

Table 3.8: Main specification of the Xbee S2B PRO and S2 module (international variant)
(Digi, 2015)

Specification	Xbee S2B PRO	Xbee S2
Supply voltage	2.7 – 3.6 V	2.7 – 3.6 V
Peak transmit current	117 – 132 mA	40 mA
Receive current	47 – 62 mA	40 mA
Frequency band	2.4 GHz	2.4 GHz
Transmit power output	10 mW (+10 dBm)	2 mW (+ 3 dBm)
Receiver sensitivity	-102 dBm	- 96 dBm
Data rate	250 kbps	250 kbps
Indoors coverage	Up to 60 m	Up to 30 m
Outdoor LOS coverage	Up to 1500 m	Up to 100 m
Frame payload	Up to 80 bytes	Up to 80 bytes
Modulation technique	Direct sequence spread spectrum (DSSS)	Direct sequence spread spectrum (DSSS)
Number of channels	15 (11-25)	15 (11-25)

A main concern in wireless transmission in the 2.4 GHz ISM band is the channel interference between the commonly used Wi-Fi and Bluetooth against the ZigBee standard. Table 3.9 shows the specification for the three standards. The effect of interference would be reduced throughput, increased latency, and lower packet delivery rate.

The 802.11b may interfere with the transmission of the ZigBee, as both uses DSSS. However, as most Wi-Fi devices have migrated to the 802.11g and n standard based on ODFM, the interference should be reduced. Rihan, El-Khamy and El-Sharkawy (2012) confirmed that the packet error rate inflicted by 802.11g on ZigBee is less than the 802.11b standard. Petrova, Lili, Mahonen and Riihijarvi (2007) also affirmed that very high traffic of 802.11g and n could severely affect the ZigBee packet delivery rate as the ZigBee's CCA could not cope with the noisy channel. However, this is only valid for direct and close

distance (less than 5 m) intrusion of the Wi-Fi into the ZigBee's airspace. Moreover, the heavy interference from 802.11*n* towards ZigBee network is a result of using the 40 MHz bandwidth, which can only be achieved in a strict 802.11*n* only network. This setup is rare considering that IT administrators and users prioritize compatibility rather than complexity in wireless services.

Table 3.9: Specification of the ZigBee, Wi-Fi and Bluetooth standards

Technology	ZigBee (802.15.4) (Digi, 2015)	Wi-Fi (802.11) (IEEE, 2012)	Bluetooth (802.15.1) (Poole, n.d)
Frequency	2.4 GHz	2.4 GHz	2.4 GHz
Bandwidth	3 MHz (for each 5 MHz, use 3 MHz, 2 MHz for gap left and right)	20 MHz wide. 40 MHz in 802.11n network only.	1 MHz
Number of channels	16 channels	13 channels. 14 channels only in Japan.	79 channels
Modulation scheme	Direct Sequence Spread Spectrum (DSSS)	Orthogonal Frequency-Division Multiplexing (OFDM)	Frequency Hoping Spread Spectrum (FHSS). Hop channels up to 1600 times per second
Interference mitigation method	CSMA-CA (if the channel is busy, it does not automatically switch to other channel)	CSMA-CA (automatically switch to other channel if the current channel is busy)	Adaptive Frequency Hopping in version 1.2 and above (marks and avoids bad channels)
Non-overlapping channels	15, 20, 25, and 26 (US) against Wi-Fi	1, 5, 9 and 13 (EU) against Wi-Fi and ZigBee	-

Bluetooth inflicts lesser interference on ZigBee compared to Wi-Fi as it employs FHSS. However, if both the ZigBee and Bluetooth networks have high utilization, then the throughput of the ZigBee may still be severely affected (Chong, Hwang, Jung & Sung, 2007).

The best and practical solution to this problem is mundane; where the devices from different standards should not be deployed close together. Alternatively, the interference between ZigBee and Wi-Fi can be reduced by opting for the non-overlapping channels as

listed in Table 3.9. ZigBee and Bluetooth could co-exist better as they are usually deployed for low-data rate usage which creates less noisy channels. So far, the initial deployment of the ZigBee network within the widely used Wi-Fi network suffers no major degradation. This is confirmed by the latency and throughput test conducted which are later discussed and analyzed in Chapter Five.

The Xbee module may operate either in transparent (AT) or Application Programming Interface (API) mode. The AT mode acts as a serial line replacement that wirelessly transmits all UART data that it received. This makes transmission very simple for the user.

The API mode is a frame-based operation that allows better and customary control over the transmission. The API is essential for mesh networking, as the destination and source addressing, acknowledgement status and IDs are specifically known by the user. This features makes it suitable for the proposed H-CDE system compared to the overly simplified AT mode.

3.3 Energy Harvesting Mechanism

The EH mechanism on the H-CDE node consists of the solar cell, PMU and battery which is responsible to power up the RF module.

3.3.1 System Architecture

The EH architecture of the H-CDE node is shown in Figure 3.6. The architecture is similar to traditional EH-based WSN system. Delving into the literature on EH-WSN revealed that the architecture has remained fairly the same from the earlier works of Zhang, Sadler, Lyon and Matroniso (2004) until a fairly recent one such as Nanda et al. (2014). The

difference between each work is often on the component and module selections, which are tinkered to match its specific application and thus offer higher efficiency.
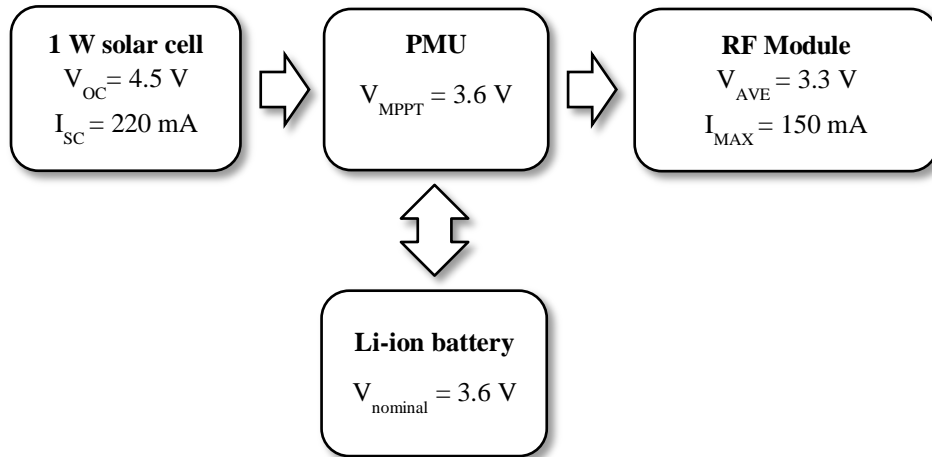
Figure 3.6: Block diagram of the proposed system design architecture of the H-CDE node

The parameters proposed for the H-CDE node in Figure 3.12 is drafted to fulfill the requirement of the transmission module (load) and li-ion battery. These values are subjected to validation, which is discussed in Chapter Five. The validation involves the measurement of power consumption, battery charging and performance.

3.3.2 Solar cell

Solar cell (panels if in arrays) is typically made of mono-crystalline or poly-crystalline silicon. There are also amorphous thin film and gallium arsenide-based solar cell but the former requires larger deployment space while the latter is largely still in research stages.

The solar cells opted for the H-CDE system is of poly-crystalline type. The actual efficiency of the solar cells is unknown due to the lack of documentation but is typically around 15% efficiency (NREL, 2016). As manufacturers produced solar cells in varying power ratings, thus the selection of poly-crystalline type is more about matching with the

power requirement of the H-CDE system rather than prioritizing for higher quality solar cells.

Table 3.10 shows the specification of the solar cells. The nominal value refers to the maximum achievable voltage when the solar cell has been heated from continuous exposure to the sunlight. In contrast, the absolute maximum voltage refers to output voltage when the solar cell operates at room temperature. This is only achievable during the first several minutes of sunlight exposure, or if a cooling mechanism is naturally (during the cold season in specific countries) or mechanically present.

There are two kinds of arrangements for the solar cell of the H-CDE node. The first employs two 500 mW solar cells that were connected in series to gain 1 W of power. The second is a dedicated 1 W solar cell. These arrangements were purely due to the availability of the solar cells.

Table 3.10: Solar cells specification

Type	Open-circuit voltage (V)			Short-circuit current (mA)		Dimension, length x width (mm)
	Official	Maximum	Nominal	Official	Nominal	
2xSandy-Worldbest 500 mW	4.50	4.62 – 5.02	4.40	280	204-210	120 x 130
Sandy-Worldbest 1 W	4.50	4.63	4.40	280	230	85 x 130

3.3.3 Power Management Unit

The PMU is responsible for ensuring proper and safe operation of the load. The PMU also functions as a battery management system (BMS) to ensure proper battery charging and protection.

The PMU mainly comprised of two operations; the voltage regulation and load protection. The voltage regulation methods are shown in Table 3.11. The best method is the buck or/and boost converter where the voltage output of the EH element can be increased or decreased automatically (by adjusting the current value) according to the requirement of the application. This is important to achieve high EH efficiency. In fact, the buck/boost converter is required for the implementation of MPPT. The buck/boost converter can both be integrated together or separately from each other.

Table 3.11: Voltage regulation methods and the related works.

Regulation method	Related works
Buck / Boost Converter	Zhang, Sadler, Lyon and Matroniso (2004), Xiaofan, Polastre and Culler (2005), Simjee and Chou (2006), Raghunathan, Kansal, Hsu, Friedman and Srivastava (2005), Schmid, Gaedeke, Scheibe and Stork (2012) and Nanda et al. (2014)
Voltage Regulator	Kim, Kang, Park, Baek & Park (2009) and Ramos, Girbau, Lazaro, Collado and Georgiadis (2015)
None	Xiaofan, Polastre and Culler (2005) and Minami, Morito, Morikawa and Aoyama (2005)

Next, the voltage regulator method is often of the low-dropout (LDO) type. The operation of the regulator is straightforward where the input voltage is regulated to supply stable and fixed output voltage. To make it work, the input voltage needs to be higher than the output voltage. This type of regulator is generally inefficient, as excess voltage is simply being dissipated as heat and the current could not be manipulated. Even in LDO mode, the power wasted as heat may still be high.

The none-regulated method is simply a direct connection from the harvesting element to the load. This approach has its disadvantages. First, as the harvesting element naturally provides fluctuating power, thus a direct connection cannot guarantee a supply of stable power. Secondly, if either the voltage or current generated by the harvesting element are below the specification of the load, then the load will cease to operate. Third, the solar cell will suffer a voltage drop when directly connected to the load. The degree of voltage drop depends on the operating voltage of the load. This situation creates an inefficient use and waste of solar cell power.

The second function of the PMU is on the load protection mechanism (Table 3.12). This feature ensures that the output voltage confirms with the threshold requirement of the load and the storage element. The dedicated technique consists of both over- and under-voltage protection. This is the best method as it protects both the load and storage element from over-charging and discharging. This is achieved by cutting off the load or the charging mechanism from the battery once the threshold is met.

Table 3.12: PMU protection methods and the related works

Protection Method	Related works
Dedicated	Chulsung and Chou (2006), Zhang, Sadler, Lyon and Matroniso (2004) and Naveen and Manjunath (2011)
Voltage Regulator	Nanda et al. (2014), Ramos, Girbau, Lazaro, Collado and Georgiadis (2015), Amaro, Ferreira, Cortesao and Landeck (2012)
None	Minami, Morito, Morikawa and Aoyama (2005)

The voltage regulator method functions similarly as discussed earlier. Here, the regulator would only provide over- but not under-voltage protection. This made the protection mechanism insufficient especially for li-ion batteries where low voltage discharging can damage it.

A PMU without a protection mechanism can be deployed if the output voltage of the PMU matches the voltage rating for both the load and storage element. However, this choice

is risky in the case of voltage spikes and circuit malfunction, which may permanently damage the system. Therefore, it should be avoided in most cases.

For the proposed H-CDE system, the PMU selection must meet the specific requirements of the RF module and the li-ion battery. Table 3.13 shows the commercially available PMU for solar EH surveyed up to the year of 2015. BQ25504, SPV1050, and LTC3105 are all suitable options. But the BQ25504 has the best parameters that match the holistic requirement of the Xbee module, li-ion battery and solar cell for the H-CDE system.

The pin layout and description of the BQ25504 IC is included in Appendix D. The BQ25504 IC utilizes resistor network for programming the MPPT, over- and under-voltage protection and normal operation. This means that the IC is programmed through hardwiring method.

Table 3.13: Commercial PMU for solar EH. The green cells indicate matching parameters to the Xbee module whereas the reds indicate unsuitability to the load. Colorless cells signify decent PMU to load matching.

PMU / Supplier	Voltage (V)	Battery / Load voltage (V)	Maximum current (mA)	MPPT
BQ24210 (Texas Instruments)	3.5 – 7.0	4.2	800	X
BQ25504 (Texas Instruments)	0.13 – 5.50	2.5 – 5.25	300	√
SPV1050 (STMicroelectronics)	0.3 – 5.0	1.0 – 5.0	1000	√
MAX17710 (Maxim)	0.8 – 5.5	4.125	20	X
LTC3108 (Linear Technology)	0.02- 5.55	2.35 – 5.00	450	X
LTC3105 (Linear Technology)	0.23 – 5.00	1.60 – 5.25	500	√
LTC3535 (Linear Technology)	0.5 – 5.0	1.50 – 5.25	750	X

√ = Implemented
X = Not implemented

The functional, circuit diagram and operation of the BQ25504 PMU are shown in Figure 3.7 (a), (b) and Figure 3.8 respectively. In principle, the BQ25504 begins in the cold start phase where the capacitor C_{STOR} is ensured to be charged up to 1.8 V (typically in 45 ms). Once reached, the Boost Charge and the MPPT Controllers are activated to power up the load and charge up the storage element. If C_{STOR} dips below 1.4 V due to the absence of solar light or deeply drained storage element, the BQ25504 IC will shut down its operation and restart in the cold phase (Cold-start Unit).
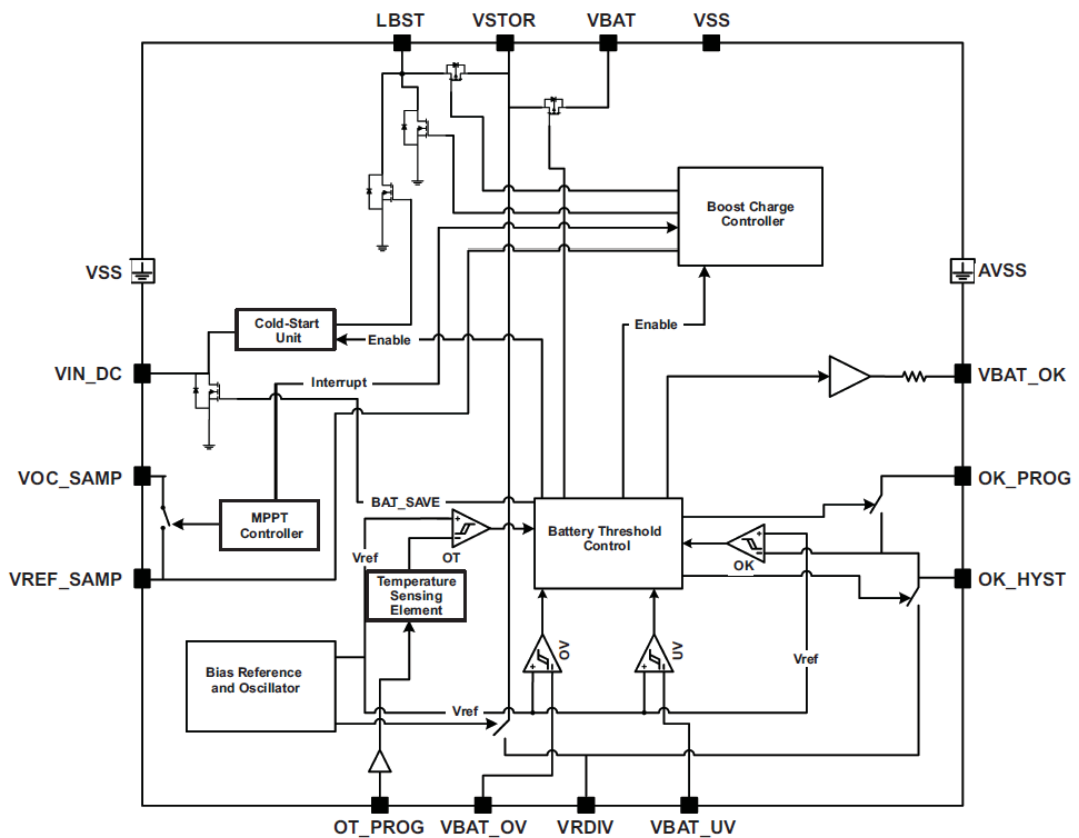
(a)
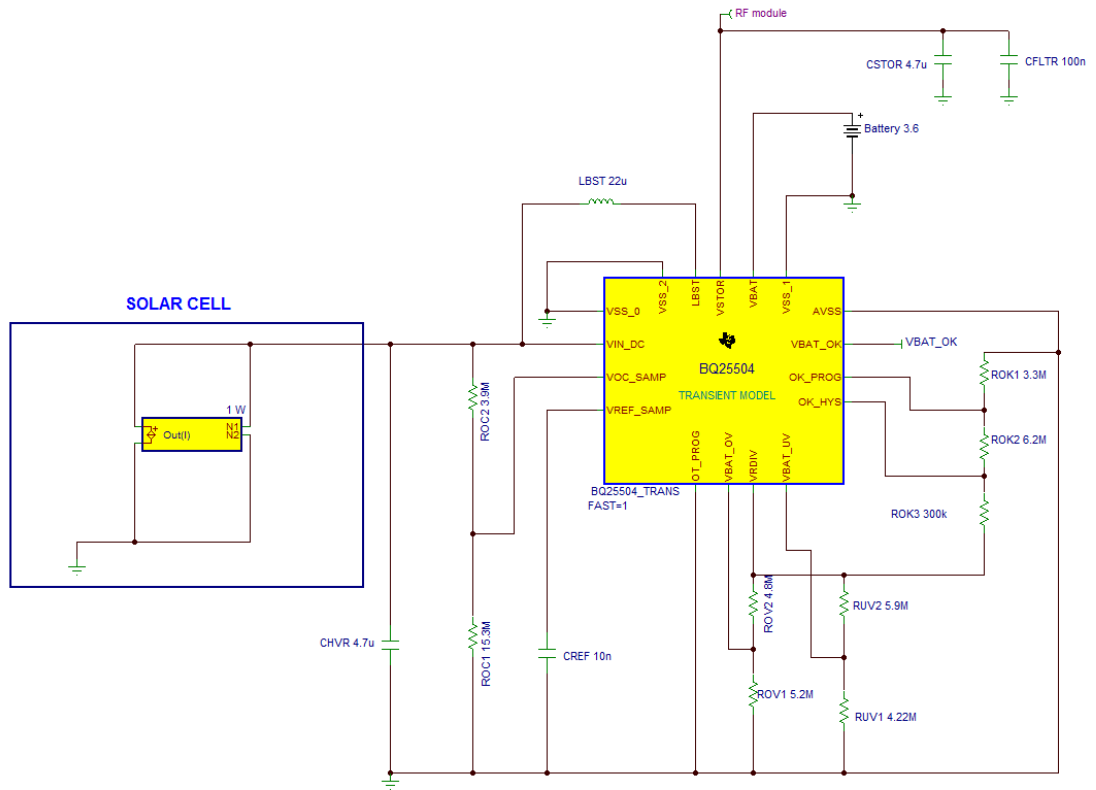
(b)

Figure 3.7 (a) Functional Diagram of BQ25504 (Texas Instruments, 2012) and (b) the schematic diagram of the BQ25504 PMU

Operation of
BQ25504

Charge C_{STOR} from storage
element for 45 ms

$C_{STOR} \geq 1.4$
V?

No

Cold start phase:
Charge C_{STOR} from EH element

Yes

Turn on BQ25504 IC and
continue to charge C_{STOR}

$C_{STOR} \geq 1.8$
V ?

No

Continue charging C_{STOR}

Yes

Turn on boost converter and wait
for 32 ms

Proceed with MPPT:
Charge load and storage element

$C_{STOR} \geq$
V_{OV} ?

No

$C_{STOR} \leq$
V_{UV} ?

Yes

Yes

Over-voltage protection:
Boost converter stops charging

Under-voltage protection:
Shutdown BQ25504 IC

Figure 3.8: Flowchart of the boost converter operation

3.3.4   Maximum Power Point Tracking

The objective of MPPT is to harvest maximum power from the harvesting element. This is achieved by combining the optimum current with the optimal voltage value, as maximizing either one would not produce maximum power. The I-V relationship in solar cells is shown in Figure 3.15. The MPPT can be implemented as part of the PMU or as a stand-alone subsystem.
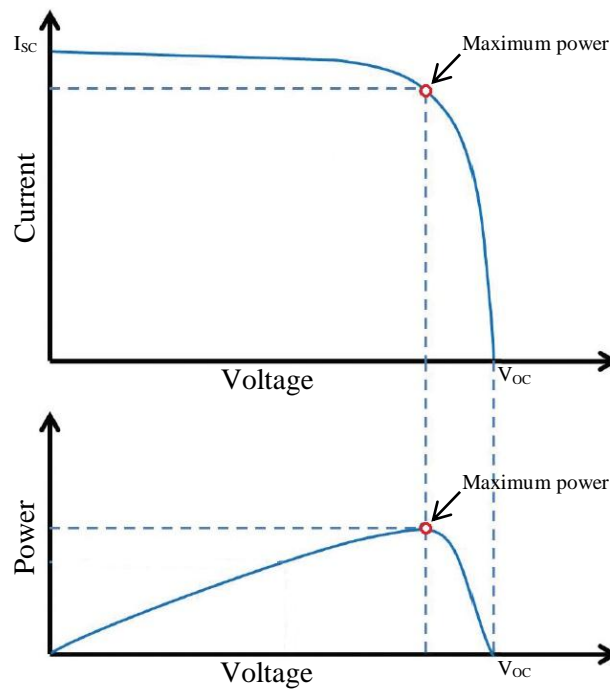
Figure 3.9: The I-V relationship for maximizing power in solar cell

Open-circuit voltage, V_{OC}, is the maximum voltage of the solar cell when there is no load connected to it and thus no current flows in the circuit (I=0 A). Short circuit current, I_{SC}, is the maximum current produced by the solar panel when the module itself is being short-circuited and the voltage eventually drops to 0 V. In solar cells, the MPP is usually set at around 80 % of the V_{OC}. Therefore, a MPPT system will always adjust the I-V values in order to produce the largest output power from the solar cell as possible.

The BQ25504 IC features a programmable dynamic MPPT mechanism. The MPPT operation of the IC is illustrated in Figure 3.16. Because the energy supplied by the solar cell is continuously fluctuating, the BQ25504 needs to periodically disable the charging mechanism to measure the open-circuit voltage input of the solar cell. This means that every 16 s, the BQ25504 will acquire a new reference voltage to operate the MPPT. This is also how the IC keeps track of the input voltage of the solar cell. In combination with the input current, this allows adjustment of the output power according to the programmed V_{OK}.
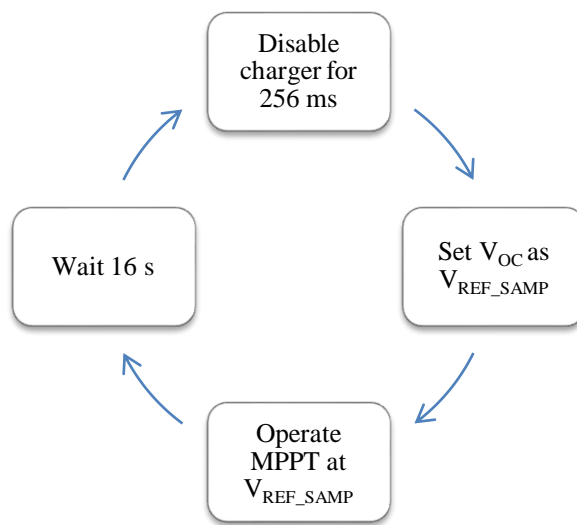
Figure 3.10: The MPPT operation of the BQ25504 IC

3.3.5 Storage Element

The storage element, primarily rechargeable batteries, functions as a power source back-up that complements the EH element to ensure perpetual load operation. The most commonly-used batteries for small and low-powered devices are li-ion based batteries as they are flat, lightweight, and offer good energy density for portable usage. These are the type of batteries used in mobile-phones and laptops. Nominally, li-ion batteries for gadgets are rated at 3.7 V, with operation ranging from 2.8 to 4.2 V.

Table 3.14 shows the rechargeable battery energy density to weight ratio quoted from Cadex Electronics, a company with 30 years of experience in servicing rechargeable batteries (Types of Lithium-ion, n.d.). Li-ion batteries actually come in several types depending on the materials used for the cathode and anode. Here, the term 'li-ion' is commonly used for all types of li-ion based batteries although their chemical compositions may be different. The $LiFePO_4$ is also a type of li-ion battery but is separately listed in the table as it is commercially separated from the others. As stated, li-ion batteries are the most suitable battery for small-sized devices and portable usage such as the laptop.

Table 3.14: Energy density to weight ratio of different rechargeable battery chemistry

Battery type	Energy density to weight ratio (Wh/kg)	Portability (human usage)
Li-ion:		
i. Lithium cobalt oxide ($LiCoO_2$)		
ii. Lithium manganese oxide ($LiMnO_2$)	100-250	√
iii. Lithium nickel manganese cobalt oxide ($LiNiMnCoO_2$)		
iv. Lithium nickel cobalt aluminium oxide ($LiNiCoAlO_2$)		
v. Lithium–titanate ($Li_4Ti_5O_{12}$)		
Lithium iron phosphate ($LiFePO_4$)	90-120	√
Nickel–metal hydride (NiMH)	60 – 120	X
Lead Acid (Pb acid)	30 – 50	X

√ = Suitable
X = Not suitable

Despite the advantages and widespread usage of li-ion batteries, the main concern when handling these types of batteries is safety. Li-ion batteries require a protection circuit to maintain safe voltage and current limit. A short-circuited or overcharged li-ion battery is flammable and may explode. This is also why li-ion batteries are subjected to transportation

regulations. In designing the H-CDE system, the BQ25504 was programmed to ensure safe operation of the li-ion battery, as discussed in Section 4.4.3 (f).

The H-CDE system uses 3.7 V li-ion prismatic polymer batteries. The specific chemistries of the batteries are unknown as the information in the documentation is undisclosed. A li-ion polymer differs slightly from traditional li-ion battery. A li-ion polymer battery has slightly higher energy density, and is lighter and can be made thinner at a slightly higher cost. The prismatic battery may be easily identified by its flexible foil-type case resembling a pouch, but is actually different from the 'pouch' type of li-ion battery.

The formula for charging rechargeable battery is given as:

$$\text{Charging time (hours)} = \text{Battery Capacity (mAh)} / \text{charge rate current (mA)} \qquad (3.7)$$

However, the formula above would mean that no charging loss occurred which is nearly impossible. A more practical approach is to add a 20 % charging efficiency loss, which is usually the standard used in determining the charging time:

$$\text{Charging time (hours)} = \text{Battery Capacity (mAh)} / \text{charge rate current (mA) x 1.2} \qquad (3.8)$$

The specification of the li-ion battery is tabulated in Table 3.15. The 2000 mAh battery is made of single cell and therefore does not require a load balancer to equalize the voltage at different cells. A discharge rate of 2 C means that the battery can provide a maximum current of 4000 mA for half an hour. In comparison, a 1 C discharge provides 2000 mA for an hour.

Theoretically, as the H-CDE node uses less than 150 mA, thus the battery can provide power to the node for 13.33 hours. However, this is not the case. A li-ion battery provides maximum capacity only at its maximum voltage of 4.2 V. At 3.7 V, its density may be half of its rated capacity. This drawback is subjected to investigation in Section 4.4.3 (e).

Table 3.15: Li-ion battery specification

Nominal voltage	3.7 V
Capacity	2000 mAh
Maximum discharge	2 C
Temperature threshold	-25 to 60 ^{0}C
Dimension	5.8 x 54 x 54 mm
Weight	36 g

3.3.6 Proposed H-CDE System

Table 3.16 shows the differences between the proposed H-CDE system with other works. For input voltage regulation, the proposed system uses similar PFM method as Simjee and Chou (2006). The PFM isolates the solar cell from any load and thus allows the solar cell to reach its intended maximum power point without being shorted to the load's voltage level (Simjee and Chou, 2006). In contrast, PWM and traditional regulator-based MPPT could not overcome this setback such as the system by Zhang, Sadler, Lyon and Matroniso (2004) and Schmid, Gaedeke, Scheibe and Stork (2012).

A different approach taken by the proposed system is the use of both over- and under-voltage mechanisms to ensure that the voltage of the load and battery are within the safe range. Whereby the use of regulator such as Schmid, Gaedeke, Scheibe and Stork (2012) and Nanda et al. (2014) would only ensure over-voltage protection. On the other hand, the absence of any protection mechanism is risky should the PMU operates in abnormal condition.

Table 3.16: Feature comparison between the proposed H-CDE system compared to related works

| System | Power Management Unit | | Storage element | Maximum power output |
	Voltage regulation (MPPT enabled)	Protection mechanism		
Proposed H-CDE system	Pulse Frequency Modulation (PFM)	Over- and under-voltage threshold	2000 mAh li-ion battery	1 W
Zhang, Sadler, Lyon and Matroniso (2004)	Pulse Width Modulation (PWM)	None	2000 mAh NiMH battery	400 mW
Simjee and Chou (2006)	Pulse Frequency Modulation (PFM)	None	100 F supercapacitor	450 mW
Schmid, Gaedeke, Scheibe and Stork (2012)	Fractional Open Circuit Voltage (FOCV) and Direct Coupling	Regulator	AA batteries	462 mW
Nanda et al. (2014)	Undisclosed	LDO regulator	1000 mAh li-ion battery	409 mW

3.4   Summary

The methodologies for the proposed system are summarized in Table 3.17. In the next chapter, detailed explanations of the actual implementation and performance verification experiments are discussed.

Table 3.17: Summarized design methods of the proposed system

Element	Objective	Approach adopted
H-CDE	Improve accuracy and crowd sensing	Extend sensing coverage to 30 m by using better RF modules
		Reduce the amount of transmission node
		Caters up to 50 people crowd
	Improve prediction accuracy	Enhance algorithm by considering significant crowd properties
One-way ANOVA	Verify effect of moving crowd	Tukey's method
DOE	Identify significant crowd properties	Full-factorial
EH	PMU	Extend operational lifetime using EH mechanism
		Safe operation of battery through over- and under-voltage protection
		Higher harvester efficiency through MPPT
	Li-ion battery	Higher density
WSN	Networking backbone	Arduino platform

CHAPTER FOUR
IMPLEMENTATION AND EXPERIMENTATIONS OF THE PROPOSED SYSTEM

Chapter Four is divided into three parts. Part A focuses on the H-CDE, Part B on EH and Part C on the experimental methods. The system implementation for H-CDE and EH is shown in Figure 4.1. The Coordinator hosts the API which collects and processes the RSSI information using the developed algorithm. Finally, the level of crowd density is determined and shown in the Graphical User Interface (GUI).
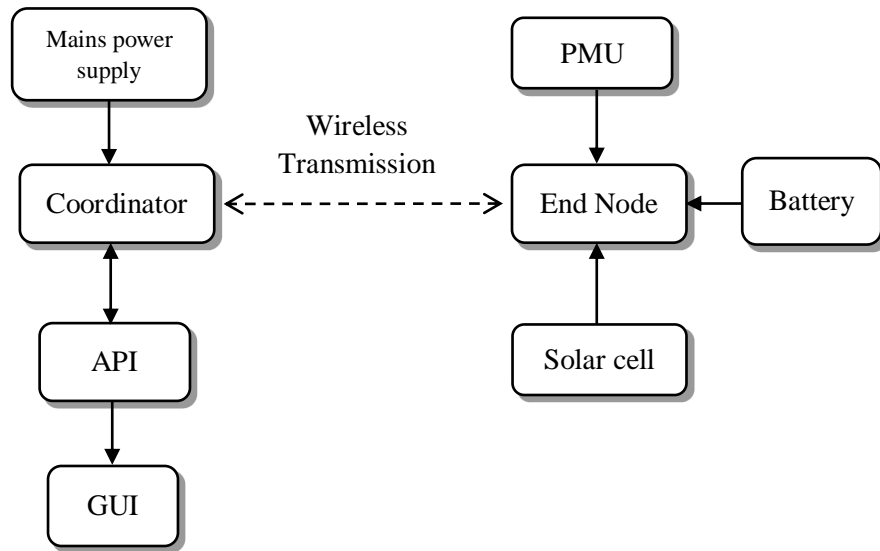
Figure 4.1: Proposed H-CDE system design structure

The End Nodes were embedded with EH mechanism, which is consists of the PMU, solar cell and battery. On the other hand, the Coordinator, which is the backbone of the network, utilizes mains power as to ensure reliable and robust WSN service.

The design concept, selections and decisions for the hardware and software development of the H-CDE system are discussed in their respective sub-sections. Then, the system is subjected to several performance and stability tests to verify its functionality and feasibility as discussed in Part C. The overall development of the proposed H-CDE system is conceptualized in Figure 4.2.
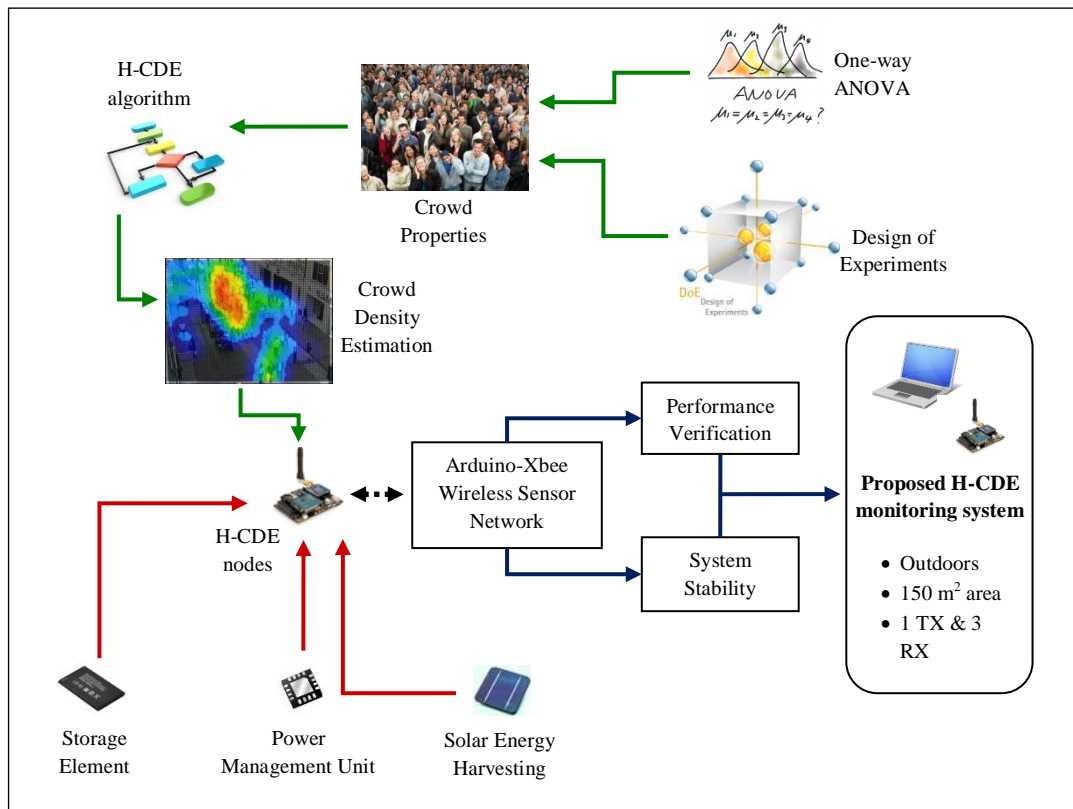
Figure 4.2: Overview of the proposed H-CDE system implementation. The green, red and blue arrows indicate the crowd density estimation, energy harvesting and embedded system segments respectively.

4.1 Part A: Implementation of Human Crowd Density Estimation System

The H-CDE system consists of the Coordinator and End Nodes that form the WSN. Only a single Coordinator is needed, whereas three End Nodes were used in this study. These devices were deployed in fixed placements during data collection and crowd monitoring in Training and Monitoring Phase respectively.

4.1.1 Wireless Sensor Network Implementation

The H-CDE system uses Xbee S2B PRO modules to increase the wireless coverage as an improved design requirement identified in Chapter Two. The modules were set to the maximum power level of 4 with enabled boost mode while the rest were kept on default settings. The boost mode increased the transmission power from 8 dBm (level 4) to 10 dBm.

Each node within the WSN is assigned its own unique address according to the Xbee specification. The Xbee 64-bit addressing scheme is illustrated in Figure 4.3. By default, the addressing is represented in hexadecimal numbering format. The SHSL stands for Serial Number High and Low which is the nodes own address. The SH is for the first 8 hexadecimal number and SL is for the remaining ones. The same applies for DHDL which indicates the destination address of the transmission. The DHDL addresses of the receiving nodes are set to sixteen zeros. This is a special feature on the Xbee to send data to the Coordinator regardless of the number of hops required as the routing is handled automatically by the ZigBee protocol.
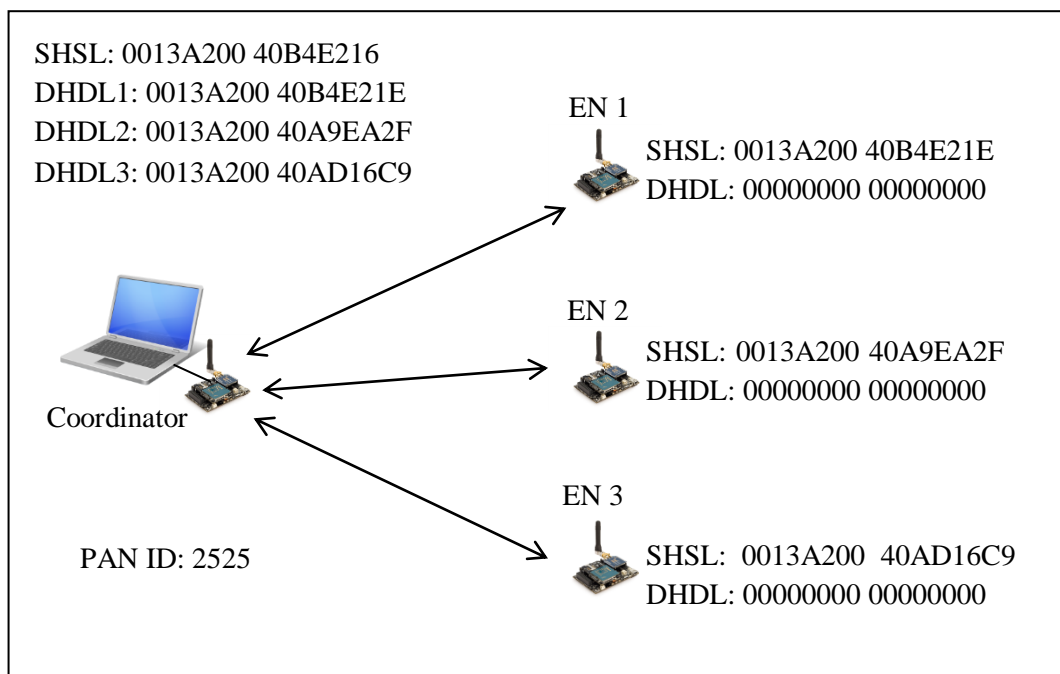
Figure 4.3: Address assignment to each End Node (EN)

The Coordinator stores the addresses of all the nodes within the PAN. Communication between each node to the Coordinator is in a sequential manner. This allows time for re-transmission and avoiding packet collision.

The 802.15.4 PHY and MAC data frame layers (bottom layers of the ZigBee protocol) are included in Appendix E for reference. The ZigBee Network and Application Support Sublayer (APS) layers are also given in Appendix F. The size of frame in each layer is different depending on the type of frame (acknowledgement, beacon and so on).

The Xbee API mode (as opposed to AT mode) is chosen as it is vital to acquire the RSSI information which is triggered by the ZigBee *DB* command. The command is a special type of frame that specifically requires the receiver to respond with the RSSI data of the last transmission. If the RSSI of multiple hops are needed, then the *DB* command or the RSSI needs to be concatenated or encapsulated within other transmit frame.

The API frame for the *DB* command is shown in Table 4.1. The proposed H-CDE system relies on the *DB* command to generate the RSSI between the Coordinator and the End Nodes. This method is faster and easier to implement by software programming compared to hardware methods through the RSSI/PWM pin although the RSSI measured for both methods would produce the same value (Digi, 2015).

The Xbee uses API mode 1 (without escape characters), as its implementation is less complex. Mode 1 allows the system to recognize individual frames by the start delimeter and frame length fields. The reliability of the system is ensured by the re-transmission (by default, up to four times), acknowledgement frame and the checksum. The acknowledgement frame is automatically handled by the protocol and is transparent to the user while the checksum ensures integrity of the content of the frame.

Table 4.1: ZigBee API frame of the Coordinator

Hex code	Field type and explanation
7E	Delimiter. To indicate the start byte of the entire API frame.
00 0F	Length. To indicate the size in byte between the length to the checksum fields.
17	Frame Type. Type 17 is for sending remote AT command.
01	Frame ID. For frame matching purposes.
00 13 A2 00 40 A9 EA 2F	64-bit Destination Address. The address given here is for End Node 3.
FF FE	16-bit Address. This feature is not used as the 64-bit address is known.
02	Remote Command Options. Feature not used.
44 42	AT Command. 44 and 42 is equivalent to *DB* in ASCII format
AB	Checksum.

The Xbee modules of the Coordinator and End Node are programmed using the XCTU software (Figure 4.4 (a) and (b)) and the configuration parameters are shown in Table 4.2 and Table 4.3 respectively.
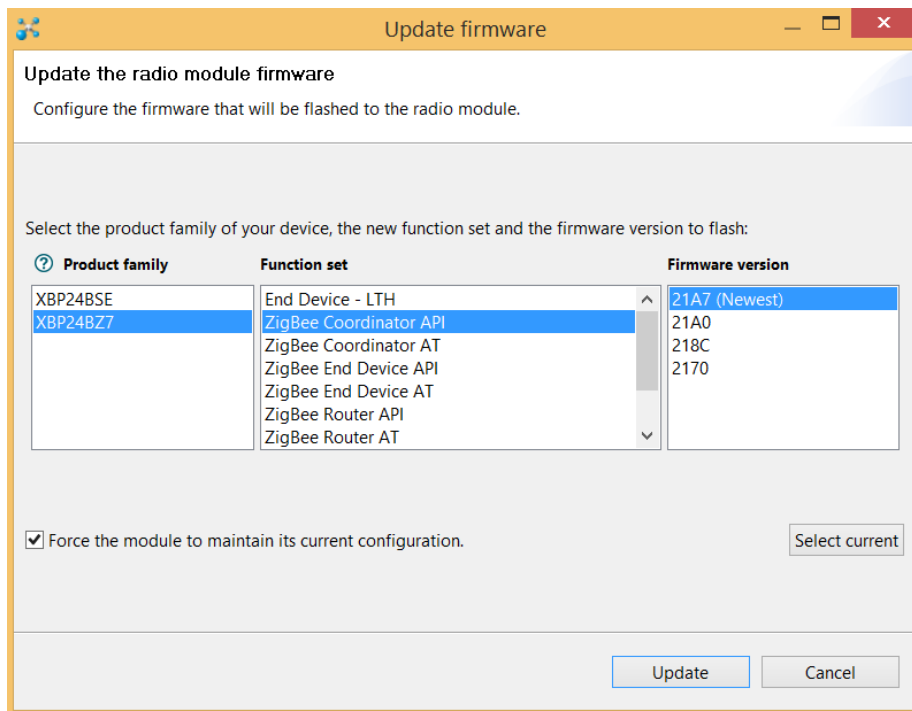
(a)
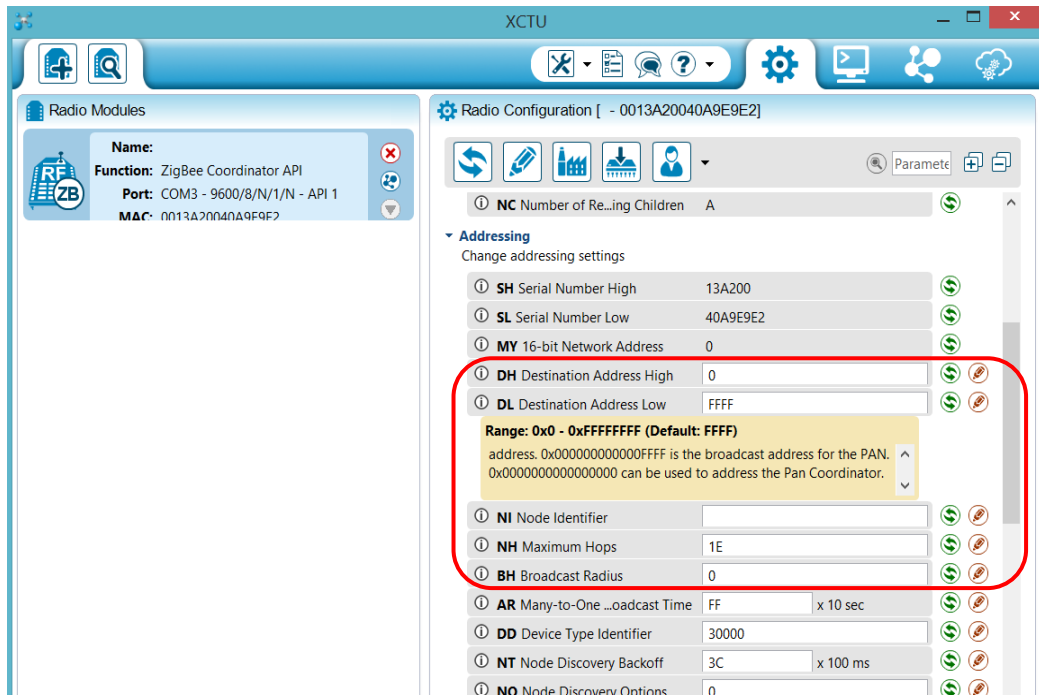
(b)

Figure 4.4: (a) XCTU firmware selection and (b) configuration window

Table 4.2: Specification of the Coordinator's Xbee module

Product family	XBP24BZ7
Type of Platform	Development board
PAN ID	2525
64-bit MAC address	0013A200 40B4E216
Function set	ZigBee Coordinator API
Firmware version	21A7

The end node function set of the Xbee made it compulsory to have a sleep cycle. This has already been set by the manufacturer and the firmware could not be tampered due to licensing. The default sleep period is 200 ms. Sleep mode is activated if no data is received within every 1.388 ms. This would slightly affect the latency of the transmission as discussed in Chapter Five.

Table 4.3: Xbee module specification of the H-CDE End Nodes

Name	End Node 1	End Node 2	End Node 3
Product family	XBP24BZ7	XBP24BZ7	XBP24BZ7
Type of Platform	Prototype board	Prototype board	Prototype board
PAN ID	2525	2525	2525
64-bit MAC address	0013A200 40B4E21E	0013A200 40A9EA2F	0013A200 40AD16C9
Function set	ZigBee End Device API	ZigBee End Device API	ZigBee End Device API
Firmware version	29A7	29A7	29A7

4.1.2   The Coordinator

The Coordinator is the brain of the system, where the API and algorithm reside inside the Atmel Atmega328p microcontroller and the GUI is programmed using the Arduino IDE. The Coordinator collects, processes and stores the data from the H-CDE End Nodes. The Coordinator also ensures that the ZigBee-based network operates correctly.

Figure 4.5 shows the framework of the H-CDE Coordinator. The laptop provides power to the Coordinator as well as the data storage medium through the USB slot. For permanent data storage, the Gobetwino data logging software is utilized at the laptop.

The Xbee module interfaced to the Arduino (Appendix G) through the Xbee breakout board converts the 5 V voltage level of the Arduino to 3.3 V voltage level of the Xbee module. The Atmel Atmega328p microcontroller on-board the Arduino provides processing power and hosts the API. The hardware is shown in Figure 4.6 and its connection is illustrated in Figure 4.7.
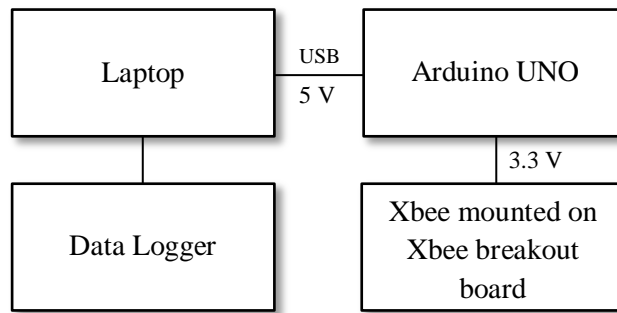
Figure 4.5: Block diagram of the H-CDE Coordinator

Figure 4.6: The H-CDE Coordinator

The Coordinator has two sets of API; one for the Training Phase and the other for the Monitoring Phase (Figure 4.8). Figure 4.9 shows the operation of the H-CDE Coordinator in both phases. In a single cycle, the Coordinator sends three ZigBee API frames with a *DB* command (payload) sequentially; one to each node. Upon receiving the API frame, the End Node will interpret the command and respond to the Coordinator by stating the RSSI for the Coordinator-End Node transmission.
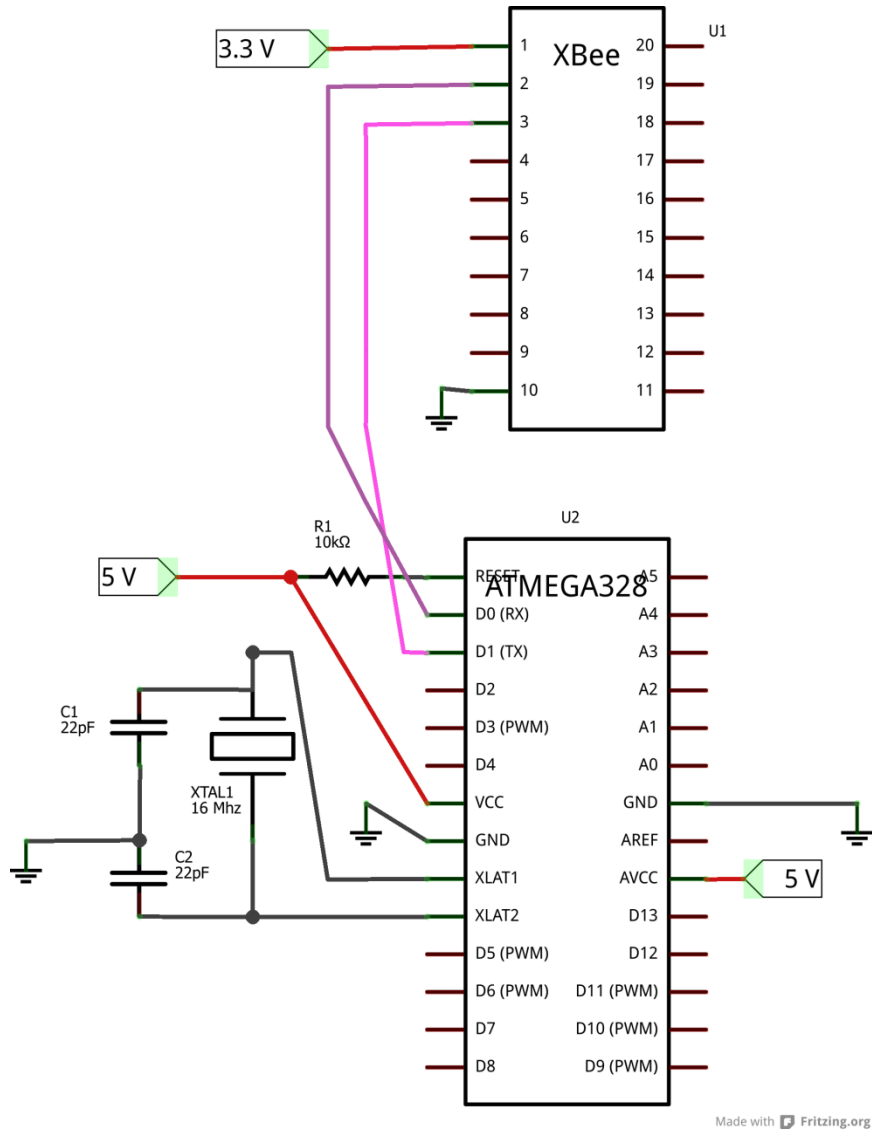
Figure 4.7: Schematic diagram of the Coordinator
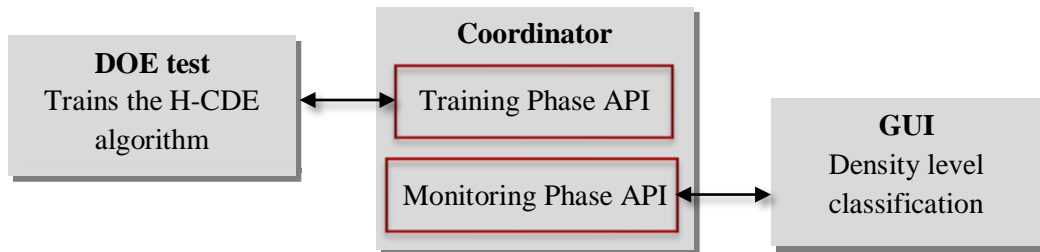
Figure 4.8: The proposed API functions for the Coordinator
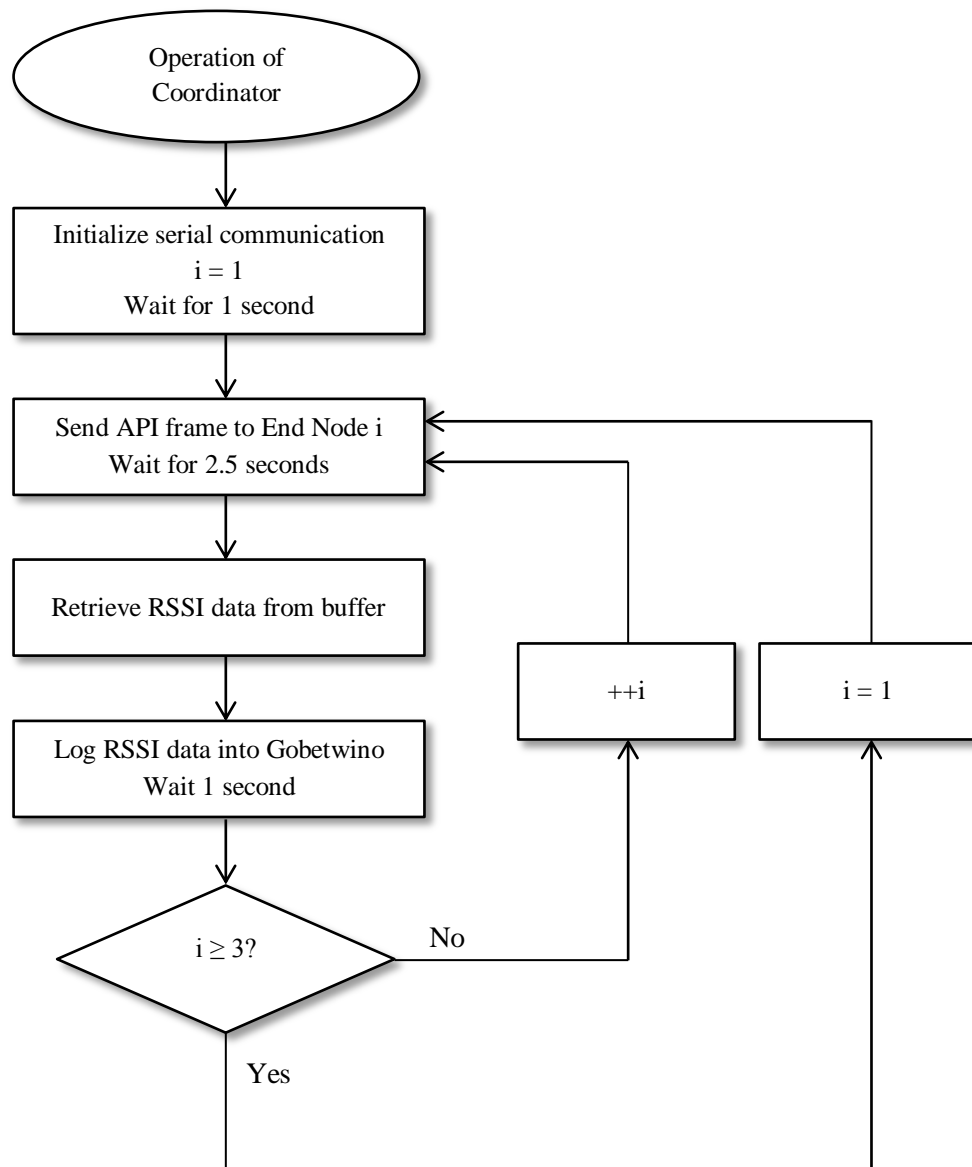
Figure 4.9: Flowchart of the operation of the proposed H-CDE Coordinator

In the Training Phase, raw RSSI data were collected based on the DOE test (Section 4.2.2). This procedure is conducted to specifically train and develop the proposed H-CDE algorithm. The API pseudo-code for the Training Phase is shown in Figure 4.10 and the source code is included in Appendix H. A delay of 2.5 seconds is allocated for each of the API frames sent. This would provide enough time for re-transmission if required.

Initialize byte size for address, RSSI, discard, receive_status and frame_ID

Initialize string length to 25

Initiate serial communication with 9600 baud rate

Allow one second delay for initialization

While Coordinator is operational, loop indefinitely

      Send Xbee API frame to Tag 1 (Step A)

      Delay for 2.5 seconds

           While received API frame size greater than 19

              If first frame is '7E'

                  For 10 subsequent frames

                      Discard the frame

                  Read address value

                  Discard two subsequent frames

                  Read receive_status

                  Read RSSI

                  Store data using Gobetwino

                  Delay for one second

                  Error handling

      Repeat (Step A) for Tag 2 and 3

Figure 4.10: Developed pseudo-code for the Training Phase

After the algorithm has been trained, the Coordinator is updated with a new API for the Monitoring Phase. The API pseudo-code for the Monitoring Phase is shown in Figure 4.11 while of the source code is given in Appendix I. The Monitoring Phase processes the raw RSSI data and displays the density level at the GUI in real-time.

The Monitoring Phase classifies the crowd density level into three categories: low, medium, and high density, based on the RSSI measured between the Coordinator and End Nodes. This is in accordance to the classification made by Yuan, Zhao, Qiu and Xi (2013) and Hiroi, Shinoda and Kawaguchi (2016) in determining the severity of the crowd density.

```
Initialize byte size for address, RSSI, discard, receive_status and frame_ID

Initialize string length to 25

Initiate serial communication with 9600 baud rate

Allow one second delay for initialization

While Coordinator is operational, loop indefinitely

        Send Xbee API frame to Tag 1  (Step A)

        Delay for 1.5 second

                While received API frame size greater than 19

                        If first frame is '7E'

                                For 10 subsequent frames

                                        Discard the frame

                                Read address value

                                Discard two subsequent frames

                                Read receive_status

                                Read RSSI

                                        If RSSI less than 58

                                                Low density crowd

                                        Else if RSSI between 58 and 76

                                                Medium density crowd

                                        Else

                                                High density crowd

                        Error handling

        Repeat (Step A) for Tag 2 and 3
```

Figure 4.11: Developed pseudo-code for the Monitoring Phase

4.1.3   The End Nodes

Figure 4.12 shows three of the fabricated End Nodes while Figure 4.13 shows the schematic diagram. End Node 1, 2 and 3 were specifically used for the entire H-CDE and EH experimentation whereas three additional End Nodes were also fabricated as backups and control units. The bill of materials for each node is included in Appendix J.
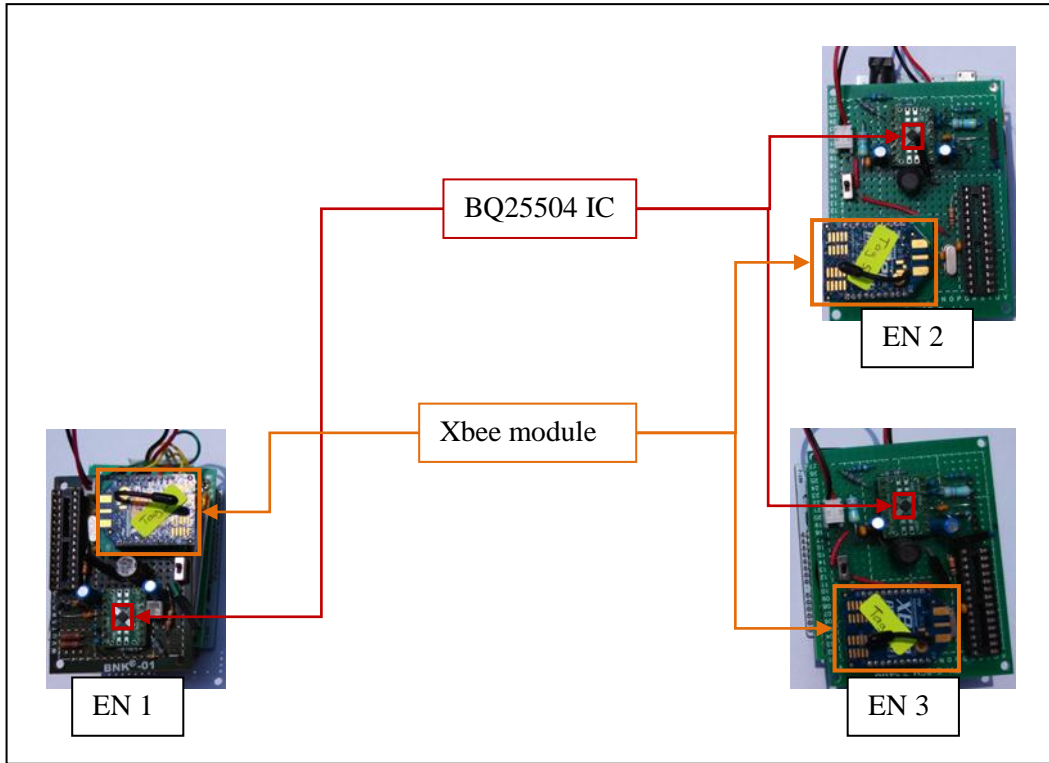
Figure 4.12: H-CDE End Nodes
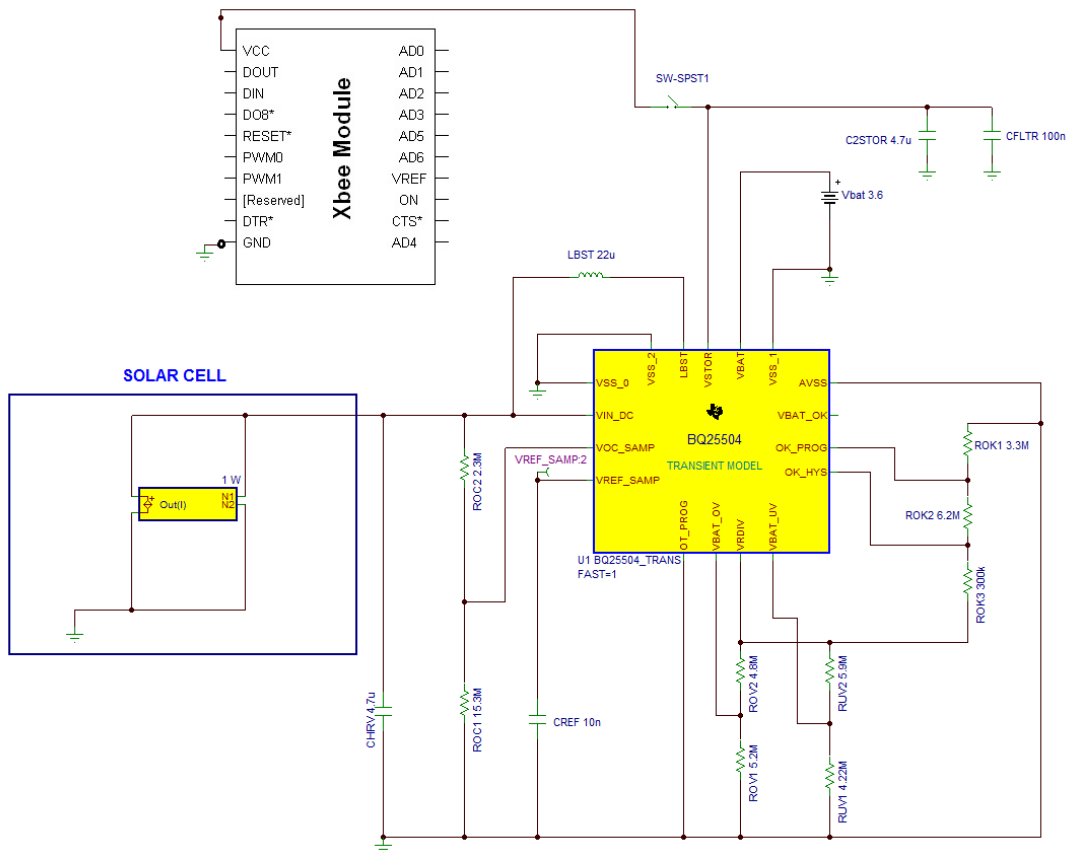
Figure 4.13: End Node schematic diagram

4.2 Statistical Methods

Recalling Chapter Three, the One-way ANOVA and DOE are implemented in different parts and the flow is illustrated in Figure 4.14. The One-way ANOVA is performed first, followed by the DOE test and the crowd density monitoring in the final phase.
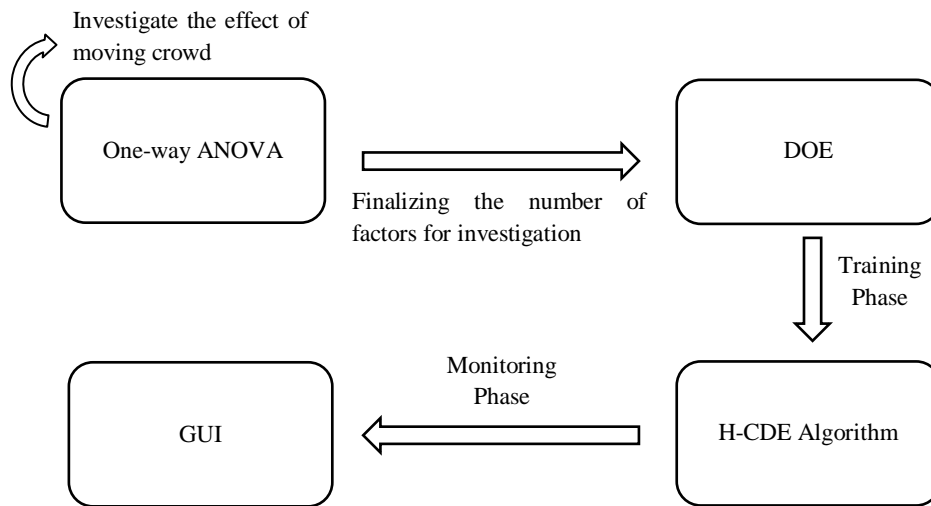
Figure 4.14: Implementation of the statistical methods in the H-CDE system

4.2.1 Implementation of One-way Analysis of Variance

Figure 4.15 shows the layout of the deployment where the people stay immobile or move to and fro within the boundaries set. The length is set to 20 m, which is the middle point between the 10 and 30 m distance investigated in the DOE section while the 5 m width follows the size of the survey (Figure 3.3).

The walking speed was assumed to be less than 1.2 m/s (Arai, Kawamura, & Suzuki, 2010). The analysis was conducted by using Minitab 16.2.3 software with the default 5 % Tukey's family error rate (the maximum probability of rejecting the null hypothesis when in reality it should not). Three types of graphs are plotted to verify and analyze the results; the Individual Value Plot, Normal Plot of Residuals (Normal Probability Plot) and Residuals versus Fits.
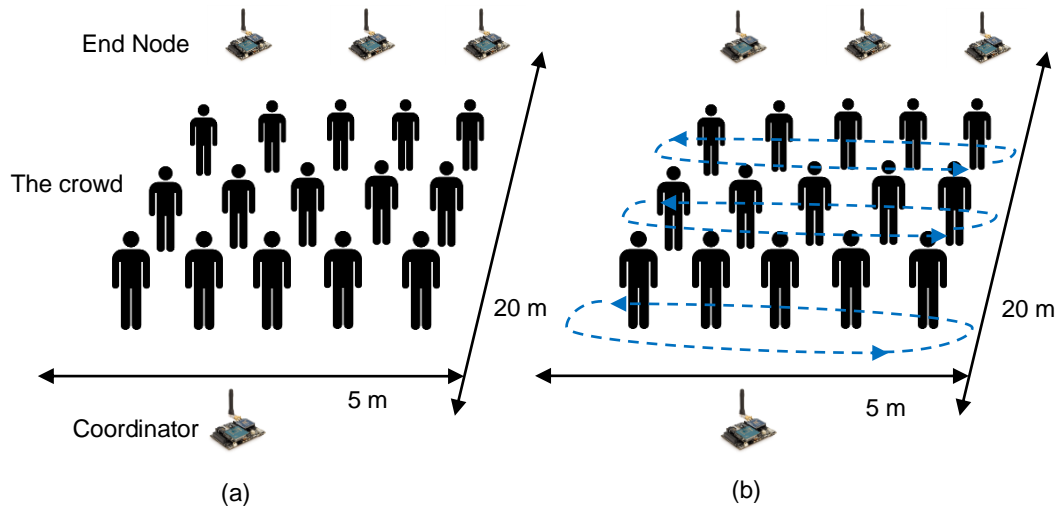
Figure 4.15: The measurement setup where (a) all the people are static and (b) the human crowd is moving about within the stipulated area

4.2.2   Implementation of Design of Experiments

The DOE full factorial template was generated by using Minitab software with two repetitions for a total of 108 experiments (3 types of crowd size x 3 crowd distance x 3 number of receiver x 2 crowd pattern x 2 repetitions) and 2160 raw data measured (20 data collected for each experiment). The DOE template is available in Appendix K. The collected RSSI data is then inserted into the DOE template for analysis. The selected DOE factorial plots are the main effects and interaction while the residual plots are the normal and residual versus fits.

In short, the mains effect plot will identify the individual significant factors that affect signal attenuation within crowds. The interaction will determine the degree of relationship between each factor and thus identify the strong combinational factors that affect the signal propagation. The residual plots would verify the error distribution. These plots should be sufficient to prove the validity of the data and conclude the pattern of the result.

The deployment strategy of the DOE is illustrated in Figure 4.16. The Coordinator and End Nodes were placed 1 m above the ground.
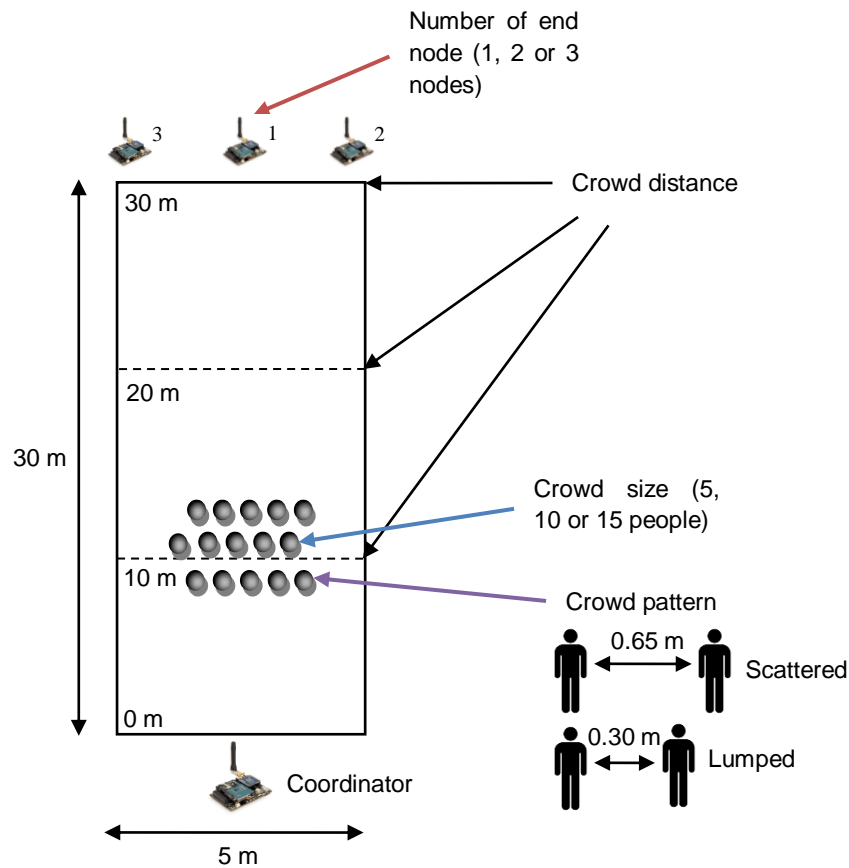
Figure 4.16: Setup of the DOE at the survey site

A unique aspect to the data collection is that the arrangement of the experiments are randomized. The randomization is generated by the DOE by assigning a seed to the built-in randomizer in the Minitab software. This feature ensures randomness that reduces biasness in data collection. For each arrangement, the experiment is repeated twice to increase reliability of data. For each data, 10 samples were taken and the average calculated.

4.3   Part B: Implementation of Energy Harvesting Mechanism

The Xbee module is typically operated at 3.3 V. During transmission, the Xbee modules may continuously shift between receive, transmit and sleep phases. Each phase uses different value of current and thus different power consumption. According to the official

documentation, the Xbee S2B Pro module has around 411 mW of peak power consumption. Therefore, the solar cell selection is important to provide enough power. A 500 mW could theoretically fulfil the minimum power requirement. However, in reality, sunlight is not always available at its optimum intensity and therefore requires reservations. Due to this very reason, the 1 W solar cell is chosen for the proposed EH mechanism, as it provides twice the power of 500 mW for sufficient power backup in light deprived situations. Furthermore, the 1 W solar cell is a standard power rating commonly produced by manufacturers.

4.3.1   End Node Power Management Unit

The proposed H-CDE End Node only implements the boost converter; where the output voltage of the solar cell is increased (step up) by sacrificing the current if the intensity of the sunlight is slightly low. This feature is vital for the H-CDE system in charging the battery, as the voltage potential supplied by the solar cell needs to be higher than the battery voltage in order to charge it. The trade-off is that the supplied current will be lower, resulting in longer battery charging time. As mentioned, to mitigate this problem, 1 W solar cell is used in the H-CDE system to increase the current generation by a factor of two (from 500 mW), while maintaining the same output voltage.

The H-CDE system does not implement the buck converter (step down voltage) due to two reasons. First, a higher powered solar cell (higher voltage) is often larger in physical size that makes it unsuitable even for semi-portable usage. The second reason is due to efficiency. The proposed H-CDE system design decision to closely match the maximum voltage rating between the solar cell and the PMU meant that there is little opportunity to utilize the buck converter. There is limited voltage available to step down to increase the current. In light deprived situations, the voltage and current of the solar cell are low enough that the voltage actually needs to be boosted up to meet the load or battery charging requirement.

Programming the BQ25504 PMU IC requires matching the correct resistor values through the hardwiring method. The resistors would form resistor networks that define the voltage thresholds for the operation of the PMU. In a sense, the PMU is not easily configurable due to lack of software programming. The values of capacitors and inductor of the BQ25504 are fixed by default by the manufacturer and these settings are strictly followed.

The circuit setup of the BQ25504 IC is depicted in the diagram in Figure 4.17. The load is connected to the V_{STOR} pin. However, upon further testing, a reverse voltage could also enter the BQ25504 through this V_{STOR} pin. Thus, the battery or any other power source should not be connected to this pin unless regulated, for example, by a simple diode. Due to troubleshooting and measurement processes, the BQ25504 and its components were not fabricated in a SMD version. To solder the parts of BQ25504 onto the main board, a special type of QFN-16 mounting board was utilized. The SMD circuit design, however, has still been prepared and included in Appendix L for future use.

By default, a total of nine resistors are required to program the BQ25504 IC. However, it is possible to reduce the number of resistor to seven if a specific condition is met. This is discussed in Appendix M.

The MPPT is programmed according to the equation below.

$$V_{REF\_SAMP} = V_{IN} \left(\frac{R_{OC_1}}{R_{OC_1} + R_{OC_2}} \right) \qquad (4.1)$$

$$V_{REF_{SAMP}} = V_{IN} \left(\frac{15.3 \text{ M}\Omega}{15.3 \text{ M}\Omega + 3.9 \text{ M}\Omega} \right)$$

$$= (0.797) \ V_{IN}$$

The calculation for the battery's under-voltage protection is shown below. V_{BIAS} is fixed to 1.25 V by the manufacturer, and the addition of both resistors reach approximately 10 MΩ.

$$V_{UV} = V_{BIAS} \left(1 + \frac{R_{UV2}}{R_{UV1}} \right), \quad R_{UV1} + R_{UV2} = 10 \text{ M}\Omega \qquad (4.2)$$

$$V_{UV} = 1.25\ V \left(1 + \frac{5.9\ M\Omega}{4.22\ M\Omega}\right), R_{UV1} + R_{UV2} = 10.22\ M\Omega$$

$$= 2.998\ V$$
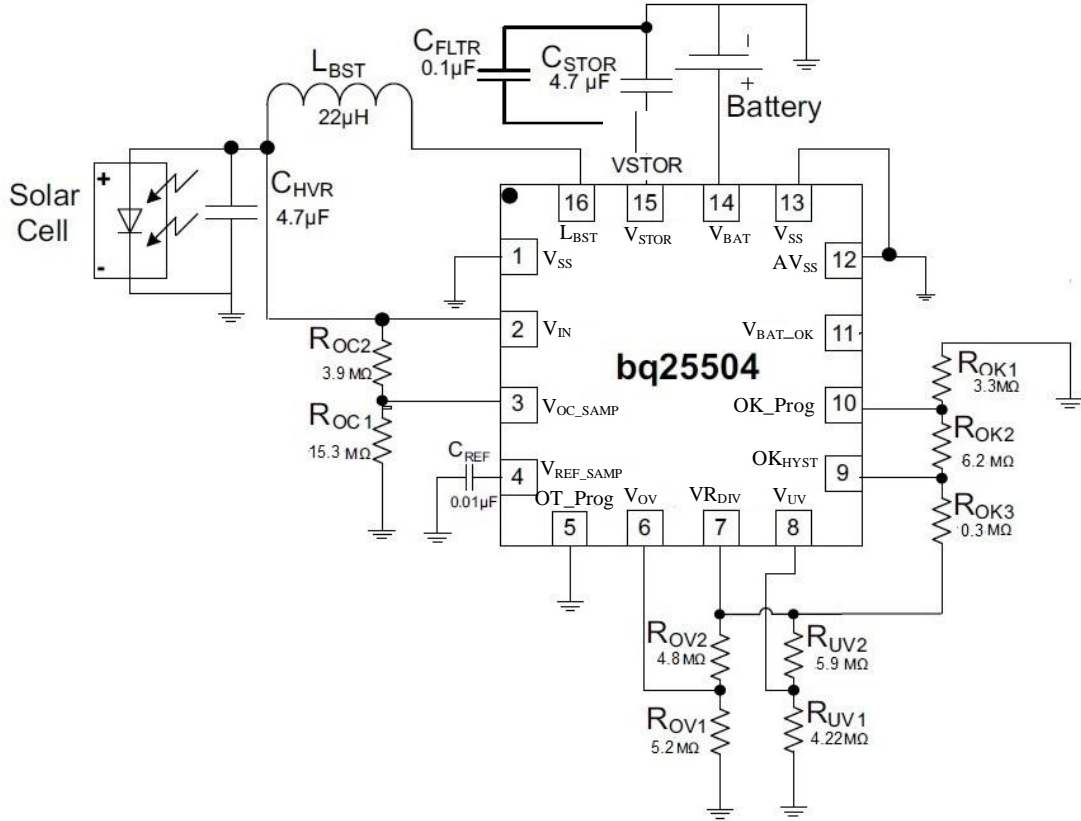
Figure 4.17: Programming the BQ25504 IC for the H-CDE End Node

The calculations for the battery's over-voltage protection are given as:

$$V_{OV} = \frac{3}{2}\ V_{BIAS} \left(1 + \frac{R_{OV2}}{R_{OV1}}\right), \quad R_{OV1} + R_{OV2} = 10\ M\Omega \qquad (4.3)$$

$$V_{OV} = \frac{3}{2}\ 1.25\ V \left(1 + \frac{4.8\ M\Omega}{5.2\ M\Omega}\right), \quad R_{OV1} + R_{OV2} = 10\ M\Omega$$

$$= 3.606\ V$$

The battery's 'okay' indicator follows the equation below.

$$V_{BAT\_OK} = V_{BIAS} \left(1 + \frac{R_{OK2}}{R_{OK1}}\right) \qquad (4.4)$$

$$V_{BAT\_OK} = 1.25\ V \left(1 + \frac{6.2\ M\Omega}{3.3\ M\Omega}\right)$$

$$V_{BAT\_OK} = 3.598 \text{ V}$$

The battery's 'okay' hysteresis, which is the threshold for acceptable operation is as below.

$$OK_{HYST} = V_{BIAS} \left(1 + \frac{R_{OK2} + R_{OK3}}{R_{OK1}}\right), \quad R_{OK1} + R_{OK2} + R_{OK3} = 10 \text{ M}\Omega \quad (4.5)$$

$$OK_{HYST} = V_{BIAS} \left(1 + \frac{6.02 \text{ M}\Omega + 0.3 \text{ M}\Omega}{3.3 \text{ M}\Omega}\right), \quad R_{OK1} + R_{OK2} + R_{OK3} = 9.8 \text{ M}\Omega$$

$$= 3.712 \text{ V}$$

The parameters and phases of the H-CDE End Node are shown in Figure 4.18. The conditions set determine whether the boost converter in the PMU will turn on or off accordingly. The End Nodes with solar cell attached is shown in Figure 4.19.
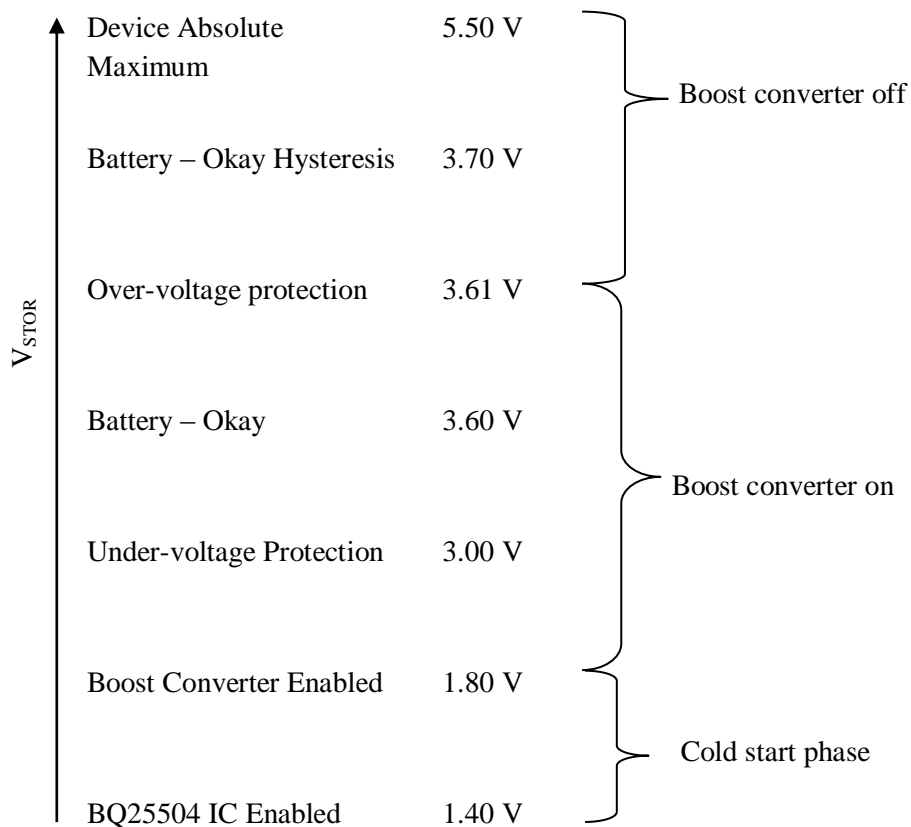
Figure 4.18: The parameters and PMU status of the H-CDE End Node
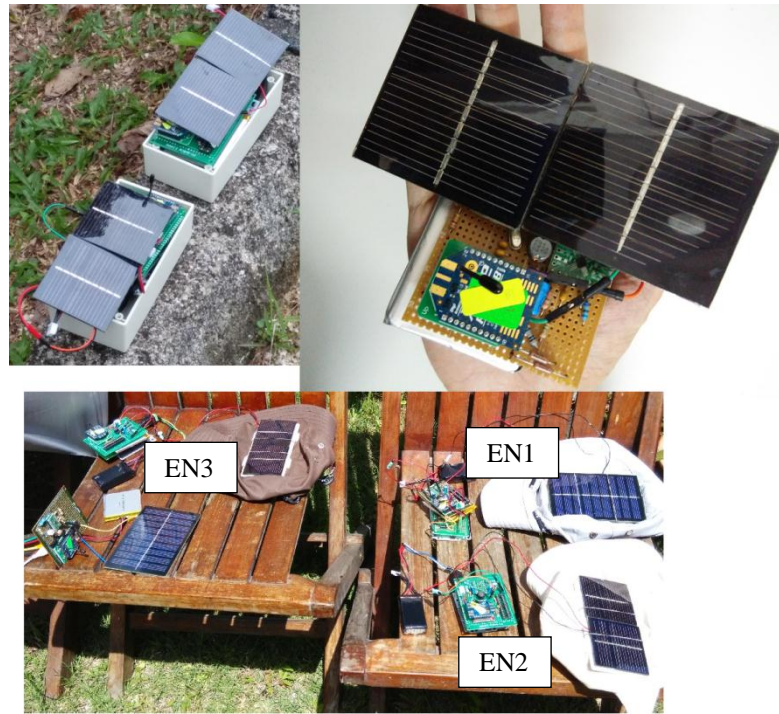
Figure 4.19: H-CDE End Nodes with solar cells attached

Eventually, the overall performance of the EH mechanism on the End Nodes depends on several factors as listed in Table 4.4. The parameters that can be controlled for the solar cell are its type and alignment. However, for post-design, only the alignment of the solar cell with respect to the sunlight can be adjusted freely. For the PMU and battery, their efficiency will be investigated. Specifically, the PMU is programmed using 9 resistors which intrinsically have different degree of tolerance that may affect the programmed value.

Table 4.4: Factors affecting the EH performance of the End Node

Main factor	Sub-factor			
Solar cell efficiency	Temperature	Material	Light intensity	Alignment
Power management unit	Tolerance of resistors	Resistance of bus and jumpers	Battery quality	Leakage
Data logger	Calibration	Resolution	-	-

4.3.2 Energy Harvesting Design Optimizations

The BQ25504 has no actual visibility of the instantaneous voltage and current supplied to the load. Apart from the MPPT, the IC would only ensure that the voltage at V_{STOR} and V_{BAT} do not violate the condition set by V_{UV} and V_{OV}. This creates a problem where the voltage and current can only be tracked by external devices. Installing such devices would only increase the design complexity and cost. Specifically, the output voltage of the IC is vital as to avoid over-voltage at the RF module and battery.

Unfortunately, a limitation of the BQ25504 is that it assumes that both the battery and load has exactly the same voltage profile. The BQ25504 IC has two outputs; one for the battery and the other for the load. The BQ25504 would provide the same exact voltage to both outputs. This do not fit well for the proposed H-CDE system where the maximum voltage rated for Xbee is 3.6 V whereas the li-ion battery has maximum capacity at 4.2 V. Thus, the design should be balanced to justify any compromise made. The stated limitation is illustrated in Figure 4.20.

(a)

Solar cell 4.4 V	⬌	Power Management Unit BQ25504 IC	⬌	RF Module 3.52 V

MPPT (80%) 3.52 V   Battery 3.52 V

(b)
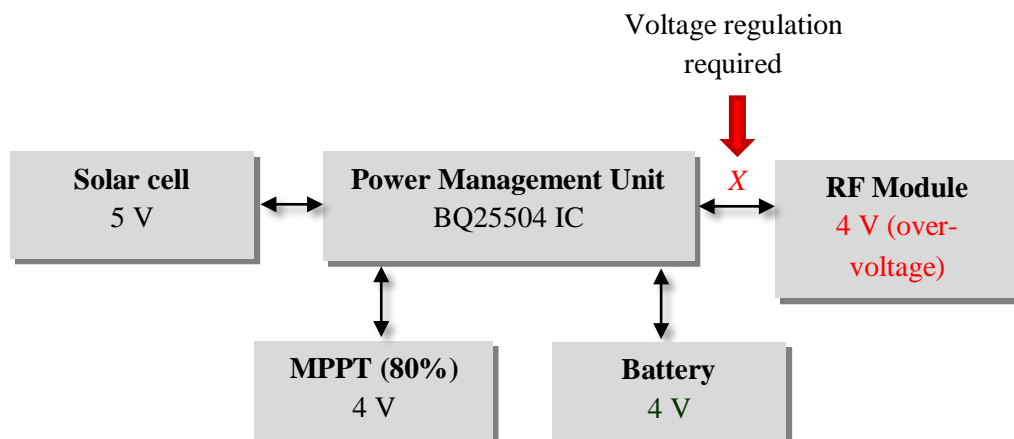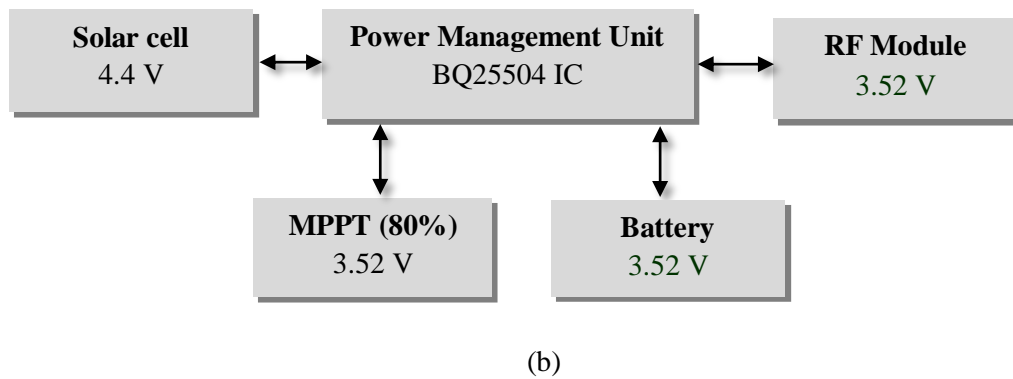
Figure 4.20 (a) Over-voltage at RF module due to mismatching of solar cell and (b) the proposed solution adopted by the H-CDE system

In the first arrangement (Figure 4.20 (a)), the solar cell is rated at 5 V, which after MPPT is applied, would produce an output of 4 V. This voltage exceeds the threshold of the RF module. The BQ25504 does not have a buck converter to reduce the voltage and this has been justified in Section 4.3.1.

Alternatively, a voltage regulation method can be installed at the *X* mark in Figure 4.20 (a). A simple diode or an LDO voltage regulator can be placed to bring down the voltage to 3.6 V. However, these two options are considered a poor design decision as they would only add to power inefficiency. For example, if the sunlight intensity is reduced and the solar cell only generates 3 V, a diode with a 0.6 V voltage drop would bring down the output voltage of the PMU to 2.4 V, which is below the 2.7 V threshold of the Xbee. Thus, the diode is inflexible and inefficient for implementation.

On the other hand, the LDO voltage regulator is also not suitable to be used with the fluctuating nature of the solar cell, especially when the voltage provided by the solar cell is not near optimal. For example, the 3.3 V LM1117L LDO voltage regulator requires a fix input voltage of 5 V. If the input voltage is lower, the output of the regulator would drop below 3.3 V. As mentioned, for the H-CDE system with the MPPT mechanism, the output voltage of the solar cell is only 4 V. This is an insufficient input voltage for the regulator. In

fact, it has been lab tested that the RF module would stop operating if the input voltage of the LM1117L regulator is below 3.82 V. In short, the solar cell simply cannot provide enough voltage to operate the regulator.

Therefore, a solution is proposed to handle the matching of requirements between the subsystems. Instead of using the commonly found 1 W, 5 V solar cell, a 1 W, 4.5 V solar cell is opted. Once MPPT is applied, the 4.5 V solar cell would produce 3.6 V which matches with the voltage specification of the Xbee. In reality, the 4.5 V solar cell produces around 4.4 V as described in Section 3.3.2, which would eventually supply 3.52 V to the load after factoring in the MPPT. As a result, the additional voltage regulation as discussed earlier is not needed. This decision is implemented in the H-CDE system, as shown in Figure 4.20 (b).

The next issue for consideration is on the V_{BAT_OK} pin as the battery voltage indicator. The V_{BAT_OK} pin at the BQ25504 IC is actually not part of the main EH mechanism. It is simply a digital output pin to indicate whether the battery is within the value programmed. To utilize this pin, it needs to be connected to an external microcontroller and processed there. Furthermore, the microcontroller needs an output device to signal the status of the battery. This adds complexity to the design and a waste of resource. Even if the V_{BAT_OK} pin can be connected to a simple LED or a SMD LED, the 20 mA current draw from the LED would only add burden to the EH mechanism.

Thus, in the End Node, the V_{OK} pin was set to 3.6 V but is otherwise not utilized. The OK_{HYST} pin is also not used in the design. The End Node does not have a battery indicator but instead rely on the over- and under-voltage protection mechanism to ensure safe battery operation. Another safety feature available on the End Node is the over-temperature protection. The OT_Prog pin in the PMU is grounded. This means that the BQ25504 will shut down its operation when the temperature of the IC exceeds 65^0 C.

Next, the H-CDE End Node over-voltage protection is discussed. The over-voltage protection was set to 3.61 V. It was originally meant to set the protection to 3.6 V but the specific resistors ratio could not be exactly matched according to equation 4.3. As the End Node lacks traditional battery sensing feature, thus, the over-voltage protection mechanism of the IC is manipulated to limit the maximum voltage supplied to the load and battery. This means that if the output voltage of the PMU is above 3.61 V, the PMU will disconnect both the load and battery from the boost charger. During this period, the load has to rely on the battery to supply power. The PMU will resume charging the battery and powering up the load once the voltage does not exceed 3.61 V. Based on the design decision in Figure 4.20 (b), the over-voltage protection will trigger if the solar cell generates more than 4.52 V.

The End Node operates optimally at 3.6 V. The main reason for this is the battery capacity. At 3.3 V, the battery has extremely low density, making them impractical as a storage element. Initial density test on two types of li-ion batteries shown in Table 4.5 indicates that at 3.3 V, both batteries have less than 4 % of its rated capacity. At 3.7 V, the capacity is about half of its official rating. Arguably, every battery has its own density depending on various factors such as type, quality and lifecycle.

Table 4.5: Voltage versus capacity for two types of 1000 mAh battery

Battery	Initial voltage (V)	Termination voltage (V)	Capacity (%)
Type 1	3.70	3.03	54.63
	3.30	3.03	3.96
Type 2	3.70	3.03	40.85
	3.30	3.03	3.06

To address the capacity issue, the battery used for the End Node is increased from 1000 to 2000 mAh with an increase in weight (from 22 g to 36 g) and dimension. By 2014, the 2000 mAh is the most practical battery to use in terms of density, price, weight and dimension for custom-made electronics. The voltage for the battery is limited to 3.6 V due

to the Xbee stability issue which is discussed in 5.1.2 (f). In theory, the Xbee should not operate above 3.6 V and the battery voltage should match this requirement.

A possible workaround to this load-battery matching problem is that the load is connected directly to the battery (pin 14) instead of pin 15 (the official output pin) of the BQ25504 IC. A Schottky diode can then be placed between the battery and load to reduce the voltage according to Xbee specification. A Schottky diode normally has between 0.3 to 0.4 V of forward voltage drop. From this setup, the BQ25504 IC and li-ion battery can provide 4 V of voltage, which would drop to around 3.7 V through the diode once it reaches the load. Initial test on this method is shown in Table 4.6.

Table 4.6: Voltage regulation methods on the 1000 mAh battery

Initial voltage (V)	Termination voltage (V)	Voltage regulation method	Battery capacity (%)
3.70	3.03	None	54.63
4.10	3.43	Schottky diode (0.4 V forward bias voltage drop)	78.17
4.00	3.73	Diode (0.7 V forward bias voltage drop)	30.46

The Schottky diode approach looks promising as higher battery capacity can be utilized. If implemented, it allows the battery to operate at around 4.0 to 4.1 V of maximum voltage with an increase of battery capacity from 54.63 to 78.17 %. This method provides voltage of around 3.6 to 3.7 V to the load.

However, this approach would require a solar cell with higher voltage. Recalling that the MPPT mechanism drops the input voltage of the solar cell by 80 %, thus charging the battery to 4.1 V requires a solar cell providing 5.13 V.

Secondly, the same argument can be made that the use of Schottky's diode would only waste precious resources harvested at the first place. This increases the power

inefficiency of the system. Moreover, charging the battery to 4.1 V would take too much time and therefore does not fit with the design of the H-CDE system. Initial tests conducted showed that it will take more than a single day of daylight exposure to charge a 2000 mAh battery from 3 to 4.1 V. This is discussed later in Section 5.4.3 and 5.4.5.

Either way, this requires a larger sized solar cell to meet the intended specification. This reduces the portability factor of the End Node. Furthermore, a custom-made solar cell might be needed which would only increase the cost of the design. This alternate setting would also make the battery the primary power source to the load while the PMU will primarily charge the battery. This is undesirable as li-ion battery has limited charging cycle lifetime. Therefore, the idea of using the Schottky diode is not pursued.

Next is the discussion on the under-voltage protection. The H-CDE End Node has double layered under-voltage protection. The first layer is provided by the BQ25504 IC where the cut-off voltage is 3.0 V. If the voltage at V_{STOR} (load) and V_{BAT} is below 3.0 V, then the V_{BAT} is disconnected from the load. However, the harvesting element may still continue to provide voltage to the V_{STOR} although the voltage may not be enough to power up the load. The second layer is the built-in under-voltage protection circuit at the li-ion battery. The cut-off voltage for the built-in is around 2.8 V from lab test conducted.

During normal operation, the BQ25504 would power up the load from $V_{IN.}$ If additional resource is available, it would try to charge the battery. If V_{IN} is unable to fulfil the power requirement of the load, the IC utilizes the battery. The H-CDE End Node has a switch placed between the IC and the Xbee module. This allows dedicated battery charging when the load is not required for operation.

As the MPPT is sampled every 16 seconds and the reference voltage is stored in V_{REF_SAMP}, if the V_{IN} from the solar cell drops below V_{REF_SAMP}, then the boost converter would boost the voltage to match V_{REF_SAMP} by sacrificing a portion of the current. If the V_{IN}

is above V_{REF_SAMP}, the boost converter would be by-passed. If the voltage of V_{IN} is by-passed, it will then be subjected to regulation by the over-voltage protection mechanism

4.4   Part C: Experimentation

This section explains the tests conducted to verify the performance of the H-CDE system. The proposed H-CDE system is compared with the standalone (un-embedded) system or with other related works from the literature. Similar to previous sections, the experiments cover the topic of RF transmission, crowd density estimation and EH with the majority of the tests conducted in the USM Engineering Campus.

4.4.1   Calibration

For the H-CDE system, two types of calibrations are conducted. First, the transmission power level of the RF module is investigated and followed by the power level comparison between the proposed with the standalone system. The former must be conducted to match the module with the manufacturer's specification while the latter is to verify that the proposed system would also operate based on the specification.

The power level of the Xbee module is adjusted using XCTU software version 6.1.3 and the Xbee is connected to the spectrum analyser as shown in Figure 4.21. The proposed system uses the whip antenna type. However, for the calibration, the Reverse Polarity-SubMiniature version A (RP-SMA) had to be chosen as the whip antenna module could not be connected to the spectrum analyser for measurement. This setup should pose no problem as the power output of both antennas should be almost similar. The difference between the two would be the EM radiation and this only affects the range and radiation pattern test. The power loss incurred by Connector 1 is calculated from the difference between the output power of the Xbee and the measured power at the spectrum analyser.

For the calibration test, the Arduino UNO (Coordinator) housing the Xbee is programmed to send 10 bytes of payload periodically every 10 seconds to trigger the transmission. For digital identification purposes, 10 bytes of data is more than enough to represent a huge number of users, at 2^{80} IDs.
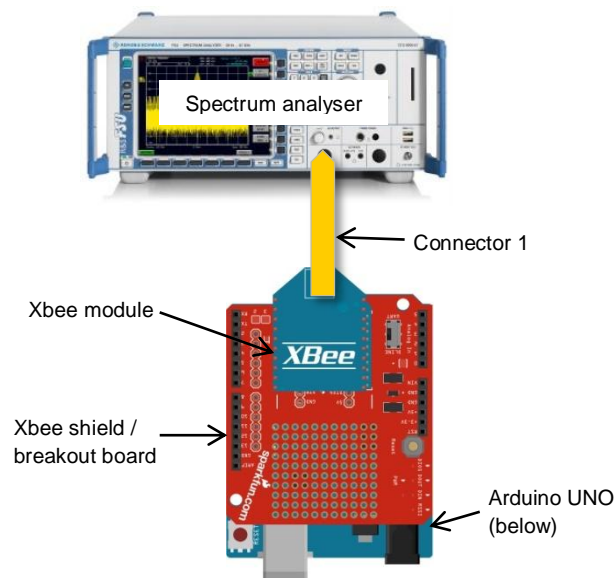
Figure 4.21: Direct connection from the Xbee to the spectrum analyser through an RP-SMA connector using Connector 1

The transmission power performance setup of the H-CDE End Node prototype compared to the standalone system is not straight forward. The test involved the power divider and thus its power loss must be measured first. The formulation of the power divider is given as follows:

N-way power divider loss = -10 log10 (1/N)   (4.6)

where N is the number of ports. Thus, a 2-way power divider incurs 3.01 dB of power loss to both sides of the output port.

The experimental setup to measure the power loss at the power divider is illustrated in Figure 4.22. However, the experiment also requires power loss values at Cable 1 and the

50 Ω terminator to complete the measurement. The procedure to find the power loss of Cable 1 is shown in Figure 4.23.
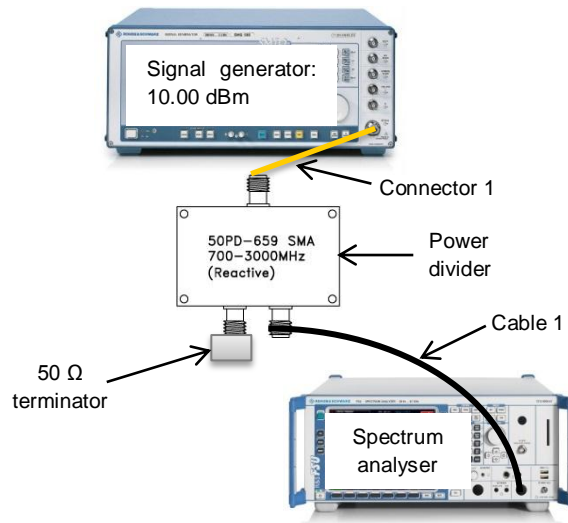
Figure 4.22: Experimental setup for measuring the power loss of the power divider
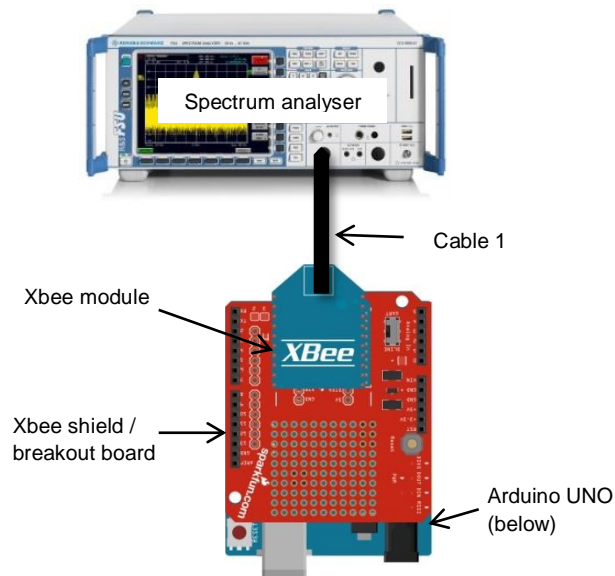
Figure 4.23: The arrangement for measuring the power loss incurred by Cable 1

Next, the power loss incurred by the 50 Ω terminator can be calculated from the measurement at the spectrum analyzer and then applying it to equation 4.7. The calculation for the power loss of the power divider is given as follows:

$$PD = SG - CT1 - T - SA - CB1 \qquad (4.7)$$

where the power loss at each part are denoted as *PD, SG, CT1, T, SA* and *CB1* for power divider, signal generator, Connector 1, 50 Ω terminator, spectrum analyzer and Cable 1 respectively.

Once *PD* has been determined, the transmission power of both the prototype and standalone systems can be determined by the experimental setup illustrated in Figure 4.24.
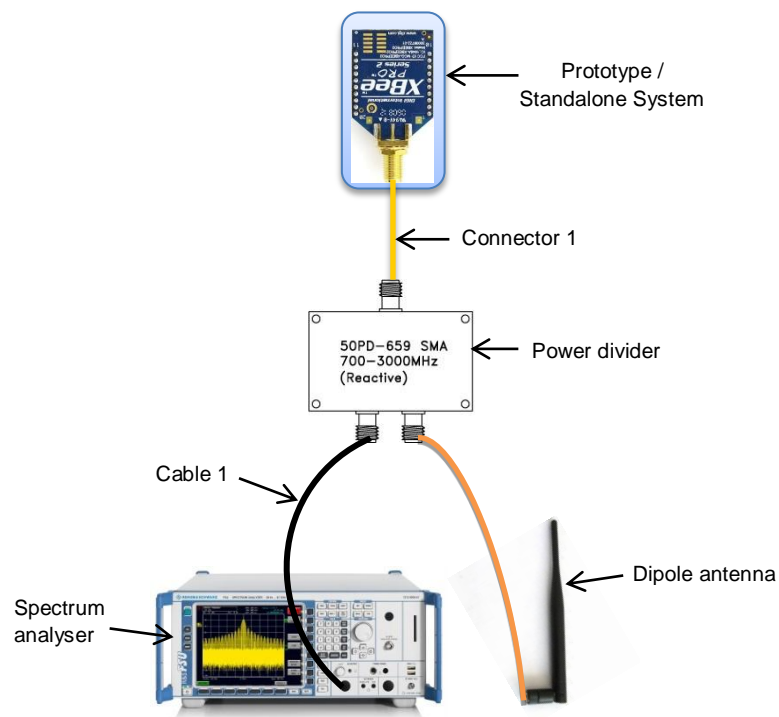
Figure 4.24: Equipment arrangement for measuring transmission power with respect to power level. The dipole antenna is connected directly to the power divider without any cables.

4.4.2   Stability and Specification Adherence

As a portion of the H-CDE system involved hardware development, thus the stability test is vital to verify conforming operation of the system according to specification. The stability and service test would also ensure that the system is reliable and its operational threshold defined. There are two approaches covered by the test where the RF-WSN transmission and electrical specification are evaluated and verified.

4.4.2 (a) Latency

Latency is the delay between the stimulus and response of a system. There are two types of latency; single trip and round trip. The latter is widely practical in most communications and also determines the actual response of the system. The factors affecting latency in the H-CDE system are illustrated in Figure 4.25 and their descriptions are in the following list.
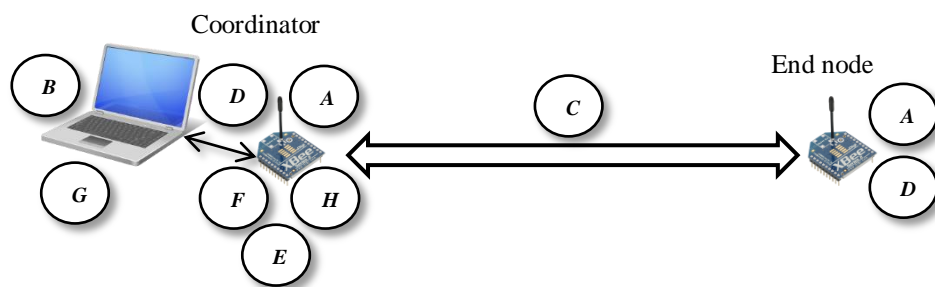
Figure 4.25: The relative positions of the factors affecting latency

A. Xbee module processing time, including Carrier Sense Multiple Access - Collision Avoidance (CSMA-CA), DC to AC conversion and wired internal/external data transfer

B. Computer processing time

C. Time on air

D. Buffering time

E. Re-transmission for up to 4 attempts at MAC layer

F. Error correction

G. Software processing time

H. Size of payload

The formulation of round trip latency without any re-transmission and error correction is given in equation 4.8. The variables in equation 4.8 refer to the labelling in Figure 4.25.

$$\text{Latency} = (\ 2 \text{ x } A\ ) + B +\ (\ 2 \text{ x } C\ ) + (\ 2 \text{ x } D\ ) + G + H \qquad (4.8)$$

However, none of these parameters can be empirically measured independently, as the mechanism to perform such thing could not be identified within the scope of this study. As such, the latency measured in this study is the combination of all the parameters denoted in equation 4.8. Parameters that can be theoretically calculated are time on air and CSMA-CA re-transmission given below (Digi, n.d.).

$$\text{Time on air (B)} = 0.416 \text{ ms} + 0.032B \text{ ms} \qquad (4.9)$$

where the data is sent in byte (B) size.

$$\text{CSMA-CA re-transmission} = \text{CCA} + \text{random delay} + \text{time on air} \qquad (4.10)$$

where the clear channel assessment (CCA) is fixed at 0.128 ms and the random delay is 0.320n ms, where n is between 0 and 15.

Table 4.7 shows the related latency studies on 802.15.4 and ZigBee. The latency reported from each work differed due to the factors as illustrated in Figure 4.25. In addition, the baud rate also affects the latency. On average, it is expected that a typical latency of ZigBee based modules is less than 100 ms. The latency test of the H-CDE will determine its performance compared to the literature and standalone system. In addition, the latency caused by crowd presence is also investigated.

Table 4.7: Related works on 802.15.4 and ZigBee single hop latency. Maximum payload of an 802.15.4 frame is 100 bytes as opposed to 84 bytes for the ZigBee protocol.

Related works	Protocol	Latency (ms)	Payload (bytes)	Baud rate (bps)
Randolph and Hirsch (2010)	802.15.4	43	100	115200
Randolph and Hirsch (2010)	802.15.4	308	90	9600
Abdulla (2011)	802.15.4	275	Undetermined	9600
Abdulla (2011)	ZigBee	68.75	Undetermined	9600
Piyare and Lee (2013)	ZigBee	110	80	Undisclosed
Mayalarp et al. (2010)	ZigBee	64-67	10	Undisclosed
Zanal and Ismail (2013)	ZigBee	4000	26	Undisclosed

The first step is to determine the single hop latency performance of the H-CDE prototypes and the standalone system. The Docklight software version 2.0.5, which is a tool for serial communication, is used to generate transmit request API frames to the Coordinator node. Upon receiving the API frames, the Xbee module on the Coordinator will send ZigBee frames to the end node. All of the data transmitted will be received without error, which can be verified by the API acknowledgment frame with a hexadecimal code of 00 (success) delivery status.

A total of five Xbee modules (three in End Node and two in Router modes; denoted as Router 1 and 2) are selected for the test, placed in both the standalone and prototype nodes one after the other. The latency test setup is shown in Figure 4.26. The latency is calculated from the average of five measurements from the period the payload is transmitted and received by the Docklight. Data is transmitted every second.

Next, the two hop latency is investigated. Due to limited number of End Nodes, the latency of multiple hops could not be performed. Instead, a different approach is taken. From the two hop latency, a formulation is derived that would represent an estimation of multi-hop latency in an Xbee-based WSN (Javaid et al., 2013; Yu, 2013).
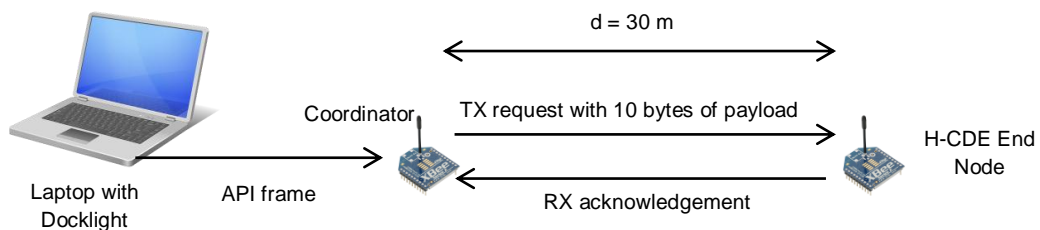
Figure 4.26: The arrangement of the single hop latency test

Xbee does not allow manual routing as all the routings are handled automatically by the ZigBee protocol. However, force routing can be achieved by putting a node entirely out of reach from the Coordinator, forcing a router in between to route the packet from the isolated node. The topology of the routing can be confirmed from the 'Networking working' mode, exclusively available in the XCTU software.

The site layout of the two hops latency test is illustrated in Figure 4.27. The same hardware and software setup were used as in the single hop latency test with the addition of Router 1 placed between the Coordinator and the End Nodes. The shortest distance between nodes is also shown in the figure, although practically the signal suffers from multi-path propagations due to solid obstructions from the building and vehicles in the parking lot.

The final step is to investigate the effect of crowd on latency. The crowd is formed by fifteen individuals standing about 65 cm apart from each other, forming five rows where each row consists of three people as shown in Figure 4.28. The software and hardware setup for measuring latency is exactly the same as in the single hop latency.
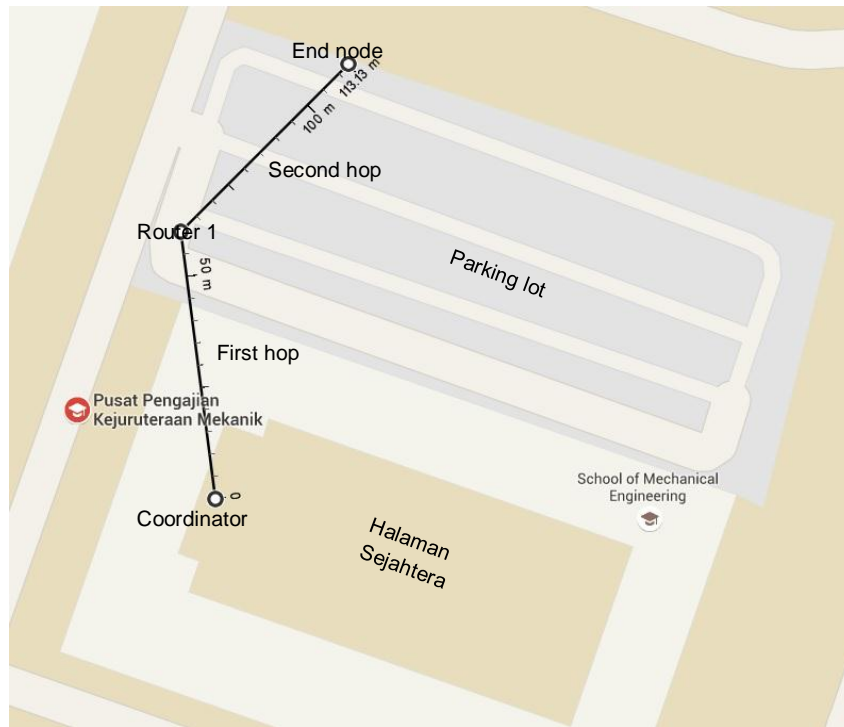
Figure 4.27: Aerial view of the two hops latency test arrangement captured from Google Maps
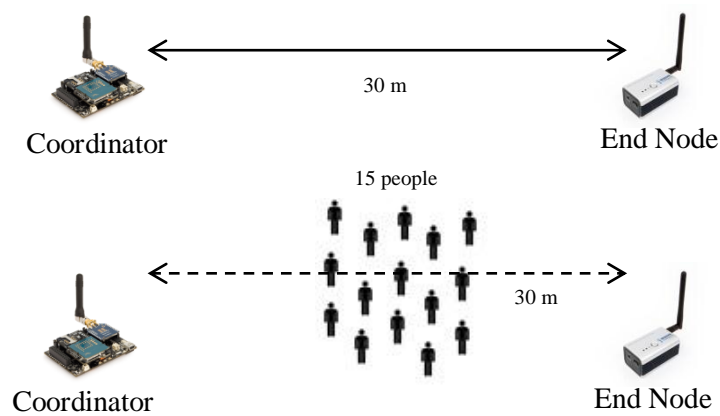
Figure 4.28: Latency test from the Coordinator to the End Node with and without the crowd (top)

4.4.2 (b) Throughput

Throughput is defined as the rate of meaningful information that was successfully transmitted over time. This definition is translated to the number of frames successfully received by the Xbee module in a given time without errors.

The size of each ZigBee API frame differs depending on the size of payload and its type. The API frame is then encapsulated into the PHY layer frame for wireless transmission. In general, each API frame consists of protocol, mode and payload frames. The protocol and mode frames are the overheads. The mode options are broadcast, unicast, encryption, and source routing.

According to the official documentation (Digi, 2015), a single hop, router to router connection without encryption allowed for 35 kbps of throughput. Table 4.8 shows the related works on the throughput of 802.15.4 and ZigBee. The latency reported by Piyare and Lee (2013) was based on 80 bytes of payload. Apparently, the baud rate would also affect the throughput of the system.

Table 4.8: Related works on single hop throughput

Source	Throughput (kbps)	Baud rate (bps)
Datasheet (Digi, 2015)	35.0	115200
ZigBee (Piyare & Lee, 2013)	5.4	115200
ZigBee (Piyare & Lee, 2013)	3.2	9600
ZigBee (Abdulla, 2011)	10.92	9600
802.15.4 (Abdulla, 2011)	7.24	9600
ZigBee/802.15.4 (Sarvghadi & Tat-Chee, 2013)	8.65	Undisclosed

As a requirement of the H-CDE system, a single frame is desirable for instantaneous crowd size estimation. In fact, for identification purposes, a few bytes of payload are often

sufficient. For the H-CDE system, only two bytes of payload is needed to send the *DB* API command.

Thus, reflecting the objective of the study, the aim of the throughput test of the H-CDE system is to examine throughput performance based on the continuous transmission of single ZigBee frames. As such, results would not reflect a true or the absolute maximum throughput of the Xbee modules, but rather on the effect of crowd on throughput from a single frame point of view.

The throughput experiment uses the same setup as in the latency test in the previous section. However, the latency test is meant for a round trip transmission, whereas the throughput only requires single trip transmission.

To convert the timestamp in Docklight to a single trip, the period for a complete round trip is divided by two, giving an approximate value of the data transmission. The Docklight is programmed to send 80 bytes of payload in a single API frame periodically every 10 s.

4.4.2 (c) Self-healing

One of the most important aspects in a multi-hop network is its ability to reroute traffic or recover from broken connections due to dropped routing nodes. When these missing nodes reconnect, the network should be able to rediscover and reroute the traffic. This feature is known as self-healing.

For any S2 Xbee network, the self-healing is handled automatically by the ZigBee protocol, and is therefore transparent to the end user. Any reconnecting router and end node will send beacon requests recursively and sequentially to all channels in its list to discover any nodes with the same PAN ID. The requests are limited to 9 scan per minute for the first

111

5 minutes and 3 scans hereafter based on the requirement of the ZigBee Alliance. Once discovered, the node should join the network within a few seconds (Digi, 2015).

The objective here is to measure the time it takes for the Xbee network to recover from a broken connection. The experimental arrangement is again the same as in the latency test (Section 4.4.2 (a)), albeit with slight modifications, as shown in Figure 4.29.
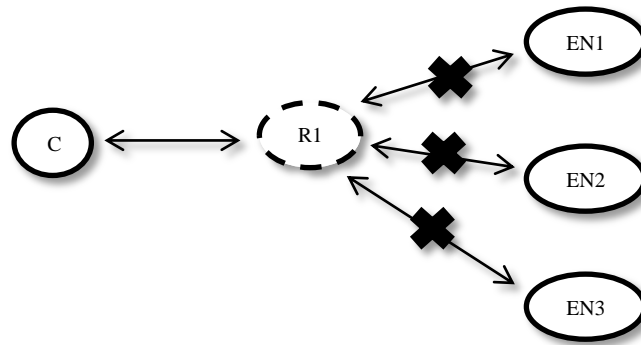
Figure 4.29: Node arrangement for self-healing where C, R1, EN1, EN2 and EN3 represent the Coordinator, Router 1, End Node 1, 2 and 3 respectively. The dashed outline of R1 indicates disconnection resulting in the loss connections of the EN from C.

Router 1 is shut down for 10 seconds to break the connections from the Coordinator to the end nodes; labeled by the bolded X symbol. After, the router is re-activated and the Node Discovery button is pressed in the XCTU (Figure 4.30). The amount of time to re-discover all the nodes are recorded using a stopwatch. Network Working Mode in the XCTU software is used to verify that the topology of the network is correct before and after the self-healing is initiated.
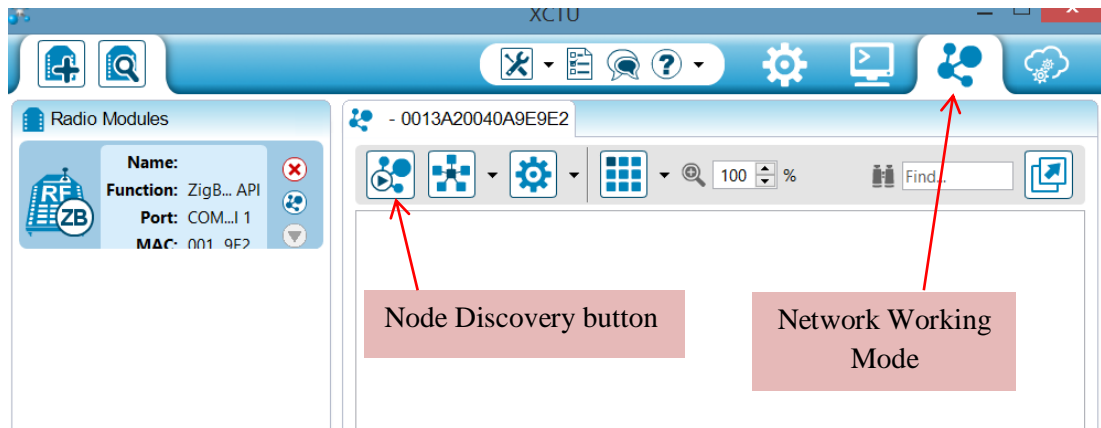
Figure 4.30: Network Working Mode and Node Discovery feature

4.4.2 (d) Antenna Radiation Pattern

The antenna radiation pattern presents a visualization of the radiated power from the antenna. For a 1.5 dBi quarter wave monopole whip antenna used in the S2B Xbee module (Digi, 2015), its radiation pattern is omnidirectional (non-directional) as illustrated in Figure 4.31 (De Vita, 2012).

The objective of the test is to investigate the field radiation pattern of the Xbee module on-board the prototype versus the standalone system. The Range Test Tool of the XTU software is used to record the RSSI information from the Coordinator to the end node. The RSSI is recorded for every 5 degrees of rotation and the average of five measurements is calculated. The distance from the Coordinator to end node is 50 m which is in the far-field region. Figure 4.32 shows the arrangement of the antenna radiation pattern test, while the results are plotted using Antenna Radiation Diagram Plotter version 1.0.3. Unfortunately, only a single axis mounting pole is available from the facilities and its effect on the eventual radiation pattern is discussed in Chapter Five.
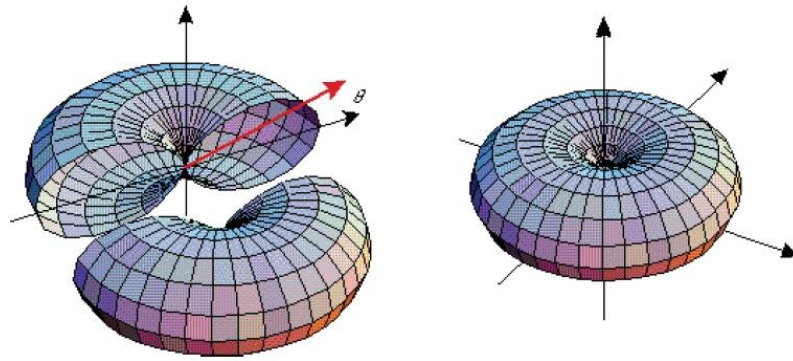
Figure 4.31: Whip antenna radiation pattern which resembles a doughnut shape
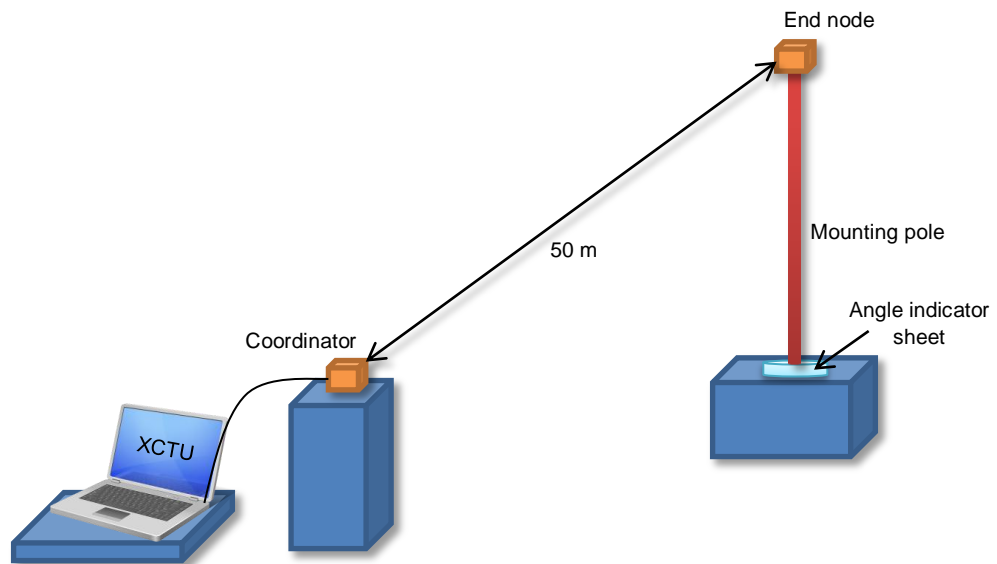
Figure 4.32: Experimental setup of the antenna radiation pattern

4.4.2 (e) Outdoor Range Test

The range test serves as a verification of the wireless coverage of the Xbee module. The test would ensure that the H-CDE End Node have comparable coverage according to specification. The test is conducted outdoors as the H-CDE system is meant to be deployed outdoors.

For the experimentation, the coverage distance between the standalone and proposed system is investigated. The range test is carried out in a line-of-sight (LOS) environment on

a straight road from coordinates 5°09'20.9"N 100°28'53.8"E to 5°08'57.2"N 100°29'09.7"E, which is near the Engineering Campus of Universiti Sains Malaysia.

The Range Test Tool in XCTU is utilized to collect the RSSI data every 100 m based on 10 bytes of payload. The Coordinator is placed on the rear of a parked car while the End Node is placed at the rear of a second car (Figure 4.33). The distance, d is measured using the odometer of the second car and the average of five RSSI is calculated for each distance. Figure 4.34 shows arrangements for the test.
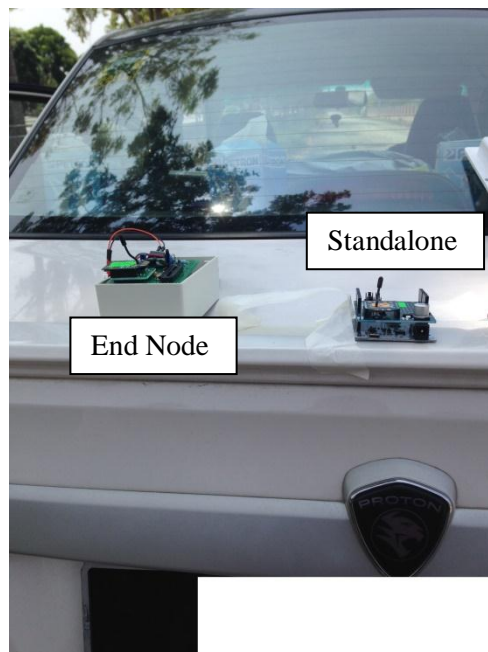
Figure 4.33: The End Node and standalone taped to the car
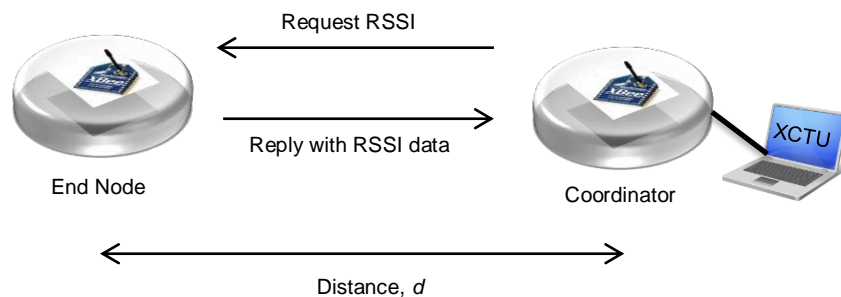
Figure 4.34: Conceptual illustration of the range test

4.4.2 (f) The Effect of Voltage on RF Transmission

The official voltage rating of the Xbee is 2.7 until 3.6 V although usually referred as 3.3 V. Verifying this information would be essential for the EH design as it will determine the over- and under-voltage protection mechanism. More importantly, the experiment also aims to investigate the effect of voltage on RF transmission once the voltage thresholds have been crossed.

The experimental setup is shown in Figure 4.35. The RSSI information of the prototypes is gathered by the Coordinator using the XCTU software. The voltage supplied by the DC power supply unit is incremented and decremented from 3.3 V. Although one of the initial objectives is to design a 3.3 V based WSN, this voltage level is expanded to 2.7 V and 3.6 V to match the Xbee voltage rating. In fact, this voltage range threshold is more practical in the actual design.

As a side note, a laboratory DC power supply does not represent well a solar cell due to its ability to supply high current. For example, the DC power supply could theoretically supply as much current demanded by the battery. This may violate the over-voltage threshold of the PMU. However, the usage of DC power supply is still necessary in certain tests for consistent performance gauging due to the fluctuating nature of the intensity of the sunlight.
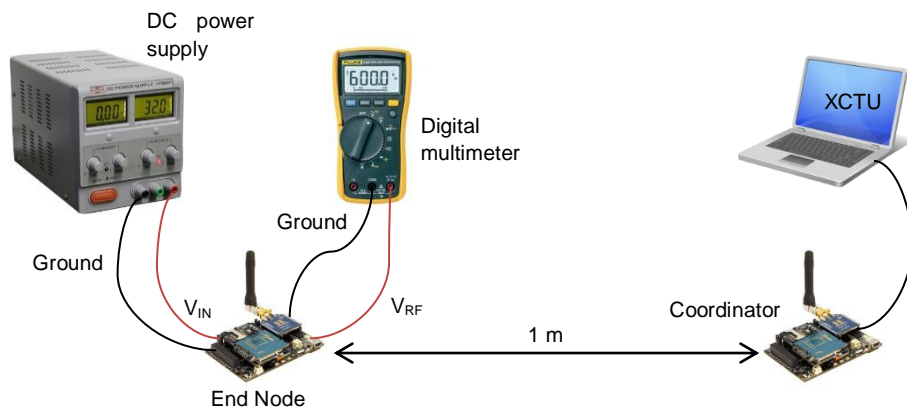
Figure 4.35: Stability test hardware setup. V_{IN} is the input voltage while V_{RF} is the voltage at the Xbee module.

To further strengthen the findings, the effect of added resistance on RF transmission is investigated. In contrast to the stability test earlier where the voltage is varied at the power source, now the voltage is varied by directly adding the resistance into the circuit.

A shunt resistor is placed in series with the Xbee module and a digital multimeter (DMM) is placed in parallel with the resistor to record the voltage across it as shown in Figure 4.36. The current and resistance can be calculated by utilizing these basic electric circuit equations when connected in series:

$$V_S = V_R + V_{RF} \qquad\qquad (4.11)$$

$$I_S = I_R = I_{RF} \qquad\qquad (4.12)$$

$$R_{TOTAL} = R_R + R_{RF} \qquad\qquad (4.13)$$

where V_S, V_R and V_{RF} represents the voltage at the supply, shunt resistor and the Xbee module respectively. The RSSI values were read from the Range Test Tool at 1 m T-R separation.
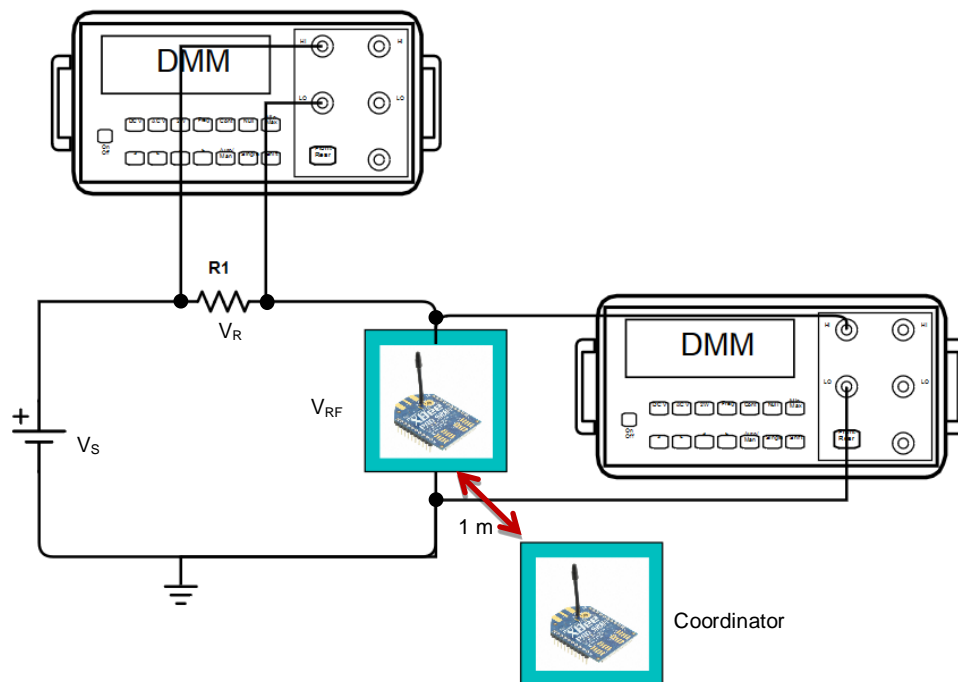
Figure 4.36: Experiment setup for resistance stability test

4.4.2 (g) Current and Power Consumption

The power consumption is a fundamental parameter that would determine whether the EH design is successful or a failure. By applying Ohm's law, V=IR which then relates to power, P=IV, the electrical specification of the End Node can be determined.

The voltage is measured using a DMM at the End Node shunt resistor at pin 14 as shown in Figure 4.37. The current is then calculated using Ohm's law. Alternatively, the shunt resistor may be replaced by directly putting an ammeter between the power source and Xbee. Subsequently, the power consumption can be calculated from the voltage and current obtained.

The experiment requires the battery to be disconnected from the End Node. For measuring the voltage and current of the BQ25504, the switch on the End Node is shifted to Mode 2 to disconnect the load. To measure the voltage and current at the Xbee module, the switch is shifted to Mode 1.
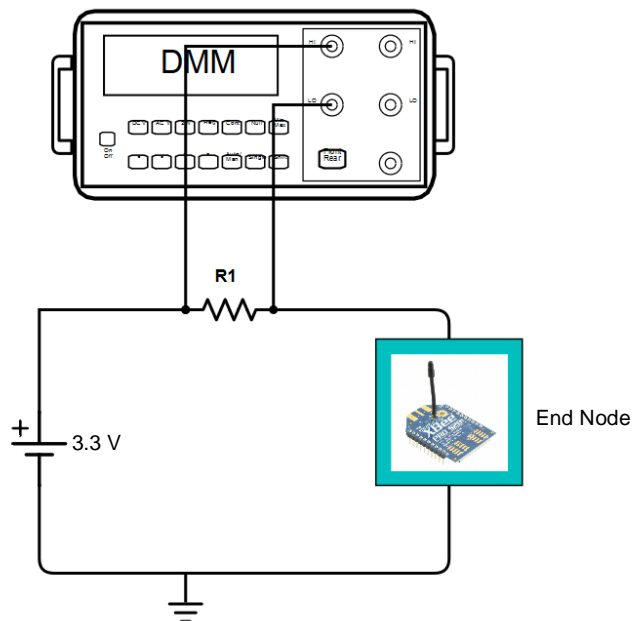
Figure 4.37: Measuring the current using shunt resistor (R1 = 1 Ω) method at the End Node

4.4.2 (h) Crowd Density Estimation Accuracy

The proposed H-CDE algorithm given in equation 3.1 until 3.3 is compared with three crowd-sized based estimation algorithms from the literature to verify its prediction accuracy. The algorithms are SCPL by Xu et al. (2013) (equation 2.1), WB by Yuan, Zhao, Qiu and Xi (2013) (equation 2.2) and EFE by Xi et al. (2014) (equation 2.3). The RSSI measured in the Training Phase will provide the inputs for these algorithms.

$$SCPL = \beta(RSSI_x) - |RSSI_1|$$

$$WB = \sum_{k=1}^{n} \left(\frac{RSSI_x}{RSSI_{ave}} \right)$$

$$EFE = \frac{\alpha(RSSI_x)}{(RSSI_x)}$$

Proposed H-CDE

Low density (LD): $LD \leq RSSI_{ave\_5} + RSSI_{crowd\_pattern}$

Medium density (MD): $RSSI_{ave\_5} + RSSI_{crowd\_pattern} < MD \leq RSSI_{max\_15} + RSSI_{crowd\_pattern}$

High density (HD): $HD > RSSI_{max\_15} + RSSI_{crowd\_pattern}$

As only Yuan, Zhao, Qiu and Xi (2013) provided information on the density classification, thus the SCPL and EFE algorithms would follow the density level defined by this research as given in Table 4.9. The density classification by Yuan, Zhao, Qiu and Xi (2013) is also adjusted to better fit the number of people from the Training Phase.

Table 4.9: Crowd Density Classification

Related work	Low Density	Medium Density	High Density
Proposed H-CDE system	5 people	6 to 15 people	16 to 50 people
Yuan, Zhao, Qiu and Xi (2013)	0-5 people	6 to 10 people	> 11 people

Next, the accuracy comparison between the path loss models by Haochao et al. (2015) (equation 2.4) and Hiroi, Shinoda and Kawaguchi (2016) (equation 2.5) with the proposed H-CDE model (equation 3.4) by this research is performed. The path loss models would predict the number of people within the area monitored.

$$PL\_Haochao = -74 + 44e^{(-0.126x)}$$

$$PL\_Hiroi = 6.9 + 20\log\sqrt{(v-0.1)^2 + 1} + v - 0.1$$

$$v = h\sqrt{\frac{2}{\lambda}\left(\frac{1}{d_1} + \frac{1}{d_2}\right)}$$

Proposed H-CDE $= PL_0 - 10n\log_{10}(d) - RSSI_{crowd\_pattern} - BAF$

The average RSSI data collected from the crowd of 5, 10 and 15 people is then used in a regression analysis to produce a linear equation. This allows extrapolation of the graph for up to 50 people which is matched with the sensitivity of the RF module (-98 dBm). The RSSI data for the crowd of 20 to 50 people is randomly generated using Microsoft Excel's RANDBETWEEN ( ) command based on the calculated average RSSI data and one standard deviation.

4.4.3 Energy Harvesting Performance

In this section, the performance related to the EH mechanism is evaluated. Every part of the EH system is tested to guarantee compliance according to the manufacturer's specification. This also includes the safety feature for charging the li-ion battery, as it is the most risky, albeit generally safe to use in the proposed EH system.

4.4.3 (a) Effect of Solar Cell Alignment

Solar cell misalignment will reduce its output power. The misalignment is caused by poor cell positioning or by a fixed deployment. In the fix deployment, the solar cell is pointed in a single direction, often perpendicular to the ground to maximize the power gained in the noon. A solution to this problem is by installing a sun tracker. Tracking the sun is the act of ensuring maximum solar light exposure by orienting the solar cell towards the direct position of the sun. However the sun tracker adds considerable cost and maintenance to the system. Instead, the solar cell can be made larger to compensate with the misalignment.

Here, the effect of solar cell alignment on its power output is investigated to verify its performance. A manual solar tracker had to be built to ensure the correct orientation of the solar cell towards the sun. The tracker also serves as a point of reference for the angle of misalignment. The solar tracker is built using two IXYS solar cells, a board and Arduino UNO as illustrated in Figure 4.38. The actual tracker is shown in Figure 4.39.
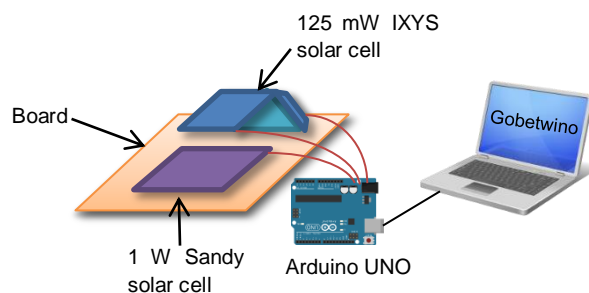
Figure 4.38: Conceptual illustration of the solar cell alignment test
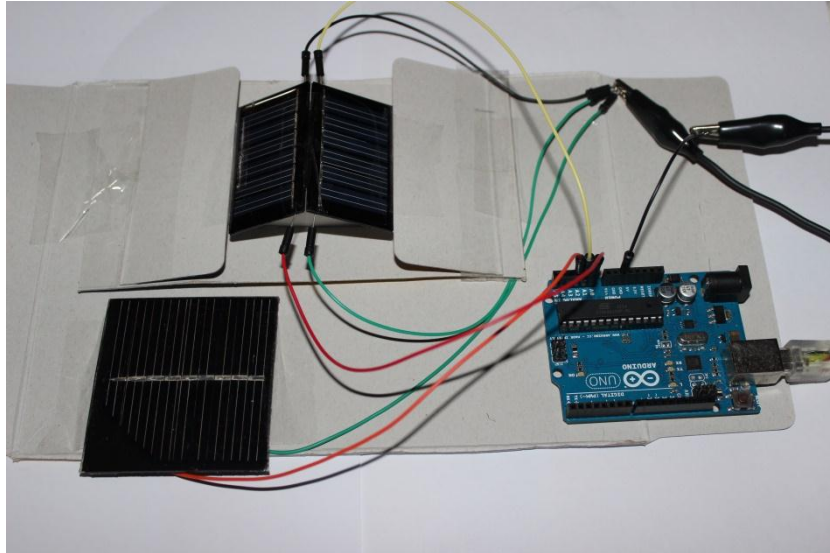
Figure 4.39: The makeshift solar tracker with a 500 mW solar cell for an initial test

The angle of inclination of the IXYS solar cells is shown in Figure 4.40 and their characteristics are given in Table 4.10. The 30^0 angles are determined by measuring the threshold of acceptable performance of the solar cell when tilted (its discussion provided in Chapter Five). By balancing the output voltage of both the IXYS solar cells, the starting point (perfectly aligned) angle can be determined. The alignment test is conducted from 0 until 180 degrees at 12 pm and the data collected by the Arduino UNO. The angles are confirmed manually using a protractor. This means that with the absence of a mounting mechanism, the sun tracker had to be manually rotated by hand for the targeted angles. The voltage is measured using Arduino UNO's analog pins and stored by the Gobetwino software inside the laptop.
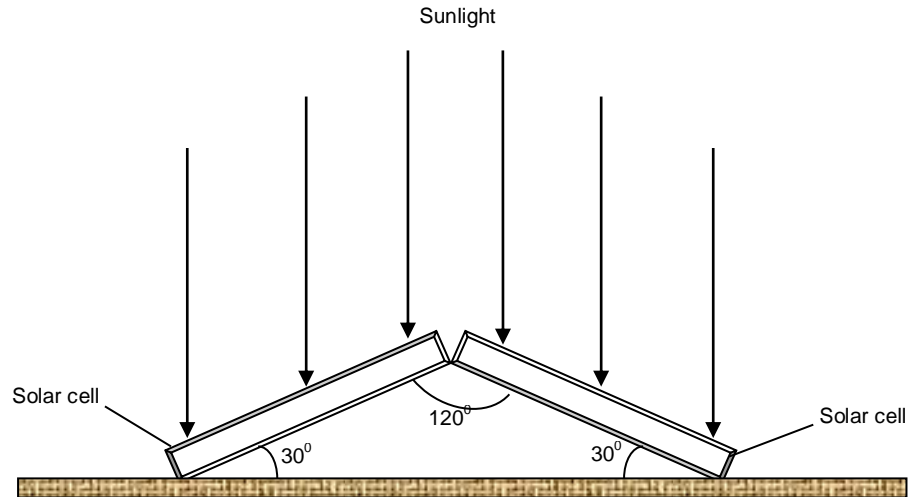
Figure 4.40: Angle of inclination of the IXYS solar cells

Table 4.10: Characteristics of the solar cell for the alignment test

Brand	IXYS SLMD121H04L
V_{sc}	2.52 V
I_{sc}	50.0 mA
V_{mpp}	2.00 V
I_{mpp}	44.6 mA

4.4.3 (b) Maximum Power Point Tracker

The impact of the MPPT is investigated by comparing the performance of an enabled MPPT versus non-MPPT. This procedure would verify the benefit of the MPPT. Thus, it is expected that the MPPT mechanism will harvest higher amount of power as opposed to a non-MPPT system. The MPPT feature is disabled from the prototype board by changing the setup in pin 2 until 4, as shown in Figure 4.41.
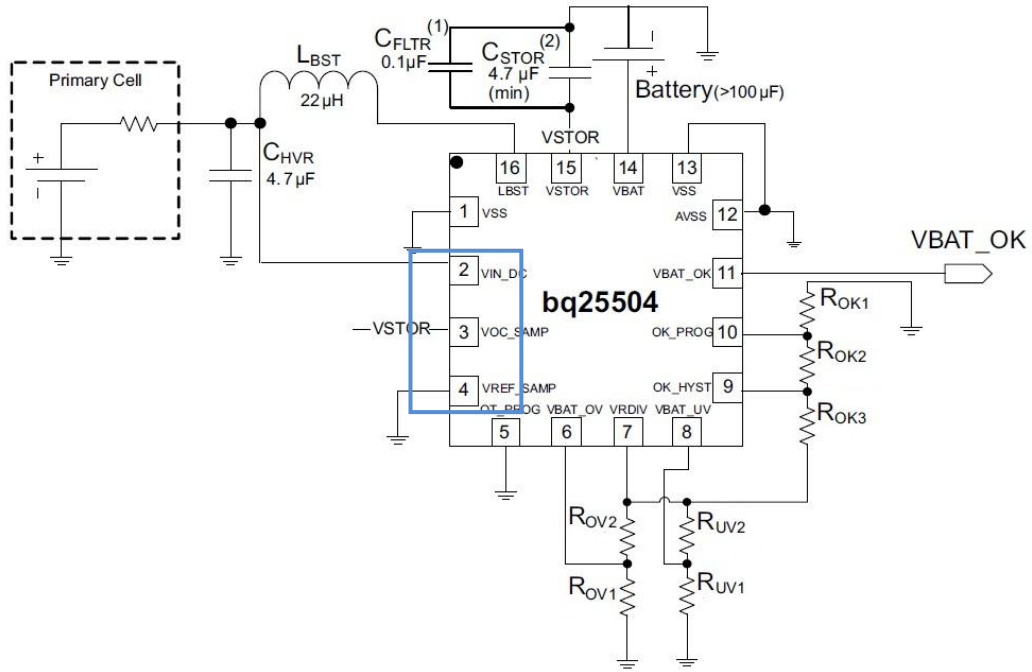
(a)
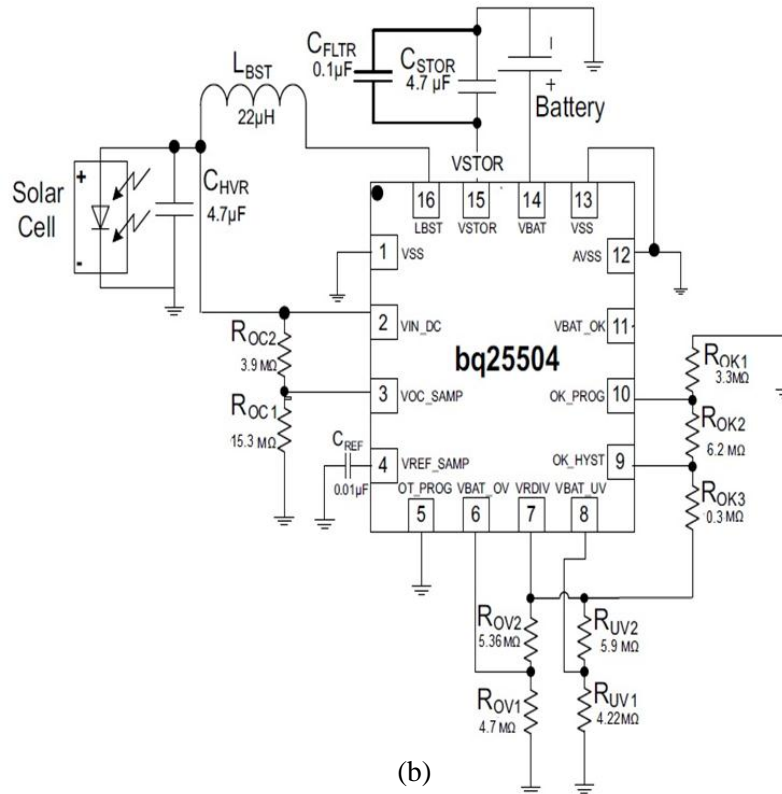
(b)

Figure 4.41: Circuit diagram of (a) non-MPPT versus (b) MPPT. The blue rectangle
highlights the amendments made to disable the MPPT.

Figure 4.42 shows the experimental arrangement of the test. The V_{IN} and I_{IN} are
supplied by Arduino UNO as to guarantee equal power for both cases. The voltage of the

battery is recorded every minute by Arduino UNO and the Gobetwino software. The EH mechanism of the proposed H-CDE system will definitely reduce the amount of time to charge the battery and also prolong its operation by allowing the battery to replenish its energy from the sunlight. This is a clear advantage compared to non-EH and non-MPPT conventional systems such as Naveen and Manjunath (2011), Xi et al. (2014) and Yuan, Zhao, Qiu and Xi (2013).
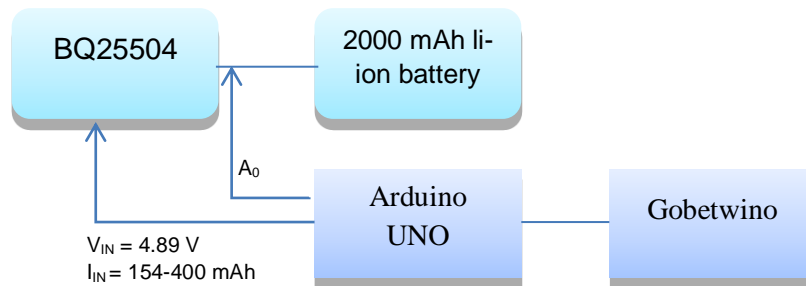
Figure 4.42: Block diagram of the MPPT versus non-MPPT experimental setup. A_0 is the analogue input pin of the Aduino UNO board.

4.4.3 (c) Energy Harvesting Mechanism Functionality Test

The objective of this section is to verify the functionality of the EH mechanism embedded on the End Nodes. The experimental setup is shown in Figure 4.43. The Router 1 is added which acts as the controlled unit. The distance between the Coordinator to Router 1 and End Node 3 is about 30 cm. However, the T-R separation for End Node 1 and 2 is around 50 cm. The difference is due to the outdoor device placement. The batteries for the End Nodes were initially set to 3.0 V and all of the solar cells were pointed perpendicular to the ground.

The Coordinator is programmed to sequentially execute the *DB* command to all End Nodes and Router 1 every minute. Two Gobetwino programs are run at the same time on the laptop with different ports; one for the Coordinator and the other for Router 1. The Router 1's Arduino source code is similar to the one given in Appendix I. The first Gobetwino

program is used to collect RSSI information of all nodes while the second is used to record the voltage measurements for Router 1.
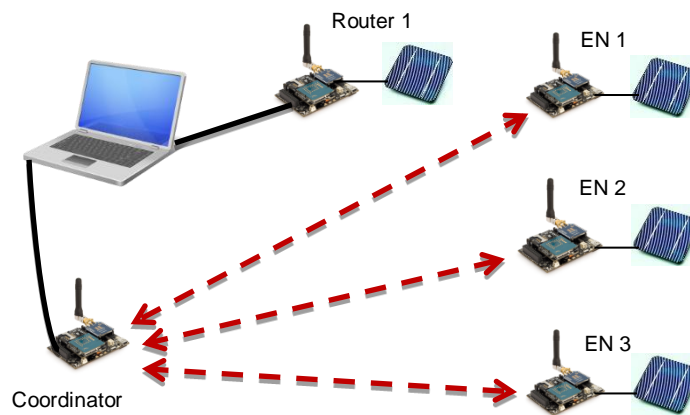
Figure 4.43: Experimental setup for the EH functionality investigation

4.4.3 (d) Energy Harvesting Performance in Range Test

Continuing from the previous section, the EH performance is further evaluated by subjecting it to a range test. This experiment would verify that the EH mechanism does not disrupt the RF transmission. The arrangement of the test is illustrated in Figure 4.44, which is similar to the range test conducted in Section 4.4.2 (e). For the first experiment, the End Node is connected to the solar cell and battery. The RSSI data is then collected using XCTU and the voltage of the battery is collected using the data logger. For the second run, the End Node is connected to the solar cell without the battery. The third experiment only assigned the battery to the End Node without the solar cell.
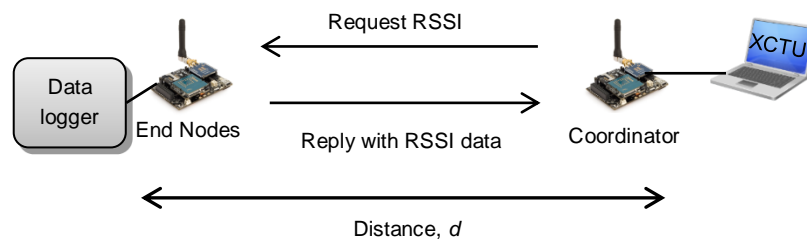
Figure 4.44: Setup for EH range test

4.4.3 (e) Battery Performance

The battery performance test is imperative as it will determine the length of operation of the H-CDE system, especially with the extended absence of sunlight. The performance investigation of the 2000 mAh li-ion battery is carried out using two methods.

First is to investigate the actual battery capacity at 3.61 V, which is the maximum voltage allowed by the PMU to match with the voltage threshold of the Xbee module. Reducing the voltage of the battery will also reduce its capacity. Thus, this step would define the degree of battery capacity reduction.

The batteries of the End Nodes were initially charged to 3.61 V and the load is turned on while the solar cell is removed. The RF data transmission is initiated and remained continuous for the duration of the test as to imitate an actual scenario. The transmission is monitored by the Gobetwino software at the Coordinator. Deducting the begin time with the end time (transmission stopped) would yield the duration of the operation.

Second is to measure the battery charging time without the presence of the load. This method will determine the time it would take to charge the battery from 3 to 3.61 V when transmission is deactivated. This method will also determine whether the solar cell is rightly matched with the battery. This is so that the battery charging time will not consume too much time, making the entire EH subsection impractical in real scenarios.

The load is turned off by changing the switch on the H-CDE End Node to mode 2 and the V_{BAT} information is collected by the data logger. The setup of the second objective is illustrated in Figure 4.45. The initial voltage of the battery is set to 3.0 V.
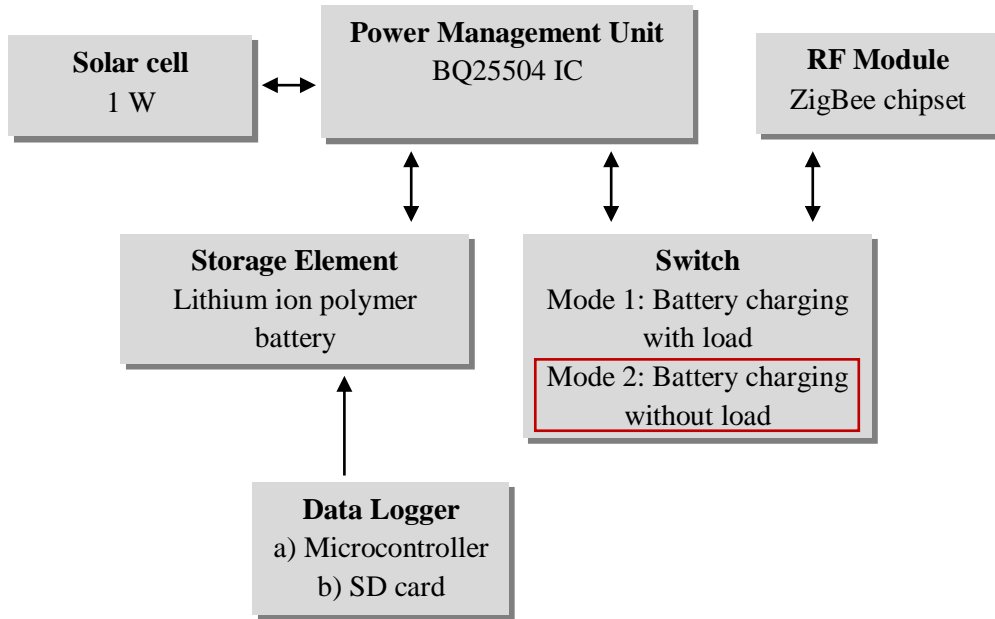
Figure 4.45: The block diagram of the battery charging without the load experiment

4.4.3 (f) Over- and Under-voltage Protection

The over- and under-voltage protection mechanisms keep the battery and load within the safe voltage range. In particular, the main safety issue is to ensure the battery does not go over or below its rated voltage, as their impacts would negatively affect the battery as explained in Chapter Three. The experimental arrangement is shown in Figure 4.45 and Figure 4.46.
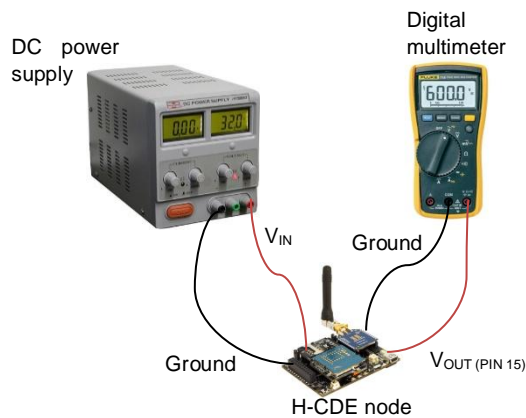
Figure 4.46: The setup for over- and under-voltage protection experiment (Texas Instruments, 2012; Texas Instruments, 2013b)

The DC power supply unit replaced the solar cell as the power source, as the former allows discrete increments of voltage. For the over-voltage experiment, the input voltage range was set from 3.0 to 5.5 V with a 0.2 V of increment. The voltage of 5.5 V is the maximum rated voltage of the BQ25504 IC.

For the under-voltage investigation, the batteries are removed while the DC power supply unit remains connected to the input of the BQ25504. The voltage ranges from 1 to 3 V with an increment of 0.2 V.

4.4.3 (g) Power Efficiency

According to the official documentation, the BQ25504 has between 80 to 90 % efficiency, depending on the level of voltage operation (Texas Instruments, 2012). Therefore, the H-CDE system should have comparable efficiency based on the specification.

The setup of the experiment is illustrated in Figure 4.47. To obtain the best case scenario, the experiment is conducted at 1 pm with the presence of clear sky and bright sunlight. To represent a worse case, another experiment is conducted at 1 pm during a cloudy day. The DMM is set to ammeter mode and connected in series to the H-CDE node to obtain the current measurement. Calculation of power efficiency is based on equation 4.14 given below whereas the comparison between the optimal and non-optimal scenario (relative efficiency) is given in equation 4.15.

$$\text{Efficiency} = \frac{P_{OUT}}{P_{IN}} = \frac{V_{STOR} \cdot I_{STOR}}{V_{IN} \cdot I_{IN}} \qquad (4.14)$$

$$\text{Relative efficiency} = \frac{P_{NonOptimal}}{P_{Optimal}} \; x \; 100 \qquad (4.15)$$
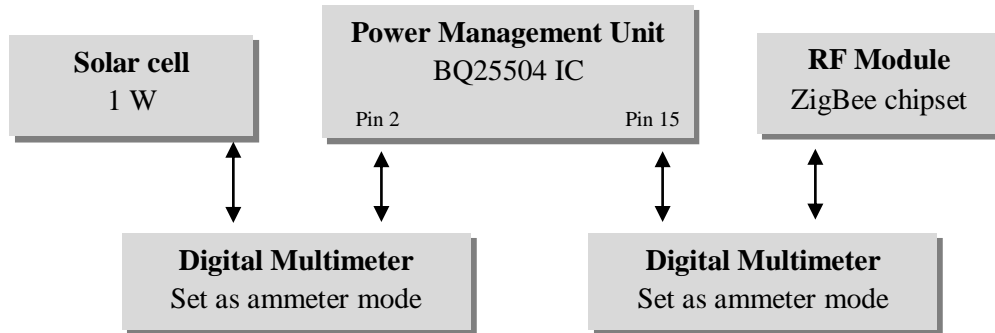
Figure 4.47: Power efficiency test (Texas Instruments, 2013b)

4.4.3 (h) Energy Harvesting Performance in Actual Deployment

Finally, after the functionalities of the H-CDE End Node confirmed in previous experiments, the End Nodes are deployed in an actual crowded area during the Training and Monitoring Phase (Figure 4.16). The initial voltage of the batteries on the End Nodes was set to 3.4 V which is a notch above the default 3.3 V of the RF module. This ensured proper energy backup in case the sunlight was not bright during the duration of the experiment.

In addition, Router 1 is also placed which acts as a controlled unit for benchmarking the performance of the End Nodes. The solar cells on all of these devices were pointed perpendicular to the ground.

4.5   Summary

In Part A, the hardware and software implementations involving the Coordinator and End Nodes were explained. Both of these nodes were implemented in ZigBee-based WSN. The Coordinator was designed in Arduino platform as it provides a rapid and configurable environment for prototyping and testing. The developed API is programmed into the microcontroller at the Coordinator. Finally, the implementation of the One-way ANOVA and DOE statistical methods were explained.

In Part B, the EH mechanism implemented at the End Nodes is discussed. The main discussion in this subsection is on programming and optimizing the usage of the PMU. The PMU is especially important to ensure abiding and safe operation of H-CDE End Node.

Part C lists and discusses 16 experiments that were conducted on the proposed H-CDE system. These experiments cover the topics of overall stability, H-CDE and EH performance verification that is meant to validate the feasibility of the designed system. The description of the experiments should provide enough information for the experiments to be reproduced by other researchers.

CHAPTER FIVE
RESULTS AND DISCUSSIONS

Chapter Five is organized into three main parts covering the topic of WSN-RF transmission, H-CDE and EH. These topics address the objectives of the research to form the overall conclusion later in Chapter Six. The summary of each subsection is presented to wrap up the discussion.

5.1 Wireless Sensor Network-Radio Frequency Performance Evaluation

The scope of the analysis is to evaluate the functionality and feasibility of the designed WSN-RF solution. This section indirectly addresses the first objective of the research where the system's sensing capability is improved.

5.1.1 Calibration

The power level of the RF front-end of the proposed system refers to the international variant. This should not be confused with the more commonly used US variant within the literature which has different specifications. The power level measurement result is tabulated in Table 5.1. The results show that the transmit power increases as the power level is incremented, which is in accordance with the manufacturer's specification of the Xbee module. The best performing power level is at level 4 with only 0.04 difference between the official documentation and the actual measurement.

The measured transmit powers are less than the values stated in the manufacturer's documentation partly due to the power loss incurred by the Connector 1. Another possible explanation is the accuracy of the spectrum analyser itself but a calibration process prior to the experiment should already have reduced the inaccuracies. Thus, it is assumed that the difference in power losses incurred by Connector 1 versus power level is due to the varying

responses of the Connector in varying transmitted power. Power level 4 is chosen for the H-CDE system as it has the least power loss which is suitable as to maximize the RF coverage and to cater for the amount of cumulative signal attenuations by the crowd.

Table 5.1: Transmission power level comparison between the official documentation and the actual measurement seen at the spectrum analyser. The highlighted box shows the best performing power level.

Power Level	Transmit power (dBm)		Difference (dBm)
	Official Documentation	Actual Measurement	
0	2	-0.45	2.45
1	4	2.01	1.99
2	6	5.15	0.85
3	8	6.76	1.24
4	10	9.96	0.04

Next, the comparative analysis of the RF transmission power performance between the proposed and standalone system is presented. The power loss incurred by Cable 1 is shown in Table 5.2. With this information, equation 4.7 can be solved to determine the power loss incurred by the power divider. The overall results are shown in Figure 5.1 and a sample of measurement shown in Figure 5.2.

Table 5.2: Power loss incurred by Cable 1

Power level	Proposed system power output (dBm)	Spectrum analyser (dBm)	Cable loss (dBm)
4	10.00	8.57	1.43 dBm
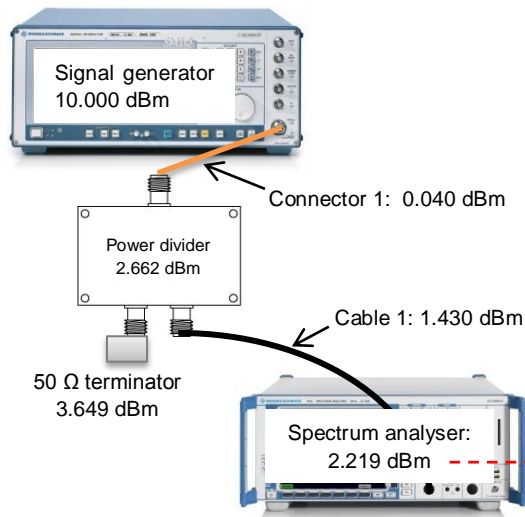
Figure 5.1: Power losses at each segment based on equation 4.7
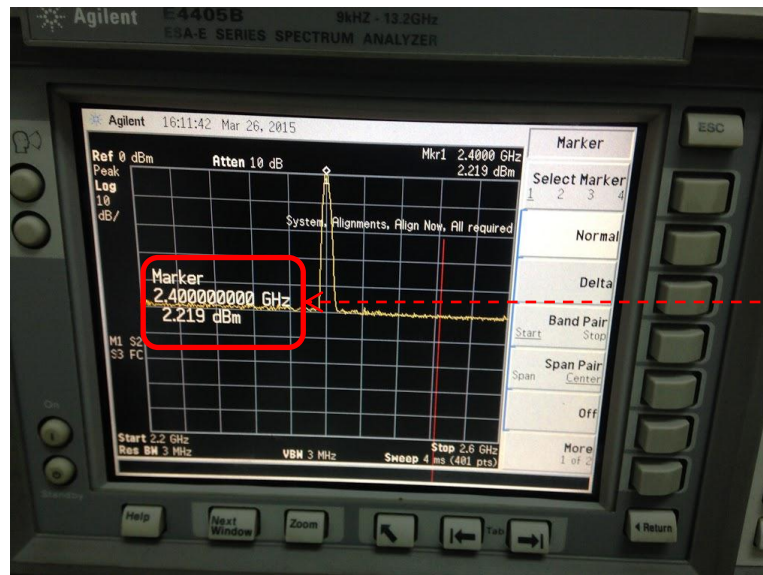
Figure 5.2: Spectrum analyser calibration measurement

The calculation for equation 4.7 is solved as follows:

$$PD = SG - CT1 - T - SA - CB1$$

$$PD = 10 \text{ dBm} - 0.04 \text{ dBm} - T - 2.219 \text{ dBm} - 1.43 \text{ dBm}$$

T is equal to SA + CB1. This is in accordance to the equal output power from a 2-way power divider.

$PD = 10$ dBm $- 0.04$ dBm $- 3.649$ dBm $- 2.219$ dBm $- 1.43$ dBm

$PD = 2.662$ dBm

With the power loss at the power divider determined, the comparative analysis is performed and the results shown in Table 5.3. The results show insignificant differences between the transmit power of the standalone and prototype systems. These small differences suggest that both systems have similar performances.

Table 5.3: Transmit power versus power levels of the prototype and standalone system

Power level	Transmit Power (dBm)		Difference (%)
	Standalone	Prototype	
0	3.3583	3.3387	0.584
1	4.6428	4.5953	1.023
2	5.8667	5.8220	0.762
3	7.3742	7.3005	0.999
4	8.3222	8.2942	0.334

The analysis of the calibration tests can be summarized into two points. First, power level of 4 has the least transmit power loss and suits the requirement of the H-CDE prototype for maximizing signal coverage. Herewith, for the rest of the analysis in this chapter, the power level of the Xbee module is set to 4 whereas the lower power levels are waived from analysis due to application irrelevance. Secondly, the RF portion of H-CDE End Node operates comparably to a standalone system. This verifies that the designed architecture of the End Node has conforming RF performance according to Xbee specification.

5.1.2 Stability and Functionality

The discussion in this section delves into performance gauging. The analyses should produce proofs on the functionality and viability of the proposed system. This would pave way for the implementation of H-CDE and EH systems in the WSN platform in the succeeding sections.

5.1.2 (a) Latency

The latency for a single hop is shown in Table 5.4, which is based on the measurements performed in Docklight (Figure 5.3). The Routers have the least latencies at around 60 ms when placed in both systems. However, all of the RF front-end assigned for H-CDE End Nodes had nearly double the latency of the modules assigned for routers, at an average of 108.44 ms. This difference is investigated according to the following hypotheses.

Table 5.4: Average latency of Xbee modules when tested in standalone and H-CDE prototype systems

Xbee module (native)	Latency (ms)	
	Standalone	Prototype
End Node 1	109.33	115.50
End Node 2	112.17	98.67
End Node 3	103.83	114.50
Router 1	59.50	59.00
Router 2	60.33	60.00

a)   First Hypothesis

The assumption is that the End Nodes, being in end node mode, have higher latency than the one in router mode. As previously stated, the Xbee module in end node mode, at

least in firmware version 29A7, has a mandatory cyclic sleep mode to save power. However, the module in router mode can turn off the sleep mode indefinitely.
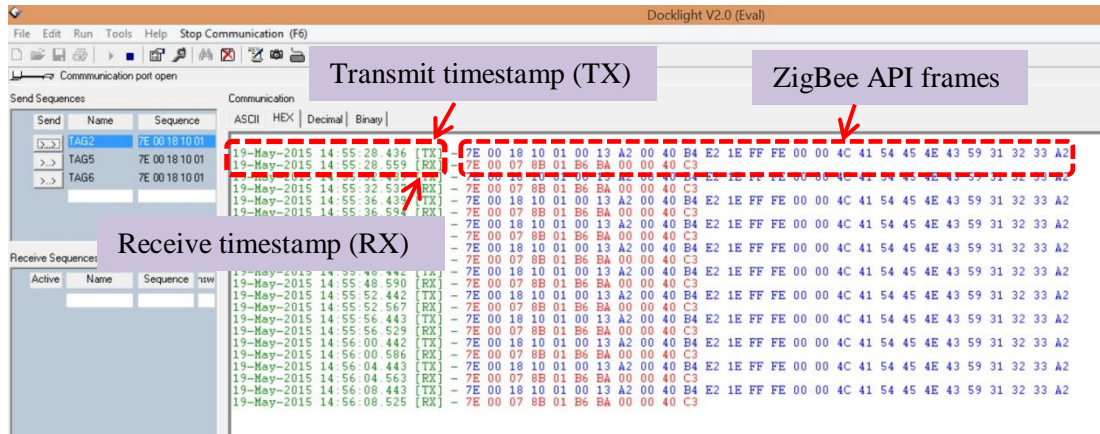
Figure 5.3: Transmit and receive timestamps generated in Docklight

The setup of the latency test defined in Chapter Four has used the default sleep mode for end nodes and no sleep mode for routers. As a result, every time an end node wants to transmit data, it needs to wait for the sleep cycle to finish, causing additional delay.

The default sleep mode is 200 ms and is triggered after every 1.388 s of idle time. This meant that multiple sleep periods occurred before a node initiate its next transmission. This is in accordance to the turn-based structure of the transmission. The concept is illustrated in Figure 5.4.

For the case of End Node 1, by the time it is ready for a new transmit session, it has already experienced three sleep cycles which took about 4.764 s. However, this serves only as a rough approximation. Every time the node is awakened, it will send a poll transmit request to the Coordinator to check for any data inside its buffer that needs to be sent to the end node. A single poll phase has a 100 ms cycle. If there is data for transmission, then the end node will remain active until the completion of transmission. If the time elapsed is still less than 1.388 s, then the end node will keep on sending another poll request until it sleeps again.
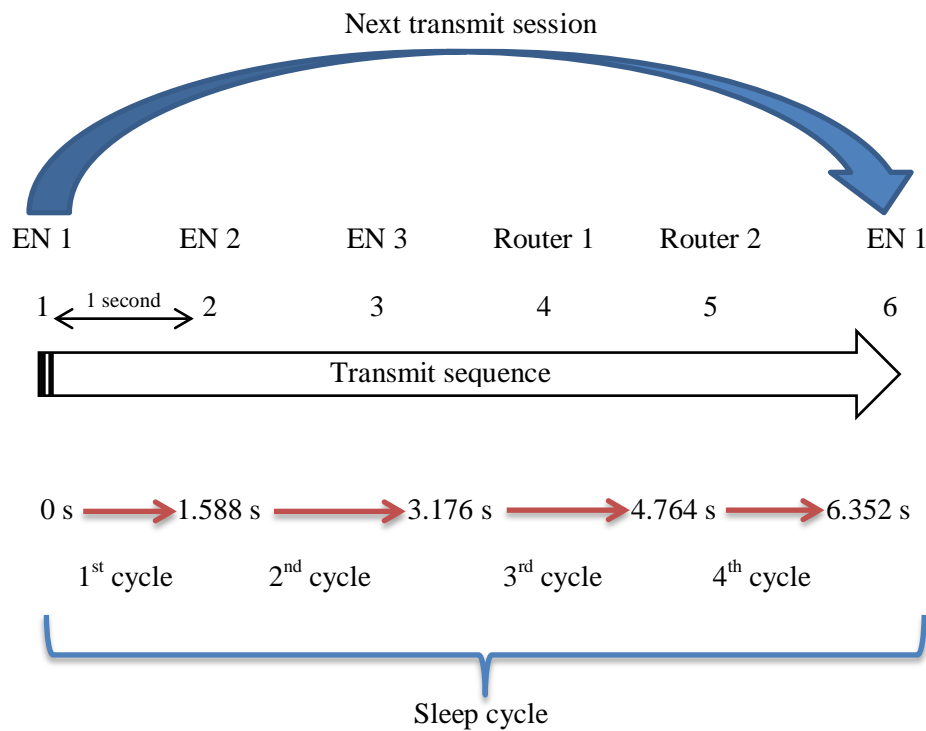
Figure 5.4: Transmit and sleep cycle for End Node 1

Due to sleep, poll and transmission phases, the overall latency would be affected. Thus, the first hypothesis is considered true.

b)   Second Hypothesis

The assumption is that the voltage profiles of the Xbee modules affect latency. The voltage measurements of all the modules were taken during data transmission. The results from the test, as measured by placing all the modules consecutively on the same standalone unit and three H-CDE End Nodes, are shown in Table 5.5. The results indicate that there is very small difference in the voltage profiles to connect voltage to latency. Therefore, the second hypothesis is rejected. It can be concluded that the latency difference between router and end node mode is caused by the sleep mode.

Table 5.5: Average voltage of each RF module in router (standalone) and end node. Each End Node has different battery voltage, resulting in the difference of voltage between them.

	End Node 1	End Node 2	End Node 3
End node	3.522 V	3.534 V	3.484 V
Router	3.521 V	3.504 V	3.450 V

The next step is to compare the measured latency with the literature. Figure 5.5 shows the average latency comparisons between the H-CDE system with the related works from the literature. The results show conforming values. It can be deduced that Abdulla (2011) and Mayalarp et al. (2010) used router mode as they have similar setup, while Piyare and Lee (2013) used end node mode. For the record, the latency test was also conducted with the presence of six Wi-Fi networks with varying levels of signal strength. The results positively indicate that the WSN-based network of the H-CDE could co-exist with the Wi-Fi networks without suffering noticeable degradation of service.
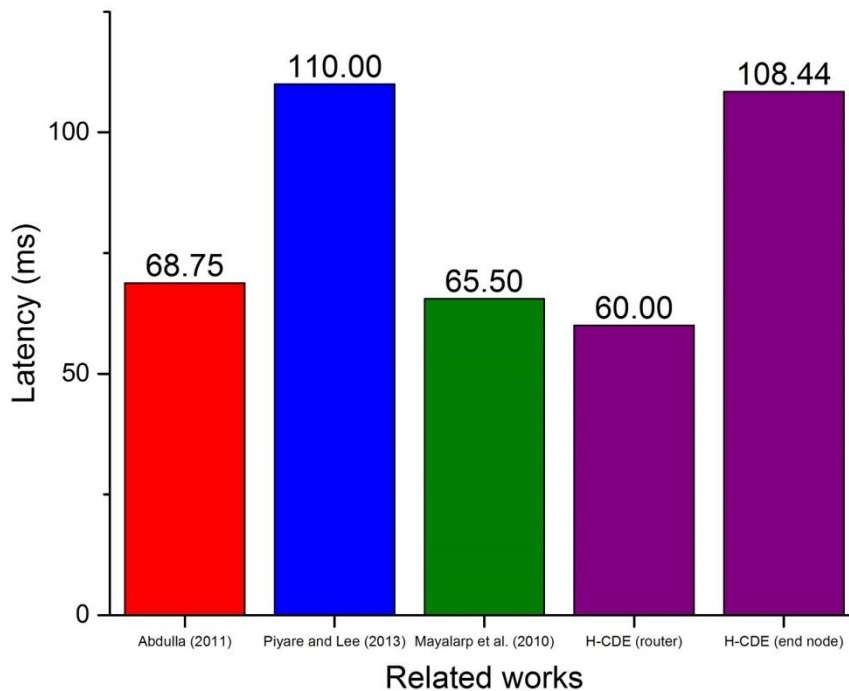
Figure 5.5: Comparison between the latency of the H-CDE system with the literature

In summary, single hop round trip latency takes about 60 ms to 115.50 ms for router and end node mode respectively. This difference is caused by the compulsory sleep cycle at the end nodes. The RF front-end operated on the standalone system have similar magnitude of latency to the front-end operated on the H-CDE board, indicating stable operation for the latter in its design.

The next phase is the two-hop latency performance evaluation. The aim is to derive a formulation to model multi-hop latency due to limited number of receiver availability. In fact, the model can be used to predict the latency in any *n* number of hops in a ZigBee-based network.

The results are shown in Figure 5.6. The average latency recorded is around 140 to 150 ms. A glaring contrast is the maximum latency which is almost twice the average. This is caused by the re-transmission. The presence of many parked vehicles and passing pedestrians has caused heavy signal attenuation, requiring re-transmission on all the End Nodes in specific cycles. This occurred due to the test conducted during the day on a normal semester of the university, where students were actively moving and attending classes. As re-transmission has both random delay and CCA, thus causing additional delay to the latency.

If re-transmission is omitted, the average latency for all modules for two hops is 149.78 ms. The breakdown of latency, calculated in average, between single hop (Table 5.4) and two hops is given in Table 5.6. The table shows that two hops have higher latency than a single hop.

An interesting discovery is that the Router to end node is nearly 20 ms less than the latency in the single hop (labelled in Table 5.6). In network with multiple nodes, the poll requests and data transmissions are broadcasted to all the nodes. This made the nodes more occupied with the increased of traffic and thereby reducing its sleep phase. Thus, this factor is assumed to contribute to the decrease of latency. However, this also means that the end nodes will consume more power due to a lesser sleep cycle count.
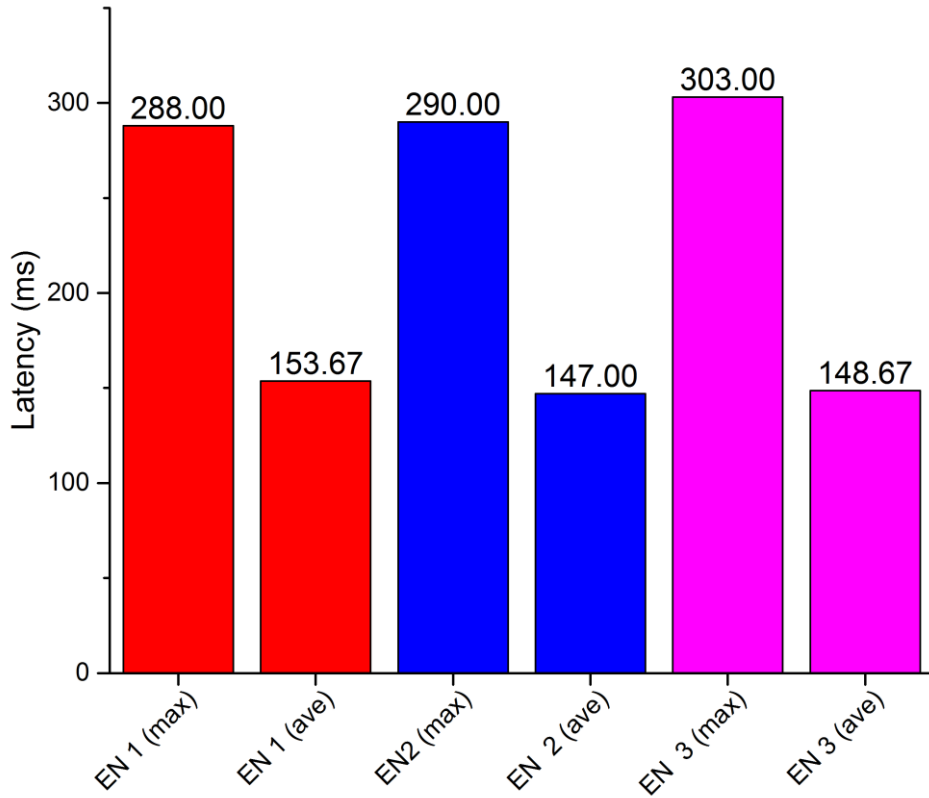
Figure 5.6: Two hop latency

Table 5.6: Single versus two hop latency. Router to end node and Coordinator to end node have similar latency due to absence of sleep mode at one end.

Mode matchup	Single hop (ms)	Two hop (ms)
Coordinator to Router	60 .00	60.00 (single hop)
Router to Router	60.00	60.00 (single hop)
Coordinator to End Node	108.44	-
Router to End Node	-	89.78* (single hop)
Coordinator to End Node (through Router)	-	149.78

Nearly 20 ms difference

* approximation

Table 5.6 also shows that single hop latency in a two hop transmission can be treated discretely if the number of routers and end nodes is known. This means that the latency

profile of single and two hops can be used to estimate multi-hop using a similar network setup.

The equation for estimating the multi-hop round-trip latency without re-transmission is given as:

$$L_{MH} = (n \text{ x } A) + (m \text{ x } B) \qquad\qquad (5.1)$$

where n and m are the number of hops consisting of a router and end node, respectively, and A and B is the average latency of a single hop in router and end node mode respectively. This equation assumes that the latency from coordinator to router is the same as a router to router due to both modes having no sleep mode.

The H-CDE latency model is compared with the works of Abdulla (2011) and a corrected Mayalarp (2010) as shown in Figure 5.7. The H-CDE (R) model assumes all the nodes were in router mode while the (EN) model has an end node at the very last hop. The small latency differences can be attributed to different types of microcontroller and software processing time. The results show that the proposed model has promising prediction accuracy.

In summary, two hops has higher overall latency than single hop network, which is evidently clear as each node within the entire hop requires its own transmission time to transmit data to its neighbouring node. This is in accordance with the works of Sarvghadi and Tat-Chee (2013), but contradicts that of Mayalarp et al. (2010). The latter stated that the four-hop connection does not affect latency. This notion is therefore rejected based on proves obtain in this section. Multi-hop transmission also has higher probability of getting higher latency due to increased chances of re-transmission due to increased number of hops.
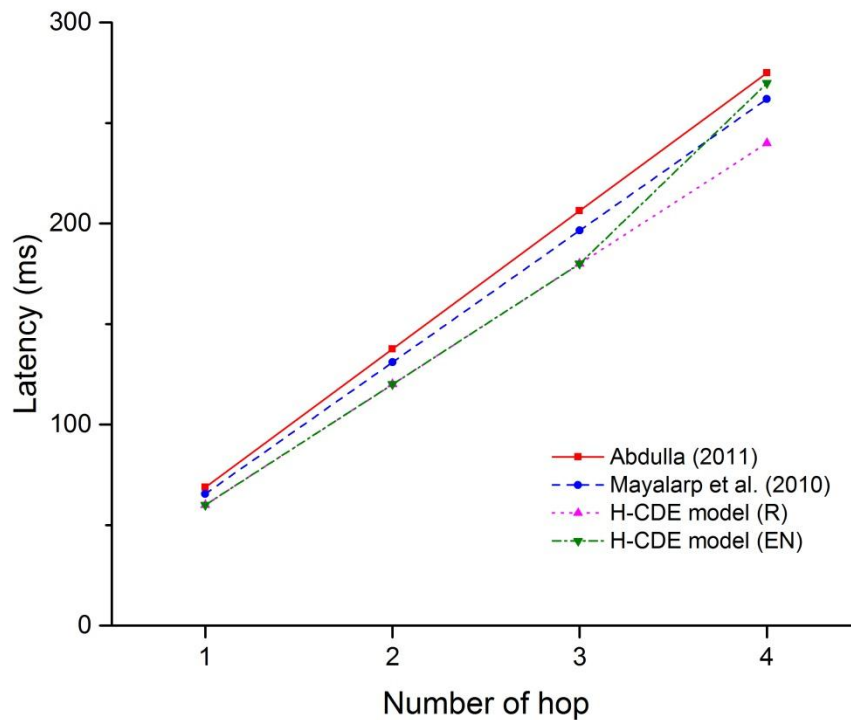
Figure 5.7: H-CDE latency model comparison. R stands for router and EN for end node

The final experiment in this sub-section is the investigation of the effect of crowd on latency. Figure 5.8 shows the latency in a fluctuating pattern in both crowded and non-crowded scenarios. The average latency for crowded and non-crowded is 60.00 and 57.67 ms respectively. Latency with the presence of crowd is about 3.88 % higher compared to without crowd. With less than 3 ms average difference, a single packet in single hop transmission, without re-tries, is largely unaffected by the crowd.

EM wave propagates almost at the speed of light in the air. Therefore, the latency is actually affected by the fluctuating pattern of the processing time of the RF front-end, the laptop and the Docklight software in accordance with equation 4.8. This also assumes that complex multipath is absent or not a factor in outdoor environment.
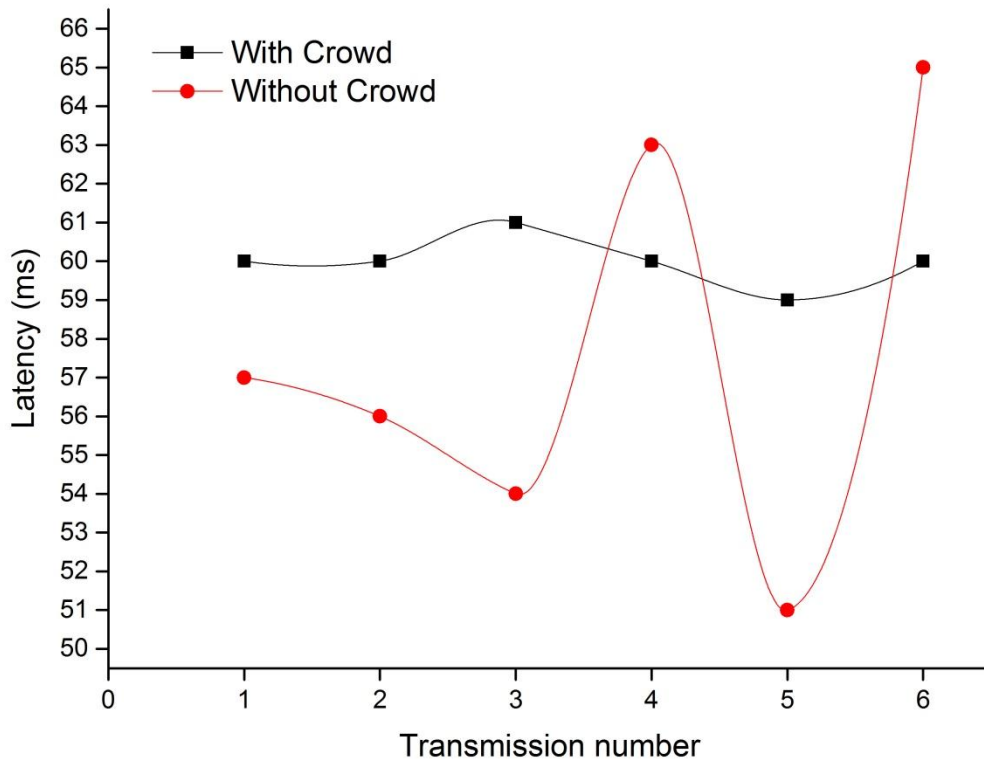
Figure 5.8: Latency of crowded versus empty area. The curves are smoothened using Akima spline fitting.

The only effective way for crowd to affect latency is when re-transmission occurs, which is due to extreme signal attenuation resulting in a packet lost. In summary, a moderate crowd consisting of 15 people has an insignificant effect on latency.

To conclude the overall results presented in this subsection, the latency is low enough to allow the proposed H-CDE system to operate in a real-time manner. As delayed information becomes less useful to system administrators, thus the impact of a real-time system is imperative for crowd sensing.

5.1.2 (b) Throughput

The throughput is important in a data driven network. The H-CDE system, however, does not require a high data rate nor throughput as its nature is for identification detection. The H-CDE system utilizes only 2 bytes of payload for frame command and 8 bytes for

addressing. Still, the throughput test can determine the capability of the RF front-end as a point of reference.

Figure 5.9 shows that the throughput for crowded and non-crowded area has similar pattern. The highest and lowest throughputs recorded were 1111.11 and 1103.45 bytes per second respectively.
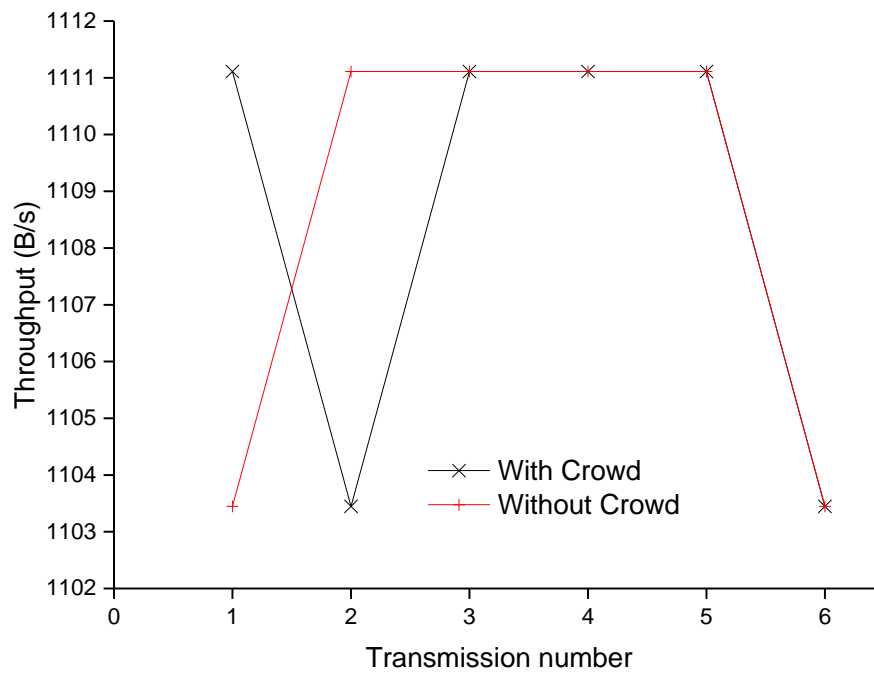
Figure 5.9: Point-to-point throughput with and without the presence of crowd

The presence of a moderate crowd shows no significant effect on the average throughput. The reason is because each transmission was entirely successful and therefore no re-transmissions were needed. This is equivalent to the findings in the latency test. Table 5.7 has been tabulated to compare the findings with selected studies from the literature.

The absolute maximum throughput as shown in the documentation by Digi (2015) uses 115200 bps baudrate and has nearly 4 times of the H-CDE measured throughput. This indicates that using 9600 bps baudrate for a single hop has around 25% utilization of the maximum possible throughput.

Table 5.7: Average throughput of several works compared to the measured

Point-to-point research work	Throughput (B/s)
Digi (2015)	4375.00
H-CDE without crowd	1108.56
H-CDE with crowd	1108.56
*Piyare & Lee (2013)	800.00
Abdulla (2011)	1365.00
Sarvghadi & Tat-Chee (2013)	1081.25

*single trip

The H-CDE system has similar throughput as Sarvghadi and Tat-Chee (2013); which used an EMLMAC protocol for measuring the physical testbed. The H-CDE system is superior to that of Piyare and Lee (2013) because they used round-trip measurement as opposed to single trip, which accumulates additional processing time at the end node. In addition, Piyare and Lee (2013) also utilized hardware loopback while the H-CDE prototypes utilized *DB* command for transmission. The work by Abdulla (2011) did not clarify the methodology used for the measurement and thus only serves as a basic comparison.

In summary, a moderate crowd does not affect the throughput of the system. The throughput measured in this study did not deviate too much from the works reported in the literature. This verifies the sound estimation of the actual throughput of the RF front-end and their performance on the H-CDE End Nodes. In addition, the low throughput utilization of the proposed H-CDE system grants space for future expansion of data and protocol usage.

5.1.2 (c) Network Self-healing

The self-healing feature of the proposed RF front-end adds functionality due to its automated operation. This makes the embedded network more reliable with reduced downtime. The H-CDE system benefits greatly from the feature, as a missing node,

disconnected due to heavy crowd, could be reconnected on the fly when the signal occlusion is removed.

The results of the self-healing experiment are tabulated in Table 5.8. The results show that Router 1 has the fastest recovery time at 5.11 s followed by the End Nodes which are in the 7.44 to 8.03 s region. Router 1 is detected faster than the End Node, as it functions as the routing (middle) node for both End Nodes.

Table 5.8: The time taken to self-heal the connections to Router 1, End Node 1, End Node 2 and End Node 3

Parameter	Router 1	End Node 1	End Node 2	End Node 3
Average (s)	5.11	7.78	7.44	8.03
Maximum (s)	6.8	10.2	9.8	10.5
Minimum (s)	4.3	5.9	5.5	6.3

A problem occurred during data collection in which the Networking Working Mode is sometimes not fast enough to detect the change in the node status. This is because the Mode has two phases in the detection cycle. In the first phase, the Coordinator will always refer to its addressing table inside its memory before initiating an actual topology check via transmission in the second phase. Thus, the first phase caused additional unwanted delay. As an alternative solution, the Discover Radio Nodes feature is utilized to complement the results obtained from the Network Working Mode (Figure 5.10).

End Node 2 successfully negotiated the self-healing faster than End Node 1 and End Node 3, plausibly due to the CSMA-CA mechanism. Furthermore, the node discovery command could broadcast the discovery frames to all nodes at the same time, making it possible for any nodes to respond faster. It is also possible that the Coordinator and Router initiated the node discovery command in a sequence, based on the addressing table within its internal memory. However, the actual algorithm of self-healing is unknown due to the proprietary nature of the XCTU and Xbee products.
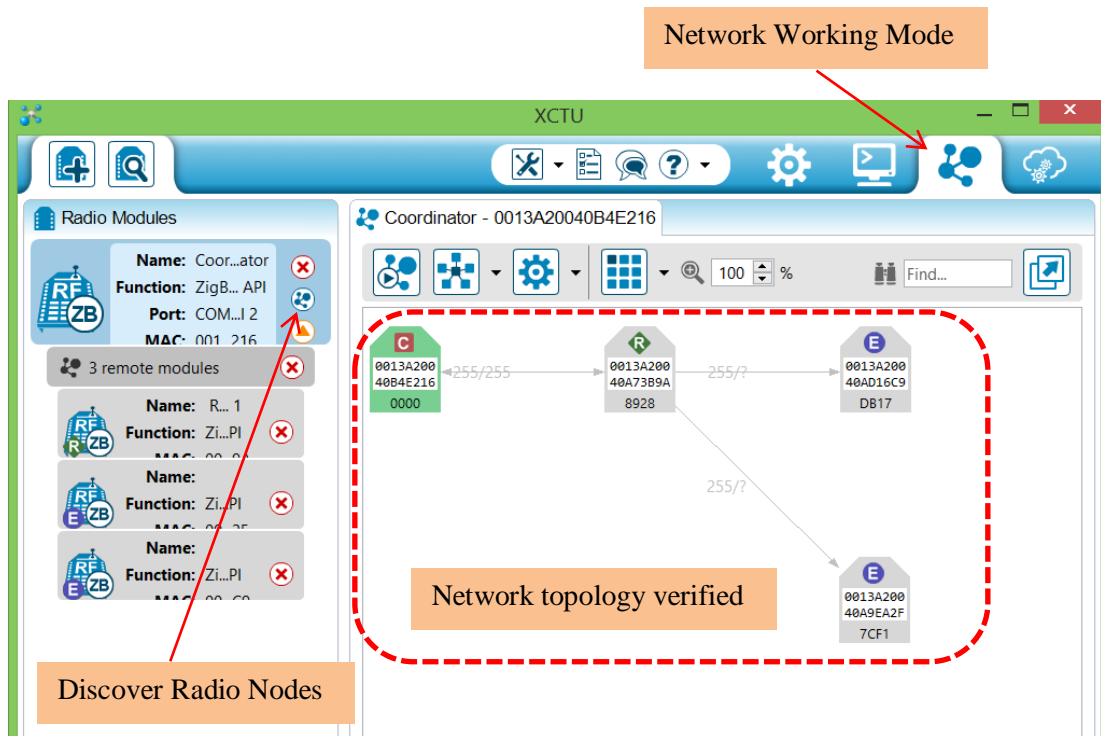
Figure 5.10: The two features utilized for measuring the self-healing time. The network topology is verified in the Networking Working Mode.

In summary, the self-healing of nodes is completed within 5 to 8 seconds in a single and two hop topology respectively. This gives an estimation of the recovery period of the H-CDE End Node which is based on a single hop transmission. This is also considered acceptable given that a typical WSN initialization and establishment using Xbee would take several seconds to complete. The node recovery time would logically be longer for complex and n-hop network where $n > 2$.

5.1.2 (d) Antenna Radiation Pattern

i)   H-Plane

Figure 5.11 shows the radiation pattern of the whip antenna of the respective systems that propagates in all directions in the azimuth plane. Notably, the End Node has weaker radiation than a standalone system.
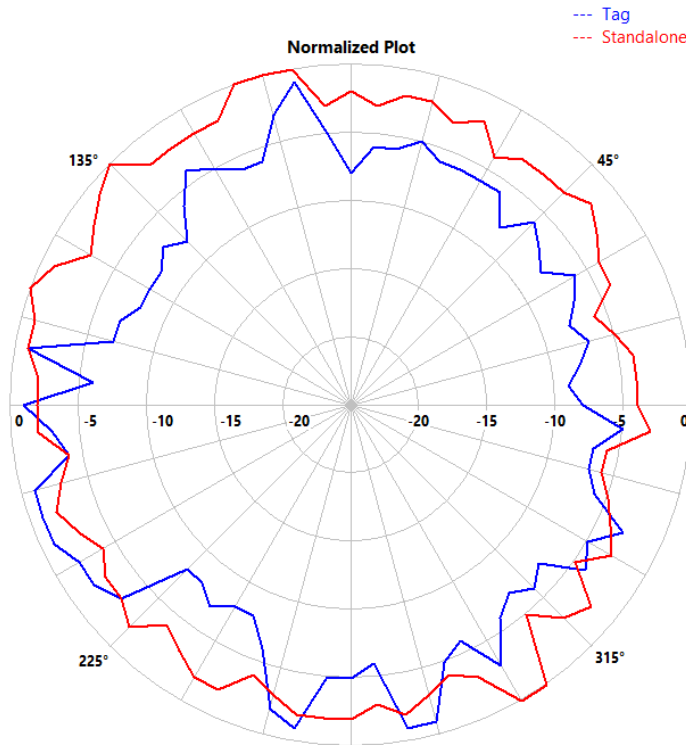
Figure 5.11: The H-plane radiation pattern of the standalone and End Node (tag)

The weaker radiation of the node may be attributed to its plastic housing made of Polycarbonate - Acrylonitrile Butadiene Styrene (PC-ABS), which is a type of sturdier plastic (Figure 5.12). This plastic housing may impede the signal and thus causing NLOS signal propagation as the height between the T-R are not the same. The housing is necessary to steadily mount the H-CDE prototype board on the pole and also as a casing itself. Whereas the standalone system does not require an additional casing as the Arduino UNO board is already solidly built for mounting purposes. A simple separate test of placing the PC-ABS casing between the T-R revealed an additional signal loss of between 1 to 3 dBm. This further strengthens the evidence of the negative effect of the casing.

Alternatively, the weaker radiation might also be caused by the whip antenna itself. By manufacturing default, the whip antenna of the Xbee module is oriented horizontally and for the purpose of testing, the antenna was forced upright vertically. There is a possibility that the antenna was not perfectly oriented vertically, suffering from a slight tilt. However,

thorough physical inspection on the antenna is not possible as the metallic portion of the whip is insulated by its cover made of Teflon.
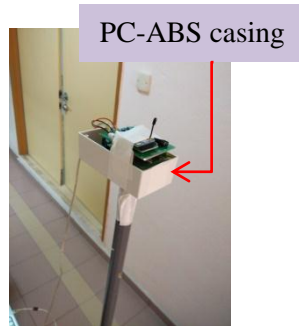
Figure 5.12: The H-CDE node in the PC-ABS casing. The top cover of the casing is not shown.

In summary, the radiation pattern propagates in all directions for both systems are in line with the theory, although the RF front-end used in the H-CDE node has weaker radiation due to its plastic housing. However, this problem is only unique to the radiation pattern laboratory experiment, as a casing is needed for mounting.

ii)   E-Plane

Figure 5.13 illustrates the radiation patterns on the E-plane with the NLOS areas labelled from 45^0 to 180^0 as their effect can be seen on both systems. The radiation pattern did not follow the pattern of a typical whip antenna for two reasons.

First, the effect of NLOS could not be avoided due to the rotation of the systems on the single axis mounting pole. This caused additional signal loss due to the obstruction from the board, its casing and the pole itself as illustrated in Figure 5.14. The effect of the PC-ABS casing of the prototype is also slightly evident as previously discussed.
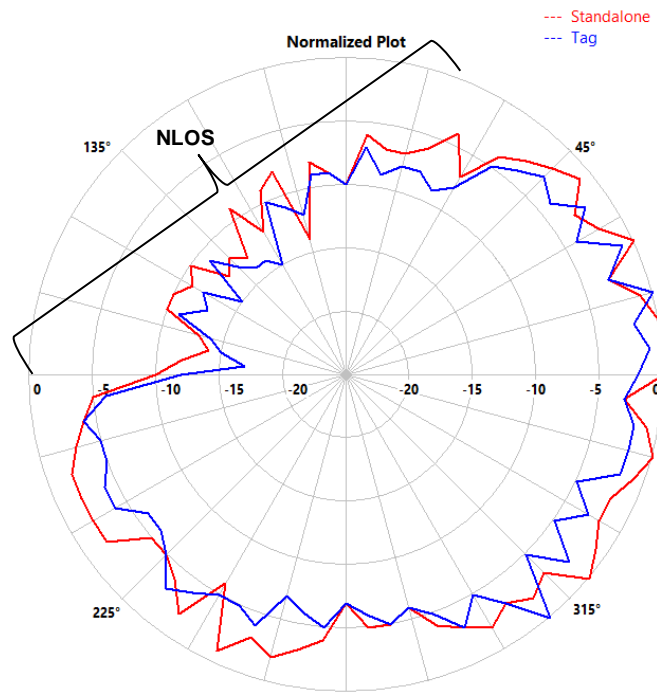
Figure 5.13: The E-plane radiation pattern of the standalone and prototype system
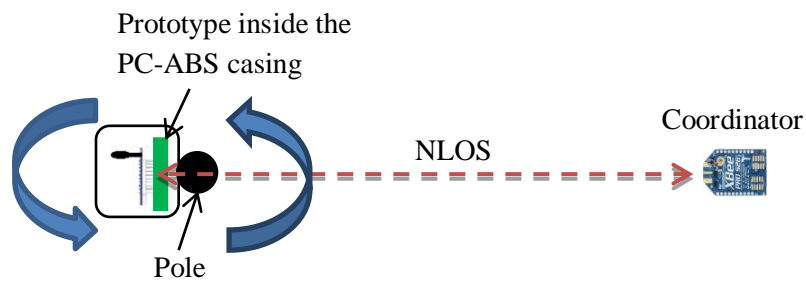
Figure 5.14: Radiation pattern NLOS due to obstructions

Secondly, the T-R distance of 50 m is below the maximum range of the RF module. Thus, relatively higher radiation than expected is observed, including the region between 90^0 and 270^0. As a consequence, the typical 'infinity' shape radiation pattern is distorted.

In summary, the H-CDE proposed system has comparable radiation pattern to the standalone system, and the effect of NLOS is observed as an uncontrollable occurrence for the test. The NLOS problem can be largely mitigated by using a dual-axis mounting system.

However, such system is not available for the test. The E-plane radiation pattern does not strictly follow the theory due to the shorter T-R distance.

5.1.2 (e) Range Test

In the official documentation, Digi (2015) claimed that the range of the Xbee transmission could reach up to 1.5 km outdoors in LOS condition. However, the antenna type, packet error and testing condition are not documented. The range test for the H-CDE uses the international variant module and whip antenna, and should have lesser range than the US counterpart.

Figure 5.15 shows the results of the range test from XCTU Range Test feature (Figure 5.16). The H-CDE and standalone system have almost similar RSSI pattern, with coverage up to 800 m.
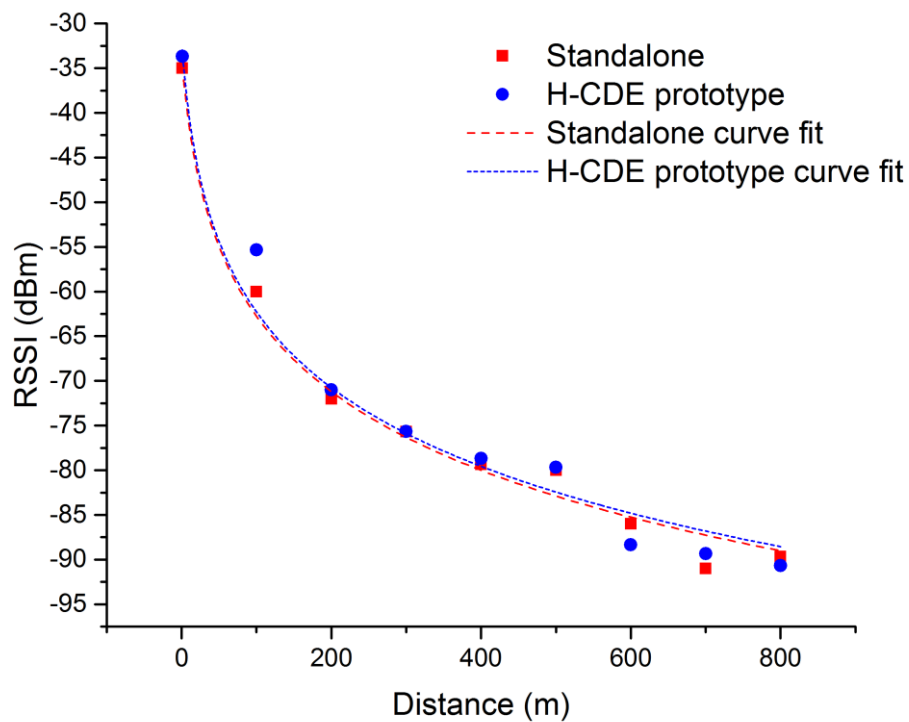
Figure 5.15: Average RSSI versus distance of end nodes with 100 % packet transmission
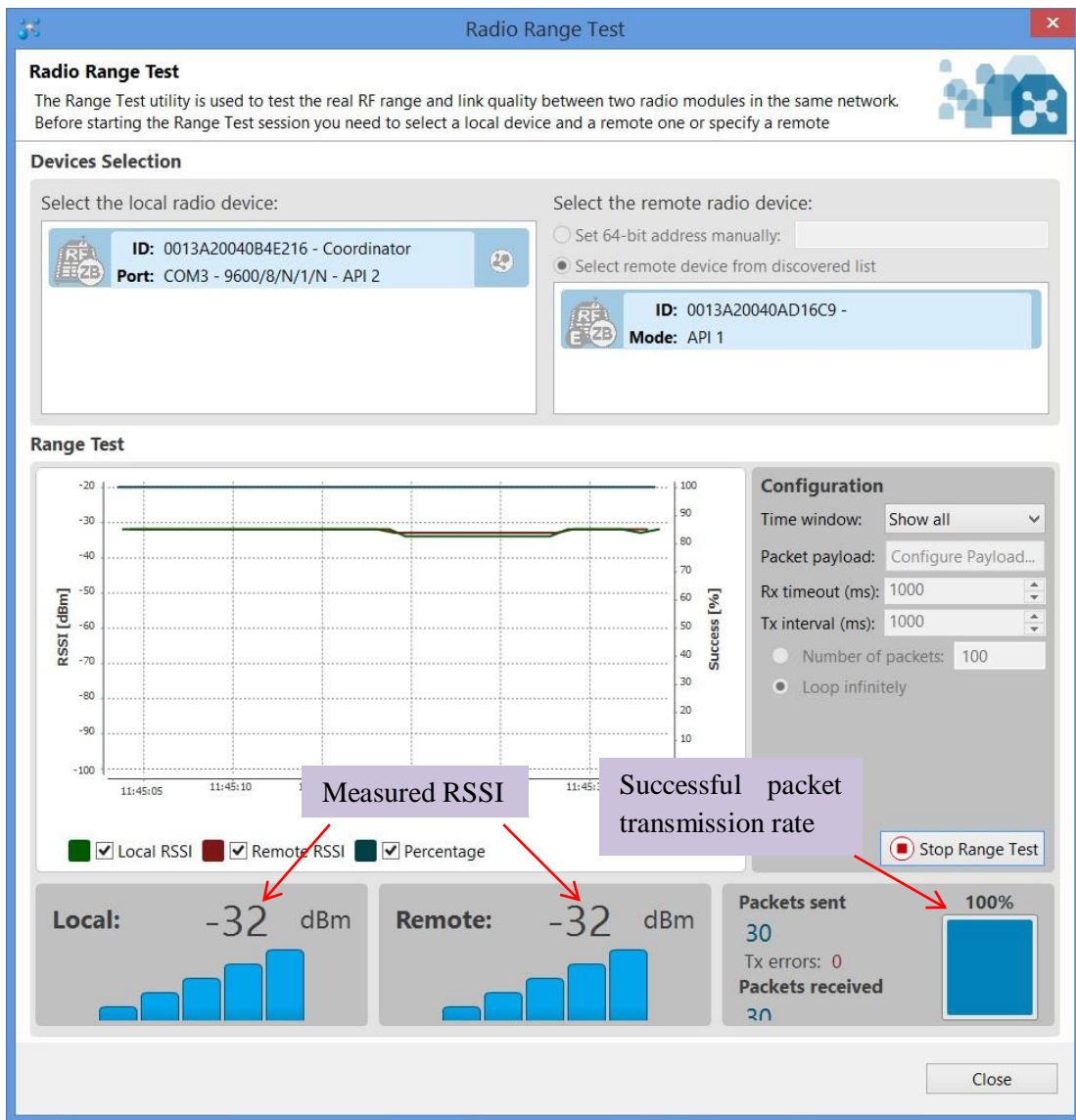
Figure 5.16: XCU Range Test. The local and remote RSSI are for the Coordinator and end node transmission side respectively.

Data collection ceased at 800 m due to the unavailability of straight and unobstructed road to reach 900 m. A test conducted at 850 m showed RSSI readings hovering around -94 to -96 dBm with about 50 % packet losses for both systems. Given that the XCTU can only record RSSI measurements up to -98 dBm, hence, it is assumed that the range test conducted at 900 m would already reach the absolute maximum of transmission distance with very high packet loss.

The curve fits are given as:

$$\text{RSSI}_{\text{standalone}} = -13.2844 \ln (d +12.61707) \tag{5.2}$$

$$\text{RSSI}_{\text{prototype}} = -13.21868 \ln (d +11.11165) \tag{5.3}$$

The shape of the curves in Figure 5.15 suggests a non-linear curve fitting as given in equation 5.2 and 5.3. Alternatively, plotting the graph in log-distance form would produce a linear regression fit (Figure 5.17). This is in accordance with typical log-distance path-loss models which would produce a linear fit.
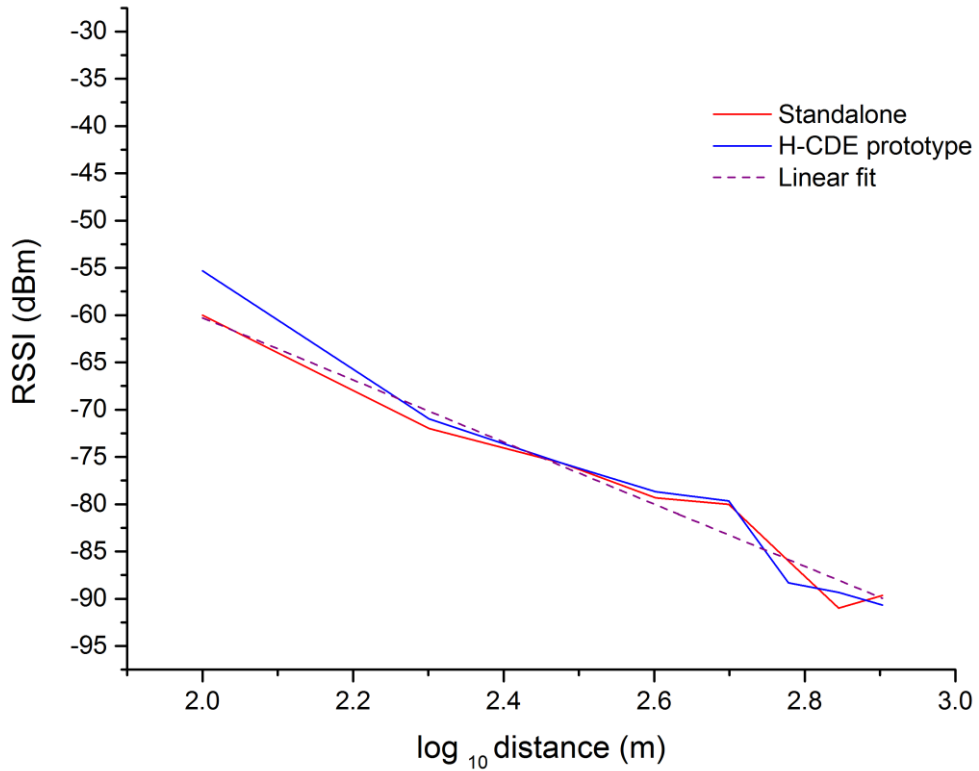
Figure 5.17: Range test results in log-distance

In summary, the Zigbee-based module has reliable outdoor LOS connections up to 800 m. The H-CDE prototype has nearly equivalent transmission range performance as to the standalone system, verifying the functionality of the former to the latter in medium range communication. The curve fits allow for quick signal prediction when using the specified RF front-end unit.

5.1.2 (f) The Effect of Voltage on RF Transmission

The voltage range of the H-CDE system should be well-defined as to avoid transmission interruption. An over-voltage may negatively impact or even damage the system whereas an under-voltage may halt its operation.

Figure 5.18 shows that the RF front-ends have a large range of voltage tolerance with normal RSSI recorded at –33 dB for all the End Nodes and router from 2.00 to 3.60 V. At the lower end of voltage, losses of RSSI were detected when the supplied voltage were 1.80 V (End Node 2), 1.85 V (End Node 1), 1.90 V (Router 1) and 1.95 V (End Node 3). At the higher end of voltage, losses of RSSI were observed when the input voltage was 3.65 V for all nodes except End Node 1, which was at 3.70 V.
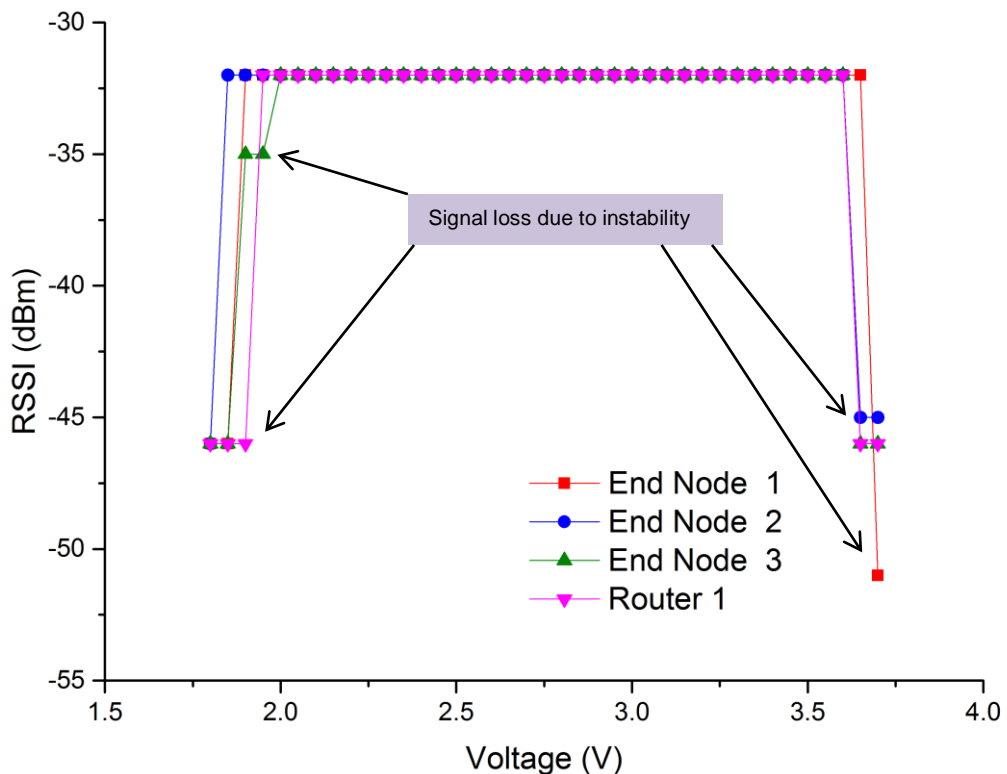
Figure 5.18: Performance of End Node and Router voltages versus RSSI

Surprisingly, the 3.3 V RF front-end unit have good tolerance at lower voltage and could operate without any additional loss of signal strength down to 2.00 V. Higher voltage

tolerance is however limited to 3.65 V before instability in RF transmission is observed. The slight differences between the End Node can be attributed to manufacturing tolerance and the wear factor. These effects are minimal and thus can be safely ignored.

The next investigation is on the transmission effect of voltage variation due to added resistance. As the DC power supply is too stable to model the solar cell, this method is applied to find a more practical result. Another reason for the investigation is the inability for the li-ion battery to supply voltage lower than 2.7 V (minimum voltage of the battery). On the other hand, the battery could easily supply the maximum 3.6 V to the H-CDE system that produced similar results as the DC power supply and solar cell.

Table 5.9 shows the measured average voltage of the shunt resistor and the RF front-ends and their RSSI data. Loss of signal was observed once the resistance reached 15.2 ohms and the voltage at the front-end dropped to 2.552 V.

Table 5.9: The parameters versus RSSI using shunt resistor method with $V_S = 3.296$ V

R (Ω)	Average V_R (V)	Average V_{RF} (V)	Average RSSI (dBm)
10.1	0.450	2.788	-33
11.3	0.503	2.647	-33
12.3	0.550	2.640	-33
15.2	0.683	2.552	-38

The results also show that equation 4.11 was not totally satisfied. This is due to the fluctuating values of current, I_S caused by the continuous fast switching of the RF front-end between transmit and receive modes. The fast switching was in accordance with the programmed infinite loop of the Range Test Tool.

In summary, an addition of at least 15.2 Ω resistances into the circuit would incur signal degradation at the front-end system. Consequently, the front-end should have at least

2.640 V of minimum voltage to avoid signal disruption. Thus, this finding supersedes the results earlier. For stable signal transmission the setting is recommended to be between 2.640 to 3.60 V.

5.1.2 (g) Current and Power Consumption

The power consumption would determine whether the 1 W solar cell and PMU could supply enough energy to the load. Moreover, any surplus of energy would be used to charge the battery.

The results tabulated in Table 5.10 shows that the RF front-end of the prototype has a maximum and minimum current consumption of 97.17 mA and 46.5 mA respectively. This reflects the transmit (peak) and receive mode of the module. The BQ25504 only consumes 16.3 uA in its operation.

Table 5.10: Current consumption of the load and PMU

Parameter	RF front-end unit	BQ25504
Maximum current consumption	97.17 mA	-
Average current consumption	54.5 mA	16.3 μA
Minimum current consumption	46.5 mA	-

Given that the voltage of the prototype based on XBee specification is 3.3 V, the maximum and minimum power consumption is 320.661 mW and 153.45 mW respectively. In average, the power consumption is 179.85 mW. As the end node is mostly in receive mode, thus the minimum current consumption is more accurate to represent its actual current rather than the average current.

This finding is compared to the performance of the solar cell shown in Figure 5.19. As labelled in the figure, the maximum power utilized by the H-CDE system during transmit session would consumed about 33.5% of the optimal power. The rest of the power is then available for battery charging. Thus, using the 1 W solar cell provides the H-CDE system with plenty of power reserves in case of limited sunlight availability.
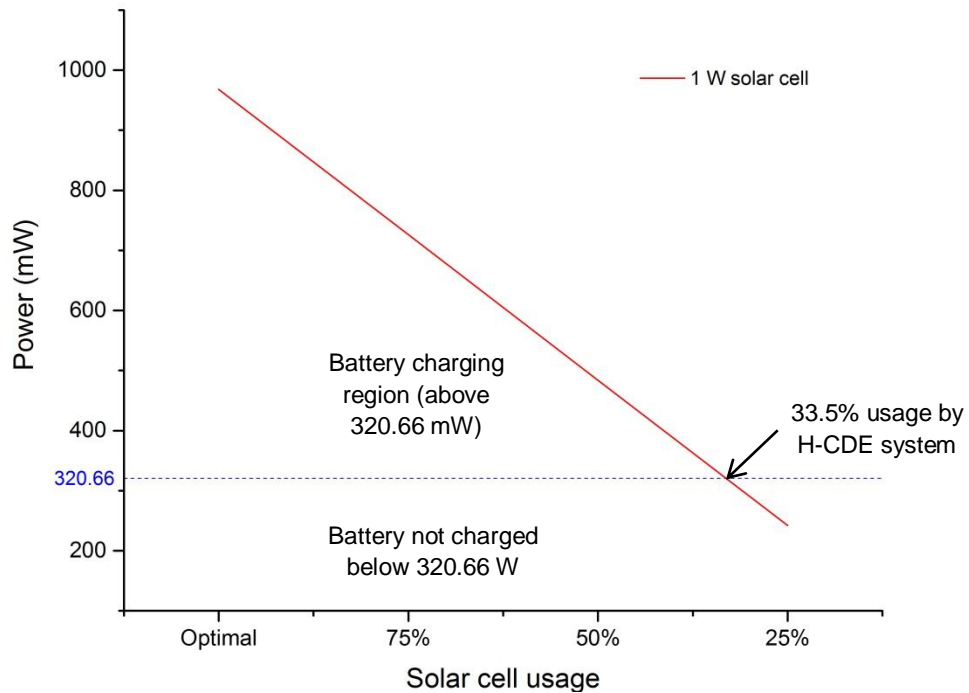
Figure 5.19: Power generated by solar cell versus H-CDE front-end power usage

In summary, the current and power consumption of the H-CDE End Node have been verified. The results show that the chosen solar cell should be able to power up the load and charge the battery at the same time. In-depth performance of the battery charging and EH mechanism are discussed in the coming sections.

5.2   Human Crowd Density Estimation Evaluation

The analysis and discussion of the One-way ANOVA and DOE formed the bulk of this section. The One-way ANOVA should finalize the decision whether dynamic and static crowd should be investigated or neglected. Next, the DOE experiment would identify the

significant crowd attributes that affect signal loss which then leads to the formation of the H-CDE algorithm. Finally, the algorithm is tested for prediction accuracy.

5.2.1   One-way Analysis of Variance

Movement within a crowd creates many possibilities of signal path propagation. A gap within a lesser crowd can even allow signal to propagate in LOS. However, in a dense moving crowd, the signal obstruction remains high. Thus, the results and analysis of the One-way ANOVA experiment is crucial to determine whether crowd dynamics is relevant as a factor affecting signal attenuation.

5.2.1 (a) Main Findings

Table 5.11 shows three important information which are the P-value (P), standard deviation (S) and R-squared (R-Sq) obtained from the crowd movement experiment.

Table 5.11: One-way ANOVA results from Minitab

Parameter	Value
P	0.492
S	7.025
R-Sq	6.09 %

As the P-value of 0.492 is greater than α (0.05), thus the null hypothesis is not rejected since the differences between the means are not significantly different. The standard deviation is mediocrely high at 7.025 dBm due to the unpredictable and fluctuating signal attenuation caused by the human crowd. This is especially prevalent as a result of LOS and NLOS signal propagation.

The value of *R*-squared at 6.09 % is extremely low indicating the effect of crowd on signal attenuation cannot be curved-fitted accurately by the Minitab software. This assumption is considered true based on the usage of three End Nodes instead of one that contributes to different sets of the RSSI, thus making a single curve-fitting inaccurate.

The close values of mean shown in Figure 5.20 strengthen the assumption that the mean of both *S* and *DS* cases are statistically indifferent. *S* has the highest mean as the signals from the nodes are relatively less fluctuated due to the fixed positions of the end nodes and human crowd. Still, the overall signal attenuation caused by moving or static crowd does not indicate a varying pattern. This is attributed to the uniform signal absorption by the overall human body as assumed by Xi et al. (2014), Haochao et al. (2015) and Arai, Kawamura and Suzuki (2010).
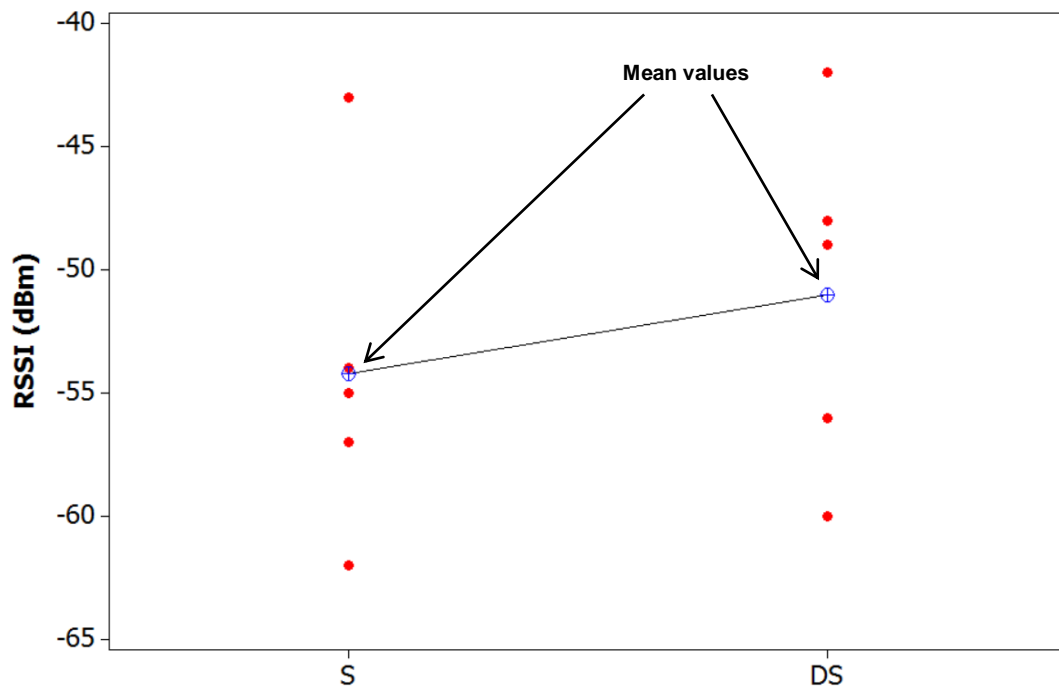
Figure 5.20: Individual Value Plot of Static Human Crowd and End Node (*S*) and Dynamic Human Crowd and Static End Node (*DS*)

In summary for Table 5.13 and Figure 5.20, the signal attenuation caused by the effect of moving and stationary human crowd is statistically the same. Thus, dynamic human crowd can be removed as factors that influence signal propagation in the DOE test. This

effectively reduced the number of DOE factors from seven to four. This finding also adds knowledge in understanding the signal attenuation effect of dynamic and static crowd on top of the information provided by Arai, Kawamura and Suzuki (2010) and Xi et al. (2014).

5.2.1 (b) Residuals

Based on Figure 5.21 (a), the residuals appear to be randomly scattered about zero. Figure 5.21 (b) shows the residuals appear to follow a straight line, indicating a normal distribution. There is also no evidence of skewness or outliers in both figures.

(a)   (b)
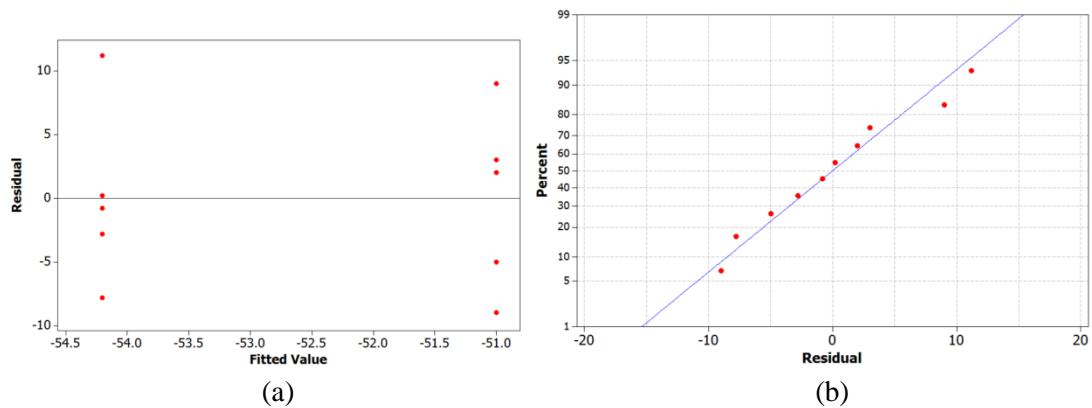
Figure 5.21: (a) Residuals versus Fits and (b) Normal Plot of Residuals for the *S* and *DS* scenarios

In summary, the residuals for signal attenuation caused by crowd are normally distributed about zero, which indicates the presence of natural randomness and unbiased signal attenuation.

5.2.2   Design of Experiment

The DOE test is set to prove the significant crowd properties that affect signal propagation. The findings would complete the H-CDE algorithm for crowd density

classification. For the Training Phase, as many as 2160 measurements were made whereas 180 data were collected for the Monitoring Phase.

5.2.2 (a) Analysis of the *P*-values

Figure 5.22 shows three sources with significant effects on signal attenuation. The effects are denoted by having *P*-value of less than or equal to α (0.050). The main effect is the human crowd size (A) with 0.000 *P*-value. The interaction effects are crowd size * number of receiver (A*D) and crowd pattern * number of receiver (B*D) with 0.001 and 0.045 *P*-values respectively.
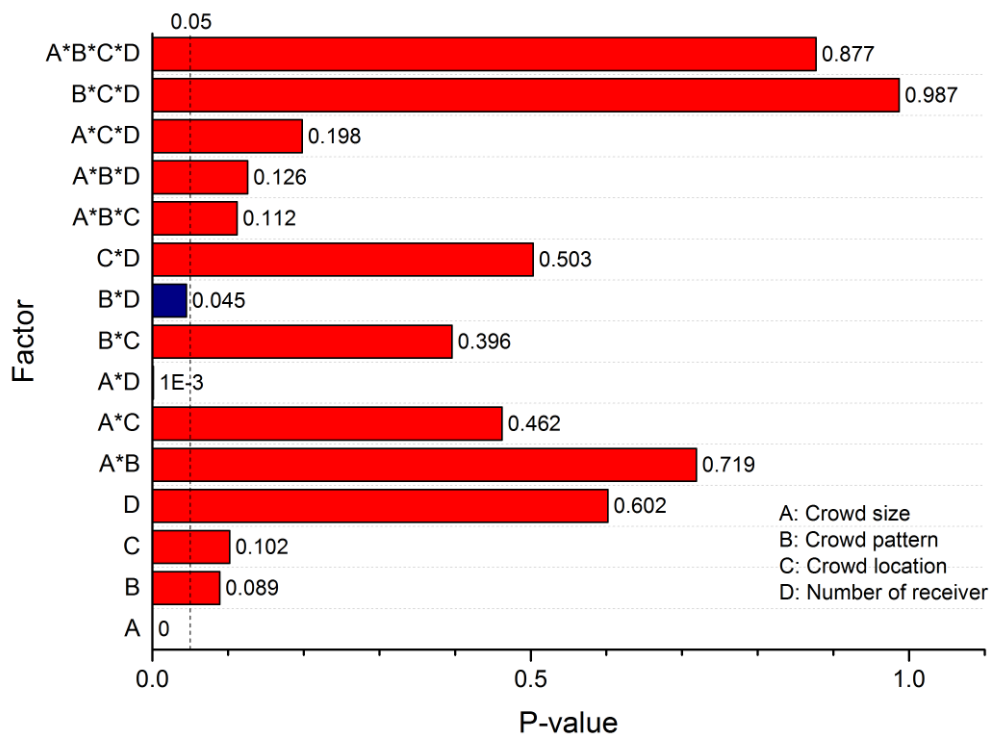
Figure 5.22: The *P*-values from the analysis of variance for RSSI (average) using adjusted sum of squares for tests

Figure 5.23 shows the second iteration of the same analysis which only involves the influences of significant main and interaction effects. The results show little discrepancy

from the first analysis. This further strengthens in verifying that only three factors inflict significant effects on signal attenuation.

The size of crowd is the most significant factor affecting signal strength due to bodily attenuation factor. The magnitude of the effect can be seen in the Mains Effect Plot (Figure 5.24). This also indicates that crowd size inflicted the highest amount of signal loss compared to any other crowd properties. The crowd size in combination with the number of receiver had significant effect to the signal strength, as do crowd pattern in combination with the number of receiver. These interactions are discussed in further detail at the Interaction Plot (Figure 5.25).
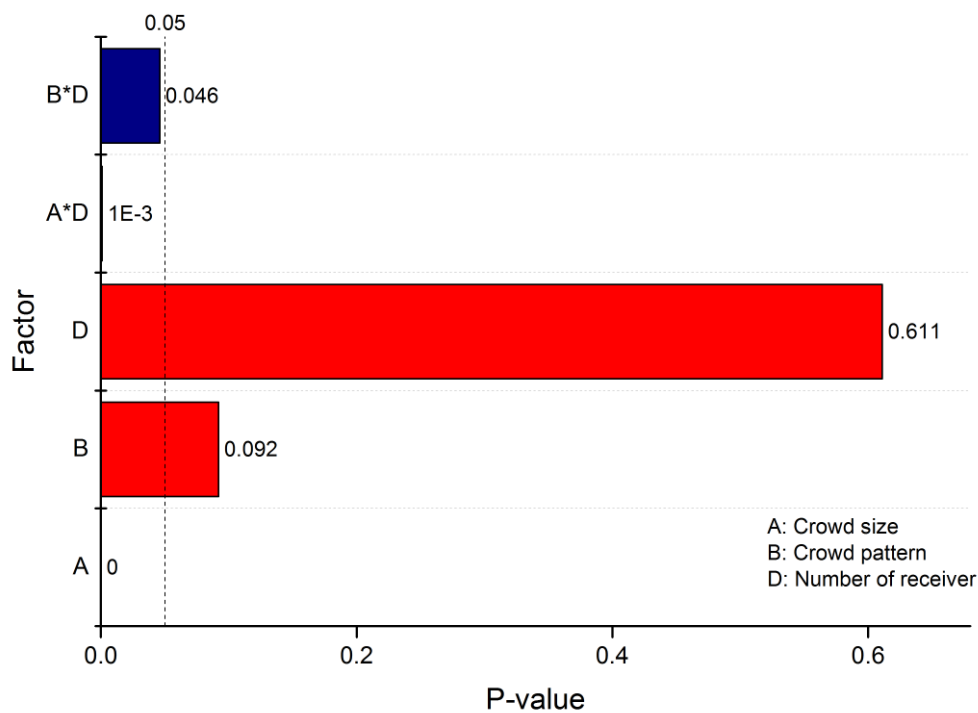
Figure 5.23: Second iteration of ANOVA for the RSSI (average) using adjusted sum of squares for tests

In summary, the strongest factor affecting the signal propagation is the human crowd size. Two of the strongest interactions are combinations of human crowd size and crowd pattern with the number of receiver. Together, these three factors are the most important parameters in determining the density of a crowd based on RSSI value. This information

provides a contribution of knowledge in understanding the relationship between human crowd and signal loss inflicted by them.

5.2.2 (b) Main Factor Influencing Signal Attenuation

Figure 5.24 shows the Mains Effect plot based on the second iteration of ANOVA. The high inclination of the slope of the crowd size plot shows significant effect on signal propagation as the number of crowd increases from 5 to 15 people. The crowd pattern and number of receiver have not been identified as main effect as their p-value of 0.092 and 0.611 indicate that these parameters do not inflict strong enough signal attenuation in relative to all other factors.
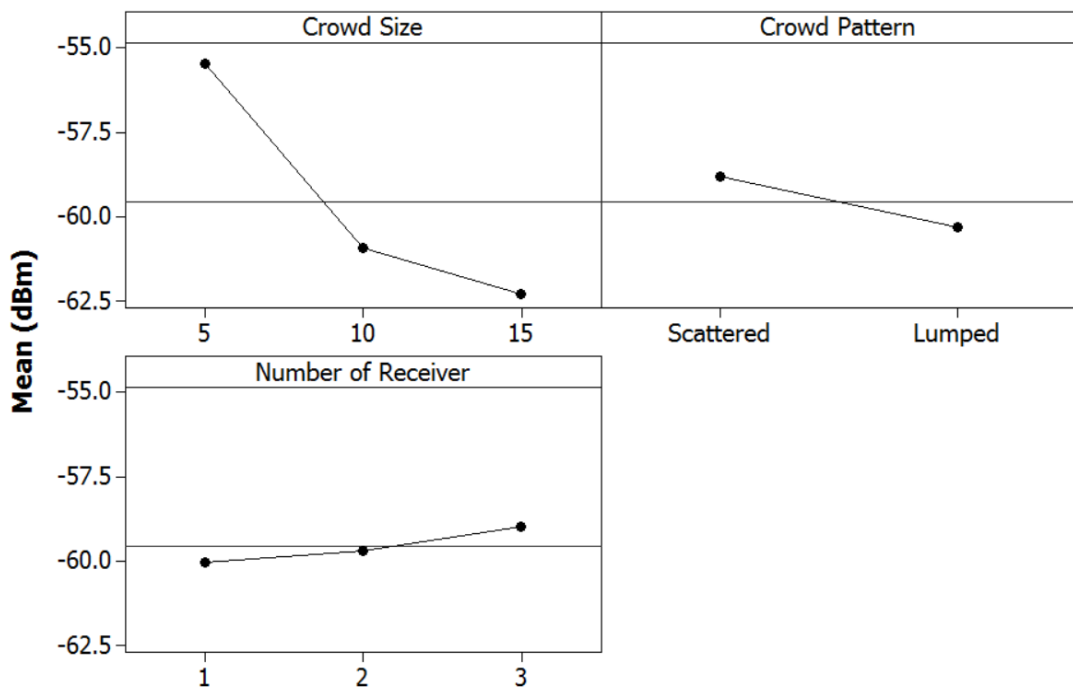
Figure 5.24: Mains Effect Plot of crowd size, crowd pattern and number of receiver

The declining slope from left to right at the crowd size and pattern plots indicate an expected observation by the effects of each level. Based on logic, higher number of people should inflict higher signal loss. Likewise, lumped crowd is expected to inflict higher signal attenuation compared to scattered crowd.

In summary, the main effects become increasingly significant as the gradient of the lines become less parallel to the mean line. Figure 5.24 verifies the magnitude of significance of the crowd size towards signal attenuation. This finding agrees with the conclusions of Haochao et al. (2015) and Depatla, Muralidharan and Mostofi (2015). Both of these research depended heavily on the human body signal attenuation in their modelings for Wi-Fi based crowd counting. This means that as the crowd size increases, so does its effect on signal loss.

5.2.2 (c) Interaction factors influencing signal attenuation

The interactions between different crowd parameters were never investigated in any of the previous work on H-CDE due to their lack of statistical usage. This meant that they lack the mechanism as to measure the correlations between the parameters. This research successfully identified two types of interaction as significant factors in affecting signal loss. This offers new knowledge in understanding the crowd properties.

Figure 5.25 (a) indicates that as the number of the End Nodes increases to two and three, the RSSI values become smaller provided that the crowd size is between 10 and 15 people. Figure 5.25 (b) shows that in average, a lumped human crowd pattern inflicts 2.57 dBm more signal loss than the scattered pattern. This difference is denoted as $RSSI_{crowd\_pattern}$ which is used in the proposed H-CDE algorithm (equation 3.1, 3.2 and 3.3) and path loss model (equation 3.5). Figure 5.25 (b) also illustrates that there is an improvement in the RSSI measurement if three receivers are used in lumped human crowd pattern.
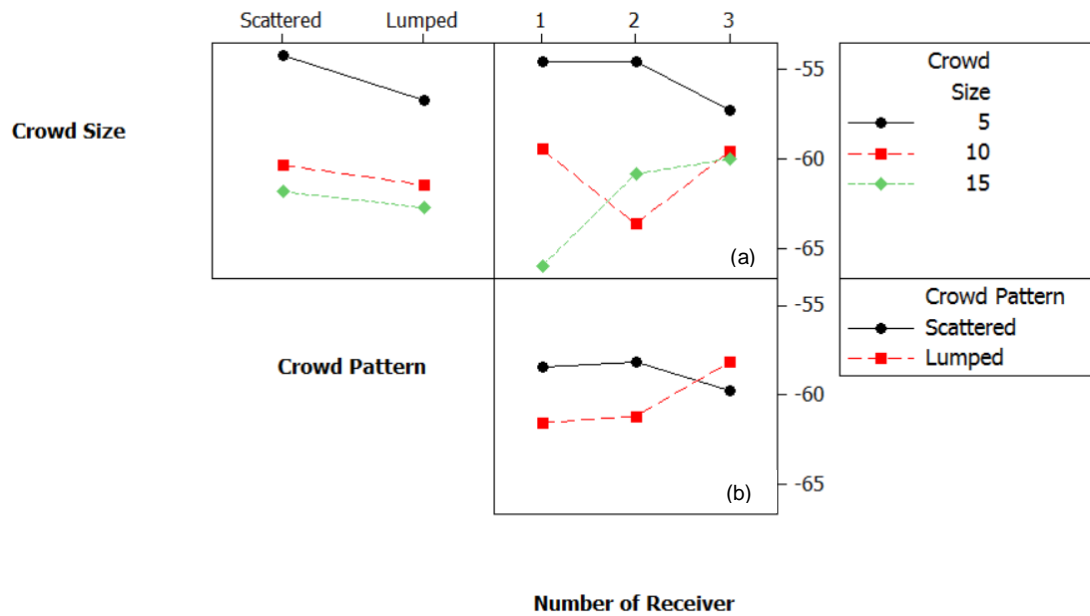
Figure 5.25: Interaction Plot for the RSSI (a) A combination of the human crowd size and number of receiver and (b) A combination of the human crowd pattern with number of receiver.

The rationale for the improvement of RSSI from the interaction of crowd size and number of receiver is attributed to the ability of the signals to propagate better through less bodily obstruction. This is possible as the distribution of humans within the crowd may create different gap between one person to the other. In other words, the human crowd distribution has a level of pseudo-randomness.

Similarly, the same rationale applies for the interaction between crowd pattern and the number of receiver in Figure 5.25 (b), where human freedom of movement and approximation of distance is responsible in creating different gaps between each person, either horizontally or vertically. For example, when the crowd is lumped together in a specific region, it would register a high signal loss to a single receiver, but would otherwise register very good RSSI to the other two receivers. This made the average RSSI for lumped crowd better than scattered when three receivers were utilized.

In summary, using higher number of receiver allows enhancement in the RSSI measurement due to the variation of the human crowd obstructions. Using increased number of receiver only significantly lowers signal attenuation in conjunction with crowd size and

pattern. In addition, this discovery also addresses the role of crowd pattern on signal loss which is incomplete from the research conducted by Arai, Kawamura and Suzuki (2010).

5.2.2 (d) Residuals

Figure 5.26 (a) shows that the residuals appear to follow a straight line without any evidence of non-normality or skewness. Some possibly slight outliers were detected (near point -10), presumably caused by a random variation.
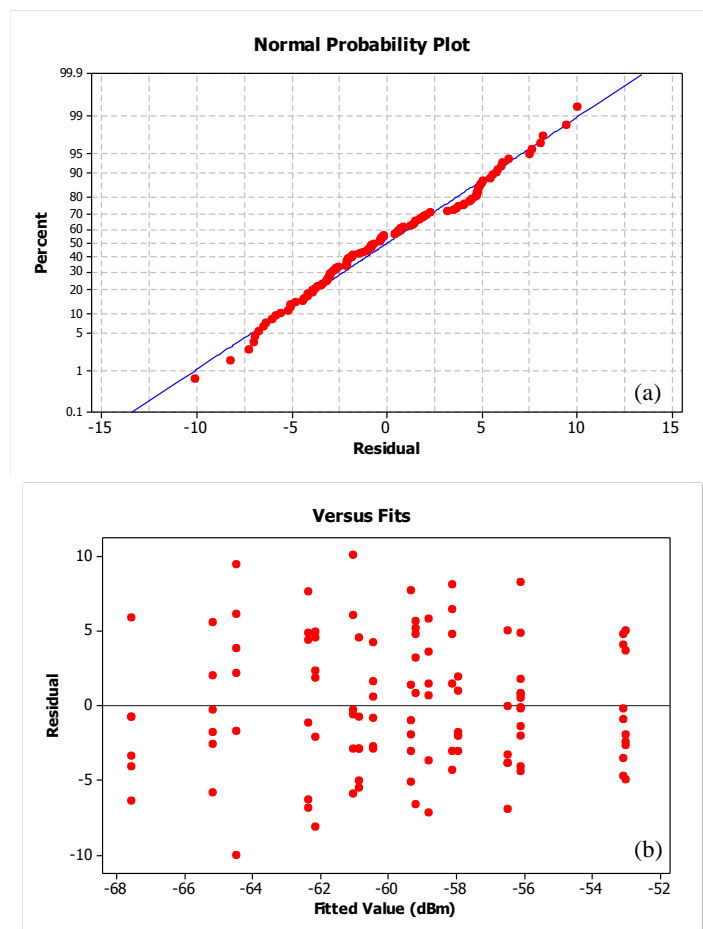
Figure 5.26: Residual plot for (a) normal probability and (b) versus fits

This uncontrolled variation may be a result of the non-strict form of how the crowd were created in every event. However, the data does not depart significantly from the linear

line and does not seriously affect the result. Thus, the overall trend of Figure 5.26 (a) indicates a normal distribution of residuals for crowd density.

Figure 5.26 (b) shows that the residuals appear to be randomly scattered about zero without any evidence of non-constant variance or outliers. This indicates that the error has constant variance. In summary, the residual follows a normal distribution and has constant variance scattered about zero, in accordance with $\varepsilon \sim N\ (0,\sigma_\varepsilon^2)$.

5.2.3   Crowd Density Estimation Classification

The results of the DOE section are tabulated in Table 5.12. $RSSI_{ave}$ is the average RSSI for the given number of people, $RSSI_{max\_15}$ is the maximum recorded RSSI for 15 people, $RSSI_{scattered\_crowd}$ is the average RSSI for crowd which consists of scattered people, $RSSI_{lumped\_crowd}$ is the average RSSI for lumped crowd and $RSSI_{crowd\_pattern}$ is the difference between $RSSI_{lumped\_crowd}$ and $RSSI_{scattered\_crowd}$.

Table 5.12: Values obtained from the DOE section

Parameter	Value (dBm)
$RSSI_{ave\_5}$	-55.50
$RSSI_{ave\_10}$	-60.90
$RSSI_{ave\_15}$	-62.30
$RSSI_{max\_15}$	-73.50
$RSSI_{scattered\_crowd}$	-58.20
$RSSI_{lumped\_crowd}$	-60.77
$RSSI_{crowd\_pattern}$	-2.57

The values from Table 5.12 are then fitted into the H-CDE algorithm (equation 3.1, 3.2 and 3.3) as below.

Low density (LD): $\text{LD} \leq \text{RSSI}_{ave\_5} + \text{RSSI}_{crowd\_pattern}$

: $\text{LD} \leq -55.5 \text{ dBm} - 2.57 \text{ dBm}$

: $\text{LD} \leq -58.07 \text{ dBm}$

Medium density (MD): $\text{RSSI}_{ave\_5} + \text{RSSI}_{crowd\_pattern} < \text{MD} \leq \text{RSSI}_{max\_15} + \text{RSSI}_{crowd\_pattern}$

: $-58 \text{ dBm} < \text{MD} \leq -73.5 \text{ dBm} - 2.57 \text{ dBm}$

: $-58 \text{ dBm} < \text{MD} \leq -76 \text{ dBm}$

High density (HD): $\text{HD} > \text{RSSI}_{max\_15} + \text{RSSI}_{crowd\_pattern}$

$\text{HD} > -76 \text{ dBm}$

The LD is modelled after RSSI_{ave_5} and $\text{RSSI}_{crowd\_pattern}$ parameters which represent the significant impact of crowd size and crowd pattern * number of receiver on signal attenuation respectively. The RSSI_{max_15} parameter is chosen for MD and HD to model the effect of higher crowd size on signal attenuation. These affectively integrate the findings of the DOE into the algorithm.

The fitting result of the proposed H-CDE algorithm is shown in Figure 5.27 along with three other algorithms, namely SCPL, WB and EFE for comparison. The RSSI values for the extrapolation of the crowd from 20 to 50 people are given in Table 5.13. Further analysis on the prediction accuracy of the models is presented in Table 5.14.
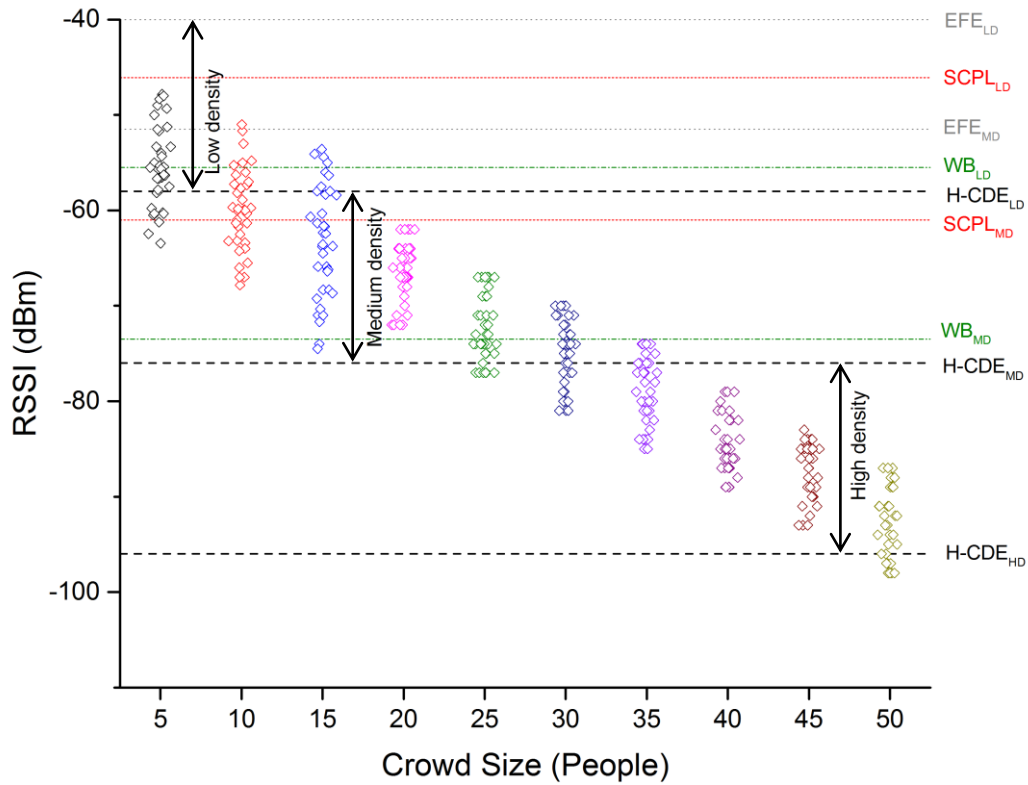
Figure 5.27: Classifying the density of the experimental data where each rhombus represents the average of 10 RSSI measurements. The horizontal lines show the prediction threshold of each technique that separate between low, medium and high density. The vertical lines indicate the density region of the proposed H-CDE. The high density threshold of all the models is the same as H-CDE$_{HD}$.

Table 5.13: Extrapolated average RSSI values for the crowd from 20 up to 50 people. σ represents the standard deviation

Crowd size	5	10	15	20	25	30	35	40	45	50
RSSI (dBm)	-55.5	-60.9	-62.3	-67.3	-71.7	-75.4	-79.0	-83.7	-87.7	-92.5
σ (dBm)	4.2	4.3	5.9	5.4	5.4	5.4	5.4	5.4	5.4	5.4

The standard deviations of around 5 dBm (Table 5.13) show that the fluctuations are quite high that overlapping data is present between low, medium and high density as can be seen from the graph in Figure 5.27. This effectively would reduce the accuracy of any type of prediction method.

Two further analyses are presented to verify the results of the H-CDE algorithm. The primary analysis would focus on the H-CDE based on the density classification guideline as defined by Yuan, Zhao, Qiu and Xi (2013), previously tabulated in Table 3.3 and 4.9. The resulting analysis is presented in Table 5.14 and 5.15.

Next, the secondary analysis would review the performance of H-CDE algorithm according to the density level provided by by Hiroi, Shinoda and Kawaguchi (2016), given in Figure 2.5. Table 5.16 is tabulated to discuss the findings.

Table 5.14: Prediction accuracy of the proposed H-CDE versus other models

Model	Low density	Medium density	High density	Overall
Proposed H-CDE	75.0 %	73.6 %	65.1 %	71.2 %
SCPL	0.0 %	50.0 %	100.0 %	50.0 %
WB	44.4 %	84.7 %	71.4 %	66.9 %
EFE	0.0%	2.8 %	100.0 %	34.3 %

Table 5.14 indicates that the proposed H-CDE algorithm produced the best overall prediction accuracy at 71.2 %. This can be attributed to the inclusion of the DOE factors (crowd size and pattern) into the algorithm. The WB algorithm came in second with 66.9 % overall accuracy. The main drawback of WB is that it does not include crowd pattern in its algorithm and this contributed to its reduction of accuracy. Thus, the H-CDE algorithm improves the prediction accuracy by 4.3 %.

Both SCPL and EFE implemented the normalization method to eradicate the overlapping effect of body obstruction. However, this method is proven to be ineffective and actually resulted in a huge drop of estimation accuracy. For example, both algorithms completely failed to detect low density crowd as the effect of body obstruction is lowered.

This made these algorithms completely missed the RSSI range of values for low density (5 people). Instead, these algorithms could only detect high density as all the RSSI were regarded as high density. This produced poor density estimation as the level of crowd severity could not be determined accurately. In addition, the effect of crowd pattern were also neglected which further degrades the prediction accuracy, similar to the WB algorithm.

Another point worth considering is that the density classification suggested by Yuan, Zhao, Qiu and Xi (2013) is actually skewed. Table 5.15 shows the comparison between their guideline with the averaged RSSI results of the related algorithms. Yuan, Zhao, Qiu and Xi (2013) defined low density consisting of an average of 5 people, medium between 10 to 15 people and high having more than 20 people. In comparison, the proposed H-CDE and WB has more relaxed classification of medium density.

Table 5.15: The H-CDE results of related algorithms mapped to the crowd density classification defined by Yuan, Zhao, Qiu and Xi (2013)

Number of people	Yuan, Zhao, Qiu and Xi, (2013)	Proposed H-CDE	WB	SCPL	EFE
5	LD	LD	LD	MD	HD
10	MD	MD	MD	MD	HD
15	MD	MD	MD	HD	HD
20	HD	MD	MD	HD	HD
25	HD	MD	MD	HD	HD
30	HD	MD	HD	HD	HD
35	HD	HD	HD	HD	HD
40	HD	HD	HD	HD	HD
45	HD	HD	HD	HD	HD
50	HD	HD	HD	HD	HD

The skewed density pattern of Yuan, Zhao, Qiu and Xi (2013) might be caused by their application and limitation. For example, they relied on an inefficiently large number of

nodes, deployed in a 4 x 4 m^2 grid to sense the crowd. Their transceivers are set up as to only sense the change in RSSI within a short 4 m radius. As a result, the density classification by Yuan, Zhao, Qiu and Xi (2013), although acceptable as a basis, may not give a clear distinction between different crowd density levels in other establishment. This warrants additional analysis on the density classification.

The density classification of Hiroi, Shinoda and Kawaguchi (2016) differs slightly from that of Yuan, Zhao, Qiu and Xi (2013). The former uses the information of the density of people per 1 m^2 area while the latter relies on the total number of people within the entire area monitored. Although Hiroi, Shinoda and Kawaguchi (2016) did not specify the site dimension of their survey, it can be deduced that they implemented their system in a 64 m^2 room. This is based on their deployment of two transceivers to cover each and every side of the room whereby each transceiver has 4 m of average wireless coverage. By dividing the number of people by 64 m^2 area, the density guideline by Hiroi, Shinoda and Kawaguchi (2016) can then be compared to the proposed and related works from Table 5.14. The results are tabulated in Table 5.16.

Table 5.16: Density classification of related works mapped to the guideline provided by Hiroi, Shinoda and Kawaguchi (2016)

Classification	Density (people/m^2)				
	Hiroi, Shinoda and Kawaguchi (2016)	Proposed H-CDE	WB	SCPL	EFE
Low	0.10-0.20	0.02-0.13	0.02-0.13	-	-
Moderate	0.21-0.52	0.14-0.52	0.14-0.44	0.02-0.22	-
High	0.53-0.80	0.53-0.78	0.45-0.78	0.23-0.78	0.02-0.78

The proposed H-CDE still has the best match in density classification as recommended by Hiroi, Shinoda and Kawaguchi (2016). This is followed by the WB algorithm where it predicts less accurately in moderate density level compared to the proposed H-CDE. Both SCPL and EFE failed to account for the low and medium density

level. As a consequence, both algorithms would not be able to differentiate between different density levels. This would only raise false alarms and misinformation on the actual crowd density.

Retracing back to each algorithm would clarify such results. As previously discussed, both SCPL and EFE rely on normalization that actually is the main reason for the inaccuracies. This signifies that a flat normalization is not necessarily beneficial to the algorithm if deployed in different venues.

On the other hand, a plain crowd size-based algorithm such as the WB performs better without any normalization. This is in accordance to the findings of DOE where crowd size is a major factor in influencing signal loss that would then be captured by the algorithm to indicate presence of crowds.

The proposed H-CDE performs slightly better than the WB algorithm in determining the varying crowd levels. Again, this is attributed to the introduction of the crowd pattern as another major factor in influencing the signal loss and thus forming the new formulation for H-CDE.

In summary, the proposed H-CDE system improved upon the current algorithms in estimating the correct density level of people. In the density classification test based on the parameters set by Yuan, Zhao, Qiu and Xi (2013), the proposed H-CDE system produces the best overall accuracy. In another density level verification according to the conditions set by Hiroi, Shinoda and Kawaguchi (2016), the proposed H-CDE system still provides the most accurate categorization between low, medium and high density.

The relevant parameters obtained from the experiments conducted to satisfy the PL models (equation 2.4, 2.5 and 3.5) are tabulated in Table 5.17. The *BAF* of the proposed H-CDE model is defined as $0.84m$, where m is the number of people and 0.84 is the average signal loss inflicted by body obstruction measured from three receivers in dBm unit.

Table 5.17: Relevant parameters for the modelling

Parameter	Value
d	30 m
PL_{30m}	-47 dBm
PL_0	-32 dBm
n	1.02
m	0.84
λ	0.125 m
h	0.3 m
d_1 and d_2	15 m
$RSSI_{crowd\_pattern}$	-2.57 dBm
BAF	0.84 m

Thus, equation 3.5 is finalized as:

$$PL = PL_0 - 10n \log_{10}(d) - RSSI_{crowd\_pattern} - 0.84m \qquad (5.4)$$

where PL_0 is -32 dBm, path loss exponent, n measured at 30 m of line-of-sight of the T-R separation is 1.02, $RSSI_{crowd\_pattern}$ is -2.57 dBm and multiplying m, the number of people, with 0.84 is the average body attenuation factor measured from three receivers.

The comparison between the models with the empirical data is imaged in Figure 5.28. The graphs show that the proposed H-CDE model could fit the actual data better compared to Haochao and Hiroi. The error analysis of the graph is shown in Table 5.18. Overall, the H-CDE model has the least error in predicting the size of the crowd. This is attributed to the inclusion of crowd size and pattern that increases the estimation accuracy.

Haochao's model only considered the signal loss by bodily obstruction (crowd size). Morever, the model does not fit the actual data well as the experimental data fits a linear line. Hiroi's model relies only on three variables; the range between T-R separation, the

frequency and the height of the node whereas the rest are constants. Hiroi's model disregarded the crowd properties and this resulted in inaccuracies in the model.
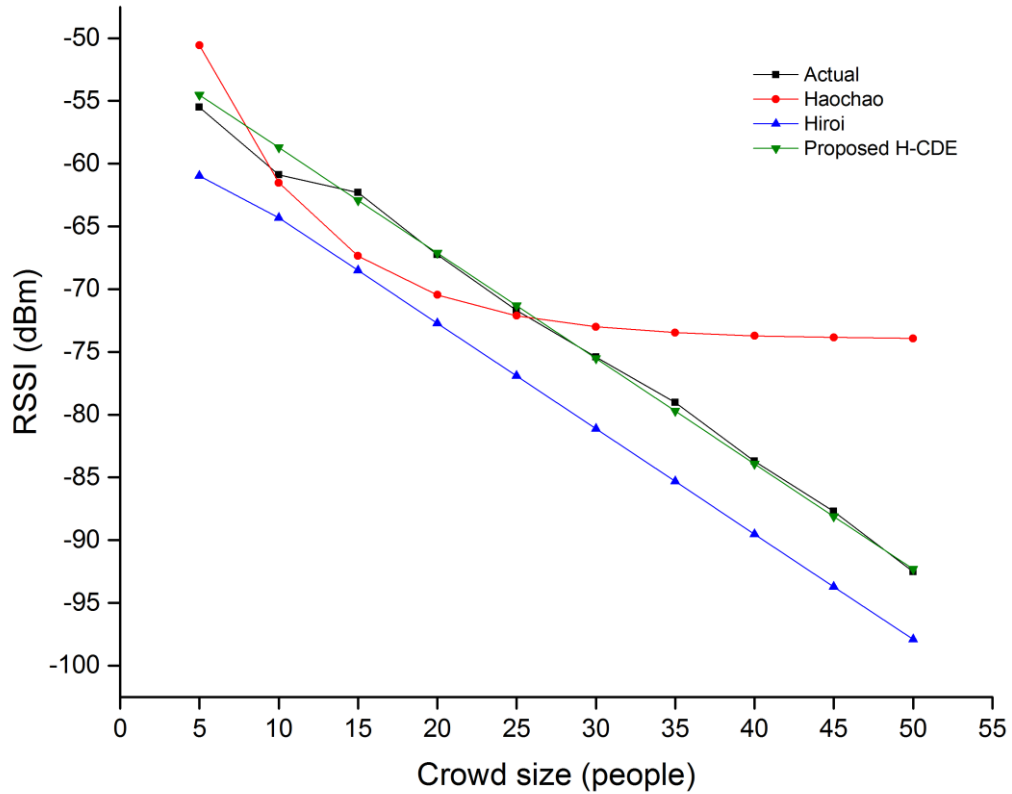
Figure 5.28: Comparison between the H-CDE prediction model with the actual and other models.

Table 5.18: Percentage error of the models compared to the actual data (the lower the better)

Density level	Model		
	H-CDE (%)	Haochao (%)	Hiroi (%)
Low density	1.8	8.9	9.8
Medium density	2.3	4.6	7.8
High density	0.4	9.0	7.3
Overall	0.9	8.2	7.6

In summary, the H-CDE algorithm and classification are able estimate the level of crowd density better compared to other methods. The H-CDE path loss model is also shown to have higher accuracy compared to the other models. This allows crowd counting with high accuracy, which complements with the H-CDE algorithm to monitor the size of the crowd in

the designated area. Therefore, the objective of improving the crowd density estimation accuracy has been satisfied.

5.3   Energy Harvesting Performance Evaluation

This section traverses through EH performance verification analyses and discussion. The findings are imperative to operating the WSN portion, as well as the overall H-CDE system. Revisiting earlier chapters would clarify that amongst the aims of the EH mechanism are portability and safety. These issues are also addressed in this section.

5.3.1   Effect of Solar Cell Alignment

Figure 5.29 shows the gradually diminishing voltage and current values of the 1 W solar cell as the angle increases to 180 degrees. The maximum voltage and current values were 4.83 V and 223.6 mA, respectively, while the lowest measured voltage and current were 3.13 V and 2.4 mA, respectively. Beyond 30 degrees of misalignment, the solar cell started to suffer from increasingly high current losses. This is attributed to the dwindling rate of photon absorption as the solar cell gets misaligned from sunlight.

The solar cell produced 50 % current efficiency when misaligned at 64 degrees. At this angle, the solar cell also produced 3.75 V, which is enough to power up the load. However, as the PMU has MPPT, the resulting voltage is 3 V, which is the minimum under-voltage threshold allowed by the PMU. The resulting current would also be reduced due to the MPPT. Thus, it is assumed that the solar cell could provide minimal power to the load when it is misaligned by at least 64 degree from an optimal sunlight presence.

Current output of solar cell is extremely sensitive towards alignment while voltage output is more tolerant in misalignment. Another factor that affects the measurements was

sunlight reflected from the surroundings. This factor was not specifically measured and was considered a natural phenomenon.
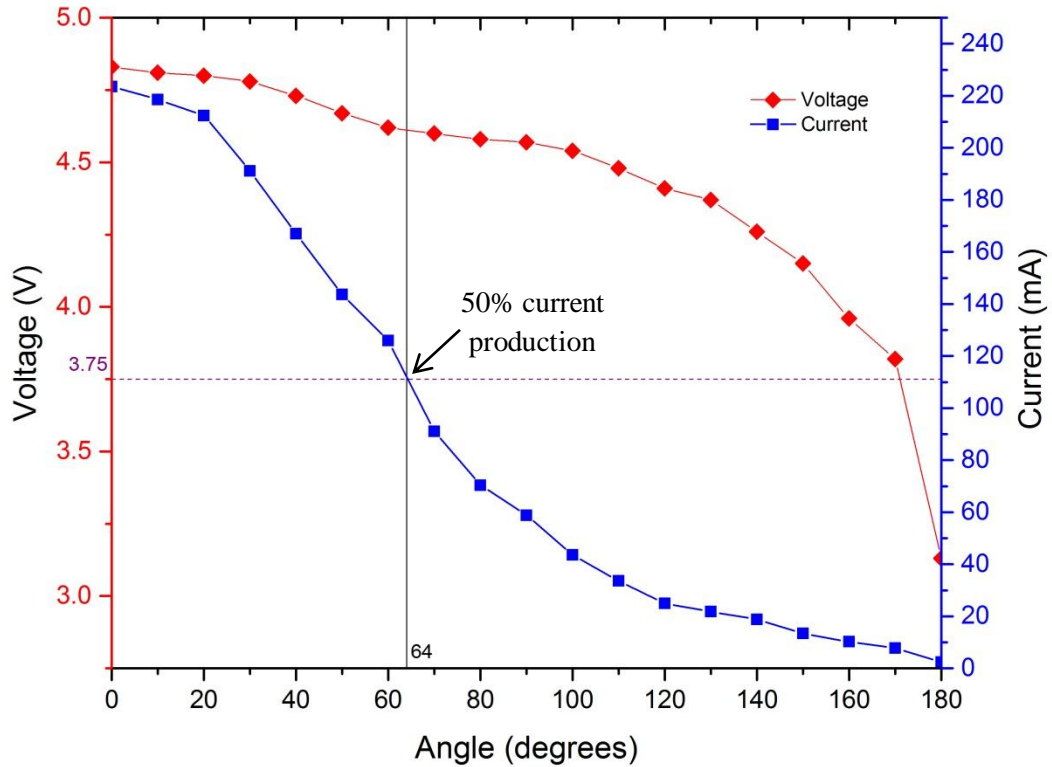
Figure 5.29: Voltage and current versus angle in solar cell alignment test

The results also indicate that the solar cell alignment experiment was conducted when the temperature of the solar cell was still relatively close to the room temperature. The initial voltage is measured at 4.83 V whereas the normal and stable voltage of the solar cell is around 4.4 V; which is caused by warming. A very warm solar cell due to prolong exposure to sun would have lower efficiency and thus lower the maximum voltage and current values.

In summary, the solar cell performs within acceptable range at a 30 degree misalignment and could barely power up the load at 64 degrees misalignment. This can be related to the findings of Titirsha, Siddique, Afrin, Sanjidah and Rabbani (2014) where they

reported a 13.4 and 30 % of power loss at 30 and 45 degrees of misalignment respectively. Furthermore, the solar cell misalignment affects the current production the most.

Interestingly, the issue of solar cell alignment lacks discussion in the EH-WSN platform such as the works of Nanda et al. (2014), Ramos, Girbau, Lazaro, Collado and Georgiadis (2015) nor any of the earlier works such as Zhang, Sadler, Lyon and Matroniso (2004) and Xiaofan, Polastre and Culler (2005). Misalignment has profound impact of solar power generation and therefore this knowledge hopefully provides a basis in solar cell usage and limitation in WSN platform.

5.3.2 Maximum Power Point Tracker

The MPPT is an important feature to maximize the harvested power efficiency. The implementation of MPPT is common nowadays and should not be neglected by EH system designers. This section verifies that the MPPT mechanism implemented is working as intended.

The MPPT versus non-MPPT performance in charging the battery is shown in Figure 5.30. The battery reached 3.6 V within 54 minutes by utilizing the MPPT mechanism while charging the battery to 3.6 V without the MPPT took 77 minutes.

The result indicates that the MPPT allows up to 29.8 % faster battery charging. This means that with MPPT, the higher harvested power allows the battery on the H-CDE system to be charged faster. However, the actual efficiency of the MPPT changes depending on the voltage and current of the solar cell, which constantly fluctuates based on sunlight availability. Still, the benefit of implementing the MPPT has been verified.

Another notable outcome is that the PMU will always try to charge the battery to 3.6 V, instead of the programmed 3.52 V. This means if available power permits, the PMU will

attempt to charge the battery to its maximum allowable voltage (3.61 V) according to the over-voltage protection feature. This finding is further investigated in Section 5.3.6.
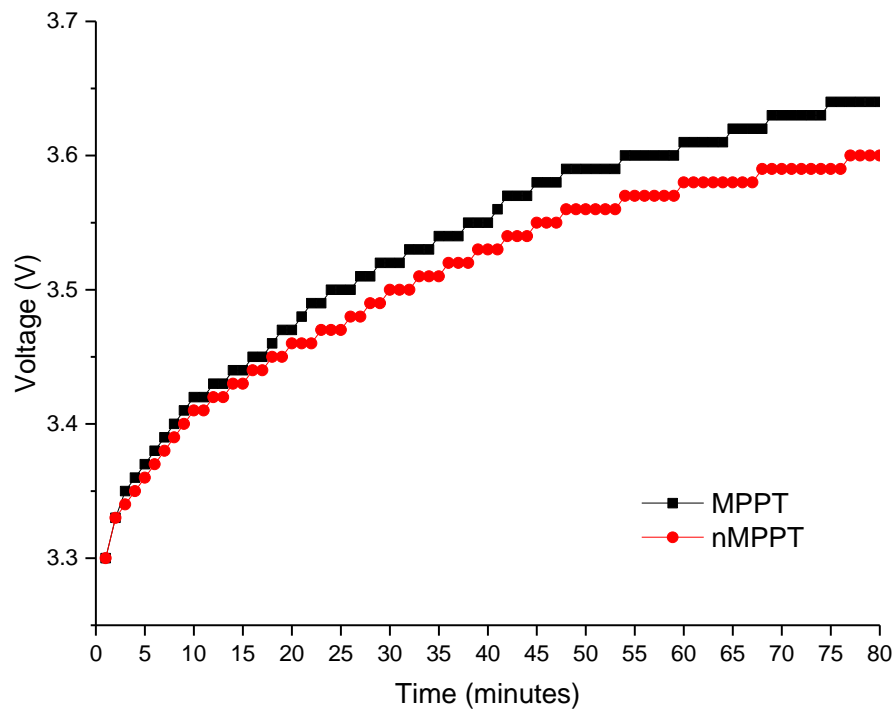
Figure 5.30: Battery charging performances subjected to MPPT and non-MPPT (nMPPT)

5.3.3 Energy Harvesting Performance of the End Nodes

In this section, the EH operation of the three fabricated End Nodes are further scrutinized to evaluate its performance in a real scenario. Figure 5.31 shows the performance of battery charging for all the three End Nodes and also Router 2. End Node 3 reached 3.6 V in 304 minutes, followed by End Node 2 in 310 minutes, Router 2 in 321 minutes, and finally End Node 1 in 373 minutes.
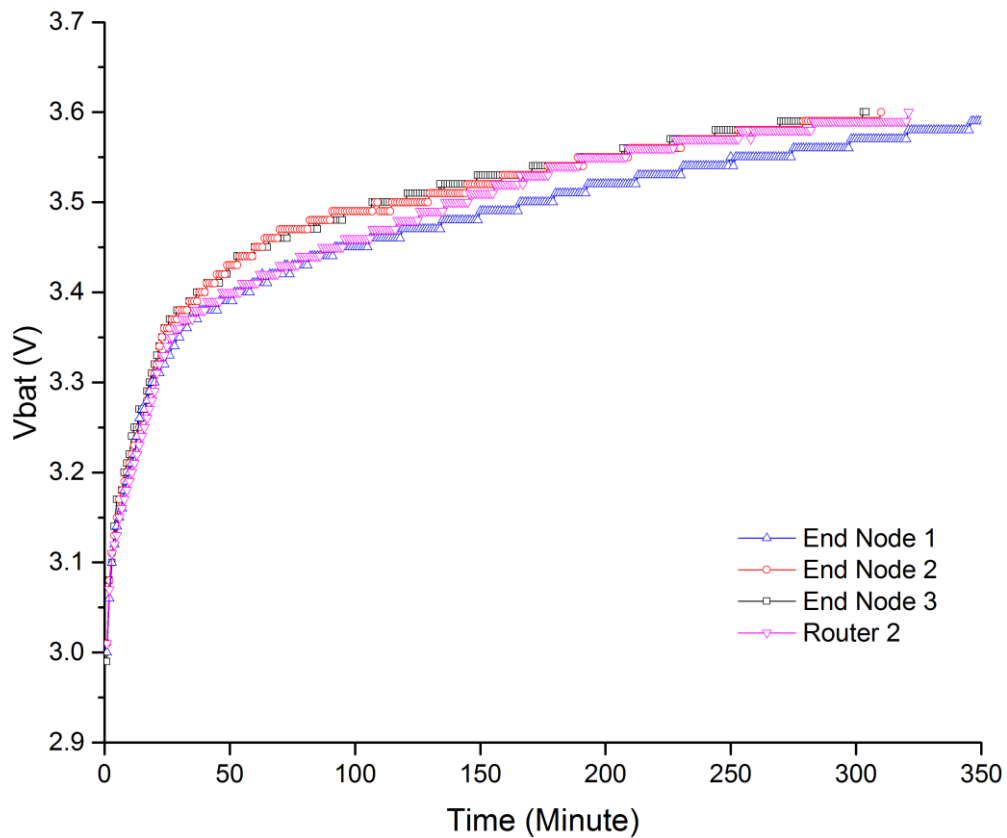
Figure 5.31: Battery charging of nodes under direct sunlight from 3.0 to 3.6 V

The EH performance discrepancies between the nodes can be attributed to the efficiency of the solar cell, battery and PMU. However, these factors cannot be controlled post-design while the data logger has already been calibrated beforehand to minimize measurement errors. The End Nodes performed comparably to Router 2, indicating that the End Nodes work as intended.

Figure 5.32 shows the RSSI collected for all the nodes. End Node 3 and Router 2 have stable RSSI at -31 dBm due to their close distance to the Coordinator. End Node 1 and 2 have lower but insignificant RSSI losses due to distance and physical obstructions inflicted by End Node 3 and Router 2 during the test (Figure 5.37). The results show that the EH mechanism did not interfere with the RF transmission in both low (3 V) and high voltage (3.6 V).
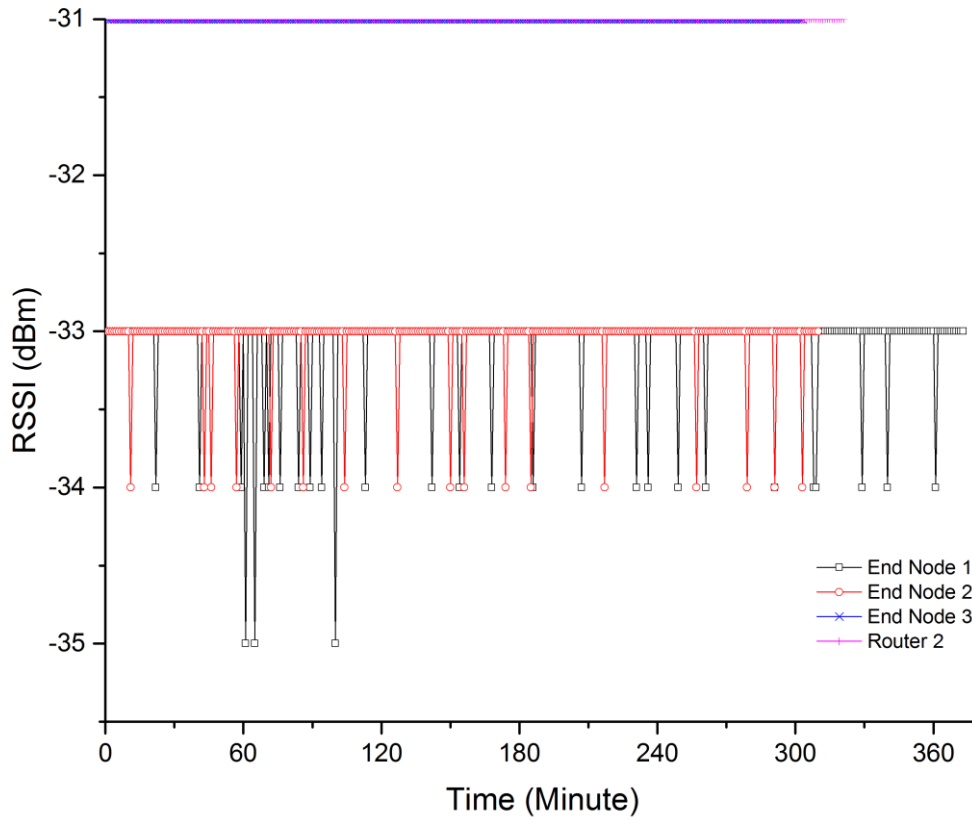
Figure 5.32: RSSI of nodes for the duration of the experiment

The results also indicate that the End Nodes were able to charge the battery and power up the load at the same time. It takes 5 to 6.2 hours to fully charge the battery from 3.0 V to 3.6 V. This means that if sunlight is available daily around 5 to 6 hours, then the H-CDE End Nodes are able replenish its own energy. The graph in Figure 5.33 confirms this condition where the battery of the End Node was continuously charged using sunlight during the day and battery-powered for the remaining hours. This also proves that the EH mechanism proposed solves the H-CDE system's finite power problem. For example, the WB system by Yuan, Zhao, Qiu and Xi (2013) can only operate for 83 hours before requiring a change of battery or a manual battery recharge.
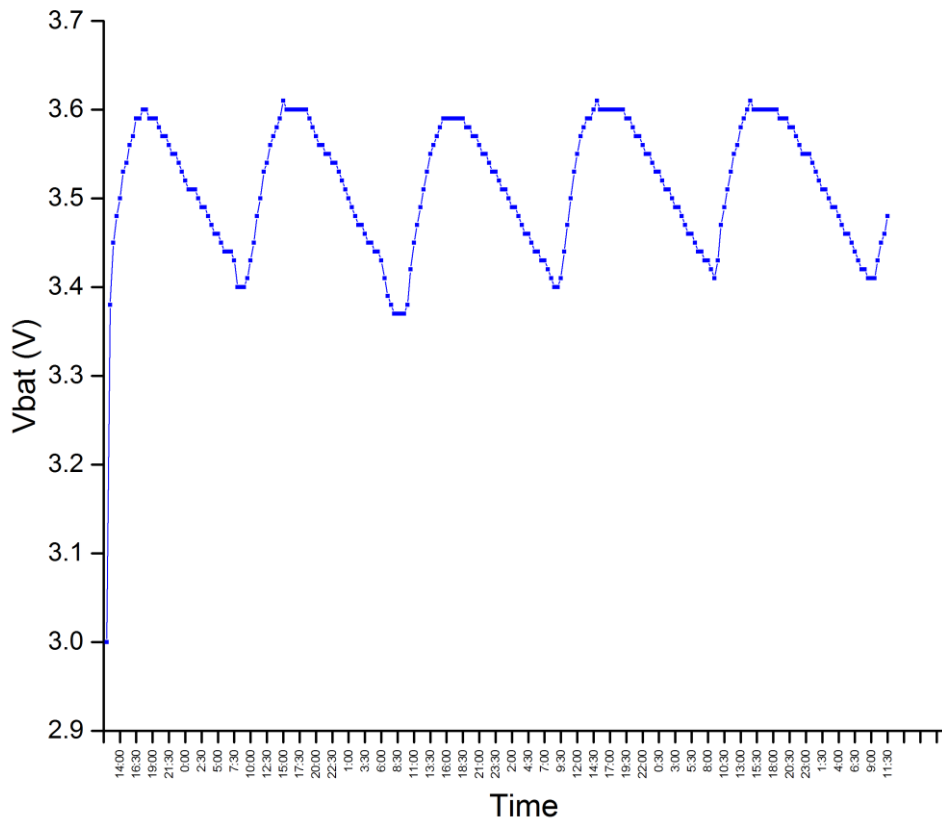
Figure 5.33: End Node outdoor operation for five days (120 hours)

In summary, the End Nodes require around 5 to 6 hours to recharge the 2000 mAh battery from 3.0 to 3.6 V. This is significantly better than the performance of Smartmote by Nanda et al. (2014) where they took 9 hours to charge their 1000 mAh battery to 90 % capacity. The RSSI measurement of the nodes proved stable RF transmission during EH operation. As sunlight is available around 8 hours per day in equatorial regions, an H-CDE node could perpetually operate without human intervention.

5.3.4 Energy Harvesting Performance in Range Test

In the previous section, the EH mechanism is performed in close distance. The results in this section would ensure that the EH operation does not negatively affect the overall RF transmission in long distances.

The results of the test are shown in Figure 5.34. The RSSI from the Router 1 (controlled unit) and the End Node shows similar performance. Throughout the 15 minute experiment, the voltage of the battery remained at 3.46 V (V_batt_solar) and 3.48 V (V_wo_solar) while the voltage supplied by the solar cell without the battery (V_wo_batt) fluctuated between 3.29 V to 3.57 V.
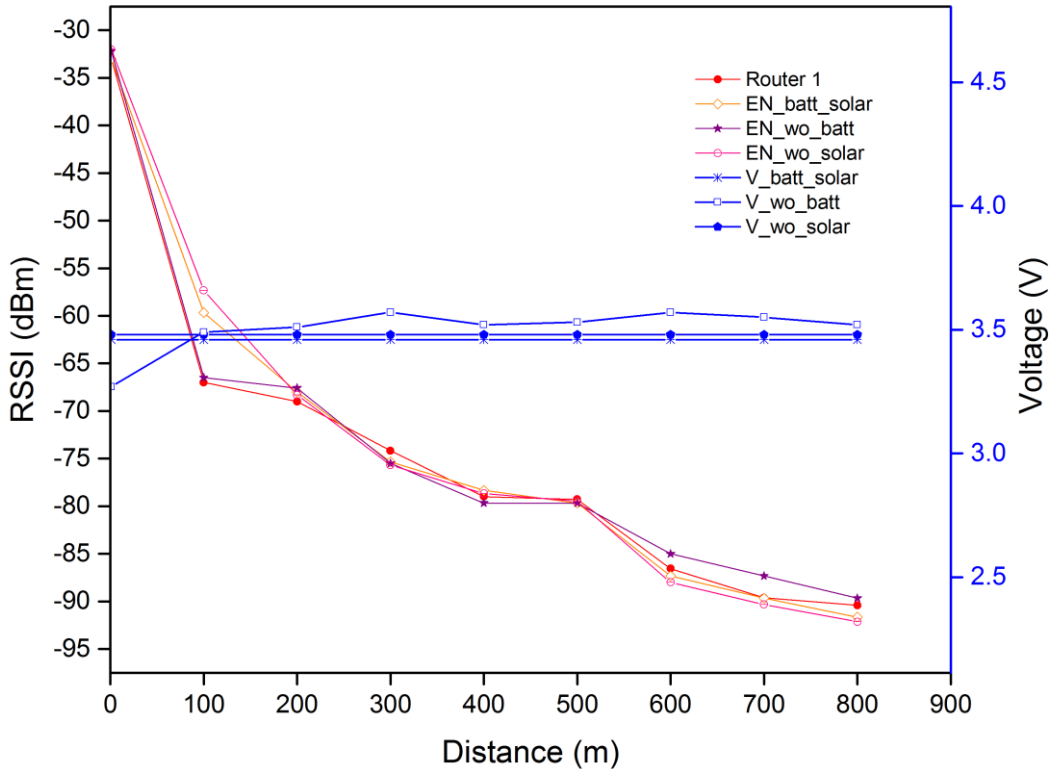
Figure 5.34: Signal strength versus distance of Router 1 and End Node 3. The End Node with both battery and solar cell connected is labelled as batt_solar. The End Node without battery and solar cell is denoted as wo_batt and wo_solar respectively. The voltage of the End Node versus distance is also shown.

The results verified the RF stability of the H-CDE End Node in all three cases: with both the battery and solar cell connected, with only the battery connected and with only the solar cell attached. With the EH mechanism at work (batt_solar and wo_batt), there is no indication of RF disruption for up to 800 m of T-R distance. However, without the battery, the End Node will depend entirely on the solar cell to provide power. This makes it possible for disconnection and intermittent operation when not enough sunlight is available.

In summary, the EH H-CDE End Node performs comparably as a standalone system, thus validating its transmission operation. Thus, in general, it can also be concluded that EH is a viable power solution for low-powered WSN and H-CDE system establishment. In particular, the introduction of EH mechanism contributed to the longevity of the H-CDE system which is not found in any of the previous works as listed in Table 2.3 in Chapter Two.

5.3.5 Battery Performance

The battery capacity of End Node 1, 2 and 3 shown in Table 5.19 indicates a fairly high density even at lower voltage. This is an indication of good performing batteries in terms of electrical energy absorption.

Table 5.19: The 2000 mAh battery capacity with the initial voltage at 3.61 V

Node	Operation duration	Capacity
End Node 1	35 hours 21 minutes 8 seconds or 35.35 hours	70.70 %
End Node 2	35 hours 31 minutes 56 seconds or 35.53 hours	71.06 %
End Node 3	33 hours 28 minutes 9 seconds or 33.47 hours	66.94 %

The results show that the H-CDE End Node could operate perpetually between around 33 to 35 hours from the battery alone without the EH mechanism. Combining with the results from Section 5.3.3, once an End Node is fully charged to 3.6 V, it could remain operational for the next 1.4 to 1.5 days. Therefore, the H-CDE End Nodes could operate continuously without downtime if sufficient sunlight (5 to 6 hours of exposure) is available within the 33 hour bracket. Theoretically, the wireless node can operate independently for

five years until the next battery replacement due to the limited life cycle of a lithium ion battery.

The battery charging time without load is shown in Figure 5.35. End Node 1 took the least amount of time to charge its battery (115 minutes), followed by End Node 2 (119 minutes) and End Node 3 (131 minutes).
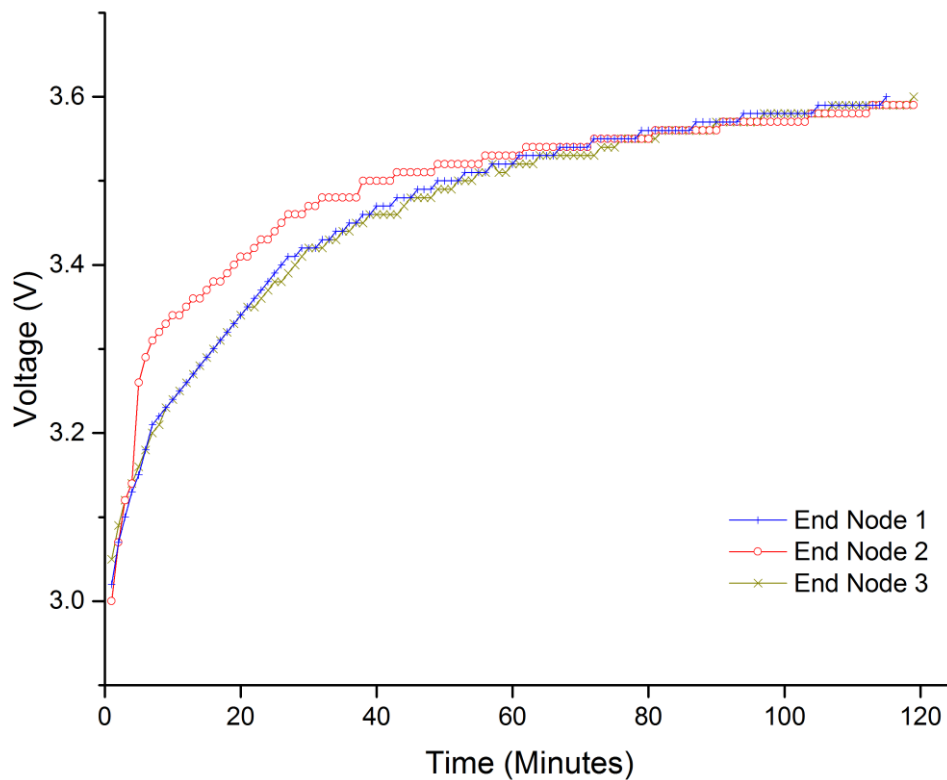
Figure 5.35: The duration to charge the batteries to 3.60 V

The results indicate that the H-CDE End Node only requires around 2 to 2.5 hours to fully charge the battery from 3.0 to 3.6 V with optimal presence of sunlight. Allowing a drained battery to charge under sunlight for nearly three hours will make the H-CDE End Node available for operation for at least 33 hours.

In summary, without sunlight, the 2000 mAh battery allows continuous operation for at least 33 hours due to its good density utilization at 3.6 V. It takes no more than three hours to charge the battery from 3.0 to 3.6 V at optimal sunlight presence when the load is turned

off. If good sunlight is present within the 33-hour duration, then the H-CDE End Node could replenish its battery energy on its own (Figure 5.33) and continue to operate without downtime through each 33-hour cycle. This makes the system practical for prolong outdoor usage. This would contribute to the extension of H-CDE monitoring system as the power issue were not discussed within the literature of H-CDE (Table 2.3). Thus, the proposed EH mechanism addresses this gap in hope of improving the operation duration of the H-CDE system.

5.3.6 Over- and Under-voltage Protection

The safety of the battery and load is guaranteed by the over- and under-voltage protection programmed at the BQ25504 IC. The graph in Figure 5.36 showed that End Node 1, 2 and 3 have over-voltage threshold of around 3.607, 3.578 and 3.570 V respectively when subjected to 3.0 V to 4.2 V input voltage. As expected, the varying threshold values of the over-voltage mechanism were the result of the resistor network tolerance values in their hardwired programming method.

However, an alarming observation is the increase of output voltage when the input voltage is above 4.4 V for all the End Nodes. This unexpected discovery meant that the over-voltage protection mechanism ceased to work properly when the input voltage surpassed 4.4 V. This is evident as the output voltage kept increasing as the voltage is increased. Nevertheless, as the 1 W solar cell works optimally at 4.4 V, the over-voltage protection mechanism should be able to work fine for End Node 2 and End Node 3.
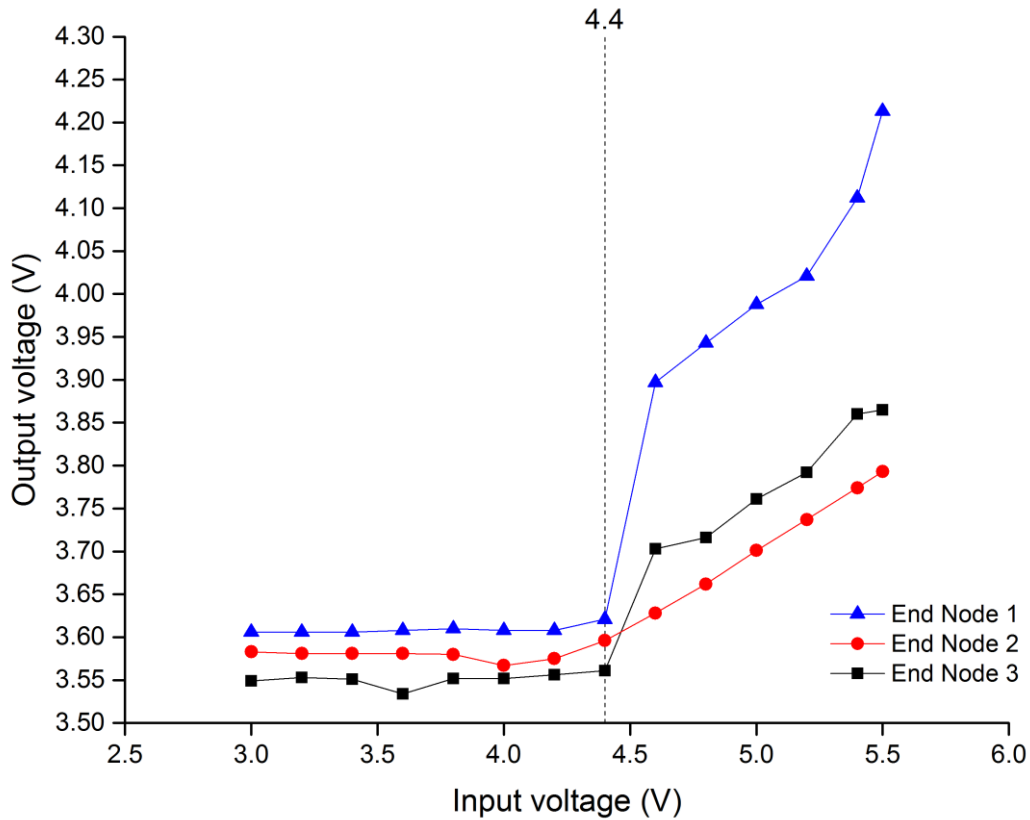
Figure 5.36: Input versus output voltage for the over-voltage protection mechanism

For End Node 1, the input voltage at 4.4 V is already producing an output above 3.61 V, which risked RF instability at its front-end module. However, the results in Section 5.1.2 (f) showed that the RF front-end embedded to End Node 1 has 3.7 V voltage tolerance. Thus, the present setting is deemed safe for End Node 1 although flagged as a potential problem. Nonetheless, this problem can be rectified by adjusting the value of R_{OV1} and R_{OV2} to lower the initial over-voltage protection threshold.

The under-voltage protection is shown in Table 5.18. Unfortunately, the under-voltage protection test did not work in conjunction with a laboratory DC power supply. By default, the BQ25504 will always try to match V_{OV} as long as available power is available. By using the DC power supply, the output will always reach V_{OV} level, as the lower voltage is boosted by the boost converter due to high input current. The real V_{UV} is therefore

recorded by replacing the DC supply with a minimally charged battery where the current is limited.

As a summary, the BQ25504 IC should not be connected to an EH element that supplies beyond 4.4 V to protect the load from over-voltage. Although a simple diode can bring down the voltage, it would in turn inflict power inefficiency to the EH system. Plus, additional circuitry would only complicate the PMU. Table 5.20 defines the overall parameters to ensure safe and stable operation of the H-CDE End Nodes.

Table 5.20: Conditions of the over- and under-voltage protection mechanism

Parameter	Theoretical	Actual		
		End Node 1	End Node 2	End Node 3
Under-voltage (V_{UV})	2.998 V	2.95 V	2.91 V	2.91 V
Over-voltage threshold (V_{OV})	3.610 V	3.607 V	3.578 V	3.570 V
RF stability condition (Section 5.2.2)	<3.60 V	<3.70 V	<3.65 V	<3.65 V
Input voltage causing over-voltage breakdown	-	>4.4 V	>4.4 V	>4.4 V
Voltage when V_{IN} = 4.4 V	3.610 V	3.621 V	3.596 V	3.561 V

5.3.7 Power Efficiency

To the best of knowledge, it is not possible to delve deep into the circuitry of the BQ25504 IC as it is sealed within the QFN package. Thus, the power efficiency of the PMU, as given in equation 4.14, should suffice to evaluate its performance.

The results of the measurement are tabulated in Table 5.21. The calculated power efficiency of the H-CDE End Node is 90.1% which indicates the best case scenario where the power source is at its optimal level. In cloudy day, the solar cell might only provide 17.1

% of power compared to its optimal operation. As a summary, the power efficiency of the H-CDE End Node has been verified in accordance to the standard benchmark from the manufacturer's specification.

Table 5.21: Parameters of the power efficiency experiment

Parameter	Optimal	Non-optimal
V_{IN}	4.4 V	3.46 V
I_{IN} (average)	50.5 mA	10.0 mA
V_{STOR} & V_{BAT} (average)	3.604 V	-
P_{IN}	202.0 mW	34.6 mW
P_{OUT}	182.0 mW	-
Efficiency (eq. 4.14)	90.1 %	-
Relative Efficiency (eq. 4.15)	-	17.1 %

5.3.8 Energy Harvesting Performance in Crowds

The analyses in this section should verify the practical usage of EH in the H-CDE system. This means that the H-CDE End Node could operate well when worn by human beings for an extended time.

5.3.8 (a) Battery Charging

The pattern of the graphs in Figure 5.37 shows that all the End Nodes were able to harvest sufficient energy to increase the capacity of the battery with continuous load usage during the entire 183 minutes of experiment. By the end of the experiment, Router 2 was able to harvest the most energy by charging the battery from 3.4 to 3.55 V. This is followed by End Node 3 (3.52 V), End Node 1 (3.48 V) and End Node 2 (3.47 V). End Node 3, 1 and 2 have 80.0 %, 53.3 % and 46.7 % EH capability respectively compared to Router 2.
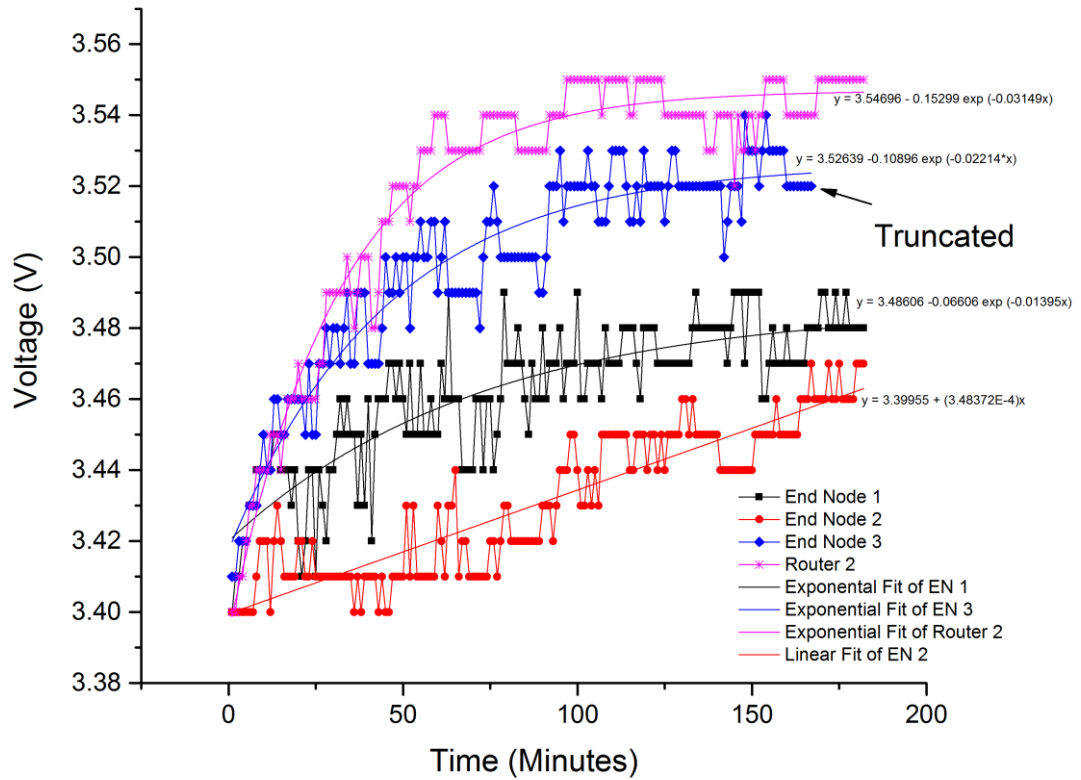
Figure 5.37: Battery voltage of each End Nodes and their corresponding curve fits

End Node 3 suffered from a truncated data log on the 167th minute due to a faulty connection to the SD card. This could not be promptly corrected due to the absence of any output display at the End Node. The curve fits give a mathematical representation of the EH capability that can be used to predict the H-CDE EH performance.

Router 2 was able to harvest the most energy due to its continual exposure to sunlight for 183 minutes (100 % exposure). This is followed accordingly by End Node 3, 1 and 2 based on the length of exposure to sunlight. According to the DOE template, there will always be an End Node that has the highest, medium and lowest exposure to sunlight as the number of receiver involved is varied from one experiment to the other. End Node 3, 1 and 2 have approximately 167 (91.3 % exposure), 120 (65.6 %) and 60 (32.8 %) minutes of direct sunlight exposure respectively.

The battery voltage of all the End Nodes kept fluctuating due to the continual usage of the load and the capacity of energy harvested from the sunlight. The exponential patterns of the graphs reflect the density characteristic of li-ion battery, which has higher density at higher voltage, resulting in longer time to charge the battery to reach upper voltage. Another factor is the weather during data collection, as cumulonimbus clouds were present and light rain occurred intermittently in the final 30 minutes of the experiment. With the least amount of energy harvested, End Node 2 fits a linear curve due to the relatively less frequent exposure to sunlight.

In summary, the results signify that implementing EH is a practical power solution for integration with the H-CDE system. The 80.0 % EH efficiency of End Node 3 compared to Router 2 shows a promising indicator for actual H-CDE application. In comparison with Smartmote (Nanda et al., 2014) which similarly uses a 1 W solar cell, the said system is reported to produce 409 mW, which is only 40.9 % of the total power. Therefore, the proposed EH mechanism may provide an improved design of power management and embedment in H-CDE platform.

5.3.8 (b) Voltage and Current of H-CDE End Nodes

Figure 5.38 (a) and (b) shows the parameters collected by the data loggers in each node respectively. The V_{BAT} at both nodes are the same results as in Figure 5.37. Figure 5.39 illustrates the direction of the current, either from or towards the battery, resulting in a positive or negative value of I_{BAT} respectively seen in Figure 5.38. The maximum V_{IN} and V_{BAT} recorded was 4.6 V for End Node 3 and 130 mA for both nodes respectively. These are in accordance with the specification of the solar cells used.
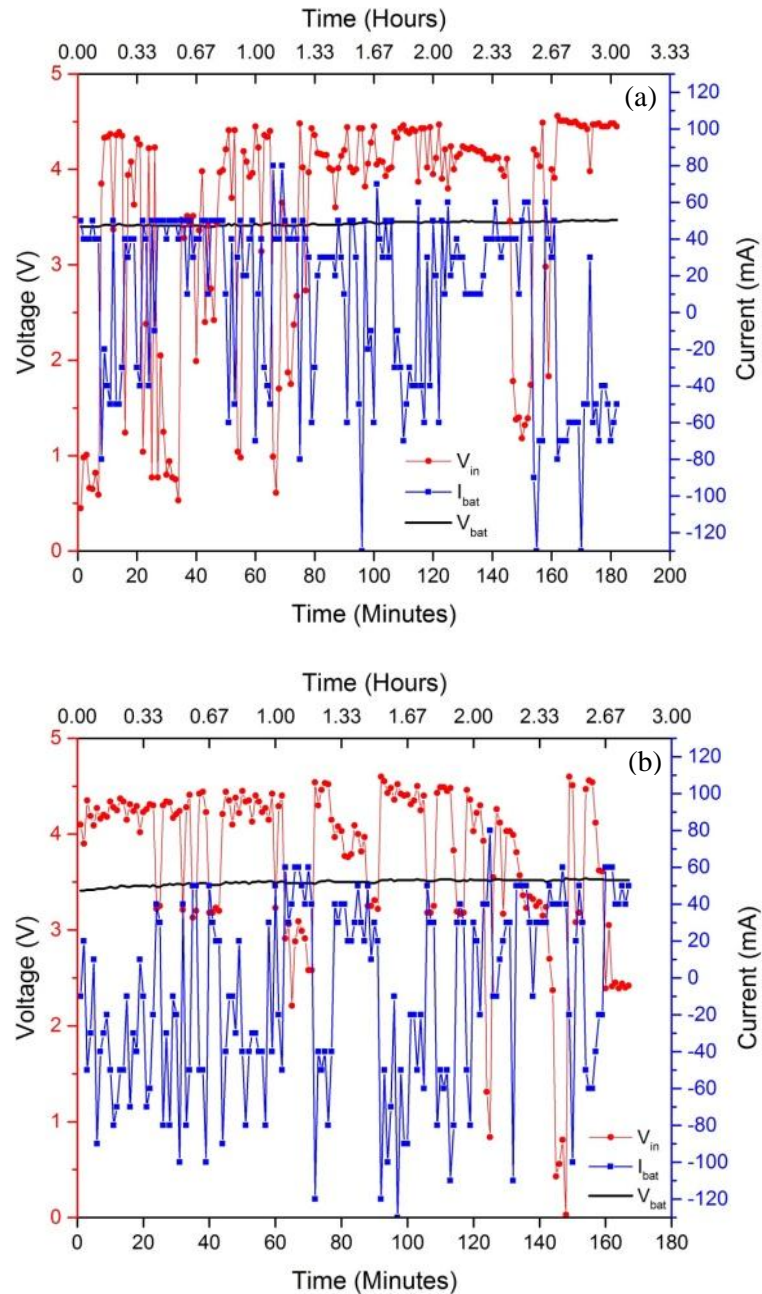
Figure 5.38: Input voltage, V_{IN}, battery voltage, V_{BAT} and battery current flow, I_{BAT} for (a) End Node 2 and (b) End Node 3

The graph for End Node 1 was omitted due to partial data corruption at V_{IN} and I_{BAT}, due to faulty connections from the EH board to the data logger. Preliminary test shows the data logger to be operational as intended prior to the actual test.

Theoretically, the batteries will only be charged when $0.80(V_{IN}) > V_{BAT}$, where 0.80 is set by the MPPT mechanism. This is in accordance with theory where a higher voltage

potential is needed to force current into another voltage potential element. Once this condition is fulfilled, the amount of current injected to the battery depends on the instantaneous current supplied by the PMU. To reflect the graphs, battery charging was in operation when V_{IN} and I_{BAT} were in the positive and negative region respectively.

When the condition is not fulfilled, the load was powered up by the battery. Even with fluctuating V_{IN} and I_{BAT}, the slow but stable increase of V_{BAT} is a proof that the EH mechanism is able to cope with varying input and non-ideal occurrences.
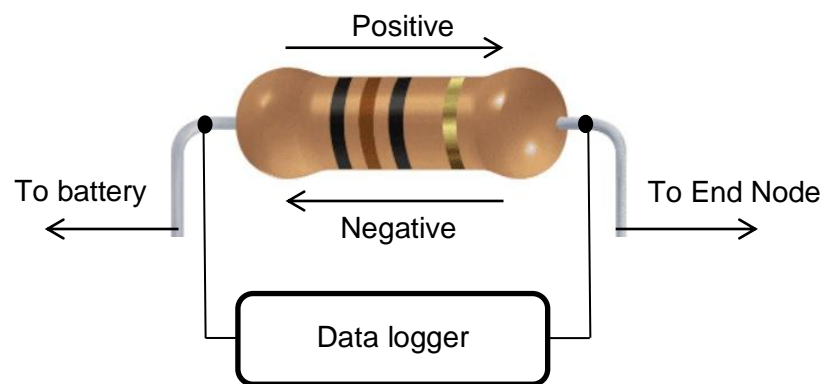
Figure 5.39: The direction of the current flow determines the positive or negative value of the current recorded by the data logger

In summary, the trends of the voltage and current show that the EH boards can concurrently and cooperatively fulfil the load power demand of the H-CDE system from both the battery and solar cell.

5.3.8 (c) Power Output

Figure 5.40 shows the power of each End Node measured between the battery and load, which excludes the power consumed by the load. Assuming that in average the load consumes 148.5 mW, this means that the maximum instantaneous power output of the solar cells are 736.1 mW and 598.3 mW for End Node 3 and End Node 2 respectively. End Node 2 has much less power than End Node 3 in accordance with the requirement of the DOE.

As the solar cells used are graded as 1 W, thus, the solar cells for End Node 2 and 3 reached 73.61 and 59.83 % maximum efficiency. The power loss can be attributed to heat, cable loss, PMU efficiency and non-alignment of the solar cells towards the sun. In summary, the selection of 1 W solar cell is suitable for the application, after considering all the factors that might affect power generation.
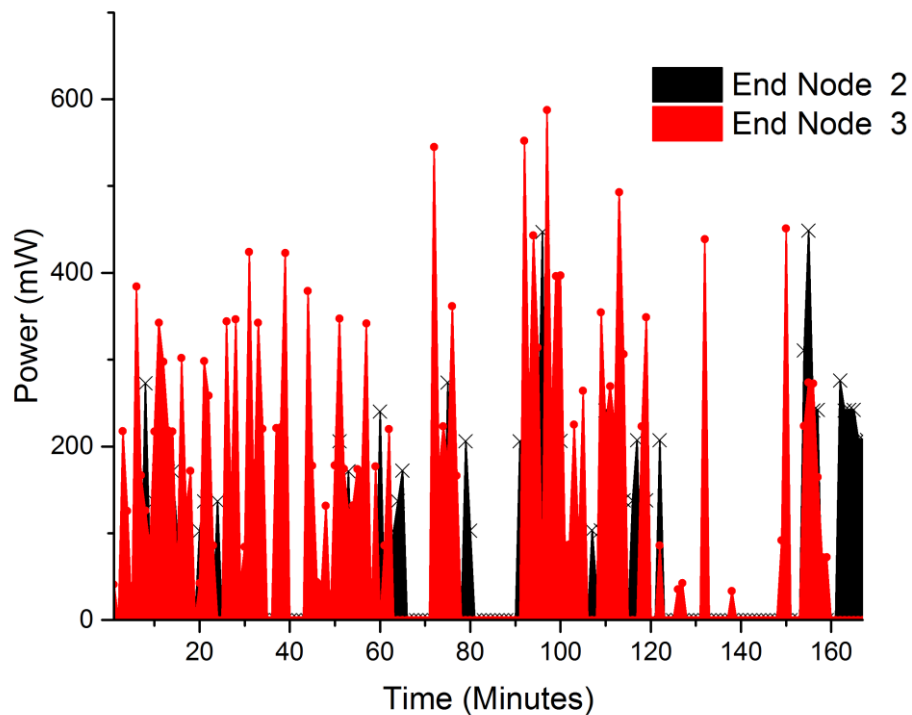
Figure 5.40: Power output approximation of End Node 2 and 3

5.4 Comparison of the Proposed H-CDE System with the Previous Approaches

In the WSN segment, the proposed H-CDE system features real-time monitoring. However, two of its main differences compared to other traditional works are the improvement of wireless monitoring coverage and the self-healing feature. In the former, the H-CDE system provides crowd sensing up to 30 m of range whereas the best direct comparison might be the SCPL system by Xu et al. (2013), which only offers up to 20 m of

range. Whereas the self-healing feature for network auto-recovery was largely left unaddressed by the related works in Table 2.3.

In the H-CDE segment, the proposed H-CDE system offers a new and structured approach in designing and verifying the performance of the system by integrating statistical methods. This contributed to the understanding of the major crowd factors that would directly affect the ability of the system to sense the density of the crowd. This also improved upon the findings of Haochao et al. (2015), Xi et al. (2014) and Arai, Kawamura and Suzuki (2010) in signal attenuation caused by human crowd occlusion. Finally, the proposed H-CDE algorithm provided the highest accuracy in detecting the severity of crowdedness, as opposed to the SCPL, WB and EFE algorithms.

For the EH section, the experiments conducted on the proposed H-CDE system provided validations that the EH mechanism is able to extend the operation of the system. The boosts of the service lifetime of the H-CDE system and its ability to replenish its own energy, made the proposed H-CDE system more complete as a standalone and independent platform compared to the systems designed by Xi et al. (2014), Yuan, Zhao, Qiu and Xi (2013), Haochao et al. (2015) and Mowafi et al. (2013). Furthermore, the safety usage of the system is also discussed. All of these contributed to the knowledge on system design.

In conclusion, the overall embedment of the WSN, EH and H-CDE contributed knowledge relevant to the H-CDE monitoring system. The findings and discussions offered by this study may serve as a guideline for feasible H-CDE system development and framework. The major differences between the proposed H-CDE system with a few relevant works are summarized in Table 5.22.

Table 5.22: Comparison between the proposed H-CDE with selected works. (Colour code: blue for WSN, red for H-CDE and green for EH)

Parameter	Proposed H-CDE	SCPL Xu et al. (2013)	WB Yuan, Zhao, Qiu and Xi (2013)	ZebraNet Zhang, Sadler, Lyon and Matroniso (2004)
WSN Platform	Arduino	C8051	TelosB	MSP430
Protocol / Modulation	ZigBee	MSK	802.15.4	802.15.4
Self-healing	√	ND	ND	X
Deployment range	30 m	20 m	4 m	-
Coverage per node	37.5 m^2	7.1 m^2	9.0 m^2	-
H-CDE	√	√	√	X
Statistical method	ANOVA and DOE	X	X	X
Prediction accuracy	71.2 %	50.0 %	66.9 %	-
Path loss model (error)	0.9 %	-	-	-
EH element	Solar	X	X	Solar
Operational lifetime	Perpetual	15 hours	83 hours	Perpetual

√ = Implemented
X = Not implemented
ND = No data
 - = Irrelevant

5.5   Chapter Summary

The H-CDE system combines the technology of WSN, crowd density and EH in a single platform. To the best of knowledge, it is the first of its kind. The performance analyses are conducted first on the operation of the WSN-RF transmission. The investigations on the latency, throughput, self-healing, wireless coverage, radiation pattern and power

consumption revealed conforming performance of the H-CDE system to the non-embedded standalone system. The success of the design paves way to the improvement of the H-CDE system in terms of functionality and sensing capability.

The One-way ANOVA statistically proved that dynamic and static crowd inflicts almost the same effect on signal attenuation. As a result, the movement of crowd can be equally modelled by a static crowd. Thus, the movement of crowd do not need to be carried out in the DOE test.

The DOE statistically proved that only three crowd factors are important in determining the density level of the crowd. The most significant single factor is the crowd size. The other two important factors are the interaction effects between crowd size with number of receiver and crowd pattern with number of receiver. These three are then inserted into the H-CDE classification algorithm; which is the formulation to determine whether the recorded RSSI is within low, medium or high crowd density level.

The results from the density level estimation experiment show that the proposed H-CDE algorithm produces the best estimation with 71.2 % accuracy. In the path loss test, the H-CDE system also presented the most consistent result with low percentage errors at 0.9 % compared to the actual data.

Finally, the EH section attempts to solve the power problem of the H-CDE on WSN platform. The solar cell alignment, MPPT, power efficiency and range test established the operational condition of the system. The performance of the over- and under-voltage protection mechanism is clarified and guarantees safe operation of the battery and load.

Under ideal sunlight conditions, the EH system can fully charge the battery up to 3.6 V in 5 to 6 hours. Once charged, the H-CDE system can operate continuously for around 33 hours without sunlight. If sunlight is available every day or every 33 hours, then the H-CDE system can operate perpetually for several years without the need of human intervention to

replace the battery. The finalized design parameters of the H-CE system are tabulated in Table 5.23.

Table 5.23: Overall specification of the H-CDE system

Parameter	Performance	Features
Transmit power	Power level 4 @ +10 dBm	Boost mode enabled
Latency	60 ms for router and coordinator 108.44 ms for end node	For single hop
Throughput	1108.56 Bytes per second	9600 baud rate
Self-healing	< 7 seconds @ single hop	Maximum value recorded
Voltage range	Xbee PRO S2B: 2.64 to 3.60 V *H-CDE End Node: 2.910 to 3.596 V	*Based on End Node 2 and 3
Current consumption	H-CDE End Node: 46.5 mA @ minimum : 97.17 mA @ maximum	Based on Xbee PRO S2B and BQ25504 IC
Solar cell	1 W @ 4.4 V and 220 mA	Normal operation
MPPT benefit	Up to 29.8 % more power harvested	Best case
Battery capacity and charging	33 hours of operation without recharging 5 to 6 hours for charging from 3.0 to 3.6 V	2000 mAh rated battery Ideal conditions
Power efficiency	Solar cell to PMU output: 90.1 %	Best case
Operational lifetime	Continuous	6 hours of battery charging required every 33 hours
One-way ANOVA	Dynamic and static crowd statistically inflicts the same signal attenuation	
DOE significant factors	Main: (1) Crowd size Interaction: (2) Crowd size * number of receiver (3) Crowd pattern * number of receiver	The three factors that affect RSSI the most in crowds
H-CDE coverage area	30 m T-R distance 150 m^2 coverage area / 37.5 m^2 per node	Best feature compared to other works
H-CDE algorithm accuracy	Overall: 71.2 %	Best results compared to other models
H-CDE path loss model accuracy	Overall: 0.9 % error	Lowest percentage error compared to other models

CHAPTER SIX
CONCLUSION

6.1 Conclusion

The concept of the H-CDE system stems from the need of better crowd monitoring system. To design the improved system, the crowd properties and its effect on signal attenuation need to be understood. The hardware and software of the system is also designed to match with the objectives of the research. The first objective of improving the sensing capability of the RF-based H-CDE system is achieved by the extension of the wireless coverage while requiring lesser amount of receiver node per area squared without sacrificing the amount of people monitored within the crowd. The experiments and subsequently their results in Section 5.1 were specifically constructed to verify the performance and functionality of the proposed system. The results in Section 5.2 addressed the second objective of improving the crowd density estimation accuracy by the proposed algorithm. The proposed H-CDE algorithm integrates three crowd parameters which have been identified using DOE to be significant in inflicting signal attenuation. With this information, the H-CDE algorithm produces good accuracy in predicting the density level of the crowd for the site under study. The proposed H-CDE algorithm also showed the best crowd prediction accuracy in comparison with the other crowd prediction algorithms from the literature. Sections 5.3 verified the performance of the EH mechanism, which aims to extend the service life span of the system (objective three). In a single day with good sunlight availability, the H-CDE End Node could charge the battery and power up the RF module simultaneously without downtime. The H-CDE EH mechanism could continue to replenish its energy independently and therefore operate continuously for several years without human intervention. Ultimately, an H-CDE system motivates enhancements in crowd security using RF-based technology as it may save lives. Hopefully, the design and findings of the H-CDE

system could be beneficial to the body of knowledge and offer better understanding of the human crowd and also prolonging the operation of the system.

6.2   Suggestions for Future Work

The H-CDE system can be significantly improved by increasing the detection of higher number of people within the crowd. This is challenging, as the current 2.4 GHz is not capable of sensing a large number of body due to its regulation for low-power usage. A potential solution is by switching to 868 MHz (Europe) or 915 MHz (USA) frequency. However, the transmission power needs to be carefully planned as to avoid hazardous effect on human beings. For example, the 900 MHz band used in Europe and most Asian countries for GSM technology could cover a distance of up to 30 km but requires between a few to a hundred Watts of transmission power. The guidelines set by the International Commission on Non-Ionizing Radiation Protection (ICNIRP) should be consulted if a high powered transceiver is to be used in close proximity to human beings.

Another suggestion is to make the H-CDE system available as a mobile application that works on the Internet of Things (IoT) platform. This makes the system accessible to the masses. However, the main concern with IoT remains in the security department where intrusion and denial of service are still a real threat. The security issues should therefore be addressed appropriately.

For fixed WSN deployment, the solar cell and battery could be replaced with better ones to extend further the operation of the system. However, this would require a different type of PMU, as BQ25504 is no longer suitable to meet the demands of a higher-powered system.

The practical use of RF-based crowd density estimation system is still limited. Thus, more research should be conducted by the scientific community to make the system more

accessible in real applications. Technology makes life better and as the saying goes; the ball should keep on rolling.

REFERENCES

Abdulla, R. (2011). *Design and Implementation of Active RFID System in Multi-hop Wireless Sensor Network.* Universiti Sains Malaysia. 170-176.

Aguirre, E., Arpon, J., Azpilicueta, L., De Miguel Bilbao, S., Ramos, V., & Falcone, F. J. (2012). Evaluation Of Electromagnetic Dosimetry Of Wireless Systems In Complex Indoor Scenarios With Human Body Interaction. *Progress In Electromagnetics Research B, 43*, 189-209.

Aguirre, J. A., Gaviria, N., & Aedo, J. E. (2009). *Data Collection And Signal Processing Strategy For Low Power Consumption In Wireless Sensor Networks Nodes.* Paper presented at LATINCOM '09 IEEE Latin-American Conference on Communications, 2009, 3-4.

Alippi, C., & Galperti, C. (2008). An Adaptive System for Optimal Solar Energy Harvesting in Wireless Sensor Network Nodes. *Circuits and Systems I: Regular Papers, IEEE Transactions on, 55*(6), 1743-1747.

Amaro, J. P., Ferreira, F. J. T. E., Cortesao, R., & Landeck, J. (2012). *Energy harvesting for Zigbee compliant Wireless Sensor Network nodes.* Paper presented at the IECON 2012 - 38th Annual Conference on IEEE Industrial Electronics Society, 2585-2587.

Angrisani, L., Moriello, R. S. L., D' Apuzzo, M. & D' Arco, M. (2011). *Design Of Experiments For Power Measurement Method In Wireless Communications Systems*. Paper presented at 2011 IEEE Instrumentation and Measurement Technology Conference (I2MTC), 1-6.

Arai, M., Kawamura, H., & Suzuki, K. (2010). *Estimation Of Zigbee's RSSI Fluctuated By Crowd Behavior In Indoor Space.* Proceedings of paper presented at the SICE Annual Conference, 696-701.

Ardito, L., Procaccianti, G., Torchiano, M., & Migliore, G. (2013). *Profiling Power Consumption on Mobile Devices*. Paper presented at the The Third International Conference on Smart Grids, Green Communications and IT Energy-aware Technologies, 101-106.

Bahl, P., & Padmanabhan, V. N. (2000). *RADAR: An In-Building RF-Based User Location And Tracking System.* Paper presented at the INFOCOM 2000 Nineteenth Annual Joint Conference of the IEEE Computer and Communications Societies, 775-784.

Blanke, U., Troster, G., Franke, T., & Lukowicz, P. (2014). *Capturing Crowd Dynamics At Large Scale Events Using Participatory GPS-Localization.* Paper presented at the IEEE Ninth International Conference on Intelligent Sensors, Sensor Networks and Information Processing (ISSNIP), 1-7.

Bol, D., De Vos, J., Hocquet, C., Botman, F., Durvaux, F., Boyd, S., Flandre, D. & Legat, J. (2013). SleepWalker: A 25-MHz 0.4-V Sub-MM Microcontroller in 65-nm LP/GP CMOS for Low-Carbon Wireless Sensor Nodes. *IEEE Journal of Solid-State Circuits, 48*(1), 20-32.

Burke, J., Estrin, D., Hansen, M., Parker, A., Ramanathan, N., Reddy, S., & Srivastava, M. B. (2006). *Participatory Sensing*. Paper presented at the Proceedings of the International Workshop on World-Sensor-Web (WSW), 10-15.

Cadex. (n.d.). Types of Lithium-ion. Retrieved from http://batteryuniversity.com/learn/article/types_of_lithium_ion

Campbell, A. T., Eisenman, S. B., Lane, N. D., Miluzzo, E., Peterson, R. A., Hong, L. & Gahng-Seop, A. (2008). The Rise of People-Centric Sensing. *IEEE Internet Computing, 12*(4), 12-21.

Chen, Y. S., Chen, S. Y. & Li, H. J. (2011). *Design And Optimization Of A Dual-Antenna Structure For Passive RFID Tags Using Design Of Experiments Technique*. Paper presented at 2011 IEEE International Symposium on Antennas and Propagation (APSURSI), 2906-2908.

Chong, J. W., Hwang, H. Y., Jung, C. Y., & Sung, D. K. (2007). *Analysis of Throughput and Energy Consumption in a ZigBee Network Under the Presence of Bluetooth Interference*. Paper presented at the IEEE Global Telecommunications Conference (GLOBECOM '07), 4749-4753.

Chulsung, P., & Chou, P. H. (2006). *AmbiMax: Autonomous Energy Harvesting Platform for Multi-Supply Wireless Sensor Nodes*. Paper presented at the 3rd Annual IEEE Communications Society on Sensor and Ad Hoc Communications and Networks (SECON '06), 168-177.

Cypress Semiconductor (2014). 2.4 GHz CyFI Transceiver. Retrieved from https://upverter.com/datasheet/77f9b7f43cf8e166e9c475fdb1d2d16ecb8e93bb.pdf

De Vita, P. (2012). Antenna Selection Guidelines. Retrieved from http://www2.st.com/content/ccc/resource/technical/document/application_note/82/38/3f/9f/fd/4d/4f/ab/DM00068254.pdf/files/DM00068254.pdf/jcr:content/translations/en.DM00068254.pdf

Depatla, S., Muralidharan, A., & Mostofi, Y. (2015). Occupancy Estimation Using Only WiFi Power Measurements. *IEEE Journal on Selected Areas in Communications, 33*(7), 1381-1393.

Dian, Z., Jian, M., Quanbin, C., & Ni, L. M. (2007). *An RF-Based System for Tracking Transceiver-Free Objects*. Paper presented at the Fifth Annual IEEE International Conference on Pervasive Computing and Communications (PerCom '07), 135-144.

Digi, I. Sending data through an 802.15.4 network latency timing. (n. d.).   Retrieved from http://knowledge.digi.com/articles/Knowledge_Base_Article/Sending-data-through-an-802-15-4-network-latency-timing

Digi International (2008). Wireless Mesh Networking: ZigBee versus DigiMesh. Retrieved from www.digi.com/pdf/wp_zigbeevsdigimesh.pdf

Digi International (2015). ZigBee RF Modules. Retrieved from http://www.mouser.com/ds/2/111/90002002_T-752925.pdf

Ding, R., Hou, J. & Xing, B. (2013). *Research of Wireless Sensor Network Nodes Based on Ambient Energy Harvesting.* Paper presented at the 6th International Conference on Intelligent Networks and Intelligent Systems (ICINIS), 286-288.

Ferro, E., Brea, V. M., Cabello, D., Lopez, P., Iglesias, J., & Castillejo, J. (2014). *Wireless Sensor Mote For Snail Pest Detection.* Paper presented at 2014 IEEE SENSORS, 114-117.

Glatz, P. M., Meyer, P., Janek, A., Trathnigg, T., Steger, C., & Weiss, R. (2008). *A Measurement Platform For Energy Harvesting And Software Characterization In WSNs.* Paper presented at the 1st IFIP Wireless Days, 1-5.

Gomaa, R., Adly, I., Sharshar, K., Safwat, A., & Ragai, H. (2013). *Zigbee Wireless Sensor Network For Radiation Monitoring At Nuclear Facilities.* Paper presented at the 6th Joint IFIP Wireless and Mobile Networking Conference (WMNC), 1-4.

Gungor, V. C., & Hancke, G. P. (2009). Industrial Wireless Sensor Networks: Challenges, Design Principles, and Technical Approaches. *IEEE Transactions on Industrial Electronics, 56*(10), 4258-4265.

Haochao, L., Chan, E. C. L., Xiaonan, G., Jiang, X., Kaishun, W., & Ni, L. M. (2015). Wi-Counter: Smartphone-Based People Counter Using Crowdsourced Wi-Fi Signal Data. *IEEE Transactions on Human-Machine Systems, 45*(4), 442-452.

IEEE. (2006). Approved IEEE Draft Revision for IEEE Standard for Information Technology-Telecommunications and Information Exchange Between Systems-Local and Metropolitan Area Networks-Specific Requirements-Part 15.4B: Wireless Medium Access Control (MAC) and Physical Layer (PHY) Specifications for Low Rate Wireless Personal Area Networks (WPANs) (Amendment of IEEE Std 802.15.4-2003). *IEEE Std P802.15.4/D6*, 1.

Javaid, N., Yaqoob, M., Khan, M Y, Khan, M. A., Javaid, A. ve Z.A. Khan. (2013). Analyzing Delay in Wireless Multi-hop Heterogeneous Body Area Networks. Maxwell Science Publication, 1-16.

Katabira, K., Huijing, Z., Nakagawa, Y., & Shibasaki, R. (2008). *Real-Time Monitoring of People Flows and Indoor Temperature Distribution for Advanced Air-Conditioning*

Control. Paper presented at the 11th International IEEE Conference on Intelligent Transportation Systems, 664-668.

Kim, H. S., Kang, S. M., Park, K. J., Baek, C. W., & Park, J. S. (2009). Power Management Circuit For Wireless Ubiquitous Sensor Nodes Powered By Scavenged Energy. *Electronics Letters, 45*(7), 373-374.

Litvinski, O., & Gherbi, A. (2013). *Openstack Scheduler Evaluation Using Design Of Experiment Approach.* Paper presented at the IEEE 16th International Symposium on Object/Component/Service-Oriented Real-Time Distributed Computing (ISORC), 1-7.

Liu, X.-L., Chen, Y.-g., Jing, X.-r., & Chen, Y.-W. (2010). *Design of Experiment Method for Microsatellite System Simulation and Optimization.* Paper presented at the International Conference on Computational and Information Sciences (ICCIS), 1200-1203.

Luo, R. C., & Chen, O. (2012). Mobile Sensor Node Deployment and Asynchronous Power Management for Wireless Sensor Networks. *IEEE Transactions on Industrial Electronics, 59*(5), 2377-2385.

Mayalarp, V., Limpaswadpaisarn, N., Poombansao, T., & Kittipiyakul, S. (2010). *Wireless Mesh Networking With Xbee.* Paper presented at the 2nd ECTI-Conference on Application Research and Development (ECTI-CARD 2010), 1-5.

Meli, G. C. R. (2013). *Electromagnetic Absorption by the Human Body from 1 to 15 GHz.* The University of York, 11-18.

MEMSIC. (2011). TelosB. Retrieved from http://www.memsic.com/userfiles/files /Datasheets/WSN/telosb_datasheet.pdf

Mikhaylov, K., & Tervonen, J. (2010). *Optimization Of Microcontroller Hardware Parameters For Wireless Sensor Network Node Power Consumption And Lifetime Improvement.* Paper presented at the International Congress on Ultra Modern Telecommunications and Control Systems and Workshops (ICUMT), 115-1156.

Minami, M., Morito, T., Morikawa, H., & Aoyama, T. (2005). *Solar biscuit: A Battery-less Wireless Sensor Network System for Environmental Monitoring Applications.* Paper presented at the 2nd International Workshop on Networked Sensing Systems, 1-6.

Minitab. (2012). One-way ANOVA (Version 16).

Montgomery, D. C. (2009). *Design and Analysis of Experiments* (7th ed.): Wiley & Sons Ltd., 174-175.

Morrison, A., Bell, M., & Chalmers, M. (2009). *Visualisation of Spectator Activity at Stadium Events.* Paper presented at the 13th International Conference Information Visualisation, 219-226.

Mowafi, Y., Zmily, A., Abou-Tair, D. E. D. I., & Abu-Saymeh, D. (2013). *Tracking Human Mobility At Mass Gathering Events Using WISP.* Paper presented at the Second International Conference on Future Generation Communication Technology (FGCT), 157-162.

Musiani, D., Lin, K., & Rosing, T. S. (2007). *Active Sensing Platform for Wireless Structural Health Monitoring.* Paper presented at the 6th International Symposium on Information Processing in Sensor Networks, 390-399.

Nakatsuka, M., Iwatani, H., & Katto, J. (2008). *A Study on Passive Crowd Density Estimation using Wireless Sensors.* Paper presented at the The Fourth International Conference on Mobile Computing and Ubiquitous Networking (ICMU 2008), 1-6.

Nanda, K., Babu, H., Selvakumar, D., Dwarakanath, T., Nayak, K. & Venkatesh (2014). *Smartmote - An innovative autonomous Wireless Sensor Node architecture.* Paper presented at IEEE International Conference on Electronics, Computing and Communication Technologies (IEEE CONECCT 2014), 1-6.

Naveen, K. V., & Manjunath, S. S. (2011). *A Reliable Ultracapacitor Based Solar Energy Harvesting System For Wireless Sensor Network Enabled Intelligent Buildings.* Paper presented at the 2nd International Conference on Intelligent Agent and Multi-Agent Systems (IAMA), 20-25.

Niyato, D., Hossain, E., Rashid, M. M., & Bhargava, V. K. (2007). Wireless sensor networks with energy harvesting technologies: a game-theoretic approach to optimal energy management. *IEEE Wireless Communications, 14*(4), 90-96.

Nordic Semiconductor (2007). nRF24L01 Single Chip 2.4 GHz Transceiver.

O'Neill, E., Kostakos, V., Kindberg, T., Fatah gen. Schiek, A., Penn, A., Stanton Fraser, D., & Jones, T. (2006). *Instrumenting The City: Developing Methods For Observing And Understanding The Digital Cityscape*, Springer, 315-332.

Paradiso, J. A., & Starner, T. (2005). Energy Scavenging For Mobile And Wireless Electronics. *IEEE Pervasive Computing, 4*(1), 18-27.

Patwari, N., & Wilson, J. (2010). RF Sensor Networks for Device-Free Localization: Measurements, Models, and Algorithms. *Proceedings of the IEEE, 98*(11), 1961-1973.

Petrova, M., Lili, W., Mahonen, P., & Riihijarvi, J. (2007). *Interference Measurements on Performance Degradation between Colocated IEEE 802.11g/n and IEEE 802.15.4 Networks.* Paper presented at the Sixth International Conference on Networking, 1-6.

Piyare, R., & Lee, S. (2013). Performance Analysis of XBee ZB Module Based Wireless Sensor Networks. *International Journal of Scientific & Engineering Research, 4*(4), 1615-1621.

Poole, I. (n.d.). Bluetooth radio interface, modulation, & channels. Retrieved from http://www.radio-electronics.com/info/wireless/bluetooth/radio-interface-modulation.php

Raghunathan, V., Kansal, A., Hsu, J., Friedman, J., & Srivastava, M. B. (2005). *Design Considerations For Solar Energy Harvesting Wireless Embedded Systems.* Paper presented at the Fourth International Symposium on Information Processing in Sensor Networks (IPSN), 457-462.

Rai, S., Lataye, D. H., Chaddha, M. J., Mishra, R. S., Mahendiran, P., Mukhopadhyay, J., Wasewar, K. L. (2013). An Alternative to Clay in Building Materials: Red Mud Sintering Using Fly Ash via Taguchi's Methodology. Advances in Materials Science and Engineering, 2013, 1-7.

Ramos, A., Girbau, D., Lazaro, A., Collado, A. & Georgiadis, A. (2015). Solar-Powered Wireless Temperature Sensor Based on UWB RFID With Self-Calibration. *IEEE Sensors Journal.* Vol 15 (7), 3764-3772.

Randolph, G., & Hirsch, N. (2010). PIC32MX: XBee Wireless Round-trip Latency. Retrieved from http://hades.mech.northwestern.edu/index.php/PIC32MX:_XBee_Wireless_Round-trip_Latency#Overview

Reusens, E., Joseph, W., Latre, B., Braem, B., Vermeeren, G., Tanghe, E. & Blondia, C. (2009). Characterization of On-Body Communication Channel and Energy Efficient Topology Design for Wireless Body Area Networks. *IEEE Transactions on Information Technology in Biomedicine, , 13*(6), 933-945.

Rihan, M., El-Khamy, M., & El-Sharkawy, M. (2012). *On ZigBee Coexistence in the ISM band: Measurements and Simulations.* Paper presented at the International Conference on Wireless Communications in Unusual and Confined Areas (ICWCUCA), 1-6.

Robomart.com. (n.d.). Arduino Uno R3 Board. Retrieved from https://www.robomart.com/arduino-uno-online-india

Sarvghadi, M. A., & Tat-Chee, W. (2013). *An Experimental Methodology For Evaluation Of Multi-Hop Medium Access Control Protocols Of Wireless Sensor Networks.* Paper presented at the IEEE International Conference on RFID-Technologies and Applications (RFID-TA), 1-6.

Schmid, J., Gaedeke, T., Scheibe, T. & Stork, W. (2012). *Improving Energy Efficiency for Small-Scale Solar Energy Harvesting.* Proceedings of 2012 European Conference on Smart Objects, Systems and Technologies (SmartSysTech), 1-9.

Seidel, S. Y., & Rappaport, T. S. (1992). 914 MHz Path Loss Prediction Models for Indoor Wireless Communications in Multifloored Buildings. *IEEE Transactions on Antennas and Propagation, 40*(2), 207-217.

Simjee, F., & Chou, P. H. (2006). *Everlast: Long-life, Supercapacitor-operated Wireless Sensor Node.* Proceedings of the International Symposium on Low Power Electronics and Design, 197-202.

Simjee, F. I., & Chou, P. H. (2008). Efficient Charging of Supercapacitors for Extended Lifetime of Wireless Sensor Nodes. *IEEE Transactions on Power Electronics, 23*(3), 1526-1536.

SKMM (2007). Technical Specification for GSM Mobile Terminals. Retrieved from http://www.skmm.gov.my/skmmgovmy/files/attachments/WTS_GSM_ MT.pdf

Somov, A., Minakov, I., Simalatsar, A., Fontana, G., & Passerone, R. (2009). *A Methodology For Power Consumption Evaluation Of Wireless Sensor Networks.* Paper presented at the IEEE Conference on Emerging Technologies & Factory Automation, 1-8.

Still, G. K. (2000). *Crowd Dynamics.* University of Warwick, 1-30.

Stofka, M. (2013). DC-DC converter starts up and operates from a single photocell. Retrieved from http://www.edn.com/design/power-management/4410364/DC-DC-converter-starts-up-and-operates-from-a-single-photocell-

Sultanul Kabir, A. F. M., Shorif, M. A., Hua, L., & Qian, Y. (2014). *A Study Of Secured Wireless Sensor Networks With Xbee And Arduino.* Paper presented at the 2nd International Conference on Systems and Informatics (ICSAI), 492-496.

Taneja, J., Jaein, J., & Culler, D. (2008). *Design, Modeling, and Capacity Planning for Micro-solar Power Sensor Networks.* Paper presented at the International Conference on Information Processing in Sensor Networks, 407-418.

Texas Instruments. (2009). CC1000 Single Chip Very Low Power RF Transceiver. Retrieved from www.ti.com/lit/pdf/swrs048

Texas Instruments. (2012). Ultra Low Power Boost Converter with Battery Management for Energy Harvester Applications. Retrieved from www.ti.com/lit/ds/symlink/bq25504.pdf

Texas Instruments. (2013a). 2.4 GHz Bluetooth Low Energy System-on-Chip. Retrieved from www.ti.com/lit/ds/symlink/cc2540.pdf

Texas Istruments. (2013b). Measuring Efficiency of the bq25504 Energy Harvesting Battery Charger. Retrieved from http://www.mouser.com/pdfDocs/TI-Measuring-Efficiency-of-the-bq25504-Energy-Harvesting-Battery-Charger.pdf

Titirsha, T., Siddique, A. R. M., Afrin, F., Sanjidah, S., & Rabbani, A. (2014). *Introducing Dual Axis Solar Tracker With Reflector To Increase Optimal Electricity Generation In Bangladesh.* Paper presented at the 3rd International Conference on the Developments in Renewable Energy Technology (ICDRET), 1-6.

Versichele, M., Neutens, T., Delafontaine, M., & Van de Weghe, N. (2012). The Use Of Bluetooth For Analysing Spatiotemporal Dynamics Of Human Movement At Mass Events: A Case Study Of The Ghent Festivities. *Applied Geography, 32*(2), 208-220.

Versichele, M. N., T.; Goudeseune, S.; van Bossche, F.; Van de Weghe, N. (2012). Mobile Mapping of Sporting Event Spectators Using Bluetooth Sensors: Tour of Flanders 2011. *Sensors, 12*(10), 14196-14213.

Vullers, R. J. M., Schaijk, R. V., Visser, H. J., Penders, J., & Hoof, C. V. (2010). Energy Harvesting for Autonomous Wireless Sensor Networks. *IEEE Solid-State Circuits Magazine, 2*(2), 29-38.

Vunabandi, V., Matsunaga, R., Markon, S., & Willy, N. (2015). *Flood Sensing Framework By Arduino And Wireless Sensor Network In Rural-Rwanda.* Paper presented at the 16th IEEE/ACIS International Conference on Software Engineering, Artificial Intelligence, Networking and Parallel/Distributed Computing (SNPD), 1-6.

Wan, Z. G., Tan, Y. K., & Yuen, C. (2011). *Review On Energy Harvesting And Energy Management For Sustainable Wireless Sensor Networks.* Paper presented at the IEEE 13th International Conference on Communication Technology (ICCT), 362-367.

Weppner, J., & Lukowicz, P. (2013). Bluetooth Based Collaborative Crowd Density Estimation with Mobile Phones. *2013 IEEE International Conference on Pervasive Computing and Communications (Percom)*, 193-200.

Weppner, J., Lukowicz, P., Blanke, U., & Troster, G. (2014). Participatory Bluetooth Scans Serving as Urban Crowd Probes. *IEEE Sensors Journal, 14*(12), 4196-4206.

Xi, W., Zhao, J., Li, X.-Y., Zhao, K., Tang, S., Liu, X., & Jiang, Z. (2014). *Electronic Frog Eye: Counting Crowd Using Wifi.* Paper presented at the IEEE Proceedings of INFOCOM, 361-369.

Xiaofan, J., Polastre, J., & Culler, D. (2005). *Perpetual Environmentally Powered Sensor Networks.* Paper presented at the Fourth International Symposium on Information Processing in Sensor Networks, 463-468.

Xu, C., Firner, B., Moore, R. S., Zhang, Y., Trappe, W., Howard, R., & An, N. (2013). *SCPL: Indoor Device-Free Multi-Subject Counting And Localization Using Radio Signal Strength.* Paper presented at the Proceedings of the 12th International Conference On Information Processing In Sensor Networks, 79-90.

Ya'acob, M. E., Hizam, H., Radzi, M. A. M., & Kadir, M. Z. A. A. (2013). Field Measurement of PV Array Temperature for Tracking and Concentrating 1 k Generators Installed in Malaysia. International Journal of Photoenergy, 2013, 1-8.

Younis, S. A., El-Azab, W. I., El-Gendy, N. S., Aziz, S. Q., Moustafa, Y. M., Aziz, H. A., & Amr, S. S. A. (2014). Application of Response Surface Methodology to Enhance

Phenol Removal from Refinery Wastewater by Microwave Process. *International Journal of Microwave Science and Technology, 2014*, 1-12.

Yu, C. (2013). *Mathematical Modelling of End-to-End Packet Delay in Multi-hop Wireless Networks and their Applications to QoS Provisioning.* (PhD), University College London, 1-159.

Yuan, Y. (2014). *Crowd Monitoring Using Mobile Phones.* Paper presented at the Sixth International Conference on Intelligent Human-Machine Systems and Cybernetics (IHMSC), 261-264.

Yuan, Y., Qiu, C., Xi, W., & Zhao, J. (2011). *Crowd Density Estimation Using Wireless Sensor Networks.* Paper presented at the Seventh International Conference on Mobile Ad-hoc and Sensor Networks (MSN), 138-145.

Yuan, Y., Zhao, J. Z., Qiu, C., & Xi, W. (2013). Estimating Crowd Density in an RF-Based Dynamic Environment. *IEEE Sensors Journal, 13*(10), 3837-3845.

Zanal, F. H. M., & Ismail, W. (2013). *Motion Sensitive RFID In Wireless Sensor Network Platform.* Paper presented at the IEEE International Conference on RFID-Technologies and Applications (RFID-TA), 1-5.

Zhang, P., Sadler, C. M., Lyon, S. A., & Martonosi, M. (2004). *Hardware Design Experiences In Zebranet.* Paper presented at the Proceedings Of The 2nd International Conference On Embedded Networked Sensor Systems, 227-238.

Zhao, J., Xi, W., He, Y., Liu, Y., Li, X.-Y., Mo, L., & Yang, Z. (2013). Localization of Wireless Sensor Networks in the Wild: Pursuit of Ranging Quality. *Networking, IEEE/ACM Transactions on, 21*(1), 311-323.

<div align="center">**APPENDICES**</div>

Appendix A: Planck-Einstein Relation

$$E = hv$$

where E is the energy of a photon, h is the Planck constant and v is the frequency. In quantum mechanics, a photon is the basic unit of energy that moves at the speed of light in a vacuum.

Appendix B: Quantum Field Theory

Quantum field theory (QFT) is a set of theories aiming to explain the basic constituents of the world and their interactions. QFT is heavily mathematical driven and is a very important scientific advancement in understanding how the world works.

For example, it is theorized in the Standard Model that the mass of matter itself comes from quarks and gluons; these are elementary and sub-atomic particles. To complicate things even more, the mass of quarks and gluons are actually predicted to be derived from the Higgs boson. The Higgs boson is the current subject of study at the Large Hadron Collider in Switzerland. To date, the Higgs boson is still a mystery unsolved.

Classical physics cannot be separated from QFT. However, QFT has made obsolete a number of classical physics models. For example, the ever-famous Bohr's atom model is inaccurate (Figure 79). Here, the electron is depicted as single discrete spherical particle orbiting the nucleus. Whereas QFT has proven that the electron takes the form of 'cloud' around the nucleus. Electrons are not single spherical entities but exhibit wave-particle duality. This duality meant that electron has both particle and wave properties at the same time, and thus the 'cloud-like' property.
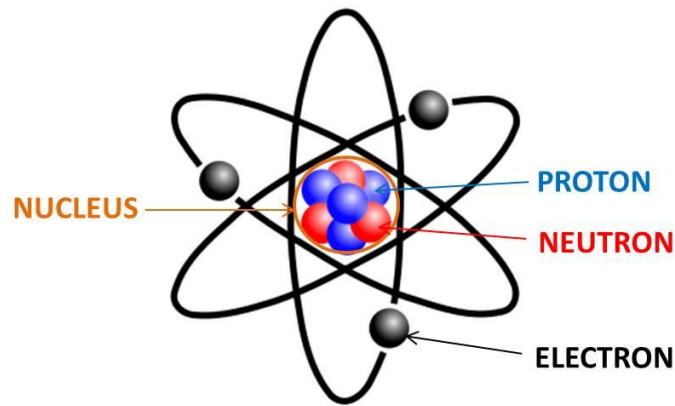
Figure A: Bohr's model also known as the Rutherford–Bohr model. Image by Indolences.

Appendix C: Capacitor versus Battery (Density)

$$Q = CV$$

where Q is the charge of the capacitor in Coulombs, C is the capacity in Farad and V is the voltage.

$$Q = It$$

where I is the current in Ampere and t is time in seconds.

Using the above equations, a supercapacitor rated at 2.3 V and 50 F connected to a load consuming 55 mA will be able to supply power for 34 minutes and 51 seconds. This is almost equivalent to a 32 mAh battery which is an extremely low capacity for a battery.

Appendix D: BQ25504 Power Management Unit

Figure B shows the layout of the BQ25504 PMU IC and Table E lists the description of each pin.
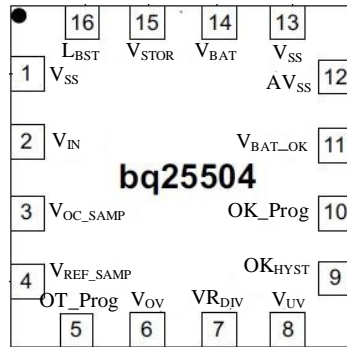
Figure B: IC layout of the BQ25504 IC. The IC is in a QFN-16 package with a 3 x 3 mm dimension.

Table A: Pin description of the BQ25504 IC

Pin number	Pin name	Description
1	V_{SS}	Ground
2	V_{IN}	DC voltage input from EH element
3	V_{OC_SAMP}	Sampling pin for MPPT
4	V_{REF_SAMP}	The holding pin for V_{OC_SAMP}
5	OT_Prog	Digital programming pin for over-temperature threshold
6	V_{OV}	Over-voltage programming pin
7	VR_{DIV}	Voltage resistor bias pin
8	V_{UV}	Under-voltage programming pin
9	OK_{HYST}	V_{BAT_OK} hysteresis threshold
10	OK_Prog	V_{BAT_OK} threshold
11	V_{BAT_OK}	Digital battery good indicator
12	AV_{SS}	Ground
13	V_{SS}	Ground
14	V_{BAT}	Connection for storage element
15	V_{STOR}	Output of PMU
16	L_{BST}	Inductor connection for boost converter switching

Appendix E: ZigBee PHY and MAC layer frame

Table B: 802.15.4 PHY layer frame

Preamble	Start of packet delimiter	PHY header	PHY service data unit (PSDU)
4 bytes	1 byte	1 byte	≤ 127 bytes

As the PHY layer frame gets encapsulated by more protocol sub-frames in each layer, the size of the payload decreases as it goes up to the APS layer. For example, 6 bytes are reserved for PHY layer protocols, leaving at most only 127 bytes for MAC layer payload.

Table C: 802.15.4 MAC layer data frame

Frame Control	Sequence number	Addressing fields	Data payload	Frame check sequence
2 bytes	1 byte	4 or 20 bytes	≤ 102 bytes	2 bytes
PSDU				

Appendix F: ZigBee Network layer and APS data frame

Table D: ZigBee Network layer general frame

Frame control	Addressing		Radius	Sequence number	IEEE Addressing		Multicast control	Source route	Payload
2 bytes	2 bytes	2 bytes	1 byte	1 byte	≤ 8 bytes	≤ 8 bytes	≤ 1 byte	Variable	Variable
≤ 102 bytes									

Table E: ZigBee APS data frame

Frame control	Addressing	APS counter	Payload
1 byte	≤ 8 bytes	1 byte	Variable
≤ 94 bytes			

Appendix G: Arduino UNO

The Arduino UNO (shown in Figure C) has 14 digital input and output pins including 6 PWM outputs, 6 analog pins, an ICSP header, USB connection and a DC power jack. The Atmega328p microcontroller works at 16 MHz speed, 5 V operating voltage and has 32 KB flash memory. These specifications make it suitable for the H-CDE system and also as the data logger.
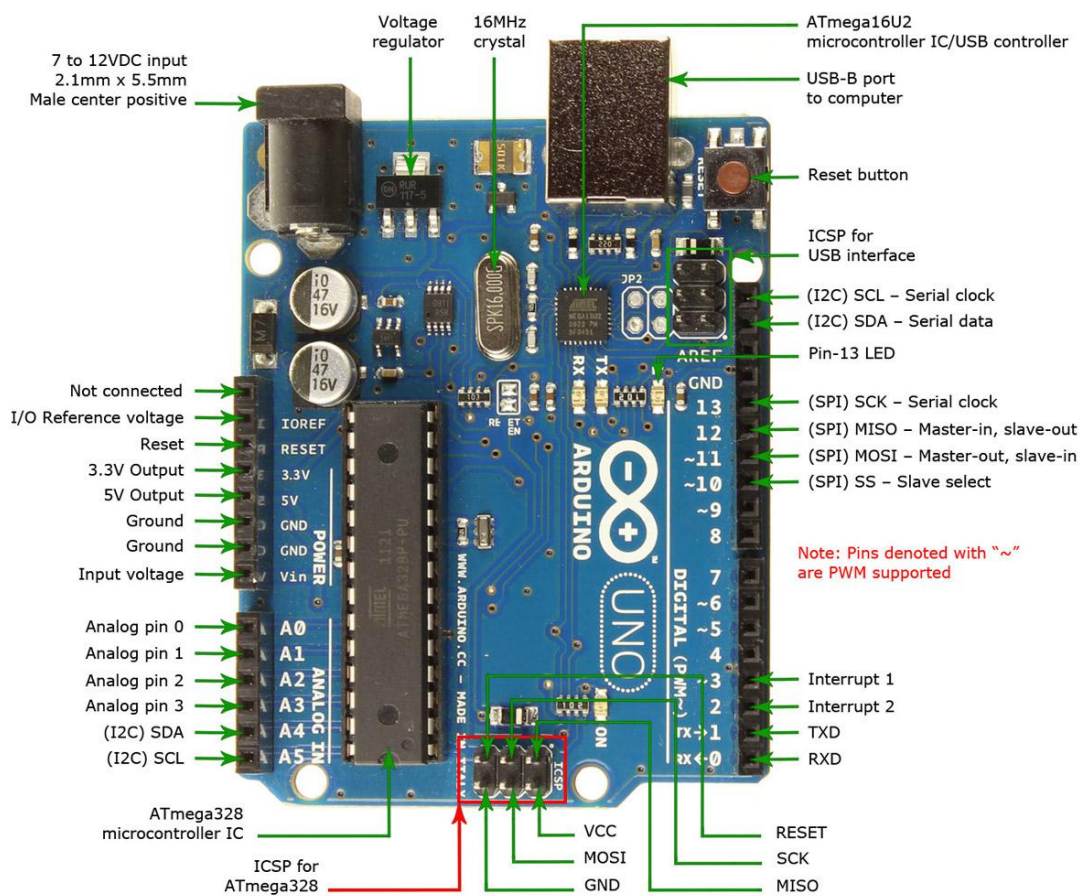
Figure C: The Arduino UNO board and its pins allocations (Robomart.com.)

Appendix H: API source code of the Training Phase

The coding should be inside a single .ino (Arduino format) file. The coding shown below are separated in different blocks for ease of understanding. Alternatively, the source code can also be downloaded at:

https://mega.nz/#!95oX3SrI!rw10vOTxda2swLoQbIJaWH_ijTnu6MUrmiQyDjjCYuU

or by scanning the QR code:

```
byte address16H, address16L, rssi, frameID;
byte discard, rstatus;

int serInLen = 25; //for Gobetwino non-zero and error handling
char serInString[25];
```
Definitions

```
void setup() {
  // initialize serial communication at 9600 bits per second:
  Serial.begin(9600);
  readSerialString(serInString,1000);
  delay(1000); //allow Serial initiation
}
```
Initializations

```
void loop() {
 //Tag 5: 7E 00 0F 17 01 00 13 A2 00 40 A9 EA 2F FF FE 02 44 42 AB
 Serial.write(0x7E);
 Serial.write(0x00);
 Serial.write(0x0F);
 Serial.write(0x17);
 Serial.write(0x01);
 Serial.write(0x00);
 Serial.write(0x13);
 Serial.write(0xA2);
 Serial.write(0x00);
 Serial.write(0x40);  //64 bit address for Tag 5 .16 bit optional or just put FF FE
 Serial.write(0xA9);
 Serial.write(0xEA);
 Serial.write(0x2F);
 Serial.write(0xFF);
 Serial.write(0xFE);
 Serial.write(0x02);
 Serial.write(0x44);
 Serial.write(0x42);
 Serial.write(0xAB); //checksum for Tag 5

 Serial.println("DB command sent"); //confirmation in Arduino and activation in GetBetwino
 delay(2500); //must wait for retransmission to finish, if any

 while (Serial.available() >=19) {  //frame size checkup
  if (Serial.read()==0x7E){  //by now, the tag should have responded with its RSSI data

  for (int i=0; i<5; i++){
    discard = Serial.read(); //ignore frame fields that are not used
   }

  for (int i=0; i<8; i++){
    discard = Serial.read();
   }
  address16H = Serial.read(); //Serial.read removes 1 byte from rx buffer and inserts into the
//variable
  address16L = Serial.read();
  discard = Serial.read();
  discard = Serial.read();
  rstatus = Serial.read();

  rssi = Serial.read();

  logData();

  delay(1000);
  }
 }
```

Sending the API frame and reading the RSSI data from the buffer. This part is repeated another 3 times for Tag 2, 6 and Router 1.

```
void logData()
{
                            //Data logging to Gobetwino
  Serial.print("#S|CDE|[");        //write data to .txt file named CDE

  if (rstatus == 0x04){  //rx failure
    Serial.print("No response from node");
    Serial.println("]#");
  }
  else if(rstatus ==126){  //Xbee not available
    Serial.println("Xbee not responding");
    Serial.println("]#");
  }
  else{
    Serial.print(address16H,HEX);
    Serial.print(";");
    Serial.print(address16L,HEX);
    Serial.print(";");
    Serial.print(rssi,DEC);  //if RSSI=5, it's local loop (destination address wrong)
    Serial.println("]#");
  }


  readSerialString(serInString,1000);
  // There ought to be a check here for a non 0 return value indicating an error and some error
//handling
}
```

Gobetwino defined the data format that enables it to capture the serial data from Arduino.

```
void readSerialString (char *strArray,long timeOut)
{
  long startTime=millis();
  int i;

  while (!Serial.available()) {
    if (millis()-startTime >= timeOut) {
      return;
    }
  }
  while (Serial.available() && i < serInLen) {
    strArray[i] = Serial.read();
    i++;
  }
}
```

Error handling required by Gobetwino

Appendix I: Source code for the Monitoring Phase

The GUI only shows the crowd classification for a single node. The GUI is based on the Arduino IDE.

<table>
<tr>
<td>

```
byte address16H, address16L, rssi, frameID;
byte discard, rstatus;

int serInLen = 25; //for Gobetwino non-zero and error handling
char serInString[25];


void setup() {
 // initialize serial communication at 9600 bits per second:
 Serial.begin(9600);
 readSerialString(serInString,1000);
 delay(1000); //allow Serial initiation
}
```

</td>
<td>Definitions and initializations</td>
</tr>
</table>

<table>
<tr>
<td>

```
void loop() {

//Tag 6: 7E 00 0F 17 01 00 13 A2 00 40 AD 16 C9 FF FE 02 44 42 E1
 Serial.write(0x7E);
 Serial.write(0x00);
 Serial.write(0x0F);
 Serial.write(0x17);
 Serial.write(0x01);
 Serial.write(0x00);
 Serial.write(0x13);
 Serial.write(0xA2);
 Serial.write(0x00);
 Serial.write(0x40);
 Serial.write(0xAD);
 Serial.write(0x16);
 Serial.write(0xC9);
 Serial.write(0xFF);
 Serial.write(0xFE);
 Serial.write(0x02);
 Serial.write(0x44);
 Serial.write(0x42);
 Serial.write(0xE1);
 //Serial.println("DB command sent"); //confirmation in Arduino and activation in
GetBetwino

 delay(1000);
```

</td>
<td>Sending the API frame</td>
</tr>
</table>

```
while (Serial.available() >=19) {
  if (Serial.read()==0x7E){

    for (int i=0; i<5; i++){
      discard = Serial.read();       //Serial.read removes 1 byte from rx buffer and inserts into the
variable, then ++ pointer
    }

    for (int i=0; i<8; i++){
      discard = Serial.read();
    }
    address16H = Serial.read();
    address16L = Serial.read();
    discard = Serial.read();
    discard = Serial.read();
    rstatus = Serial.read();

    rssi = Serial.read();

    if (rssi <= 58)
    Serial.println("Low Density");
    else if (rssi <=76 && rssi >58)
    Serial.println("Medium Density");
    else
    Serial.println("High Density");

    delay(1000);
    }
  }
}
```

```
void readSerialString (char *strArray,long timeOut)
{
  long startTime=millis();
  int i;

  while (!Serial.available()) {
    if (millis()-startTime >= timeOut) {
      return;
    }
  }
  while (Serial.available() && i < serInLen) {
    strArray[i] = Serial.read();
    i++;
  }
}
```

Appendix J: Bill of Materials of the H-CDE Tag

Name	Brand / Label	Value / Description
BQ25504	Texas Instruments	Power management unit
16-pin 0.5 mm pitch QFN board	Schmartboard	Breakout board for BQ25504
500 mW solar cell	Sandy-Worldbest	-
1 W solar cell	Sandy-Worldbest	-
Lithium ion polymer battery	-	3.7 V, 2000 mAh
Xbee module	Digi International	Series 2 PRO S2B
Xbee module breakout board	Cytron	Requires 2 mm pitch female pins and 2.54 mm pitch male pins
Switch	-	2 poles
JST female pin	-	To match with li-ion battery connector
L_{BST}	Inductor	22 µH
C_{STOR}	Capacitor	4.7 µF
C_{REF}	Capacitor	0.01 µF
C_{FLTR}	Capacitor	0.1 µF
R_{OC1}	Resistor	15.3 MΩ
R_{OC2}	Resistor	3.9 MΩ
R_{OK1}	Resistor	3.3 MΩ
R_{OK2}	Resistor	6.2 MΩ
R_{OK3}	Resistor	0.3 MΩ
R_{OV1}	Resistor	5.2 MΩ
R_{OV2}	Resistor	4.8 MΩ
R_{UV1}	Resistor	4.22 MΩ
R_{UV2}	Resistor	5.9 MΩ

Appendix K: DOE Template

The DOE template contains 109 rows and is deemed unsuitable for display in the thesis. The template can be downloaded at:

https://mega.nz/#!xogW2bRB!dHA2_s5btjRIRe-kdZlCobNtiY-ia89M2JHwBRmiqSs

or by scanning the QR code:

The template can be viewed using the Minitab software.

Appendix L: SMD Circuit Design for the H-CDE Tag
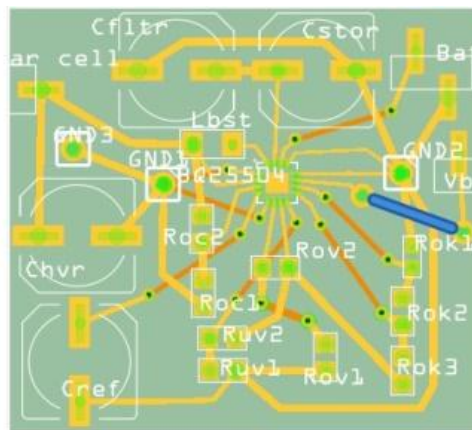
Appendix M: A Small Improvement in the BQ25504 Design

The BQ25504 IC requires exactly 9 resistors to program its function correctly. The drilldown of the settings is listed below:

- 2 resistors for MPPT

- 2 resistors for battery over-voltage protection

- 2 resistors for battery under-voltage protection

- 3 resistors for battery normal operation

However, there is a known exploit by Stofka (2013) where only 7 resistors are sufficient to program the IC. This is done by sharing the resistor network between the over- and under-voltage settings. This feature is only possible if the over- and under-voltage protection differs exactly by a factor of 1.5. For example, consider the following case for equation 4.3:

$$V_{OV} = \frac{3}{2} 1.25 \ V \left(1 + \frac{6M}{4M}\right)$$

Thus, the over-voltage threshold is 4.69 V. The 1.5 (3/2) multiplier is already integrated inside the IC. From equation 4.2:

$$V_{UV} = 1.25 \ V \left(1 + \frac{6M}{4M}\right)$$

Therefore, the under-voltage threshold is 3.13 V.

The setup for this arrangement is shown in Figure E. Unfortunately this setup could not be applied in the H-CDE system as the parameters are not suitable for implementation.
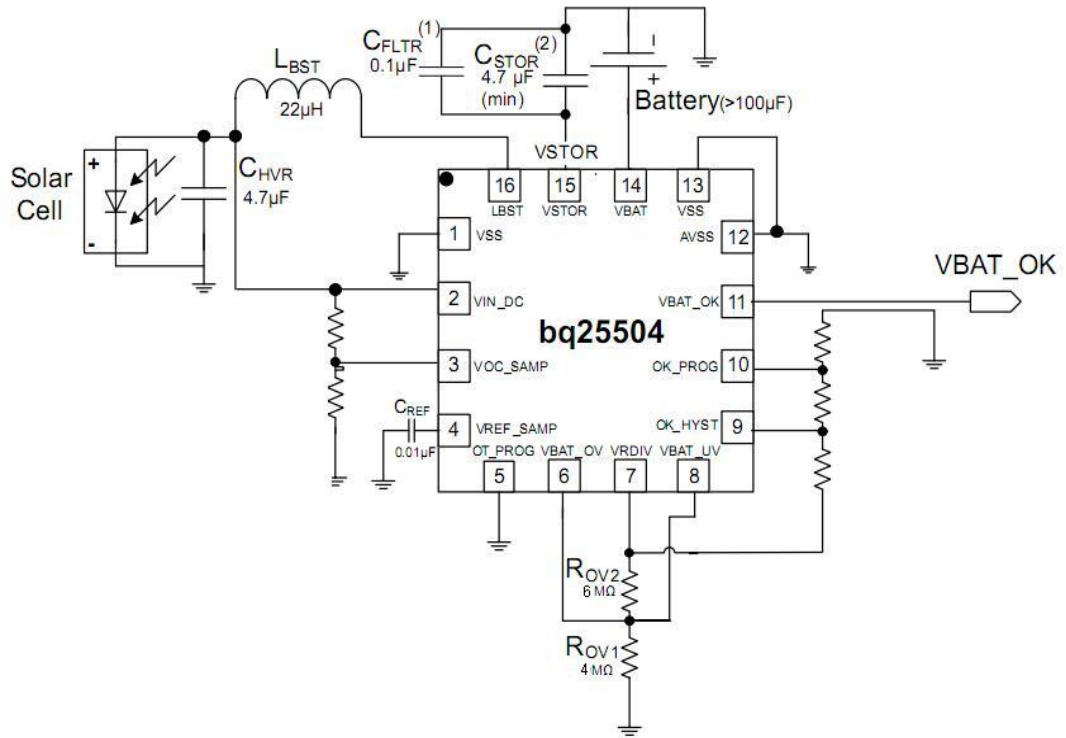
Figure D: Pin 6 (over-voltage) and 8 (under-voltage) of the IC share the same resistor network at pin 7.

LIST OF PUBLICATIONS

S. Y. Fadhlullah and W. Ismail (2014). *Data Fusion for Reducing Power Consumption in Arduino-Xbee Wireless Sensor Network Platform*. Paper presented at the 2nd International Conference on Computer and Information Science (ICCOINS), June 2014, Kuala Lumpur. Scopus indexed.

S. Y. Fadhlullah (2015). *Introduction to Energy Harvesting for Low-powered Wireless Sensor Network*. Paper presented at the 5th Postgraduate Colloquium (EEPC 2015) on 9-11th February 2015 at Harvard Suasana Hotel, Sungai Petani, Kedah.

S. Y. Fadhlullah & W. Ismail (2015). *Solar Energy Harvesting Design Framework for 3.3 V Small and Low-powered Devices in Wireless Sensor Network*. Paper presented at the 1st International Conference on Telematics and Future Generation Networks (TAFGEN2015) on 26-28th May 2015, Kuala Lumpur. Scopus indexed.

S. Y. Fadhlullah & W. Ismail (2016). *A Statistical Approach in Designing an RF-Based Human Crowd Density Estimation System*. International Journal of Distributed Sensor Networks. Volume 2016. Scopus and JCR listed. Impact factor: 0.906 (2015).

S. Y. Fadhlullah (2016). 2.4 GHz Xbee Pocket Manual. Available at: https://www.researchgate.net/publication/299448733_Xbee_Pocket_Manual